Nicolas Lorente

Christian Joachim   *Editors*

Architecture and Design of Molecule Logic Gates and Atom Circuits

Proceedings of the 2nd AtMol European Workshop

Advances in Atom and Single Molecule Machines

For further volumes:
http://www.springer.com/series/10425

Nicolas Lorente • Christian Joachim
Editors

Architecture and Design of Molecule Logic Gates and Atom Circuits

Proceedings of the
2nd AtMol European Workshop

≧ Springer

Editors

Nicolas Lorente
CIN2 (CSIC-ICN)
Bellaterra, Spain

Christian Joachim
GNS (CEMES-CNRS)
Rue Jeanne Marvig
Toulousse Cedex
France

Preface

This book encompasses contributions of the second AtMol Workshop in Barcelona, January 2012. AtMol is a research project fully supported by the European Commission's ICT-FET programme. AtMol was launched on 1st January 2011 for duration of 4 years, with the objective to construct the first ever complete molecular chip. A molecular chip is a small nanomachine where common microelectronic functionalities are brought and encapsulated at the atomic scale. The core of a molecular chip will make use of the extraordinary properties of molecule(s) and surface atomic wire(s), both regarding their chemical and quantum electronic characteristics that should be of practical use and appealing to future information technologies (ITs) manufacturing. The IT technology is approaching the atomic scale and many reports on molecular devices have filled the literature in the last decade. Hence, it was time to look at the field from the broad perspective of the different possible architectures for a molecular system to perform at least an elementary Boolean logic function at the atomic scale. This is the aim of the present book and its corresponding originating workshop. In order to steer discussions and gather the main ideas and challenges arising in molecular-based ITs, the book has been divided into five sections, each section containing contributions from different groups worldwide.

Design issues are dealt within three sections of the book. These range from extension of known hybrid molecular-electronics strategies, which correspond to Molecular Devices for Classical Logic, from designs based on intramolecular quantum behaviour in a section entitled Quantum Controlled Logic Gates and a section on the nowadays standard Molecular Qubits. The design of the molecular-chip core is not the only challenge to be faced by future IT technologies but also the interface of the molecular-chip core with the macroscopic world. These interfaces will necessarily have to match the atom scale with the macroscopic one. In this book two sections have been devoted to the study of the circuits that should connect and interconnect the active molecule logic gates. The first section builds on the gathered know-how on molecular devices, presenting how molecule(s) themselves can be used as circuits that interconnect and do the interfacing. A second section on Surface Dangling Bond Circuits presents appealing new designs to connect the

atomic world with the macroscopic one using stable solid surfaces where atomic-size wires have been constructed through modifying electronic states with an atomic precision.

The topics reported in this book have immense potential for future IT as recognized at the European Commission level. We are happy to thank the ICT-FET programme and A*STAR of Singapore for the financial support in organizing this second workshop and Springer Verlag and its staff members for the publication of this book. We are sure that this book will become a referent and an important step towards the realization of atomic- and molecular-based technologies.

For the organizing committee   Nicolás Lorente

Contents

Architecture at the End of Moore

Stefanos Kaxiras

Abstract Computer architecture in recent years shifted focus from performance to power efficiency (a combined metric or performance and energy consumption). For decades architects translated Moore's law into performance, but we are now close to hitting two major "walls": The first is the "power wall," or our inability to significantly reduce power consumption (and more importantly power density). The power wall is likely to lead us to a "dark silicon" future where the majority of the transistors on a chip will have to be turned off because of power constraints. The second is the "memory wall." Because, fundamentally, our current memory technology can be fast *or* vast, but not both at the same time, we have to rely on a complex memory hierarchy which, nevertheless, has significant limitations. In addition to power and performance, architects also worry about reliability. As we scale to very small feature sizes, devices become increasingly unreliable. A new trend that is emerging, however, is to embrace unreliability rather than fight it. This chapter discusses the challenges computer architects are facing today and the possible connections at the architectural level with novel devices that are in development.

1 Introduction

While for many years, architects have been very successful in exploiting Moore's law to provide exponential performance increases, we are now facing a power consumption problem. Compounded by the "memory wall" problem, the exponentially growing discrepancy between logic and memory speed, and complicated by increasingly unreliable devices, as we scale the technology node towards 10 nm,

S. Kaxiras
Uppsala University, Biskopsgatan 3 753 10 Uppsala, Sweden
e-mail: kaxiras@ece.upatras.gr

architects are faced with new challenges. The reaction to these problems, in many ways, can pave the way for novel devices that are distinctly different from the silicon transistors we are so used to. This chapter discusses novel directions for architecture at the end of Moore's scaling.

2   A Layered Approach

For decades computer architects translated the abundance of transistors afforded by Moore's law into performance. Unfortunately, this very successful run has come to an abrupt end in the past decade, and the main reason for this is power consumption. The job of the computer architect is to define the hardware/software interface and to exploit technology trends to translate them into computer performance, reduced power consumption, reliability, etc. The reason why this has been so successful (in fact, exponentially successful: doubling of the performance every 2 years) is because of a layered approach that has been followed in computer engineering. Each layer (from devices to architecture, to operating systems/computer languages, and to applications) is optimized independently. Thus, the software engineer need not worry how to move electrons in circuits and can instead concentrate on creating the best algorithm to solve a problem. Historically, this layered approach has been very resistant to a breach. Witness, for example, the difficulty of reconfigurable computing in the 1980s and in the 1990s to make inroads into the general-purpose processor market. This had to do more with the breach of the layered approach (the programmer had to create the hardware) rather than with any inherent problems with the technology. Today's constraints change the trade-offs in favor of such an approach: Reconfigurable computing now becomes a viable option because its benefits (power efficiency) outweigh its disadvantage. This in turn may facilitate the introduction of novel devices with novel functionality, or reconfigurable behavior, that needs to be exposed to the application layers.

3   Background: The Power Problem

The power problem is a consequence of the breakdown of Dennard's scaling rules (Table 1) that embodied Moore's law for more than three decades. In Dennard's scaling, smaller transistors give more power-efficient circuits and keep the power density constant. A breakdown occurred, however, when static power consumption suddenly became a major issue. Static power consumption was completely ignored at the architectural level until then. After all, the CMOS technology dominated simply because the complementary p- and n-networks did not allow any path from supply voltage to ground, consuming power only when switching (dynamic power and some glitch power). However, when technology scaling broke the 100-nm barrier, transistors showed their true analog nature: They are never truly off, allowing

Table 1 Dennard's scaling rules [1]

Device or circuit parameter	Scaling factor
Device dimension t_{ox}, L, W	$1/k$
Doping concentration N_a	K
Voltage V	$1/k$
Current I	$1/k$
Capacitance eA/t	$1/k$
Delay time per circuit VC/I	$1/k$
Power dissipation per circuit VI	$1/k^2$
Power density VI/A	1

leakage currents to flow. Worse, subthreshold leakage currents are exponential to threshold voltage reductions. In Dennard's scaling, the major mechanism to improve power efficiency is the reduction of the supply voltage, which assumes a reduction of the threshold voltage (since their difference dictates transistor switching speed). The rise of static power brought a complete stop to the power benefits architects took for granted for many technology generations. One-time reductions of static power consumption are possible, but the trends remain the same with scaling. For example, consider Intel's switch to 3D fin-FET transistors in their newest 22-nm technology [2]. While this change provided a step reduction in leakage going from 32 to 22 nm, the same benefit is not available for the next scaling.

4 Multicores, Dark Silicon, and the Rise of the Heterogeneous Architectures

The shift to multicore architectures started in 2004 as a reaction to the growing problem of increased power consumption and power density. Effectively, we abandoned frequency scaling (which resulted in significant increases in both dynamic and static power consumption) in favor of laying down more cores on the same chip. Figure 1 shows many of the CPU trends and the inflection point in 2004. Before this shift, architects primarily exploited instruction-level parallelism (ILP)—parallelism found in the dynamic instruction stream during execution of a program. To discover and exploit this parallelism, significant hardware resources were thrown to the problem. Sophisticated techniques such as out-of-order execution, branch prediction and speculative execution, register renaming, and memory dependence prediction, among others, were developed for this purpose. These approaches do no scale well, resulting in diminishing performance returns (number of instructions executed in parallel) for increasing hardware investments. Dynamic power scaled even worse, deteriorating the power efficiency of this approach. In fact, power dissipation scales as performance raised to the 1.73 power for the typical ILP core: A Pentium 4 is about 6 times the performance of an i486 at 24 times the power!

Our inability to scale a single core to further exploit ILP in a power-efficient manner turned computer architecture towards exploring alternative kinds of parallelism (task/thread parallelism, data parallelism). Multicore and many-core architectures
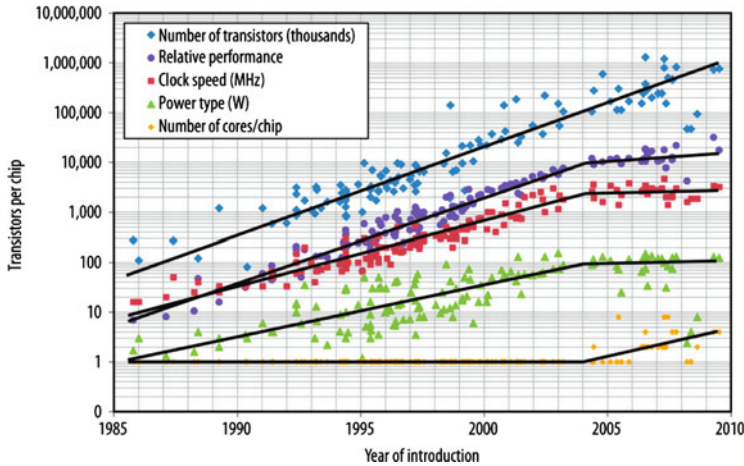
Fig. 1 Moore's law and corollaries (adapted from http://cpudb.stanford.edu/)

are designed for explicit parallelism. Unfortunately, as predicted by industry leaders (e.g., C. Moore, AMD), the multicore revolution by itself cannot solve the power problem because of the inefficiencies that appear as we scale the number of cores. We are faced with the same problems as with the single-core architecture: We are unable to extract sufficient speedup from parallel programs (see below Amdahl's law). The answer to this greater challenge is the rise of heterogeneous architectures where specific functions are accelerated (performance) by dedicated hardware (power efficiency). These architectures are fast becoming the dominant paradigm after multicore [3]. The catalyst for the proliferation of heterogeneous architectures is a possible development in the near future called dark silicon. Given a fixed power budget, only a small portion of the chip will be powered up at any point in time. This, however, allows unprecedented flexibility for specialization, because a large number of accelerators can be built on the same chip to be woken up only when needed.

But we do not need to speculate about this future as heterogeneous parallel computing is here today. If we examine the product lines from the major chip manufacturers, we see that both AMD and Intel now have separate multicore x86 architectures targeted at high performance (2–12 cores, 100W, 100 GFLOPs) and low power (1–2 cores, 10W, 10 GFLOPs) and are integrating data-parallel graphics cores onto their CPU devices with distinct programming and memory models. In the embedded world, MIPS and ARM offer a range of cores at different performance/efficiency points (1–2 cores, 2W, 10 GMIPS) with a range of programmable graphics cores. Nvidia, TI, and Qualcomm all sell heterogeneous ARM/GPU processors with many fixed-function accelerator blocks for the smart phone market, and there are multiple start-ups with 64–100-core devices for networking and telecom. This present-day processor heterogeneity forces system and software designers to address the difficult optimization challenge of choosing

the right processor (both at design time and runtime) for their product's power and performance requirements.

The motivation for this shift to heterogeneity is simple: If you can customize the hardware for a given task, you can achieve dramatically improved efficiency. By trading off performance, embedded CPU manufacturers have been able to demonstrate 10× wins in overall efficiency and 100× wins in absolute energy. Beyond tuning the architecture for the domain, astonishing efficiency gains can be obtained if the architecture is matched to the problem. Graphics processors have long leveraged this application-architecture synergy by applying massively data-parallel processors to an inherently data-parallel problem and thereby achieving $10 - 100×$ gains in efficiency. In the high-performance computing (HPC) environment, system power costs exceed hardware costs after only 3 years. This means that every 1 % saved in energy through code optimization results in a 1 % total cost reduction. Such an analysis makes the appeal of heterogeneous efficiency gains immediately obvious.

The incentive for heterogeneous architectures is augmented by the possibility of having many more transistors than what we can power up. With these "dormant" transistors, we can build a plethora of specialized accelerators that do not cost anything either in terms of "active" area or power when not in use. The argument for this possible future is exemplified in the example from ARM (Fig. 2). If transistor density increases in line with Moore's law, a current-generation 45-nm chip will shrink to a quarter the size at 22 nm in 2014 and a 16th at 11 nm in 2020. Using the ITRS roadmap for scaling, the smaller chips would be more efficient, drawing the same power at 22 nm even though the peak frequency increases by a factor of 1.6 and 40 % less at 11 nm with 2.4× peak clock speed. But, if we maintain the *same chip area*, we can pack four times the number of transistors at 22 nm and 16 times at 11 nm. For the same initial power budget, this means that only 25 % of the transistors can be power up in 22 nm and 10 % in 11 nm. These results are also supported in recent academic studies [5]. The proliferation of specialized cores is already a fact in prominent research efforts such as the *conservation core* project [6].

Today we find ourselves at a point where the whole world of computing is turning to heterogeneous multicores for efficiency. This switch to heterogeneity can be leveraged for the introduction of novel devices as accelerators since both architects and the software community are primed to deal with specialization. In other words, a novel device that accelerates a specialized function in a very power-efficient manner is a worthy investment, even when it is not practical to build a general-purpose processor out if it.

4.1 Amdahl's Law

Amdahl's law simply states that the overall speedup is limited by the part of a computation that cannot be accelerated. The law is expressed as follows:

$$\text{Speedup} = 1/\left[(1 - P) + P/N\right]$$

YEAR	2008	2014	2020	
Die				$(4\times1)^{-1} = 25\%$ Exploitable Area $(16\times0.6)^{-1} = 10\%$
Node	45nm	22nm	11nm	
Area^{-1}	1	4	16	
Peak Freq.	1	1.6	2.4	
Power	1	1	0.6	
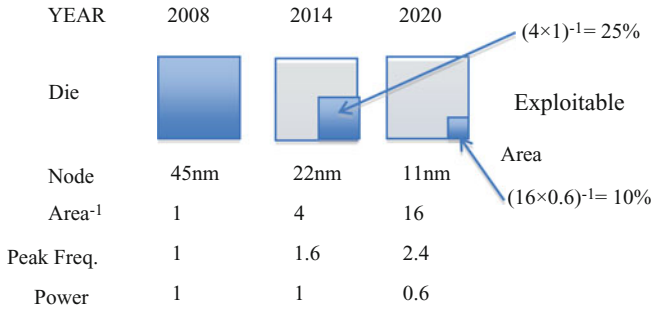
Fig. 2 Dark silicon as seen by ARM (adapted from [4])

where P is the part of the computation that is accelerated and N is the acceleration factor. Even if a novel device accelerates a function $1,000\times$ (for, say, $1,000\times$ less power), the end result can be small if this function rarely occurs in computations. It is, therefore, important to make the *common case* fast.

5 Computation Vs. Data Movement

Where is power spent? The key limitation in graphics processing unit (GPU) performance is now power consumption. Interestingly, the main source of power consumption is not calculations but transferring data over large distances on the chip or, even worse, off chip. At the International Conference on Supercomputing in 2010, Bill Dally, chief scientist and senior VP of research of NVIDIA, gave a keynote about GPU throughput computing [7]. Among others, he presented the diagram shown in Fig. 3, which illustrates the area and energy consumed by a 16-bit multiply accumulate (MAC) unit, a 64-bit floating-point unit (FPU), on-chip channels of various widths and lengths, and off-chip channels. It shows that a floating-point operation is an order of magnitude more energy efficient than moving a word across the die over a distance of half the die length (e.g., to access the last level cache). A 16-bit MAC operation is two orders of magnitude more energy efficient than fetching its operands from the last level cache. Even worse are communications over off-chip channels. They consume, approximately, a factor of $40\times$ more energy than accesses to the last level cache, which is two to three orders of magnitude more than the energy dissipated by floating-point operations and 16-bit MAC operations.

The implication is that power-efficiency gains from the introduction of a novel device can be overshadowed by data transfer costs, unless significant strides are made also for the data transfer. The advantage here probably goes to approaches that can transfer information by transferring a quantum property (e.g., spin) rather than a particle (electron).
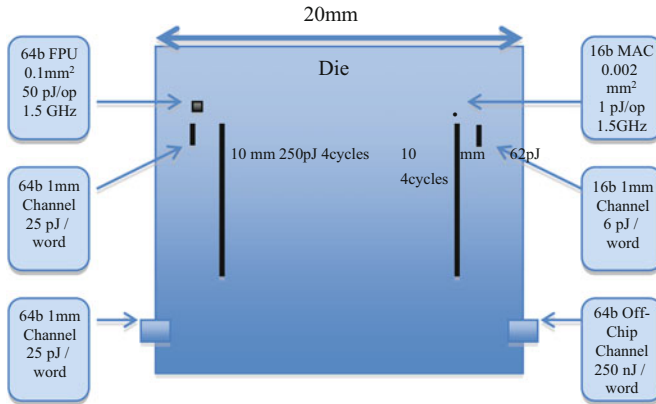
Fig. 3 Area and power consumption of functional units, on-chip channels, and off-chip channels (adapted from [7])

6   The Memory Wall

A different problem in computer architecture arises from the discrepancy between logic speed (calculations) and memory. Dynamic RAM (DRAM) main memory uses capacitors to store bits. Because the emphasis in this technology is on density, speed takes a secondary place. Of course, we also have faster memory technologies such as the 6-transitor static RAM (SRAM) or registers (gate-based flip-flops). But the faster the technology, the less dense we can make it. Furthermore, trying to increase the size of a memory array in a given technology (say, a SRAM array) makes it slower because the wires that activate the memory cells and transfer the data increase in length. Thus, a fundamental characteristic of memory (in any technology) is that it can be *vast* or *fast* but not both at the same time. A novel technology that can break this characteristic would represent a significant step forward in computer design.

Because the speed of logic circuits, following Moore's law, doubles every 2 years while memory technology increases speed much more slowly, computer architecture is faced with an exponentially increasing gap in processor-memory performance. This gap is dubbed the "memory wall" [8]. Architecturally, we close this gap using elaborate memory hierarchies, comprising successively smaller but faster memories toward the CPU (where the computation takes place) [9]. Useful or frequently accessed data are automatically transferred from slow memories to faster memories. This provides the illusion of a fast, large, and cheap memory system, most of the time. The reason why such hierarchies work is that most (but not all!) programs exhibit *locality of reference*: Accessed data are very likely to be accessed again in the near future.

This behavior has implications on power consumption. The memory hierarchy is not only a performance optimization but also a power optimization: It brings useful

data closer to the CPU and reduces data transfers over long wires. Today, memory behavior, at first order, defines both performance and power [10].

However, because the memory gap is increasing exponentially, the memory hierarchy cannot be a universal solution. Furthermore, there are several important application domains where locality simply does not exist: sparse matrix algorithms, sorting, traversing complex data structures, indexing, data mining, Google search, and, in general, every situation where we need to go over vast data sets performing very little computation. Memory ultimately limits the performance we can get from frequency scaling [10]. This raises an interesting question: Can we embed functionality in memory?

This has been tried in the past with relatively small success. Processing in memory (PIM) is arguably the most well-known approach [11]. The idea is to disperse computational units in the memory arrays and execute massively data-parallel algorithms. A more recent approach, IRAM, is to integrate DRAM and vector processing [12]. The idea is that vector processing can exploit the tremendous bandwidth that is available with direct access to the DRAM arrays, even if DRAM latency remains relatively high. Both PIM and IRAM propose to include heavy-weight computational power in memory, and this may have been the reason why they have not been widely accepted. A different approach is the IPStash proposal, which argues for very little (but very useful) added functionality in memory arrays [13]. Taking this further, while it is difficult to foresee memory-performing floating-point calculations, it is much more straightforward to see the usefulness of memory being able to do simple comparisons, taking simple decisions, and managing its own contents. In many algorithms lacking locality (e.g., sorting, searching, graph algorithms), this functionality would make processing in memory effective. In terms of novel devices, dense memories with simple processing capabilities and very high internal connectivity/bandwidth would revolutionize the way we architect memory systems.

7 Reliability

Historically, architecture has had a preoccupation with reliability. This is only natural, since hardware must be bug-free in order to allow development of very complex software on it. In addition, computers are deployed in safety-critical missions where error-free operation must be guaranteed. Reliability is achieved by incorporating hefty margins (from the VLSI design rules to operating voltages, critical voltages, threshold voltages, and frequencies) as well as architectural techniques such as triple redundancy, error detection and correction codes (ECC), and parity bits. While we have taken hardware reliability for granted for many decades, technology scaling and the pressure to reduce power consumption are changing this.

Scaling devices close to 10 nm significantly increase their variability in speed, power consumption, and leakage power [14]. This creates significant reliability

problems that require either an increase in the design margins or some other approach to mitigate them. Regarding power consumption, lowering the supply voltage close to the critical voltage for a frequency also entails reliability problems (timing errors).

One approach is to allow errors to occur, detect them, and correct them at runtime. This approach was first proposed for timing errors when the supply voltage is lowered close to the critical voltage for a frequency [15]. The Razor flip-flop double samples its inputs (sampling for a second time after a small delay) and detects timing errors arising from aggressive voltage scaling. The errors are corrected at the architectural level, for example, flushing and restarting the CPU pipeline. Similar approaches can be envisioned for novel, inherently unreliable, devices.

A different approach, however, is emerging as a new trend. Instead of trying to enforce correctness, embrace unreliability and allow errors to occur! The idea is to tolerate errors at the architectural level. Stochastic architectures are mostly correct, but the outcome of a program is not affected by possible errors [16]. This is achieved when the whole design, including the algorithm, and the software are stochastic in nature. A large class of emerging client-side applications have inherent algorithmic or cognitive noise tolerance. Such applications are not fatally affected by errors; at worse, their quality of service may degrade gracefully. Examples include graphics (e.g., video codecs or rendering), simulations (e.g., Monte Carlo stochastic simulations), searching (e.g., Google search), and applications that are self-correcting or tolerate erroneous inputs (e.g., neural networks, cortical emulation). In this case, processors can be optimized for very low power instead of always preserving correctness. Errors are tolerated by the applications instead of spending power in detecting and correcting them at the circuit or at the architecture level.

What if we could embrace uncertainty (unreliability)? Although this is difficult for the general case, it can pave the way for novel devices burdened by a small degree of unreliability that would otherwise be very expensive to remedy.

8   Conclusions

"Around 2004, 50 years of exponential improvement in the performance of sequential computers ended [17]." The culprit is power consumption due to increase in leakage power and architectural inefficiency. The reaction to the power problem was the switch to multicore architectures. While multicores encourage the world to think in parallel, parallel programming remains hard and many applications are not scalable. This leads us to a possible future or dark silicon where we will be unable to power up all but a small part of a chip. Highly specialized accelerators are the approach architects are now exploring towards increased power efficiency in the era of dark silicon. This development paves the way for a smoother introduction of novel devices as accelerators.

Beyond power, memory is still a major limiting factor for performance. Technology that can mitigate the memory gap is bound to have an immediate impact in computer architecture. In this vain, combining functionality with information storage is a promising direction to pursue.

Finally, while reliability is necessary in many cases, new algorithms and architectures are now considered that can tolerate some degree of unreliability. This makes it easier for the introduction of novel but slightly unreliable devices that would otherwise be impractical.

References

1. Dennard, R.H., Gaensslen, F.H., Rideout, V.L., Bassous, E., LeBlanc, A.R.: Design of ion-implanted MOSFET's with very small physical dimensions. IEEE J. Solid State Circ. **9**(5), 256–268 (1974)
2. Borkar, S.: Design perspectives on 22nm CMOS and beyond. In: Proceedings of the 46th Design Automation Conference, (DAC'09), (2009)
3. Kumar, R.., Tullsen, D.M., Jouppi, N.P., Ranganathan, P.: Heterogeneous chip multiprocessors. IEEE Comput. **38**(11), 32–38 (2005)
4. Muller, M.: Chief Technology Officer, ARM, "Dark Silicon and the Internet," http://www.eetimes.com/virtualshows/ArmProgramSchedule
5. Esmaeilzadeh, H., Blem, E., St. Amant, R., Sankaralingam, K., Burger, D.: Dark silicon and the end of multicore scaling. In: Proceeding of the 38th annual international symposium on Computer architecture (ISCA '11), (2011)
6. Venkatesh, G. et al.: Conservation cores: reducing the energy of mature computations. In: Architectural Support for Programming Languages and Operating Systems (ASPLOS), (2010)
7. Dally W.: Throughput computing. In: keynote at International Conference on Supercomputing, (2010), http://videos.dac.com/46th/wedkey/dally.html
8. Wulf, Wm.A., McKee, Sally A.: Hitting the memory wall: implications of the obvious. ACM SIGARCH Comput. Architect. News **23**(1), 20–24 (1995)
9. Molka, D. et. al.: Memory performance and cache coherency effects on an Intel Nehalem multiprocessor system. In: Parallel Architectures and Compilation Techniques, (2009)
10. Keramidas, G., Spiliopoulos, V., Kaxiras, S.: Interval-based models for run-time DVFS orchestration in superscalar processors. In: Proceedings of the 7th ACM International Conference on Computing Frontiers (CF '10), (2010)
11. Hall, M. et al.: Mapping irregular applications to DIVA, a PIM-based data-intensive architecture. In: Proceedings of the 1999 ACM/IEEE conference on Supercomputing, (1999)
12. Patterson, D. et al.: A case for intelligent RAM. IEEE Micro **17**(2), 34–44 (1997)
13. Kaxiras, S., Keramidas, G.: IPStash: a power-efficient memory architecture for IP-lookup. In: Proceedings of the 36th annual IEEE/ACM International Symposium on Microarchitecture, (2003)
14. Borkar, S., Karnik, T., Vivek, De: Design and reliability challenges in nanometer technologies. In: Proceedings of the 41st annual Design Automation Conference (DAC '04), (2004)
15. Ernst, D. et al.: Razor: A low-power pipeline based on circuit-level timing speculation. Proceedings of the 36th Annual IEEE/ACM International Symposium on Microarchitecture, (2003)
16. Shanbhag, Naresh R., Abdallah, Rami A., Kumar, Rakesh, Jones, Douglas L.: Stochastic computation. 47th ACM/IEEE Design Automation Conference (DAC) (2010)
17. Olukotun, K., Hammond, L.: The future of microprocessors. ACM Queue **3**(7) (2005)

Part I
Molecular Devices for Classical Logic

Towards Post-CMOS Molecular Logic Devices

Roy Hakim, Elad. D. Mentovich, and Shachar Richter

Abstract The use of molecular devices in post-CMOS devices and structures is described. Particularly we demonstrate the fabrication and characterization of two-novel devices: a two-terminal device which exhibits a two-negative differential resistance peaks and a sub-10-nm-channel vertical molecular transistor which contains a molecular quantum-dot compound. We show that the latter device can be operated in two distinct modes: gate-controlled switch and gate-controlled hysteresis.

1 Introduction

The field of molecular electronics emerged in the past couple of decades and is drawing attention largely in light of the increasing limitations of solid-state microelectronics. Moore's law, the highly cited guideline first mentioned in 1965, predicts a doubling every 18–24 months of the number of transistors on an integrated circuit [1]. With the silicon metal-oxide-semiconductor (MOS) transistor, and later on complementary MOS (CMOS) architecture, this trend has been upheld by industry for the past five decades. Indeed, a decade ago, process technology was at the $0.18 - \mu$m (180 nm) node (referring to the channel length of a MOS transistor), while today, the 22-nm node is becoming the industry standard [2].

However, performance limitations are expected to increase with the scaling of devices. Leakage currents can occur by carriers tunneling through ever-thinner gate dielectrics or as subthreshold current between ever-closer source/drain regions, when the transistor is operating in the weak-inversion region. The increase in device density due to scaling also leads to an increase in generated heat and in the need

R. Hakim · E.D. Mentovich · S. Richter (✉)
Faculty of Exact Sciences and University, Center for Nano Science and Nanotechnology,
Tel Aviv University, Tel-Aviv, 69978, Israel
e-mail: srichter@post.tau.ac.il

to dissipate it. A variety of secondary effects, collectively termed short-channel effects, also play an increasing role in degraded transistor performance [3, 4]. One such example is drain-induced barrier lowering (DIBL). This effect describes a decrease in the potential barrier between the source and channel regions, due to the closer proximity of the drain region. The applied bias on the drain would therefore influence the magnitude of the drain current, which ideally is determined only by the gate voltage. This results in a lowering of the threshold voltage of the MOS transistor and higher subthreshold currents. Another secondary effect is surface scattering. As a result of narrower channel, and together with the lateral extension of the source/drain depletion regions into the channel region, the longitudinal component of the electrical field applied from the gate increases. As a result, carrier mobility is reduced in the lateral direction, as they tend to accelerate towards the gate. These stronger electric fields also increase the probability for electron carriers to tunnel into the gate dielectric. Once there they are trapped and build up charge in the dielectric. Threshold voltage must be increased to compensate for these charges, thereby degrading device performance. This is termed the hot electron effect. Indeed, increased subthreshold conduction and power consumption and the need for effective heat dissipation are some of the most relevant issues currently addressed by the semiconductor industry [5–7].

The negative effects of leakage currents are of particular importance for static random access memory (SRAM). An SRAM cell is typically composed of six MOS transistors, and the data bit is stored on four of the transistors, as two cross coupled inverters, as shown in the following figure (Fig. 1).

A key parameter in the design of SRAM circuits is the data retention voltage (DRV) which defines the minimum supply voltage to the circuit at which a data bit can be retained. Typical SRAM operation often requires reducing supply voltage to below the threshold voltage of the transistors, where conduction is primarily by leakage currents. Thus, as subthreshold conduction increases with device scaling, the power consumption of SRAM circuits becomes even more pronounced.

Several process innovations such as the transition to high-κ dielectrics, strained silicon channels, ultra-shallow junctions, and others have been implemented to combat these device performance issues [4]. Developments such as deep UV and immersion photolithography have further pushed the resolution limit for feature patterning [4, 8]. However, these too are nearing a physical limitation. The inevitable consequence of these innovations is an increased burden on R&D and production cost, and diminishing returns with every new technology node [5]. This trend has been termed ironically as Moore's second law. Lastly, with every new technology node, the positive effects of scaling on processing power, speed, and complexity are less pronounced, with other factors such as interconnect and memory access delays being the main limitations on performance [8]. As such, the 2010 update of the International Technology Roadmap for Semiconductors (ITRS) predicts a decline in development, with transistor count doubling only every 3 years starting 2013 [2].

Molecular electronics offers both an alternative and a complement to existing semiconductor technologies [9]. In the ideal scenario, the field addresses electronic devices comprising circuits in which specific molecules, as opposed to transistors or

Fig. 1 Typical setup of
SRAM
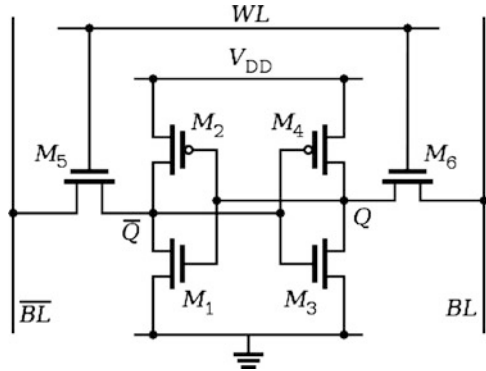
traditional thin films, are the basic building blocks. Besides the obvious advantage
of their small dimensions, individual molecules are identical and are therefore
expected to behave robustly as electronic devices, with no variance. The great
variety of molecules and the ability to synthesize them as needed leads to a
great variety in electrical, mechanical, and optical properties when considered as
practical devices. A key difference from conventional semiconductor technology
is in the fabrication, which takes on a bottom-up, as opposed to a top-down
approach. Whereas in industry, the bulk material is processed down to produce
scaled devices, in a bottom-up approach, the molecules are first synthesized and
then assembled into structures and circuits of increasing complexity [9–11]. This
requires a different approach and design for the fabrication process of molecular
circuits. While at heart it is a completely different approach to electronics, it is
expected that molecular electronics, at least in the coming years and decades, will
see increasing integration, as opposed to competition, with conventional electronics,
namely, silicon-based CMOS technology [9, 11]. Recent advances in molecular
devices, both two-terminal (such as molecular memristors [12]) and three-terminal
devices (molecular transistors [13]), offer appealing alternatives to the current logic
and memory technologies. In the following section these advances will be described.

1.1 Two-Terminal Molecular Junctions: Focusing on Negative Differential Resistance

A variety of materials can be exploited on the molecular and nanoscale levels
to produce unique electrical properties that can be then used to construct novel
electronic devices, with similar functionalities as CMOS devices. One example
is phase-change materials (PCM). A common choice of such materials is chalco-
genides family [14]. These have the ability to toggle between the amorphous and
crystalline phases when heated, for example, by applying an electrical current.
The two phases possess different electrical resistivity. Thus, when a given voltage

is applied across a PCM device, the resultant current will either be high or low, depending on the phase of the material. This applied voltage can be considered as a read voltage on a nonvolatile memory (NVM) cell. A program voltage will set the cell to a low-resistance "1" state. This voltage is determined by Joule heating, to a temperature above the crystallization point of the PCM material, but below its melting point. Once cooled, the cell is in the crystalline phase, the low-resistance "1" state. To erase the cell, a higher voltage is required to bring the cell above its melting point, to the amorphous phase, where the high resistance represents the "0" state. As such, NVM devices based on PCM materials are currently in development and production among the leading companies and slated to replace existing floating gate flash memory [15].

A positive effect of scaling such devices, besides increased memory density, is faster program and erase speeds. A PCM-based memory cell's speed is limited by the cooling time of the material following Joule heating. This cooling time is reduced along with device dimensions. However, there are several hurdles in full adoption of PCM-based memory [15].

Negative differential resistance (NDR) is another property found in some molecular systems and novel materials [16, 17]. It describes a decrease in current in response to an increase in applied bias over a given range, as shown in the following figure (Fig. 2).

An NDR device could cancel out an equal and opposite load resistance when connected in series and theoretically produce infinite power gain [18]. Incorporated into a resonance RLC circuit, an NDR element can produce high-frequency oscillators, operating in the microwave and infrared ranges [19, 20]. Rectifiers are another class of electrical devices that can be constructed using NDR elements [21, 22]. NDR can also be used to induce bistability in a circuit, a condition in which the circuit operates in two stable points. As such, circuits based on NDR elements have the potential to be used as digital logic and memory devices [23–25].

NDR has also been observed in a variety of single-molecular layers, termed monolayers [26]. For example, Chen et al. describe an NDR device in which the active region is a monolayer of 2'-amino-4-ethynylphenyl-4'-ethynylphenyl-5'-nitro-1-benzenethiolate, situated between two Au contacts [27]. An applied positive bias leads to a one-electron reduction from one of the contacts to the molecules. As a result, a radical anion is formed, acting as a charge carrier in the system, increasing the overall current. A higher applied bias leads to an additional one-electron reduction. In this scenario a nonconducting dianion state is reached, drastically reducing the overall current of the system. The group reports a peak current of 1.03 nA. The active layer was situated in circular regions of diameters 30–50 nm. As such, a current density of $\sim 53 \, A/cm^2$ was achieved in the devices. With a valley current of 1 pA, the peak-to-valley ratio (PVR, see Fig. 2) was 1,030, several orders of magnitude greater than possible with semiconductor NDR devices. However, these measurements were conducted at 60 K and significantly diminish approaching room temperature.

Earlier work conducted in our group has also shown NDR in monolayer devices [17]. In this case, a monolayer of a ferrocene-derived compound was used (Fig. 3).
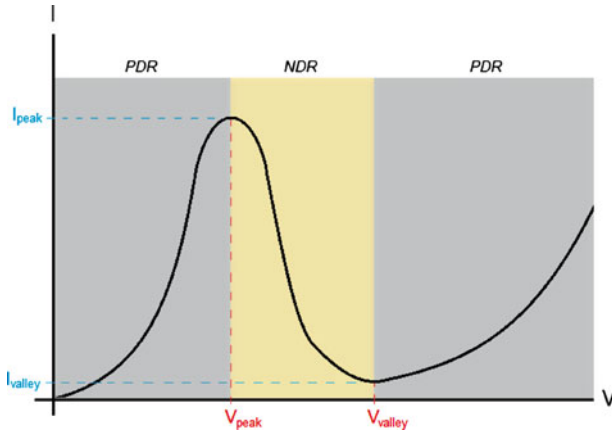
Fig. 2 Current/voltage characteristics of negative differential resistance
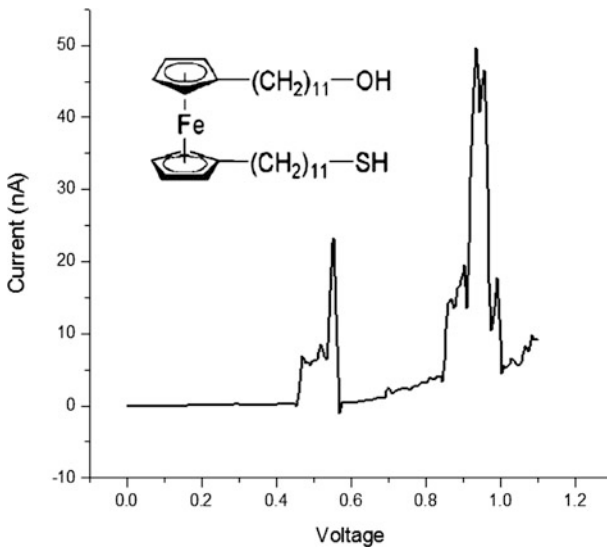
Fig. 3 Ferrocene-derivative molecule used to form a multi-peak NDR device (see [17])

The compound consists of a ferrocene molecule, $Fe(C_5H_5)_2$, synthesized with organic chains on both sides, where one chain is thiolated. The chemical structure of the compound and a typical I/V characteristics are shown in the following figure.

A monolayer of this material was formed over an Au bottom electrode and sandwiched on the opposite end by a Pd top electrode. Electrical measurements of the structure showed two NDR peaks at ~ 0.55 V and ~ 0.92 V. The mechanism responsible for these peaks has been speculated to relate to ferrocene redox reaction centers around the biases at which the peaks occur. Another hypothesis is the

formation of polaronic states which at the molecular junctions allows the formation of NDR [28].

NDR devices have been used in the pre-CMOS days to construct digital circuits. A classic implementation of such a design is the so-called Goto pair, first presented by E. Goto et al. in 1960, with a simple circuit using tunnel diodes [29, 30]. The circuit consists of two NDR devices in series and has since been named the Goto pair. Contemporary research into tunnel-diode logic circuits based on the Goto pair was also conducted by M.S. Axelrod et al. [31]. However, subsequent developments, namely, CMOS technology, have rendered this architecture as obsolete. Nonetheless, in recent years, a growing interest has been observed within academic circles in NDR-based logic and in the Goto pair as an implementation of such circuits [23, 32, 33]. A simple circuit based on the Goto pair is shown in the following schematic (Fig. 4).

The advantageous nature of this circuit for digital applications, as a consequence of the unique IV characteristics of NDR devices, is readily discernable from a load-line perspective. The voltage level of the circuit at the node between the two devices, labeled as n_2, will be stable at equilibrium points, in which the load and drive currents are equal. This can be seen in the following load-line diagrams, depicting two identical NDR devices.

These equilibrium points are marked as green dots above, at the intersections of the load and drive IV curves on the load-line diagrams. It can be seen that at biases below $\sim 2*V_{peak}$, with both devices in the PDR region, the circuit essentially behaves as a voltage divider. The corresponding current and voltage at node n_2 are shown at the intersections in Fig. 5a, b. With one stable equilibrium point, the circuit is termed monostable at these biases. Increasing V_{IN} above $\sim 2*V_{peak}$, the circuit undergoes a monostable–bistable transition (MBT), depicted in Fig. 5c, d. At these higher input biases, three equilibrium points exist for the state of the circuit at node n_2, in which the drive and load currents are equal. However, at the central point, both devices are in their NDR regions, and the circuit is at a state of unstable equilibrium. Any current fluctuation into node n_2 through the NDR devices will create an imbalance between I_D and I_L, and draw the circuit to one of the two other equilibrium points, where the circuit is at stable equilibrium. At the two stable points, minor current fluctuations will cause a charge imbalance that will dissipate within the circuit, but will not cause a change in the state/voltage at node n_2. Thus, with the ability to retain one of two voltages, the circuit is suitable for digital applications.

1.2 Three-Terminal Molecular Junctions: Towards Molecular Realization of the Floating-Body (1T) Transistor

For years, floating-body transistors have been touted as an alternative to conventional cache memory. Current capacitor-based cache memory technology is running

Fig. 4 An example of GOTO
pair circuit
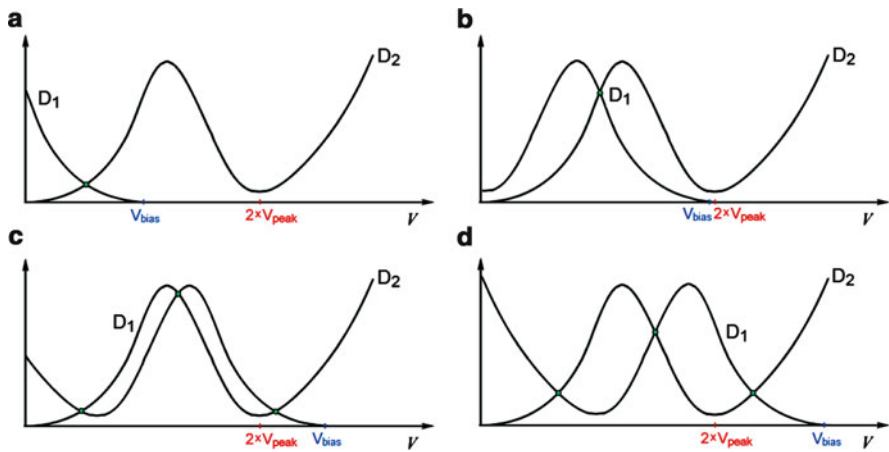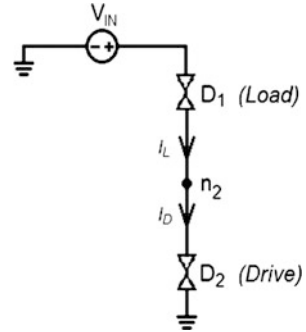
Fig. 5 Load-line diagrams of two NDR devices

out of gas. Since the storage capacitance must be kept constant, for the next
generations of conventional 1T-1C DRAM cells beyond the 22-nm technology node,
the miniaturization of the bulky storage capacitor will become more and more
difficult. In the future, several existing solutions such as trench or stacked capacitors
using high-k materials will remain expendable but at the expense of the loss of
performances and cost rising.

Several years ago, a new generation of DRAMs using only one transistor,
called 1T-DRAM, was proposed as an alternative to the usual 1T-1C DRAM
architecture. This memory cell uses the floating body of a single transistor to hold
the information, that is, to store the charge. It is also a candidate for increased
memory density, compared to the standard six transistor (6T) cache memory that
is used on all microprocessors today, as discussed in the introduction. As for
1T-1C DRAM cells, the crucial performance factors to consider are a high retention
time, sufficient-sensing margin, low programming bias which enables low power
consumption, and further cell scalability.

All the proposed and demonstrated 1T-DRAMs use the majority carriers stored at one interface to modulate the minority carrier current flowing at the opposite interface. This revolutionary principle is based on the coexistence of electrons and holes in the same body which basically requires a two-gate operation or moderately thick films (~ 50 nm). However, ultrathin films (≤ 10 nm) are needed for MOSFET scaling beyond the 45-nm node; this condition also applies to embedded 1T-DRAMs co-integrated with logic circuits. Unfortunately, the super-coupling effect forbids the simultaneous activation of the electron and hole channels, facing each other, in the same ultrathin silicon layer.

Our approach is to explore molecular systems to harvest sub-10-nm molecular transistors and to construct gate-controlled hysteresis device that can be used to form a novel 1T-DRAM. This molecular route is strongly supported by the ITRS vision which states that molecular-based electronics is one of the leading candidates to extend Moore's law [2]. However, this great potential was not realized by now due to the difficulty to fabricate reliable devices in parallel and in mass production. Recently, we and others have demonstrated several routes for the fabrication of molecular transistors which might be integrated in future device technologies. Recently, we reported on the formation of quantum-dot-based room-temperature vertical transistors that can fulfill the demands of future post-CMOS technologies.

Recently, we have demonstrated the fabrication of thousands of vertical molecular transistors on a single chip, all in fabricated in CMOS compatible facilities [13, 34–37] (see Fig. 6). Those transistors adopted a *hybrid approach* where CMOS vertical transistors structure was created while specially engineered molecular layers were self-assembled into a predetermined area. Importantly, the molecular layers defined the critical channel width (the molecular size – 1–4 nm) while offering the molecular versatility to determine the transport characteristics of the transistor.

This has been achieved by incorporation of a monolayer composed of a modified C_{60} molecular quantum-dot (MQD) system [36] or even electroactive protein layers [13, 35]. Figure 6 shows the MQT transistor in which it was asymmetrically coupled to the leads of the source and drain device *via* a thin oxide layer on the bottom contact and physical adsorption of Pd on the top contact. This vertical side-gate molecular transistor was operated at low voltages with high gate-voltage sensitivity, thus allowing reproducible and reliable measurements on various types of molecular systems. Moreover, the fabrication methodology allows the formation of multiple arrays of transistors fabricated in parallel with the use of conventional engineering processes and lithographic techniques [13, 36].

Figures 7 and 8 show the transistor and hysteresis measurements taken at two different values of VG. It can be seen that two new distinct modes of operations are demonstrated: "voltage-driven switching," in which the conductance can be modulated by the gate voltage, and a new mode of operation, "voltage-controlled hysteresis," in which the properties of the loop can be controlled by the gate voltage. While the first method can be exploited for switching applications, the second mode can be used for memory applications.
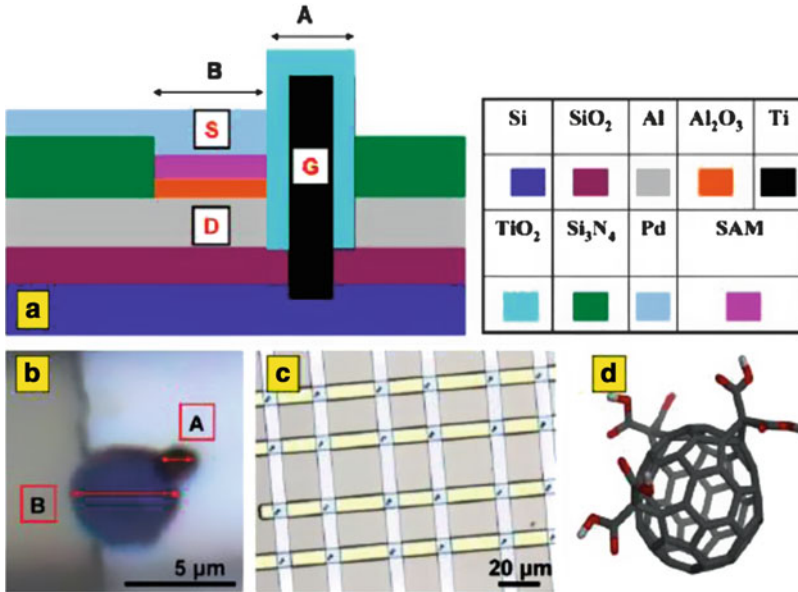
Fig. 6 Schematic representation of the transistor (the dimensions of the layer are unscaled for clarity). A side gate (A) is used to activate molecular layers stacked (B) vertically and separated from the source electrode by an oxide layer. The current is flowing between the source and the drain electrodes (S,D) and modulated by the gate lead (G). (**a,b**) Optical images of a single device (**c**) and of an array of transistors (**d**). The molecular layers are confined

Fig. 7 Gate-controlled switching of MQT transistor (see [36])
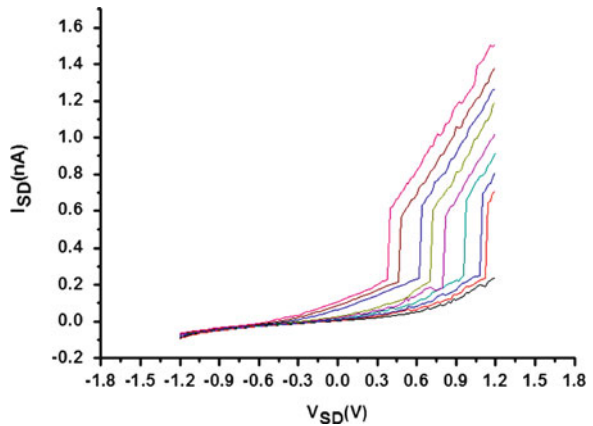
Our results can be understood from a consideration of the transistor structure and the polaronic model [28]. We have concluded that a successful operation of an MQD transistor must fulfill some of the following basic experimental conditions:
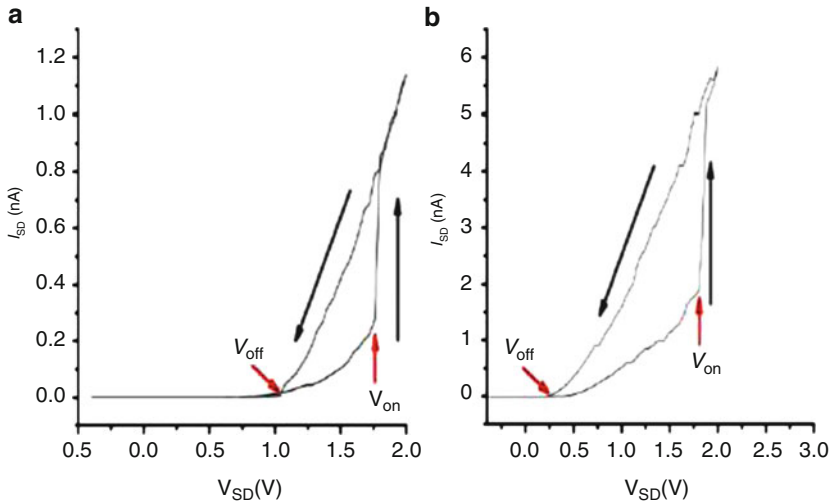
Fig. 8 Gate-controlled hysteresis. I–V curve of a typical molecular quantum-dot transistor exhibiting conductance switching and hysteresis taken at different gate voltages (0.64 V (**a**) and 1.15 V (**b**)). Von and Voff are defined at the first discontinuity point and at the crossing point of the reverse and forward scans, respectively

1. The tunneling rates in a polaronic transistor must be considerably slower than the polaronic relaxation time. In practice, this situation can be achieved by lightly coupling at least one of the electrodes to the molecular system. In our case this condition was fulfilled mainly by the introduction of the oxide spacer between the metallic electrode and the SAM.
2. Asymmetric junctions enhance the probability of measuring hysteresis effects. This point was discussed theoretically by D'Amico et al. [38] who noted that although a symmetric situation can also give rise to hysteretic behavior, this would happen only over a finite range of bias voltages, thus decreasing the probability of measuring it. On the basis of our results and on the above analysis, we conclude that asymmetrical junctions are experimentally favorable for molecular-transistor applications.
3. The vertical transistor configuration offers some advantages over the conventional lateral one, since it provides an additional degree of freedom in the choice of materials used for the source and the drain electrodes. While in our case we could easily construct asymmetric junctions by choosing different materials for the leads, in the lateral configuration, this task is very difficult. Furthermore, the vertical configuration allows the fabrication of complex (metal-oxide) contacts as demonstrated in this work.

To summarize, these post-CMOS transistors which operate in low power (below 1V) either in standard CMOS transistor operation mode or in single-electron quantum transistors mode thus offer new type of operation of gate-controlled hysteresis (see Fig. 2), hence offering new mechanism for charge storage.

Furthermore, these transistors offer the use of the inherent quantum effects allowing the operation of **1T-DRAM** in a new fashion utilizing the extraordinary switching and charging propertied of a molecular quantum do transistor [35] which allow the use of novel *advanced logic and memory platforms* that are extremely hard to achieve using current CMOS technology.

References

1. Schaller, R.R.: Moore's law: past, present, and future. IEEE Spectrum **34**, 52–& (1997)
2. International Roadmap for Semiconductors (Semiconductor Industry Association (SIA), SEMATECH, 2010)
3. Colinge, J.P., Colinge, C.A.: Physics of Semiconductor Devices. Kluwer Academic, Norwell (2002)
4. Campbell, S.A.: Fabrication Engineering at the Micro and Nanoscale. Oxford University Press, Oxford (2004)
5. Rupp, K., Selberherr, S.: The economic limit to Moore's law. IEEE T Semiconduct. M **24**, 1–4 (2011)
6. Frank, D.J. et al.: Device scaling limits of Si MOSFETs and their application dependencies. P IEEE **89**, 259–288 (2001)
7. Lemme, M.C. et al.: Subthreshold behavior of triple-gate MOSFETs on SOI material. Solid State Electron. **48**, 529–534 (2004)
8. Kim, N.S. et al.: Leakage current: Moore's law meets static power. Computer **36**, 68–+ (2003)
9. Lu, W., Lieber, C.M.: Nanoelectronics from the bottom up. Nat. Mater. **6**, 841–850 (2007)
10. Stan, M.R., Franzon, P.D., Goldstein, S.C., Lach, J.C., Ziegler, M.M.: Molecular electronics: From devices and interconnect to circuits and architecture. P IEEE **91**, 1940–1957 (2003)
11. Heath, J.R., Kuekes, P.J., Snider, G.S., Williams, R.S.: A defect-tolerant computer architecture: Opportunities for nanotechnology. Science **280**, 1716–1721 (1998)
12. Strukov, D.B., Snider, G.S., Stewart, D.R., Williams, R.S.: The missing memristor found. Nature **453**, 80–83 (2008)
13. Mentovich, E.D., Belgorodsky, B., Kalifa, I., Cohen, H., Richter, S.: Large-scale fabrication of 4-nm-channel vertical protein-based ambipolar transistors. Nano Lett. **9**, 1296–1300 (2009)
14. Strukova, D.B., Kohlstedta, H.: Resistive switching phenomena in thin films: Materials, devices, and applications. MRS Bull. **37**, 108–114 (2012)
15. Raoux, S., Ielmini, D., M., W., Karpov, I.: Phase change materials. MRS Bull. **37**, 118–123 (2012)
16. Zimbovskaya, N.A., Pederson, M.R.: Electron transport through molecular junctions. Phys. Rep. **509**, 1–87 (2011)
17. Mentovich, E.D. et al.: Multipeak negative-differential-resistance molecular device. Small **4**, 55–58 (2008)
18. Metzger, R.M.: Unimolecular electronics. J. Mater. Chem. **18**, 4364–4396 (2008)
19. Orihashi, N., Hattori, S., Asada, M.: Millimeter and submillimeter oscillators using resonant tunneling diodes with stacked-layer slot antennas. Jpn. J. Appl. Phys. **2**(43), L1309–L1311 (2004)
20. Maezawa, K. et al.: High-power oscillations in resonant tunneling diode pair oscillator ICs fabricated with metamorphic devices. Jpn. J. Appl. Phys. **1**(46), 2306–2308 (2007)
21. Metzger, R.M.: Unimolecular electrical rectifiers. Chem. Rev. **103**, 3803–3834 (2003)

22. Joachim, C., Gimzewski, J.K., Aviram, A.: Electronics using hybrid-molecular and mono-molecular devices. Nature **408**, 541–548 (2000)
23. Rose, G.S., Stan, M.R.: A programmable majority logic array using molecular scale electronics. IEEE T Circ. I **54**, 2380–2390 (2007)
24. Mathews, R.H. et al.: A new RTD-FET logic family. P IEEE **87**, 596–605 (1999)
25. Collier, C.P. et al.: Electronically configurable molecular-based logic gates. Science **285**, 391–394 (1999)
26. Heath, J.R.: Molecular electronics. Annu. Rev. Mater. Res. **39**, 1–23 (2009)
27. Chen, J.S. et al.: Negative differential resistance effect in organic devices based on an anthracene derivative. Appl. Phys. Lett. 89 (2006)
28. Galperin, M., Ratner, M.A., Nitzan, A.: Hysteresis, switching, and negative differential resistance in molecular junctions: A polaron model. Nano Lett. **5**, 125–130 (2005)
29. Goto, E. et al.: Esaki diode high-speed logical circuits. IRE. T. Electron. Comp 25–29 (1960)
30. Kuroyana, N., Inoue, N.: High speed logical circuits combining esaki-diode bistable circuits with emitter follower. Rev. Elec. Commun. Lab **13**, 701-& (1965)
31. Axelrod, M.S., Farber, A.S., Rosenheim, D.E.: Some new high-speed tunnel-diode logic circuits. IBM J. (1962)
32. Maezawa, K., Mizutani, T.: A new resonant tunneling logic gate employing monostable-bistable transition. Jpn. J. Appl. Phys. 2 Lett. **32**, L42–L44 (1993)
33. Chen, K.J., Maezawa, K., Yamamoto, M.: InP-based high-performance monostable bistable transition logic elements (MOBILE's) using integrated multiple-input resonant-tunneling devices. IEEE Electr. Dev. L **17**, 127–129 (1996)
34. Mentovich, E.D., Richter, S.: Post-complementary metal-oxide-semiconductor vertical and molecular transistors: A platform for molecular electronics. Appl. Phys. Lett. 99 (2011)
35. Mentovich, E.D., Belgorodsky, B., Richter, S.: Resolving the mystery of the elusive peak: negative differential resistance in redox proteins. J. Phys. Chem. Lett. **2**, 1125–1128 (2011)
36. Mentovich, E.D., Belgorodsky, B., Kalifa, I., Richter, S.: 1-nanometer-sized active-channel molecular quantum-dot transistor. Adv. Mater. **22**, 2182–2186 (2010)
37. Mentovich, E.D., Richter, S.: The role of leakage currents and the gate oxide width in molecular transistors. Jpn. J. Appl. Phys. 49 (2010)
38. D'Amico, P., Ryndyk, D.A., Cuniberti, G., Richter, K.: Charge-memory effect in a polaron model: equation-of-motion method for Green functions. New J. Phys. 10 (2008)

Quantum Interference Effects in Electron Transport: How to Select Suitable Molecules for Logic Gates and Thermoelectric Devices

Robert Stadler

Abstract Since the concepts for the implementation of data storage and logic gates used in conventional electronics cannot be simply downscaled to the level of single-molecule devices, new architectural paradigms are needed, where quantum interference (QI) effects are likely to provide an useful starting point. In order to be able to use QI for design purposes in single-molecule electronics, the relation between their occurrence and molecular structure has to be understood at such a level that simple guidelines for electrical engineering can be established. We made a big step towards this aim by developing a graphical scheme that allows for the prediction of the occurrence or absence of QI-induced minima in the transmission function, and the derivation of this method will form the centrepiece of this review article. In addition the possible usefulness of QI effects for thermoelectric devices is addressed, where the peak shape around a transmission minimum is of crucial importance and different rules for selecting suitable molecules have to be found.

1 Introduction

In the vivid field of molecular electronics, where tremendous advances in the theoretical description as well as experimental characterization of the conductance of single-molecule junctions have been achieved in the last two decades, two concepts emerged recently which received a lot of attention: (1) devices based on quantum interference (QI) effects [1–6] and (2) thermoelectric applications (TA) [7–11]. QI-based devices are utilising the wave nature of electrons and the resulting possibility for destructive interference of transmission amplitudes for the design of data storage elements [2], transistors [1, 5] or logical gates [3]. TAs on the

R. Stadler
Department of Physical Chemistry, University of Vienna, Sensengasse 8/7,
A-1090 Vienna, Austria
e-mail: robert.stadler@univie.ac.at

other hand focus on the conversion of thermal gradients to electric fields for power generation or vice versa for cooling or heating with so-called Peltier elements, an application for which not only homogeneous bulk materials but also single-molecule junctions might be used. The efficiency of a thermoelectric device is measured by a dimensionless number, the figure of merit ZT, which can be increased by steep declines in the transmission function describing the electronic conductance of a junction [8, 12]. This latter requirement for a high ZT value provides a link between QI and TA in the sense that QI effects can cause the transmission function to change from rather high to rather low values or vice versa within a small energy range close to the Fermi level of the electrodes for some molecules.

In this chapter I review my personal involvement in studying QI effects in single-molecule electronics, where I start with introducing QI-based concepts for data storage [2] and logical gates [3], and then highlight a graphical design scheme for predicting the occurrence of QI-induced minima in the transmission function [13] and the energies at which they occur [14] in their dependence on the molecular structure. In the second half of this chapter I present a method to analyse the structure dependence of the asymmetry of interference dips-which is crucial for TA-from simple two-site tight-binding models, where one site corresponds to a molecular π orbital of the wire and the other to an atomic p_z orbital of a side group, which allows for an analytical characterization of the peak shape in terms of just two parameters [15].

2 Monomolecular Data Storage and Logic Gates

An important task in molecular electronics is to implement active device behaviour in an electric circuit by using the structural or electronic properties of individual molecules. Since the final aim is to arrive at an overall computer architecture which is smaller than currently available semiconductor technology [16–18], it should be kept in mind that the molecules are connected to metal electrodes which need to be wired to the outside world for being addressable. Even if feasible, it would be highly impractical to consider this metal wiring scaled down to an atomic level due to the introduction of additional wire-dependent electron scattering and the necessity for those wires to be then absolutely defect free. One way to avoid these problems can be found in exploring the possibilities for intramolecular circuits, where the device behaviour of one single molecule mimics not only a single switch but, e.g. a two-input logic gate or even a more complex part of a logic circuit.

The key idea for the design of such intramolecular circuits first presented in [2] and illustrated in Fig. 1 is to take into account the influence that symmetry has on electron transmission through highly delocalised π states of aromatic molecules, which are connected to a reference electrode and a given number of output electrodes. It is assumed that the electron transfer process across the molecule could in principle be tuned by varying chemical substituents, e.g. with the help of redox reactions, or by locally acting on them, e.g. by using an STM tip. This would control
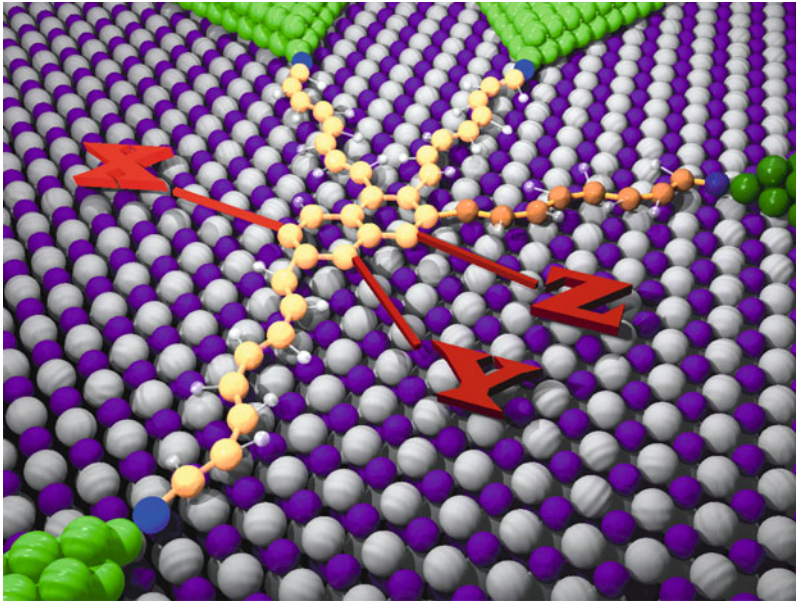
Fig. 1 A molecular data storage scheme based on an aromatic molecule (naphthalene) bonded to four gold electrodes by sulphur atoms and polyacetylene wires. For the surface, an insulator has to be chosen to prevent crosstalk between the electrodes. The variables X, Y and Z could either be chemical substituents or alternatively connections to further electrodes. Reprinted with permission from [2], Copyright (2003), Institute of Physics

the output current by changing the interference pattern of the electron scattering process, and the chemical substitution pattern could be used for data storage. Such an architectural scheme, although its structure is defined in the space domain, would share some favourable characteristic features with quantum computing, such as the possibility for dense storage scaling as 2^N, where N is a parameter reflecting the size of the system. While in [2] this original idea has been first proposed, the concept has been extended in [3] for the design of small logic circuits, where first electron transport calculations taking into account the detailed three-dimensional structure of the molecular orbitals of benzene molecules and using NO_2 groups as ligands on an extended Hückel level have been performed (Fig. 2).

Since it is not possible in the case of intramolecular architectures to decompose them into single gates and wires [19, 20] as is done in semiconductor industry, architectural design needs to take into account the system as a whole. The overall aim is to find a molecular structure on which a maximum amount of computational functionality for information storage and/or processing can be imposed. For this task, a simple graphical method can be employed [3, 13], which does not take into account the full complexity of the electron transport through the molecule. This method is derived in Sect. 3 from a topological tight-binding (TB) description, where each atom contributing to the π system is only described by a single atomic
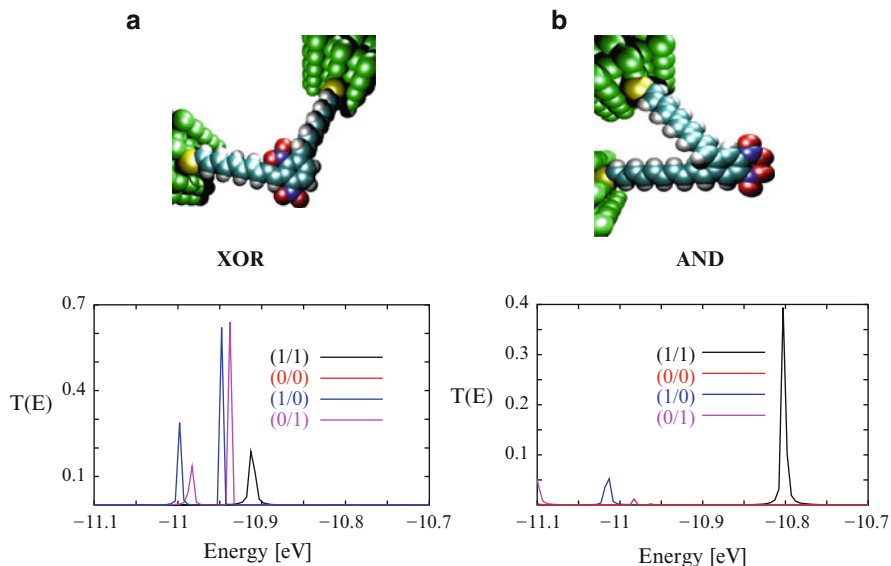
Fig. 2 A benzene molecule is connected to two gold electrodes by sulphur atoms and polyacety-lene wires, and the transmission through the molecule can be designed to have the characteristics of either (**a**) a XOR gate or (**b**) an AND gate. The type of gate is defined by the positions on the benzene ring, where the wires are connected, namely, in a meta-configuration for the XOR gate and in an ortho-configuration for the AND gate. It is also crucial on which ring positions the nitro groups are bonded to the molecules. It is envisioned that they are rotated for defining the input (with unspecified means for inducing this rotation in praxis), where the substituents interact with the π electrons of the benzene ring, when they are planar to the ring, and there is no interaction when their rotational state is perpendicular to the benzene molecule. This means that for an input of (1/1), both nitro groups are in the same plane as benzene; for (1/0) and (0/1), one nitro group is planar, the other rotated by 90°, respectively; and for (0/0), both groups are perpendicular. The output is then defined by the electron transmission probability through the junction, with a high transmission representing '1' and a low transmission representing '0'. The figure shows that the correlation between input and output for the respective molecular junctions fulfils the truth tables for XOR and AND gates. Reprinted with permission from [3], Copyright (2004), Institute of Physics

orbital (AO). The use of such a description for the comparison of different molecular topologies consisting of rings or chains of AOs already allows for an assessment of the applicability of particular molecular structures for architectural design, since its predictions have been validated by density functional theory (DFT) calculations in [13] as pointed out in more detail in Sect. 3.

3   A Graphical Design Scheme and Its Validation by DFT

Within a single-particle picture, the transmission probability of an electron entering a molecular junction with an energy E can be reduced to

$$\mathscr{T}(E) = \gamma(E)^2 |G_{1N}(E)|^2 \tag{1}$$

assuming that the Hamiltonian describing the molecule H_{mol} is given in terms of a basis consisting of localised atomic-like orbitals, $\phi_1, \phi_2, \ldots, \phi_N$ and that only the two orbitals ϕ_1 and ϕ_N couple to the leads [13, 14].

Often, the energy dependence of the lead-coupling strength, γ, can be neglected. It then follows that the transport properties are entirely governed by the matrix element $G_{1N}(E)$. The latter can be obtained using Cramer's rule

$$G_{1N}(E) = \frac{\det_{1N}(E - H_{\text{mol}})}{\det(E - H_{\text{mol}} - \Sigma_L - \Sigma_R)} \tag{2}$$

where $\det_{1N}(E - H_{\text{mol}})$ is the determinant of the matrix obtained by removing the 1st row and Nth column from $E - H_{\text{mol}}$ and multiplying it by $(-1)^{1+N}$. Taking the Fermi energy to be zero without loss of generality, we can then state the condition for complete destructive interference of the zero bias conductance, $G(E_F) = 0$, as

$$\det_{1N}(H_{\text{mol}}) = 0. \tag{3}$$

For a general three-site system, where the coupling constants between the orbitals a_{12}, a_{13} and a_{23} are unspecified and their on-site energies $\varepsilon_i = 0$ for all three atomic orbitals, the matrix H_{mol} can be written as

$$H_{\text{mol}} = \begin{bmatrix} -E & a_{12} & a_{13} \\ a_{12} & -E & a_{23} \\ a_{13} & a_{23} & -E \end{bmatrix}, \tag{4}$$

where for $E = E_F$

$$\det_{1N}(H_{\text{mol}}) = -a_{13}a_{23}. \tag{5}$$

For general four- and five-site systems under the same conditions, this expression is replaced by

$$\det_{1N}(H_{\text{mol}}) = a_{13}a_{24}a_{34} + a_{14}a_{23}a_{34} - a_{12}a_{34}^2 \tag{6}$$

and

$$\det_{1N}(H_{\text{mol}}) = a_{34}^2 a_{15}\, a_{25} + a_{35}^2 a_{14} a_{24} + a_{45}^2 a_{13} a_{23} + 2a_{12}a_{34}a_{35}a_{45} \tag{7}$$

$$-a_{13}a_{24}a_{35}a_{45} - a_{14}a_{23}a_{35}a_{45} - a_{13}a_{25}a_{34}a_{45} - a_{15}a_{23}a_{34}a_{45} - a_{14}a_{25}a_{34}a_{35}$$

$$-a_{15}a_{24}a_{34}a_{35},$$
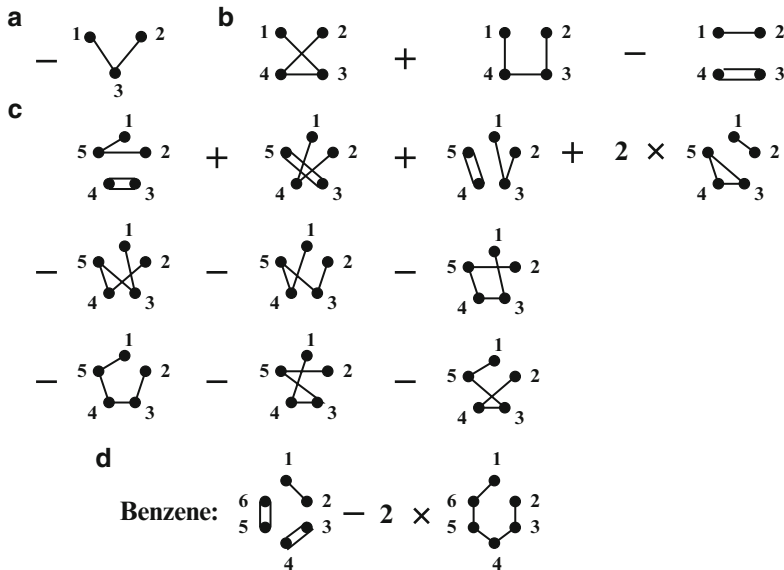
Fig. 3 Visualisation of the terms in $\det_{1N}(H_{\mathrm{mol}})$ (see text) for electron transport between orbitals 1 and 2 for (**a**) three, (**b**) four and (**c**) five atomic orbitals, respectively. Panel (**d**) is for six orbitals, with the coupling pattern of benzene being taken as a boundary condition. Atomic orbitals are drawn as *dots*; *lines* connect two orbitals when there is a factor in the respective term which has both of their indices, and *double lines* indicate that this factor is squared. Reprinted with permission from [3], Copyright (2004), Institute of Physics

respectively, where $\det_{1N}(H_{\mathrm{mol}})$ is visualised as graphs in Fig. 3a–c for three, four and five orbitals, respectively. Each term in the sums is represented by a different drawing of the orbitals as dots, with lines connecting them if there is a factor in the term which has both of their indices and with double lines when the factor is squared. Looking at the structure of these graphs, it can be seen that the terms represent all possibilities for a path between orbitals 1 and 2, where all orbitals of the molecule have to be either traversed within the path or within a closed loop, which for the comparatively small number of orbitals shown in Fig. 3 are either double lines or triangles (Fig. 3c) but can be larger loops for a larger structure. A larger number of orbitals lead also to an increase in the number of possible paths. But the individual terms contain more couplings as well, and if only one bond is missing, then the path does not exist. For six orbitals, there are 46 possible paths, but for the bonding pattern of a particular molecule, this number considerably reduces and becomes two for benzene (Fig. 3d) with the electrodes attached in an ortho-configuration.

The rationale for applying the graphical scheme for the prediction of QI effects is based on the fact that viable paths must exist for $\det_{1N}(H_{\mathrm{mol}})$ to be finite, which is a precondition for $G(E_{\mathrm{F}}) > 0$ (see (2) and (3)). A path-in this interpretation one of the terms in the sum defining $\det_{1N}(H_{\mathrm{mol}})$-is viable only if there are bonds between
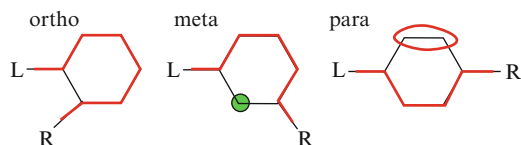
Fig. 4 Demonstration of how the graphical QI prediction scheme is applied for electron transport through benzene in ortho-, meta- and para-connections. For the connections without QI, a continuous path can be drawn either with (para) or without (ortho) pairing up remaining sites. This is not possible for the only connection, which exhibits QI for benzene (meta), where the isolated site has been marked by a green spot. Reprinted with permission from [13], Copyright (2010), American Chemical Society
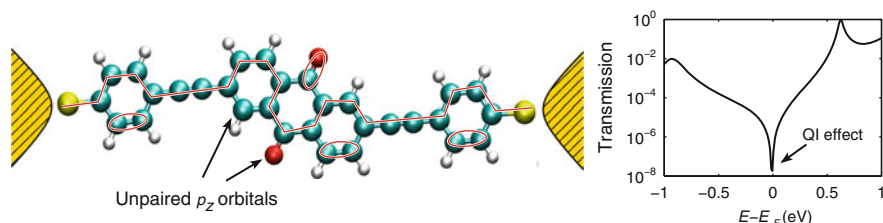
Fig. 5 Illustration of the graphical scheme (*left*) for predicting a QI-induced minimum in the electron transmission function (*right*) of an anthraquinone molecule between gold electrodes. Reprinted with permission from [13], Copyright (2010), American Chemical Society

atomic orbitals corresponding to all factors in this term. As can be extrapolated from the examples in Fig. 3, the general rule is that all atomic sites have to be either part of a continuous line connecting the two sites coupled to the leads (1 and 2 in Fig. 3) or be part of a closed loop (in praxis, i.e. for realistic molecules only pairs-with a bond between them-of isolated atomic orbitals occur, triangles or even larger loops are uncommon). In Fig. 4 we show how the method is applied for predicting QI for the well-known case of benzene connected to two leads in ortho, meta and para configurations. While for ortho all atomic sites are part of a continuous line from lead to lead, for para the two orbitals not on this line form a pair with a bond between them (marked by a red elliptical confinement in Fig. 4). As is well known, these two configurations do not exhibit QI. The meta setup on the other side has an isolated atomic site without a neighbour which is not part of the curve (highlighted by a green spot in Fig. 4), and therefore QI results from the scheme. While in more complicated molecules there may be several ways to draw continuous lines between the leads, the crucial point is whether it is possible to draw it in a way that the general rule named above is fulfilled. If, for instance, the curve for meta would be drawn in the other direction, then three sites would be left on the other side of the molecule, where two of them could form a bonded pair, but again there would be one orbital remaining.

In [13] we studied ten junctions with anthraquinone molecules (Fig. 5), which only differed in the position of the two oxygen side groups on the molecules, and

Table 1 DFT conductance values in units of $G_0 = 2e^2/h$ for a range of anthraquinone molecules where some experience QI effects (I1–I5) and others do not (N1–N5)

Molecule	G (G_0)	Molecule	G (G_0)
I1	7.71×10^{-8}	N1	1.38×10^{-2}
I2	1.82×10^{-8}	N2	8.57×10^{-2}
I3	3.03×10^{-4}	N3	7.09×10^{-3}
I4	3.55×10^{-4}	N4	8.98×10^{-3}
I5	8.84×10^{-4}	N5	6.19×10^{-3}

Note that the conductance values in the left column are systematically lower than those in the right column. This is a result of destructive QI occurring close to the Fermi energy for the molecules I1–I5. Reprinted with permission from [13], Copyright (2010), American Chemical Society

categorised them into two groups, where five of them exhibited QI inside the energy range of the HOMO-LUMO gap (I1–I5) and the others (N1–N5) did not. We made this distinction on the basis of our graphical scheme, and our conclusions were in good agreement with DFT calculations, where as can be seen from Table 1, the conductance of molecules I1–I5 is systematically and significantly lower than the conductance of molecules N1–N5. This prediction, however, was based on the assumption that the on-site energy of the side group would be approximately equal to the on-site energy of the carbon p_z orbitals. From the side-group analysis in [14], it was found that this assumption is questionable for oxygen with a side-group energy of -2 eV (relative to the Fermi level). In [14], we also showed that more quantitative estimates of the transmission node position can be obtained from a straightforward generalisation of the graphical scheme to the case of finite (and varying) on-site energies. This scheme was then used to analyse the transmission nodes in linear and aromatic molecules with side groups. For linear molecular chains, a single transmission node occurs at an energy corresponding to the energy of the side group π-orbital, while for aromatic molecules, the nodal structure of the transmission function is in general more complex due to a non-trivial interplay between molecular topology and side-group on-site energy, which explains the success of the original scheme for categorising the anthraquinone molecules as exhibited in Table 1 even beyond the limiting conditions assumed for its derivation [14].

4   Transmission Peak-Shape Engineering for Thermoelectric Devices

The TB model, which was first introduced in [15], aims at a separation of the structural aspects governing the key quantity for the electronic contribution to thermoelectric properties. I am referring to the peak shape of interference dips

in the transmission function, for which analytical expressions can be derived in dependence on just two parameters given a few simplifying assumptions are made. First, as for the graphical scheme in the last section, it is assumed that only the π electrons are relevant in the energy range of interest, which allows us to describe molecules within a TB model with only one p_z AO for each carbon- or hetero-atom. In a second step, we look at MOs of t-stub wires [21, 22] without the side group attached, which can be obtained by diagonalising the TB Hamiltonian for a chain of carbon atoms with a certain length and from them pick the single MO which is closest in energy to the p_z AO or fragment orbital of the side group. If we now assume a two-site single-particle picture where the transmission function for electrons incident on a molecular junction with an energy E is dominated by this MO and its interaction with the side-group AO, it can be written as

$$\mathscr{T}(E) = \frac{4\gamma^2}{(E - \varepsilon_0 - \frac{t^2}{E-\varepsilon_1})^2 + 4\gamma^2}, \tag{8}$$

as derived in [15], with γ being the lead coupling within a wideband approximation, ε_0 the wire MO energy, ε_1 the side-group AO energy and t the coupling between them. For an illustration, see Fig. 6b. Since the thermoelectric properties of a molecular junction are optimised if the transmission function rapidly change from a minimum to a maximum, we can define the energetic difference ΔE between the transmission minimum and its closest maximum as a simple criterion. It follows from (8) that the transmission is zero at energy $E = E_0 = \varepsilon_1$, [14], while for determining the energy of transmission peaks with $\mathscr{T} = 1$, the quadratic equation $E - \frac{t^2}{E-\Delta\varepsilon} = 0$ has to be solved where we made the substitution $\Delta\varepsilon = \varepsilon_1 - \varepsilon_0$ and set $\varepsilon_0 = 0$ without loss of generality for our following arguments. The solutions to this equation $E_{1,2}$ and the norm of their differences with the energy of the transmission zero E_0 can then be obtained as

$$E_{1,2} = \frac{\Delta\varepsilon}{2} \pm \frac{1}{2}\sqrt{\Delta\varepsilon^2 + 4t^2} \tag{9}$$

$$|E_{1,2} - E_0| = |-\frac{\Delta\varepsilon}{2} \pm \frac{1}{2}\sqrt{\Delta\varepsilon^2 + 4t^2}|, \tag{10}$$

where it can be seen that for finite $\Delta\varepsilon$, there will always be one solution for $|E_{1,2} - E_0|$ which will be closer to zero than the other. In other words, only under this condition will the energy difference of the two transmission maxima from the transmission minimum be asymmetric for the two-site model, while for $\Delta\varepsilon = 0$, we get $|E_{1,2} - E_0| = \pm t$, and the peak shape around the minimum in $\mathscr{T}(E)$ will therefore be symmetric. In the following, I will refer to the smaller of the two solutions for $|E_{1,2} - E_0|$ as ΔE, which is used as a measure indicative of thermoelectric efficiency where the thermopower is expected to be high for small ΔE. An important conclusion at this point is that $|E_{1,2} - E_0|$ is completely independent of the lead-coupling γ. Rapid transmission changes being independent
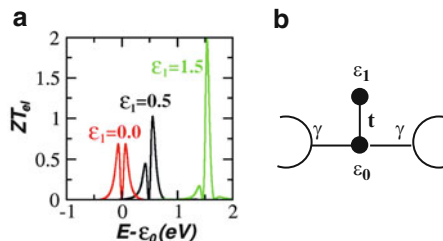
Fig. 6 (**a**) Analytical TB results for the purely electronic thermoelectric figure of merit ZT_{el} calculated from the transmission functions of a two-site model (**b**) according to (8) and (11) with $\gamma = 0.5$ eV, $\varepsilon_0 = 0.0$ eV and $|t| = 0.5$ eV for $\varepsilon_1 = 0.0$ eV (*red*), 0.5 eV (*black*) and 1.5 eV (*green*). Reprinted with permission from [15], Copyright (2011), American Institute of Physics

of lead-coupling broadenings are a general advantage of utilising QI since both transmission peaks and transmission minima are defined entirely by the molecular topology. As a consequence ΔE is completely defined by just two parameters, where peak shapes of the transmission function for molecular t-stubs are found to be the more asymmetric, the larger $\Delta\varepsilon$ and the smaller t. We note that these two parameters correspond to the length and height of the tunnelling barrier introduced in [21, 22] for a separation of the sidearm in mesoscopic waveguide t-stubs, where the authors also found that distinctly asymmetric line shapes only start to appear for weak coupling and large barrier heights.

The efficiency of a thermoelectric material can be characterised by the dimensionless figure of merit, ZT, given by

$$ZT = \frac{S^2 G\, T}{\kappa_{\mathrm{ph}} + \kappa_{\mathrm{el}}}, \tag{11}$$

where S is the Seebeck coefficient, G the electronic conductance, T the temperature and κ_{ph} and κ_{el} are the phonon and electron contributions to the thermal conductance, respectively [15]. When the phonon contribution is neglected ($\kappa_{\mathrm{ph}} = 0$), one obtains the purely electronic ZT_{el}, which is illustrated in Fig. 6a for different values of $\Delta\varepsilon$. Clearly, the maximum ZT_{el} values increase when the transmission function becomes more asymmetric which can be brought about by a rise in $\Delta\varepsilon$ for a constant t. While very large ZT_{el} values have been predicted for symmetric transmission functions [9], the results in Fig. 6a show that asymmetric transmission functions are even more promising for a thermoelectric purpose.

In order for our two-site model to be useful for the analysis of t-stub molecular wires, we need to be able to deduce the parameters t and $\Delta\varepsilon$ from the full topology of the wires' p_z AOs including the side group, which does not always have to be another carbon site. For this, we start from an AO-TB model where the on-site energy of each p_z orbital of the carbon chain is set to zero and the couplings between neighbouring sites are defined as -2.9 eV. From a diagonalisation of the chain *without* the side group, where I refer to [15] for the full mathematical details, its
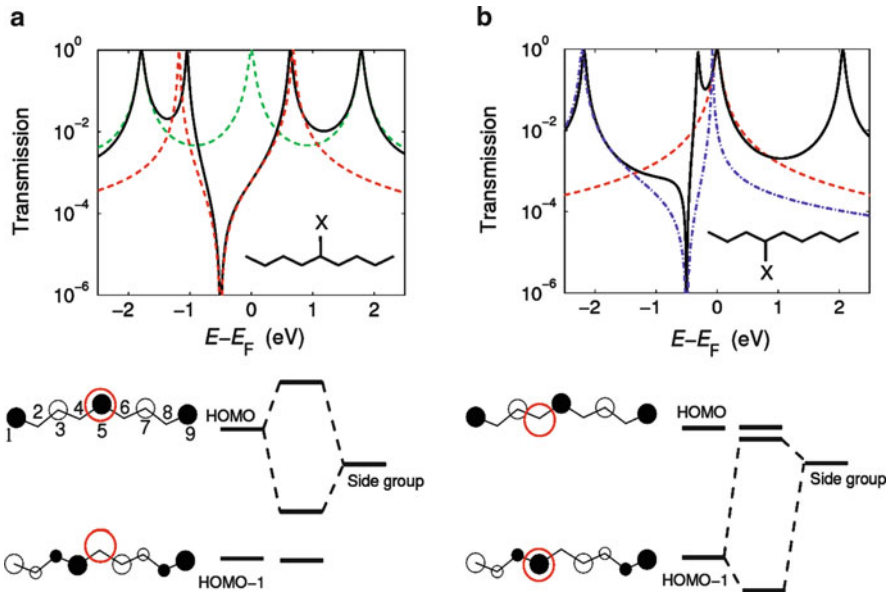
Fig. 7 Transmission functions (*upper panels*) and MO-AO hybridisation schemes (*lower panels*) for (**a**) C9-5 and (**b**) C9-4 type molecular stubs with a side group AO X ($\varepsilon_{sg} = -0.5$ eV), where the respective AO topologies are given as insets in the transmission figures. The labels 5 and 4 correspond to the atom number in the carbon chain to which the side group is coupled, where we indicate the numbering we use for the atoms in the carbon chain in the lower part of panel (**a**). The line types for $\mathscr{T}(E)$ correspond to full TB AO calculations with (*black*) and without (*green*) the side group, and a 2-site MO model with the side-group AO and the HOMO ($\varepsilon_{HOMO} = 0$ eV, *dashed red*) or the HOMO-1 ($\varepsilon_{HOMO-1} = -1.8$ eV, *dashed blue*), respectively. The Fermi level E_F is assumed to be identical to ε_{HOMO} of C9 (without any side groups). The *lower panels* also show the topologies of the HOMO and HOMO-1 where the respective position of the side group is indicated by *red empty spheres*, where depending on $|\Delta\varepsilon|$ and $|t_{sg}|$ different hybridization patterns are observed. Reprinted with permission from [15], Copyright (2011), American Institute of Physics

MO energies and the orbital weight on each chain site for each MO can be obtained. Within this scheme, the side-group AO energy ε_1 and an initial value for the MO-AO coupling t can be freely varied so that it reflects the side-group chemical nature. This initial value for t is then multiplied by the orbital weight at the chain site to which the side group is bonded. The relevant MO is typically the one closest in energy to ε_1. The two-site model finally contains this latter MO (with energy ε_0) and the side-group AO, where the lead-coupling γ in the two-site model is derived from the wideband lead-coupling Γ used in the full AO-TB model multiplied by the squared orbital weight on the terminal sites in the chain.

In Fig. 7, it is illustrated how this works in practice and which kind of information can be obtained from such an analysis. The figure focuses on molecular wires with nine atoms in the chain (C9), where a side group with $\varepsilon_1 = -0.5$ eV is attached to the fifth (C9-5, Fig. 7a) and the fourth (C9-4, Fig. 7b) site of the chain. The solid

Table 2 2-site MO model parameters $|\Delta\varepsilon|$ and $|t_{sg}|$ for a range of molecular stubs of varying length and chemical nature of side groups

Molecule	C9-CH$_2$-5	C9-O-4	C8-NO$_2$-4	C9-NO$_2$-5
$|\Delta\varepsilon|$	0.40	0.91	0.61	1.60
$|t_{sg}|$	1.03	1.12	0.32	0.40
E_0	0.26	−1.44	1.61	1.72
$|\Delta E|$	0.89	0.65	0.40	0.20
$S\ (E)$	−170 (0.21)	184 (−1.39)	199 (1.65)	349 (1.74)
ZT$_{el}\ (E)$	0.82 (0.19)	0.93 (−1.37)	1.00 (1.67)	3.00 (1.77)
ZT (E)	0.003 (0.19)	0.01 (−1.37)	0.03 (1.67)	0.48 (1.77)

The energy of the transmission zero E_0 and its difference to that of the nearest transmission maximum $|\Delta E|$ are evaluated from transmission functions calculated from DFT. The maximum values for the thermopower S and the electronic contribution to the figure of merit ZT$_{el}(E)$ (obtained at the corresponding energies in parentheses) and the full figure of merit ZT (including phonon contributions and calculated at the same energy) are listed in the bottom rows. All energies and the coupling strength $|t_{sg}|$ are given in eV, while S is defined in $\mu V/K$, and ZT$_{el}$ and ZT are dimensionless and calculated at the temperature $T = 300$ K. Reprinted with permission from [15], Copyright (2011), American Institute of Physics

black lines in the transmission functions in the upper panels of Fig. 7 are the results of full TB-AO calculations including the side group, while the dashed red and blue lines come from 2-site TB-MO models considering only the side-group AO and the HOMO (red) or HOMO-1 (blue) of the unsubstituted chain, respectively. The green line in Fig. 7a shows the TB AO result without the side group, where it can be clearly seen that the peak in $\mathscr{T}(E)$ corresponding to resonance through the HOMO splits into two, when the HOMO hybridises with the side-group AO, whereas the other two visible peaks caused by the HOMO-1 and LUMO remain unaffected. The situation is quite different for C9-4 (Fig. 7b), which exhibits a distinctly asymmetric QI feature, and the red line does not reproduce the black one at all and instead represents a single-site Lorenz peak at the HOMO energy. The blue line on the other hand shows very good correspondence with the TB AO transmission, which means that the side-group AO interacts mainly with the HOMO-1 and not with the HOMO. This difference between the two molecular t-stubs can be understood in terms of the topologies of the MOs plotted in the lower panels of Fig. 7, where the HOMO has a high weight on site 5 but none on site 4, and in contrast the HOMO-1 has its largest weight on site 4 and none on site 5.

Finally, the suitability of four candidates for t-stub molecules for thermoelectric devices is addressed in Table 2, where the thermopower S and the figure of merit ZT are explicitly calculated from DFT. The table shows both the pure electronic ZT$_{el}$, which is completely determined by the electronic transmission function assuming a vanishing phonon contribution to the thermal conductance, κ_{ph}, and the full ZT including a finite κ_{ph}, for which a constant value of 50 pW/K was used. Notably, the qualitative ranking in S and ZT reversely corresponds to that of $|\Delta E|$, reflecting that the more asymmetric $\mathscr{T}(E)$ curves result in higher values for thermopower and figure of merit. This remains true and is at the highest end even emphasised when the

contributions of phonons are considered. The two drawbacks for C9-NO$_2$-5 in terms of applications are the rather high value of E_0 and its instability as a radical. These results demonstrate that for an efficient and robust way of implementing QI-induced transmission minima for thermoelectric applications, an asymmetric transmission function with a transmission peak located close to the minimum and both near E_F in a chemically stable structure is needed. Since the analysis in Table 2 covers a large part of the chemical possibilities for t-stub-type molecules, i.e. simple wires with one side group, one has to conclude that more complex (and probably aromatic) molecules need to be investigated systematically with regard to their suitability for thermoelectric devices.

5   Summary

The purpose of this chapter was to review my involvement in the attempt to use quantum interference effects for the design of memory elements, logic gates and thermoelectric devices in single-molecule electronics. In the first half of this chapter, I recaptured the derivation of a graphical scheme which is based on a simple tight-binding model of the π electron system but can be applied to a broad range of realistic molecular junctions. By comparison to first-principle electron transport calculations, it was demonstrated that the scheme correctly predicts the presence/absence of transmission antiresonances at the Fermi energy for ten different configurations of anthraquinone as well as for cross-conjugated molecules. The graphical scheme provides a direct link between molecular structure and QI and should be a useful guideline in the design of molecules with specific transport properties.

The second part of this chapter focused on thermoelectric applications, where an engineering of the peak shape in the transmission function was suggested for an enhancement of the electronic contribution to the thermopower and figure of merit. Asymmetric peak shapes are highly desirable in terms of device applications, because they promise high thermoelectric efficiency, and the work presented here therefore provides a route towards the chemical engineering of single-molecule junctions which can be used as Peltier elements. For this purpose, another TB scheme was introduced for the systematic investigation of the dependence of the symmetry of the transmission function around the energy of QI-induced minima on the molecular structure. Within this scheme, the molecular orbitals of molecular wires with side groups were mapped onto simple two-site TB models where it was found that the shape of the transmission function just depends on two parameters, namely, the coupling between the side group and the molecular chain and the energy difference of the side group atomic orbital and the molecular orbital closest to it. The role of the topology of this molecular orbital in producing quite different peak shapes for very similar molecules could be explained from our model and was further verified by DFT-based electron transport calculations.

References

1. Baer, R., Neuhauser, D.: Phase coherent electronics: a molecular switch based on quantum interference. J. Am. Chem. Soc. **124**, 4200–4201 (2002) doi:10.1021/ja016605s
2. Stadler, R., Forshaw, M., Joachim, C.: Modulation of electron transmission for molecular data storage. Nanotechnology **14**, 138–142 (2003) doi:10.1088/09570–4484/14/2/307
3. Stadler, R., Ami, S., Forshaw, M., Joachim, C.: Integrating logic functions inside a single molecule. Nanotechnology **15**, S115–S121 (2004) doi:10.1088/0957–4484/15/4/001
4. Van Dijk, E.H., Myles, D.J.T., Van der Veen, M.H., Hummelen, J.C.: Synthesis and properties of an anthraquinone-based redox switch for molecular electronics. Org. Lett. **8**, 2333–2336 (2006) doi:10.1021/ol0606278
5. Andrews, D.Q., Solomon, G.C., Van Duyne, R.P., Ratner, M.A.: Single molecule electronics: increasing dynamic range and switching speed using cross-conjugated species. J. Am. Chem. Soc. **130**, 17309–17319 (2008) doi:10.1021/ja804399q
6. Markussen, T., Schiötz, J., Thygesen, K.S.: Electrochemical control of quantum interference in anthraquinone-based molecular switches. J. Chem. Phys. **132**, 224104 (2010) doi:10.1063/1.3451265
7. Bergfield, J.P., Stafford, C.A.: Thermoelectric signatures of coherent transport in single-molecule heterojunctions. Nano Lett. **9**, 3072–3076 (2009) doi:10.1021/nl901554s
8. Finch, C.M., Garcia-Suarez, V.M., Lambert, C.J.: Giant thermopower and figure of merit in single-molecule devices. Phys. Rev. B **79**, 033405 (2009) doi:10.1103/PhysRevB.79.033405
9. Bergfield, J.P., Solis, M.A., Stafford, C.A.: Giant thermoelectric effect from transmission supernodes. ACS Nano **4**, 5314–5320 (2010) doi:10.1021/nn100490g
10. Nozaki, D., Sevincli, H., Li, W., Gutierrez, R., Cuniberti, G.: Engineering the figure of merit and thermopower in single-molecule devices connected to semiconducting electrodes. Phys. Rev. B **81**, 235406 (2010) doi:10.1103/PhysRevB.81.235406
11. Saha, K.K., Markussen, T., Thygesen, K.S., Nikolic, B.: Multiterminal single-molecule graphene-nanoribbon junctions with the thermoelectric figure of merit optimized via evanescent mode transport and gate voltage. Phys. Rev. B **84**, 041412(R) (2011) doi:10.1103/PhysRevB.84.041412
12. Paulsson, M., Datta, S.: Thermoelectric effect in molecular electronics. Phys. Rev. B **67**, 241403(R) (2003) doi:10.1103/PhysRevB.67.241403
13. Markussen, T., Stadler, R., Thygesen, K.S.: The relation between structure and quantum interference in single molecule junctions. Nano Lett. **10**, 4260–4265 (2010) doi:10.1021/nl101688a
14. Markussen, T., Stadler, R., Thygesen, K.S.: Graphical prediction of quantum interference-induced transmission nodes in functionalized organic molecules. Phys. Chem. Chem. Phys. **13**, 14311–14317 (2011) doi:10.1039/C1CP20924H
15. Stadler, R., Markussen, T.: Controlling the transmission line shape of molecular t-stubs and potential thermoelectric applications. J. Chem. Phys. **135**, 154109 (2011) doi:10.1063/1.3653790
16. Forshaw, M., Stadler, R., Crawley, D., Nikolic, K.: A short review of nanoelectronic architectures. Nanotechnology **15**, S220–S223 (2004) doi:10.1088/0957–4484/15/4/019
17. Stadler, R., Ami, S., Forshaw, M., Joachim, C.: A memory/adder model based on single C_60 molecular transistors. Nanotechnology **12**, 350–357 (2011) doi:10.1088/0957–4484/12/3/324
18. Stadler, R., Forshaw, M.: The performance of hybrid-molecular architectures with current CMOS technology as a reference. Physica E **13**, 930–933 (2002) doi:10.1016/S1386–9477(02)00237–0

19. Stadler, R., Ami, S., Forshaw, M., Joachim, C.: A tight-binding study of computer circuits for adding numbers inside a molecule. Nanotechnology **13**, 424–428 (2002) doi:10.1088/0957–4484/13/3/336
20. Stadler, R., Ami, S., Forshaw, M., Joachim, C.: A tight-binding study of a 1-bit half-adder based on diode logic integrated inside a single molecule. Nanotechnology **14**: 722–732 (2003) doi:10.1088/0957-4484/14/7/306
21. Porod, W., Shao, Z., Lent, C.S.: Transmission resonances and zeros in quantum waveguides with resonantly coupled cavities. Appl. Phys. Lett. **61**, 1350 (1992) doi:10.1063/1.107588
22. Porod, W., Shao, Z., Lent, C.S.: Resonance-antiresonance line shape for transmission in quantum waveguides with resonantly coupled cavities. Phys. Rev. B **48**, 8495–8498 (1993) doi:10.1103/PhysRevB.48.8495

Mapping Electron Transport Pathways in Complex Systems

Gemma C. Solomon

Abstract As system complexity increases, in either biological or synthetic molecules, an understanding of structure-function relationships makes it possible to identify the essential functional units controlling physical properties from what may be a vast sea of spectator components. Until recently, the range of theoretical tools that have been implemented for elucidating structure-function relationships in molecular electron transport have been limited, and consequently, the ability to build chemical intuition for the behaviour of complex systems has also been limited. Here we present our efforts developing a local description of molecular electron transport, which has allowed us to map the interactions in a molecule that mediate the tunnelling current in a range of chemically interesting molecules. With this description of the local transport, we can understand the behaviour of a complex, fluctuating system as a force is applied that induces conformational change. We can isolate the interactions in the molecule responsible for high or low currents and can use this information to refine the system design.

1 Introduction

Nano-science has made it possible to conduct physical measurements on single molecules in a whole range of novel environments. Of particular interest for molecular electronics are measurement setups that allow single molecules to be bound between metallic electrodes while electric current passes through the junction. Unsurprisingly, traditional theoretical tools can only offer limited insight into the properties of these systems, and there is a real need for tools that take their open, nonequilibrium nature into account explicitly. Here, we explore a tool to

G.C. Solomon

Nano-Science Center and Department of Chemistry, University of Copenhagen, Universitetsparken 5, 2100, Copenhagen Ø, Demark

e-mail: gsolomon@nano.ku.dk
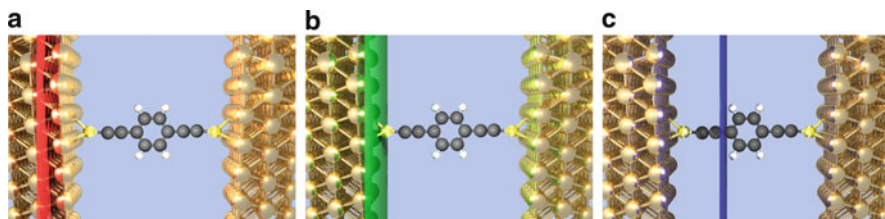
Fig. 1 Different surfaces across which the current can be calculated. (**a**) and (**b**) correspond to surfaces that might be used conventionally with either one layer of gold (*red surface* in the electrode) or no gold (*green surface* at the electrode–molecule interface) included in the extended molecule respectively. (**c**) is a surface (shown in blue spanning the molecule) where the sums of local current contributions may be examined. Reproduced with permission from [10]

visualise which parts of a molecule mediate the tunnelling current and how this tool can be used in a range of chemical systems.

2 The Local Current Description

When we calculate the current through a molecule bound between electrodes, we calculate the flux across a surface that may be somewhere deep within one electrode, at the surface of the electrode or somewhere in the molecule as shown in Fig. 1. Conservation of charge requires that the flux is independent of how this surface is defined, but different definitions allow us to isolate the role of different components of the molecule.

The local current description comes from prior work in the area [5, 12], and here, we will simply provide a limited description of the theory. A fuller account can be found elsewhere[10]. The essential idea is that we can define the current that flows between two atoms m and n, and with this definition, we can calculate the current across any surface by summing over all pairs of atoms that span the surface.

The current I_{mn} between the two atoms is given as a sum over all the basis functions i and j on atoms m and n, respectively, as

$$I_{mn} = \frac{2e}{\hbar} \sum_{i \in m} \sum_{\substack{j \in n \\ n \neq m}} \int \frac{\mathrm{d}\varepsilon}{2\pi} (V_{ij} G_{ji}^{<}(\varepsilon) - V_{ji} G_{ij}^{<}(\varepsilon)) \tag{1}$$

$$= \frac{2e}{\hbar} \int \frac{\mathrm{d}\varepsilon}{2\pi} K_{mn}(\varepsilon), \tag{2}$$

where e is the charge on an electron, $\hbar$ is Planck's constant divided by 2π, V_{ij} is a matrix element of the system Hamiltonian and $G_{ij}^{<}$ is a matrix element of the lesser Green's function. We have defined the integrand, $K_{mn}(\varepsilon)$, as

$$K_{mn}(\varepsilon) = \sum_{\substack{i \in m}} \sum_{\substack{j \in n \\ n \neq m}} (V_{ij} G_{ji}^{<}(\varepsilon) - V_{ji} G_{ij}^{<}(\varepsilon)). \tag{3}$$

In theory, atoms m and n can be anywhere in the system, but in practice, we are most interested in the role that different parts of the molecule play in mediating the current flow, so most often we use m and n that are part of the "extended molecule" (i.e. the real molecule, plus some number of electrode atoms that we designate as being part of the device). In this case, the lesser Green's function can be determined from the Keldysh equation, which in the steady-state situation is given by $G^{<}(\varepsilon) = G^{\mathrm{ret}}(\varepsilon) \Sigma^{<}(\varepsilon) G^{\mathrm{adv}}(\varepsilon)$. The retarded Green's function is defined as $G^{\mathrm{ret}}(\varepsilon) = (\varepsilon - H + i\eta)^{-1}$, where η is a positive infinitesimal. The advanced Green's function is obtained by complex conjugation, $G^{\mathrm{adv}}(\varepsilon) = (G^{\mathrm{ret}}(\varepsilon))^{\dagger}$. For a noninteracting Hamiltonian, the lesser self-energy is given by $\Sigma^{<}(\varepsilon) = i f_L(\varepsilon) \Gamma^L + i f_R(\varepsilon) \Gamma^R$. The spectral density is defined as $\Gamma_{ij}^{X}(\varepsilon) = 2\pi \sum_k V_{ik} V_{kj} \delta(\varepsilon - \varepsilon_k)$, where $X = L, R$. Together, we have

$$G_{ji}^{<} = \sum_{kl} (i f_L G_{jk}^{\mathrm{ret}} \Gamma_{kl}^{L} G_{li}^{\mathrm{adv}} + i f_R G_{jk}^{\mathrm{ret}} \Gamma_{kl}^{R} G_{li}^{\mathrm{adv}}). \tag{4}$$

The integrand in (2) can now be written as

$$K_{mn}(\varepsilon) = \sum_{\substack{i \in m}} \sum_{\substack{j \in n \\ n \neq m}} \sum_{kl} (i f_L (V_{ij} G_{jk}^{\mathrm{ret}} \Gamma_{kl}^{L} G_{li}^{\mathrm{adv}} - V_{ji} G_{il}^{\mathrm{ret}} \Gamma_{lk}^{L} G_{kj}^{\mathrm{adv}}) \tag{5}$$

$$-i f_R (V_{ji} G_{il}^{\mathrm{ret}} \Gamma_{lk}^{R} G_{kj}^{\mathrm{adv}} - V_{ij} G_{jk}^{\mathrm{ret}} \Gamma_{kl}^{R} G_{lj}^{\mathrm{adv}}))$$

A surface through the molecular region is defined by specifying which sites are to the left, in region M_L and which are to the right, in region M_R. In the steady state, the current I_S through the surface S can be expressed in terms of I_{mn} as

$$I_S = \sum_{m \in M_L} \sum_{n \in M_R} I_{mn}. \tag{6}$$

When trying to understand the coherent transport properties of molecules, we often plot the electronic transmission instead of the current as this provides a richer, energy-resolved picture of the propensity for charges to tunnel through the molecule. The transmission, $T(\varepsilon)$, is related to the current through the system at the so-called Landauer level as

$$I = \frac{2e}{h} \int d\varepsilon (f_L(\varepsilon) - f_R(\varepsilon)) T(\varepsilon) \tag{7}$$

where $f_L(\varepsilon)$ and $f_R(\varepsilon)$ are the Fermi functions for the two electrodes. This expression relies on a factorization of the integrand, which is valid for a noninteracting

Hamiltonian. In order to calculate something resembling a local transmission, we need to understand how the integrand K_{mn} relates to the transmission. The factorization can be expressed as

$$\sum_{m \in M_L} \sum_{n \in M_R} K_{mn}(\varepsilon) = (f_L(\varepsilon) - f_R(\varepsilon)) T(\varepsilon). \qquad (8)$$

Most often (and in particular throughout this chapter), we assume zero temperature in our calculations, which means we have a transmission window where $f_L(\varepsilon) = 1$ and $f_R(\varepsilon) = 0$, and consequently

$$\sum_{m \in M_L} \sum_{n \in M_R} K_{mn}(\varepsilon) = T(\varepsilon). \qquad (9)$$

Thus, in this restricted sense, we can think of the total transmission through a surface as a sum over terms associated with each local contribution between pairs of atoms, $T_{mn}(\varepsilon) = K_{mn}(\varepsilon)$.

It is important to note that the equations above assumes a local and orthogonal basis set, which is not the case in most commonly used computational methods. Before calculating the local transmission contributions, we perform a Löwdin orthogonalization on the molecular subblock and transform the matrices required to this new basis. The calculations performed in this chapter make use of the gDFTB method[3, 5, 6] for a description of the electronic structure of the system. Molecular geometries were obtained by optimising the isolated molecule using Q-Chem 3.0 [7] with density functional theory using the B3LYP functional and 6-311G** basis. The molecules were then chemisorbed (terminal hydrogens removed) to the FCC hollow binding site of a Au(111) surface with the Au–S bond length of 2.48Å, taken from the literature [2]. A wideband approximation is employed to describe the electrodes with the density of states used to construct the self-energies set to a value for bulk gold $(1.9\,eV^{-1})$. No gold atoms were included in an extended molecule so that the symmetry of the molecule could be used to separate the transmission into σ and π components [9]. The electrode unit cell varied in size depending on the size of the molecule, with a minimum of 6×8 gold atoms perpendicular to the transport direction and three layers in the transport direction, and periodic boundary conditions were used.

The relationship we have between $T(\varepsilon)$ and $K_{mn}(\varepsilon)$ can be used as a check on our calculations. Figure 2 shows the transmission for two molecules, calculated either as $T(\varepsilon)$ or as the sum of $K_{mn}(\varepsilon)$ over a range of surfaces. In both cases, the sums of the local elements are indistinguishable from $T(\varepsilon)$. With this control in place, we can start to examine the nature of the local transmission elements for a range of molecules.
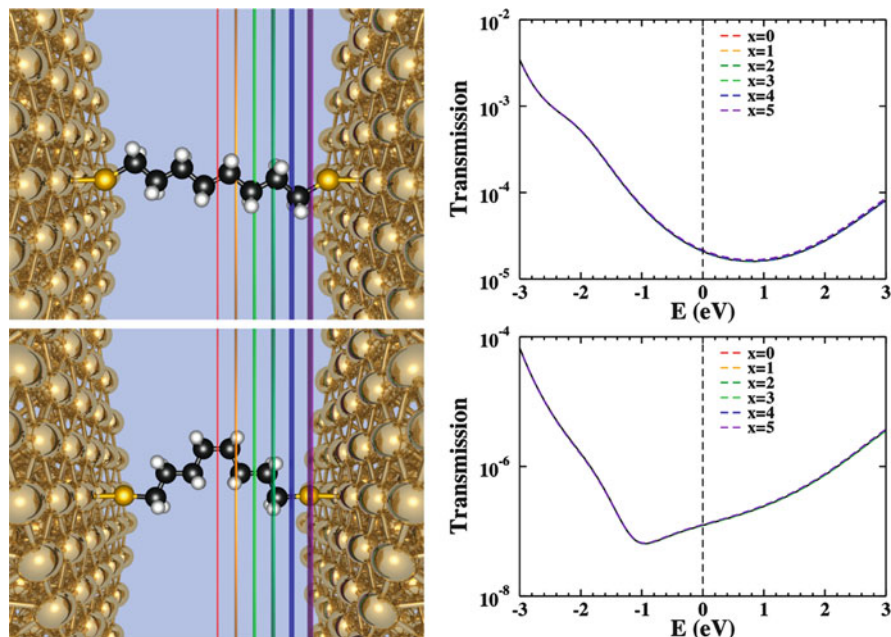
Fig. 2 The transmission (*black*) and sums of local transmission elements across a range of surfaces (*colours*) for an all-trans octanedithiol (*top*) and the same molecule with higher energy defect (*bottom*). While the transmission differs significantly between the two molecules, the sums of the local transmission elements overlay the total transmission almost exactly for all surfaces. Reproduced with permission from [10]

3 Simple Molecules

Summing the local transmission elements over a surface gives us an alternative method for calculating the transmission, but the sum itself does not give us more information about the transport through the molecule than we had previously. The advantage of the local transport theory comes if we instead plot the local transmission elements for a molecule graphically. We can represent the local transmission components by arrows that overlay the molecular geometry. As with any such plotting method, there are choices that have to be made in converting the matrix $K_{mn}(\varepsilon)$ into such a plot, and these choices need to be understood so that the plots can be interpreted correctly. Here, we make use of the following conventions:

- The local transmission plots are normalised so that the largest arrow in each plot is of the same size, irrespective of the magnitude of the total transmission at that energy.
- An arrow is only drawn when the magnitude of the local transmission between a pair of atoms is at least 10% of the maximum local transmission at that energy.

This restriction can result in an apparent lack of conservation in the drawn figure when a number of subthreshold contributions are acting to increase or reduce transmission in a particular region.

- Arrows may have different colours. When we have multiple colours in the same figure, we use the convention that arrows are coloured red when the transmission from the first atom to the second atom is positive and the second atom lies further along the transport direction; in this case from left to right, otherwise, they are coloured blue. The red arrows give components of the current in the direction of the net current flow, thereby contributing to the current, whereas the blue arrows give components in the opposite direction, thereby reducing the net current.

The local transmission for four molecules is shown in Fig. 3. These four molecules fall into two classes: those with destructive interference effects dominating their transmission near the Fermi energy (cases (c) and (d)) and those without (cases (a) and (b)).

3.1 Molecules Without Dominant Destructive Interference: Cases (a) and (b) from Fig. 3

In terms of the local transmission, the behaviour molecules without dominant destructive interference are reasonably simple. The transmission simply follows the bonds over the whole energy range under investigation, with the transmission simply dividing in two and recombining as it flows around a cyclic structure. These types of systems constitute the class of molecules that have been most extensively studied both theoretically and experimentally, and it is a useful result that the local transport is so simple in these cases. As the transmission simply follows the bonds, we can infer that modifications in the molecule that change the interaction through these bonds or change the topology of the system will result in changes in the transport. This is an intuitive and unsurprising result, but a result that is nonetheless useful to see emerging from the local transport picture.

3.2 Molecules with Dominant Destructive Interference: Cases (c) and (d) from Fig. 3

The local transmission characteristics of molecules with dominant destructive interference are more complicated. The interference effects are present in the π-system transport alone, and for that reason, we examine the local transmission through the π-system. In this case, it is clear that through-space interactions also play a significant role in the transport near interference features, with dominant
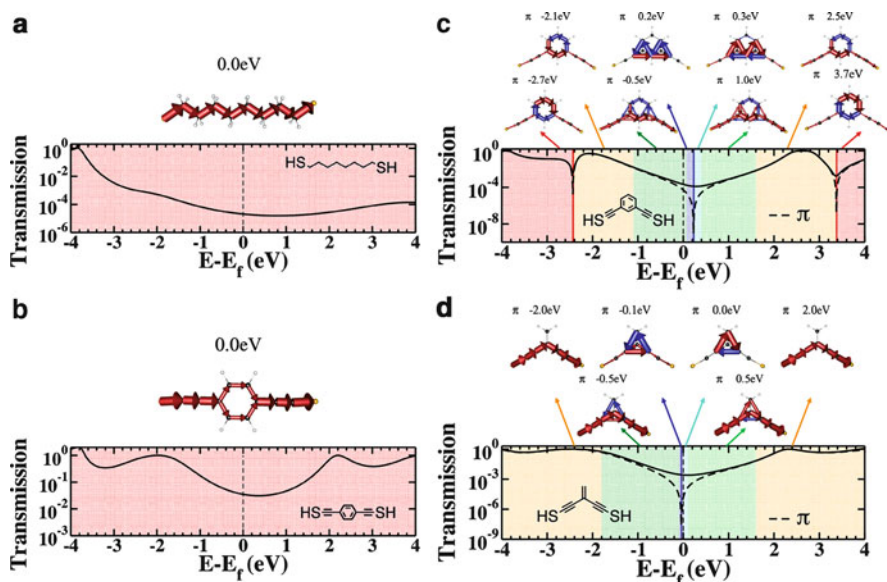
Fig. 3 *Left*: The local transmission at the Fermi energy and total transmission as a function of energy for two commonly studied molecules. In each case, the entire energy range of the transmission plot is coloured red to indicate that the local transmission exhibits a single characteristic domain over this range. The local transmission is typified by the plots shown above at the Fermi energy (0.0 eV on the relative energy scale used as indicated). *Right*: The local π-transmission contributions through two molecules exhibiting dominant destructive interference at a selection of energies and the π transmission (*dashed line*) and total transmission (*solid line*) are plotted across a large energy range below. Above each local transmission plot, the energy is given (relative to the Fermi energy) as well as a π to indicate that this is only the local components of the π transmission. The total transmission plot is shaded to indicate the various domains of characteristic local transmission. The Fermi energy is indicated with a *dashed vertical line*, and the *red and blue vertical lines* indicate the energies at which destructive interference features in the π system transport occur. Note the reversal of the ring currents around the interference features. Reproduced with permission from [10]

components between nonbonded pairs. We also see the signature of the interference effects in the local transmission, which manifests as transmission loops that reverse direction on either side (with respect to energy) of the interference feature. In these molecules, π-system transmission revealed the interference feature as a sharp node, and the local transmission only provided additional verification. However, in systems such as saturated molecules where symmetry cannot be used to separate the component with dominant interference, the local transmission can be used to confirm that a reduction in transmission is due to an interference effect [10].

Interference effects in conjugated molecules are a promising avenue for tuning the transport properties of molecular junctions. The interference features have been shown previously to be very sensitive to bias (both gate and source–drain) and also to chemical substituents[1]. More recently, we have shown that
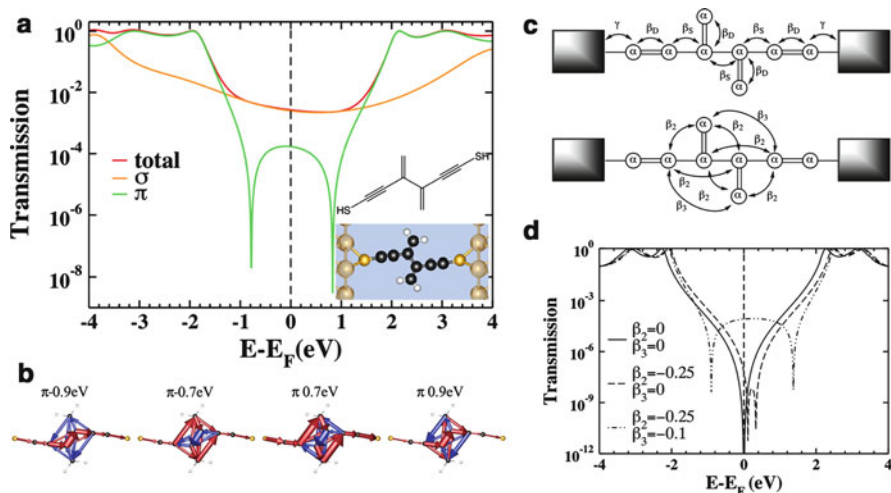
Fig. 4 (**a**) The chemical structure (inset top), space-filling model (inset bottom) and transmission for the 2cc system calculated using gDFTB. The total transmission (*red*) is plotted along with the σ (*orange*) and π (*green*) components. The π transmission exhibits two interference features separated by approximately 1.6 eV. (**b**) The local π transmission either side of the two interference features, showing the complex ring reversals of the coupled cross-conjugated units. (**c**) A modified Hückel model for the molecule and its transmission (**d**) with first (*solid*)-, second (*dashed*)- and third (*dashed-dot*)-nearest-neighbour interactions included. The large, symmetric splitting of the interference features observed in the gDFTB calculations is only recovered when the very small third-nearest-neighbour coupling elements were included. Reproduced from [8]

non-nearest-neighbour coupling elements can also result in a coupling between the interference features[8] (as shown in Fig. 4) with the local transmission reflecting the more complex nature of the unit responsible for the interference.

4   Going Beyond Bonds

In the molecules examined so far, there always existed a through-bond pathway that could be utilised for transport; however, this will not always be the case in all systems. In physisorbed molecules or complex supramolecular structures, it may be necessary for through-space interactions to mediate transport, and in a complex system (e.g. a protein) it may be that through-space pathways offer a lower barrier and thus compete with through-bond pathways. As a first step to understanding how through-space interactions mediate transport, we investigated the transport through a series of molecules, designed to resemble cyclophanes minus the saturated tethers that would normally hold the π-stacked components together[11], as shown in Fig. 5. These molecules force the current to flow through a pathway dominated
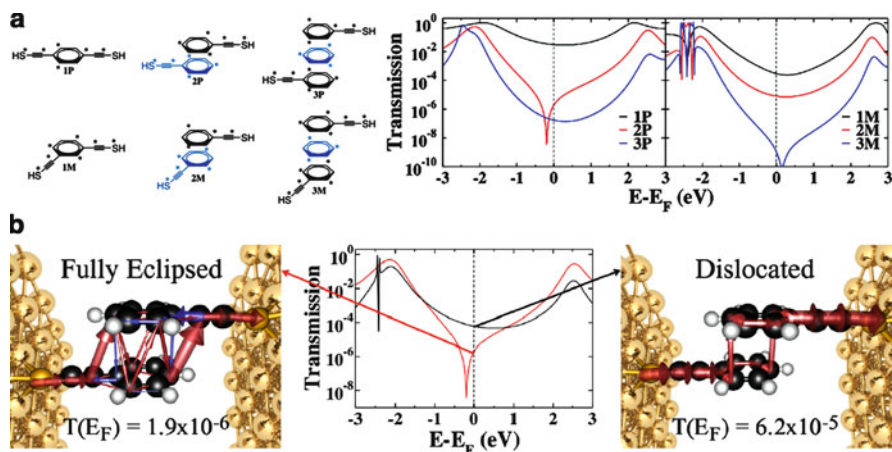
Fig. 5 (**a**) A series of thiol-substituted benzene systems (*left*) and the transmission through these systems (*right*). The systems are all even alternant hydrocarbons and are marked with stars to show when alike (low) or disjoint (high) coupling is expected. In each case, adjacent layers are coloured differently for clarity. (**b**) The local transmission and total transmission through **2P** in the case of a fully eclipsed structure and a dislocated structure. In this case, the dislocation increases the total transmission as it removes the interference effect and maximises the overlap between the positions on each ring that are strongly coupled to the electrodes. Reprinted with permission from [11]. Copyright 2012 American Chemical Society

by through-space interactions across the stack, and by examining two families (a pseudo-*para* series and a pseudo-*meta* series), we can see some of the influence of chemical substitution.

The transmission through these molecules is shown in Fig. 5, illustrating how a relatively simple series of molecules can exhibit complex trends in transport behaviour. As the number of molecules in the stack increases, we see an alternation between the case where the transport through the pseudo-*para* system is higher than the pseudo-*meta* system (for 1 molecule and 3 molecules) and the reverse (for 2 molecules in the stack). In the case of the pseudo-*para* series, there is even a range of energies where the transmission through the 3-molecule stack is higher than that through the 2-molecule stack, which is very unusual for tunnelling through an increasingly long system. The reason behind this behaviour is that destructive interference effects come and go as the system size is increased. In the same way that the transmission through a benzene ring can shift from high to low to high as the substitution is varied from *ortho* to *meta* to *para*, the transmission can also go from high to low to high as the stack size is increased.

The other interesting consequence of the interference that emerges the stacked systems is that dislocation (shifting the structure away from the fully eclipsed stack) can actually increase the transmission, as shown in Fig. 5b. In the dislocated structure, the simple local transmission is a signature of the absence of interference. While this result might seem counterintuitive at first, careful inspection of the

structures illustrates why it occurs. In the dislocated structure, the positions in the rings with maximal overlap are both strongly coupled to the electrodes, whereas in the fully eclipsed case, sites that were strongly coupled to one electrode were in close proximity to sites that were weakly coupled to the other.

5   A Complex System

With this picture of transport pathways in molecules thus developed, we can apply the local transport analysis to a complex system and investigate how we can characterise the transport pathways that dominate. We consider a flexible molecule with two conjugated units, bound to a gold surface and a conducting atomic force microscope tip, shown in Fig. 6a, b. When the molecule is relaxed, it folds into a π-stacked conformation, which is further stabilised by four hydrogen bonds. Using molecular dynamics (full details given elsewhere [4]), a force was applied to the molecule resulting in it stretching and unfolding while at the same time the current was calculated.

As the molecule unfolds the transmission drops off significantly, as a consequence of the favourable π-stacked pathway no longer being available. The local transmission analysis was used in this instance to characterise the nature of the pathways that dominate the transport over the unfolding process. Rather than plotting the local transmission, or summing over a surface, a range of chemically relevant interactions were considered, and the local transmission elements contributing to those pathways were summed. The four situations considered are illustrated in Fig. 6c, namely, transmission across the stack as a whole, transmission through the four hydrogen bonds, transmission through a single hydrogen bond that is favoured just before the system unfolds and transmission through a single hydrogen bond that is possible after the system unfolds. If the sum of these local transmission elements was greater than 80% of the total transmission that geometry was coloured. This analysis allowed us to demonstrate the role of these different interactions in mediating the tunnelling current at various stages during the pulling simulation. Of particular interest were the high levels of transport through the single hydrogen bond that dominates transport in the unfolded conformations. These conformations dominated the high transmission region of the unfolded conformation and significantly reduced the "on/off" ratio that could be expected between the folded and unfolded conformations. This result provides an important feedback for molecular design, a single change in a substituent could result in a molecule that could form three hydrogen bonds to stabilise the stacked structure, but that was unable to form this hydrogen bond in the unfolded state, thereby improving the "on/off" ratio significantly.
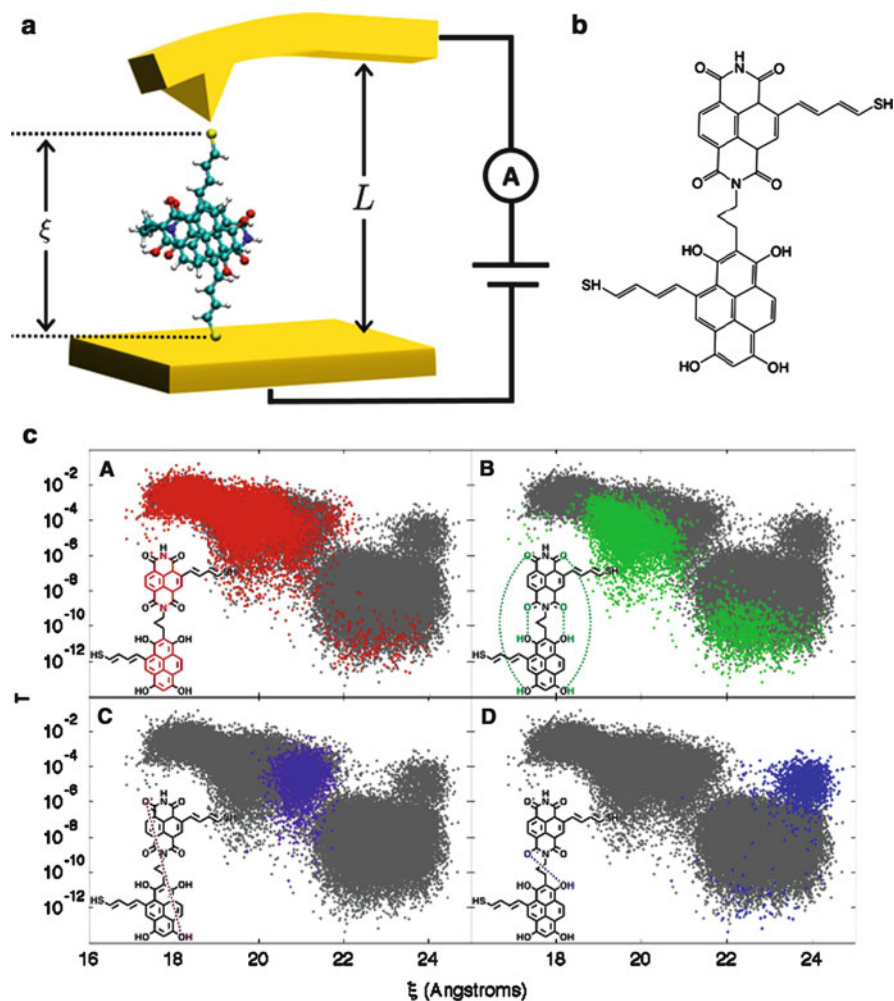
Fig. 6 (**a**) Schematic of a single-molecule pulling/molecular electronics setup. In it, a molecule is attached to a metallic surface and a conducting AFM tip. The distance between the surface and the cantilever (L) is controlled, a voltage is applied across the junction and the resulting current measured. (**b**) The molecule considered. (**c**) Conformational signatures in the transport properties. The figure highlights geometries where the absolute value of the local contribution to the transmission coming from a particular transport mode is at least 80% of the total gDFTB transmission. The insets specify the different modes of transport considered. Reprinted with permission from [4]. Copyright 2012 American Chemical Society

6 Conclusions

We have illustrated here some of the ways in which a local transport description can be used to characterise the interactions within a molecule that mediate a tunnelling current. Some of the results that emerge from this picture are unsurprising,

for example, that current flows through bonds in systems without dominant destructive interference; however, some of the results are less obvious. We have shown that interference features can be characterised by ring-current reversal, coupling of interference features can be seen in increased complexity in the local currents, and the nature of the interactions that dominate transport in complex systems can be identified using local transmission analysis. This method is not the only tool available for analysing the transmission through molecules, and as more tools are developed, so too will the richness of the picture we have of molecular transport develop.

References

1. Andrews, D.Q., Solomon, G.C., Van Duyne, R.P., Ratner, M.A.: Single molecule electronics: increasing dynamic range and switching speed using cross-conjugated species. J. Am. Chem. Soc. **130**(51), 17,309–17,319 (2008)
2. Bilic, A., Reimers, J.R., Hush, N.S.: The structure, energetics, and nature of the chemical bonding of phenylthiol adsorbed on the au(111) surface: implications for density-functional calculations of molecular-electronic conduction. J. Chem. Phys. **122**(9), 094, 708–15 (2005)
3. Elstner, M., Porezag, D., Jugnickel, G., Elsner, J., Haugk, M., Frauenheim, T., Suhai, S., Seifert, G.: Self-consistent-charge density-functional tight-binding method for simulations of complex materials properties. Phys. Rev. B **58**, 7260–7268 (1998)
4. Franco, I., George, C.B., Solomon, G.C., Schatz, G.C., Ratner, M.A.: Mechanically activated molecular switch through single-molecule pulling. J. Am. Chem. Soc. **133**(7), 2242–2249 (2011)
5. Pecchia, A., Di Carlo, A.: Atomistic theory of transport in organic and inorganic nanostructures. Rep. Prog. Phys. **67**(8), 1497–1561 (2004). 0034–4885
6. Porezag, D., Frauenheim, T., Kohler, T., Seifert, G., Kaschner, R.: Construction of tight-binding-like potentials on the basis of density-functional theory: application to carbon. Phys. Rev. B **51**, 12,947–12,957 (1995)
7. Shao, Y., Molnar, L.F., Jung, Y., Kussmann, J., Ochsenfeld, C., Brown, S.T., Gilbert, A.T.B., Slipchenko, L.V., Levchenko, S.V., O'Neill, D.P., Jr, R.A.D., Lochan, R.C., Wang, T., Beran, G.J.O., Besley, N.A., Herbert, J.M., Lin, C.Y., Voorhis, T.V., Chien, S.H., Sodt, A., Steele, R.P., Rassolov, V.A., Maslen, P.E., Korambath, P.P., Adamson, R.D., Austin, B., Baker, J., Byrd, E.F.C., Dachsel, H., Doerksen, R.J., Dreuw, A., Dunietz, B.D., Dutoi, A.D., Furlani, T.R., Gwaltney, S.R., Heyden, A., Hirata, S., Hsu, C.P., Kedziora, G., Khalliulin, R.Z., Klunzinger, P., Lee, A.M., Lee, M.S., Liang, W., Lotan, I., Nair, N., Peters, B., Proynov, E.I., Pieniazek, P.A., Rhee, Y.M., Ritchie, J., Rosta, E., Sherrill, C.D., Simmonett, A.C., Subotnik, J.E., Iii, H.L.W., Zhang, W., Bell, A.T., Chakraborty, A.K.: Advances in methods and algorithms in a modern quantum chemistry program package. Phys. Chem. Chem. Phys. **8**(27), 3172–3191 (2006). 10.1039/b517914a
8. Solomon, G.C., Bergfield, J.P., Stafford, C.A., Ratner, M.A.: When small terms matter: coupled interference features in the transport properties of cross-conjugated molecules. Beilstein J. Nanotechnol. **2**, 862–871 (2011)

9. Solomon, G.C., Gagliardi, A., Pecchia, A., Frauenheim, T., Di Carlo, A., Reimers, J.R., Hush, N.S.: The symmetry of single-molecule conduction. J. Chem. Phys. **125**(18), 184, 702–5 (2006)
10. Solomon, G.C., Herrmann, C., Hansen, T., Mujica, V., Ratner, M.A.: Exploring local currents in molecular junctions. Nat. Chem. **2**(3), 223–228 (2010). 1755–4330 10.1038/nchem.546 10.1038/nchem.546
11. Solomon, G.C., Herrmann, C., Vura-Weis, J., Wasielewski, M.R., Ratner, M.A.: The chameleonic nature of electron transport through –stacked systems. J. Am. Chem. Soc. **132**(23), 7887–7889 (2010)
12. Todorov, T.N.: Tight-binding simulation of current-carrying nanostructures. J. Phys. Condens. Matter **14**(11), 3049–3084 (2002). 0953–8984

Switching Mechanisms for Single-Molecule Logic Gates

C. Toher, F. Moresco, and G. Cuniberti

Abstract Single-molecule logic gates have the potential to fundamentally revolutionize computer architecture. However, performing any type of logic function within a single molecule requires using external inputs to modify one or more of the intrinsic properties of the molecule, such as its geometrical conformation, electronic structure, or spin configuration. In this chapter, we will discuss the variety of different physical mechanisms which have been proposed to induce and control such changes, ranging from applied potential bias and electric fields to chemical interactions to mechanical pressure, focusing in particular on their suitability for use in single-molecule logic circuitry.

1 Introduction

Architectures based on single-molecule logic gates have the potential to revolutionize computer science, leading to smaller, faster, cheaper, more energy-efficient computer circuitry [1–10]. However, performing any type of computational procedure within a single molecule requires using external inputs to modify one or more of the intrinsic properties of the molecule, such as its geometrical conformation, electronic structure, or spin configuration. Several different physical mechanisms have been proposed to induce such changes, ranging from applied potential bias and electric fields to chemical interactions to mechanical pressure [11]. In this chapter, we will discuss such mechanisms, focusing in particular on their suitability for use in single-molecule logic circuitry and on some of the solutions which have been

C. Toher (✉) · F. Moresco · G. Cuniberti (✉)
Institute for Materials Science and Max Bergmann Center of Biomaterials,
Dresden University of Technology, 01062 Dresden, Germany
e-mail: cormac.toher@tu-dresden.de; research@nano.tu-dresden.de

developed to the various problems which come up in trying to create functioning examples of such devices.

Progress in conventional semiconductor electronics at the logic gate level has run into a wall in recent years and is failing to keep up with Moore's law. The primary reason for this is power consumption and the resulting heat dissipation problems. This is due to the fact that as transistors become smaller and gate dielectrics become thinner, quantum tunneling of charge carriers becomes a significant contributor to the current, even when the component is in the "off" state, resulting in leakage currents and thus energy wastage. As well as the obvious economic and environmental problems, this increased energy usage in a shrinking volume results in overheating of the computer chip, shortening its lifespan. Another current performance bottleneck in computational operations is transferring data from memory to the processor in order to perform operations on. Indeed, for simple operations, it can often take longer to retrieve data from memory than it takes to perform the operation itself.

Solutions to this problem which are currently being implemented include the use of multi-core processors and parallel programming and the used of specialized power-efficient accelerators to perform specific functions, such as graphical processing units (GPUs). Other suggestions include incorporating a certain amount of processing capability into memory to perform simple operations, such as sorting numbers, or to use transistors to turn off entire sections of the processor which are not currently in use. The use of advanced materials with high thermal conductivity such as fullerenes to act as heat sinks has also been investigated [12]. However, these methods are primarily work-arounds and do not address the fundamental long-term problems which need to be overcome in order to achieve significantly higher computational performance. In order to do this, new computational paradigms need to be investigated, such as single-molecule logic gates.

A logic gate functions by comparing the values of one or more inputs and then producing an appropriate output for these values. Therefore, for any device to function as a logic gate, it must be able to produce a readable output which is determined by a property which can be modified in a predictable way by the values of external inputs. In logic gates based on conventional electronic circuits, the inputs and outputs are voltage levels, and the modifiable property is its conductance. For single molecules, there are a wide range of intrinsic properties which can be modified and several different physical mechanisms which can be used to modify them and thus be used as external inputs. However, when a single-molecule logic gate is intended to function as part of a larger circuit to perform complex computational operations, certain constraints must be considered as to which types of mechanisms are suitable for use. In particular, it must be possible to produce and control the values of the inputs within nanoscale circuits. Additionally, for single-molecule logic gates to be connected together in sequence to produce computer circuits, the output of the logic gate should ideally be of the same form as the inputs, or at least transformable into the same form at the nanoscale.

2 Switching Mechanisms

Intrinsic properties of molecules which can be altered using controllable external inputs include its geometrical conformation, its charge state, its electronic structure, its spin configuration, and even its chemical makeup. In addition to the intrinsic geometry of the molecule itself, the entire position of the molecule, and thus, its bonding to the electrodes can also be changed. These properties are also interdependent, as a change in the charge state or geometry of a molecule can have a significant impact on its electronic structure. Several different physical mechanisms can be used to induce changes in these properties, including electric fields and applied bias, magnetic fields, light, vibrational heating due to inelastic scattering of tunneling electrons, mechanical pressure and strain, temperature, and chemical interactions. It is often possible to control these properties using more than one of these mechanisms. For example, conformational changes in the geometry can be induced by light, electric fields, vibrational heating due to inelastic scattering of electrons, pressure, etc. In this section, we will discuss examples of each type of mechanism, illustrating the types of molecular properties, which they can be used to control, and examining their advantages and disadvantages for use in the implementation of single-molecule logic gates.

2.1 Current-Induced Switching

One of the first examples of a switch at the single-atom or molecule level was constructed by Eigler et al. [13] using a scanning tunneling microscope (STM) [14, 15], where a Xe atom was found to jump between a Ni substrate and a STM tip when a voltage of 0.8 V was applied, resulting in a change of the conductance. This switching behavior was shown to be due to be current driven, specifically due to vibrational heating of the adsorbate by the inelastic scattering of tunneling electrons [16]. The electrons progressively excite vibrational modes of the adsorbate, supplying it with enough energy to overcome the potential barrier between the substrate and the tip. The switching rate for this mechanism was found to have a power law dependence on the voltage, where the exponent was the number of vibrational levels which needed to be excited to overcome the potential barrier. This mechanism was also used to induce the switching of Ag adatoms between different adsorption sites on Ag(111) [17] and to induce conformational changes in a PTCDA molecule so that it switched in and out of contact with a STM tip [18]. Tikhodeev et al. [19] combined the concept of the progressive excitation of vibrational levels with tunneling to formulate the vibrational assisted tunneling model. In this mechanism, the successive excitation of the adsorbate is combined with the fact that the barrier height and width reduces near the top of the potential well. This mechanism was used to describe the hydrogen-bond exchange in water dimers on Cu(110) observed by Kumagai et al. [20]. The vibrational heating mechanism is described in more detail in the chapter by Brumme et al. [3].
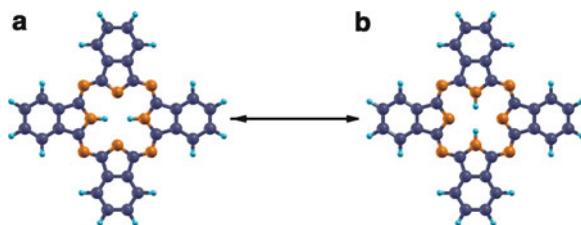
Fig. 1 Hydrogen tautomerization in a phthalocyanine molecule. The two H atoms in the center move so that they are attached to different N atoms, effectively rotating the structure of the molecule by 90°, thus changing the conductance properties of the different ligands. Color code: C = black, N = orange, H = blue

The inelastic scattering of a single electron can also be used to induce conformation changes in molecules for situations where the energy barrier is low or the applied bias is sufficiently high. As it takes only one electron to induce a switching event, the switching rate will be directly proportional to the number of electrons passing through the molecule and so will depend linearly on the current. Single-electron inelastic scattering has been used to induce conformational changes in an azobenzene derivative on Au(111) [21] at a bias of 650 mV, with the reverse isomerization at biases of less than 640 mV and in dibenzo[a,h]thianthrene (DBTH) on a NaCl thin film on Cu(111) [22]. The energy barrier for the two naphthalene side units to switch with respect to the S atoms so they went from pointing down to the substrate to pointing upward was calculated with DFT to be 200 meV. Single-electron processes have also been used to drive hydrogen tautomerization in naphthalocyanine molecules [23] and tetraphenyl-porphyrin molecules [24] using STM, where the two H atoms in the center of the molecule switched between the central N atoms with a frequency which depended linearly on the current, as demonstrated for the phthalocyanine molecule shown in Fig. 1. This mechanism has also been used to form and break chemical bonds, such as the formation bond between PVBA molecules and Cu adatoms on a Cu(111) substrate to form Cu(PVBA)$_2$ complexes [25] or for the sequential dehydrogenation of Co-salen complexes using STM [26].

2.2 Charge-Induced Switching

The total charge on an atom or molecule can be altered using electric fields, either in the form of a bias applied across the molecule or by a gate field. However, unless the atom or molecule is somehow decoupled from the electrodes, the electron will tunnel back into the electrodes, and the molecule will revert to its original charge state. This decoupling can be done by growing a thin insulating film on top of the electrodes or by adding nonconjugated spacer groups to the ends of the molecule. The insulating film method was used by Repp et al. [27] and Olsson et al. [28], where

a NaCl film was used to separate Au or Ag atoms from the underlying Cu substrate. For the Au atoms [27], a voltage pulse was used to induce a negative charge on the atom, and both the charged and neutral states of the atom appeared to be stable, apparently due to their occupation of different binding sites. Similarly for the Ag atoms [28], a voltage pulse of 1.3 V was used to switch between neutral (Ag^0), positively charged (Ag^+), and negatively charged states (Ag^-). These different charge states were stabilized by changing the binding site from a bridge site to a top site. A similar dependency between binding site and charge state was observed for a monolayer made up of the electron acceptor tetracyanoquinodimethane (TCNQ) and the electron donor tetramethyltetrathiafulvalene (TMTTF) [29] . In this case, the TCNQ molecules in one row displayed a Kondo resonance at low bias, indicating that they had a singly occupied molecular orbital and thus had a net electric charge, whereas the other type displayed no Kondo peak and was charge neutral. It was possible to switch between the two charge states by applying a bias across the molecule. Different molecular charge states can also be stabilized by conformational changes in the molecule, as observed for bisdibenzoylmethanato-copper (Cu(dbm)$_2$) on an insulating NaCl thin film on Cu(111) [30]. This molecule could be charged and discharged by applying a bias of $+2$ V and -2 V, respectively, changing the molecule geometry between square planar and tetrahedral. This change in conformation and charge state shifted the molecular orbitals upward in energy, resulting in a hysteresis in the I–V. Conductance hysteresis was also observed for magnesium porphyrin (MgP) on a thin film of alumina on NiAl(110) [31]. An electron could be injected or removed by applying a bias of 0.85 V and -1.2 V, respectively, and measurements of the effective barrier height suggested an ionic relaxation in the alumina film stabilized the charge states.

The charge state on a molecule can also be controlled using gate electric fields applied orthogonal to the transport direction. The gate field adjusts the energies of the molecular orbitals relative to the chemical potentials of the electrodes, allowing the molecule to charge and discharge. However, unless this is combined with conformational changes to stabilize the different charge states, the charge state of the molecule is usually dependent on the presence of this gate field, and thus there is no hysteresis in the I–V curve. Gate potentials can be generated for molecular junction using electrochemical gating where the device is in a solution, or by fabricating the junction on top of a gate electrode. Cyclic voltammetry was used to investigate redox interactions in Fe-protoporphyrin (FePP) [32] and a complex consisting of a Co ion bonded to polypyridyl ligands [33]. A redox peak was observed in the cyclic voltammogram at -0.48 V for FePP, whereas no such peak was observed for PP [32], while a redox peak was observed for the Co complex at 0.25 V corresponding to the transition between the Co^{2+} and Co^{3+} states. A STM molecular junction was used to measure the conductance of a mercaptohexyl-bipyridine-hexanethiol-iodide molecule with a viologen redox center in the presence of electrochemical gating [34]. An increase in the conductivity was observed between -0.2 V and -0.6 V, which was associated with the reduction of the viologen group from a 2+ state to a radical 1+ state. For PTCDI molecules, a small hysteresis was observed when sweeping the gate voltage [35], which was attributed to a structural reorganization

of the molecules which stabilized the different charge states. Three different charge states were observed in tetrathiafulvalenes (TTFs) on an ITO substrate[36]. The charge state of the molecule was switched from neutral to cation to dication using an electrochemical gate at voltages of 0.74 V and 1.30 V, respectively. AuPd electrodes formed by electromigration on top of an Al/Al_2O_3 gate electrode were used to investigate the electron transport and addition energies for the different charge states of a thiol end-capped oligophenylenevinylene molecule (OPV-5) [37, 38] . The charge state of the molecule was controlled using the gate electrode, and Kondo resonances were observed for odd numbers of electrons.

Recently, a single-atom transistor was fabricated by Fuechsle et al. [39] using STM and hydrogen resist lithography. Source, drain, and two gate electrodes were fabricated by heavily doping the Si substrate with P atoms, and then a single P atom was implanted in the center. The gate field was then used to control the charge and conductance of the P atom.

2.3 Electric Field-Induced Conformational Changes

As well as inducing changes in the charge state, electric fields can be used to directly change the conformation of a molecule. This was observed using STM for Zn(II) etioporphyrin (ZnEtio) on NiAl(110) [40]. The molecule switched between two different conformations, from a saddle shape to a clover shape at 1.35 V, and then back to the saddle shape at −1.38 V. The two different conformations had different conductivities, so that the I–V curve displayed hysteresis. The magnitude of the negative bias required to switch from the clover shape to the saddle shape depended linearly on the tip height, indicating that this was an electric field effect, whereas the switching from the saddle shape to the clover shape was driven by inelastic electron tunneling. Electric field driven conformational changes were also observed using STM for an azobenzene derivative on Au(111) [41]. The cis to trans isomerization in the azobenzene molecule could be induced by an applied voltage, even for very large tip heights where there would be no current, indicating that this was an electric field effect. A more complex version of this mechanism was observed for Si adatoms contained in dimeric chlorododecane corrals on a Si(111) substrate [42]. Changes in the configuration of the pair of dipolar molecules forming the corral resulted in changes to the local electric field on the adatom, which in turn resulted in changes in its conductance. Switching and I–V hysteresis were induced in bipyridyl-dinitro oligophenylene-ethynylene dithiol (BPDN-DT) molecules [43] in a mechanically controllable break junction setup. This hysteresis was not observed for reference bipyridyl oligophenylene-ethynylene dithiol (BP-DT) molecules, which have the nitro groups removed. DFT calculations indicated that this change was due to the interaction between the applied electric field and the electric dipole moment of the BPDN-DT molecule [44], which was of the order of 3.0 Debye. This interaction caused a change in the conformation of the molecule, altering its conductance and inducing hysteresis in the I–V characteristics.

An electrochemical potential was used to alter the contact between a specially synthesized cruciform molecular structure and the electrodes [45]. The molecule consisted of an oligophenylenevinylene and an oligophenyleneethynyl molecule connected at the center in a cruciform structure. The electrochemical potential changed the orientation of the entire molecule, so that the pyridine groups were shifted in and out of contact with the electrodes.

2.4 Mechanically Induced Conformational Changes

The conformation of a molecule can also be changed using direct mechanical manipulation, such as with a STM tip or by stretching a mechanically controlled break junction. This was demonstrated by Moresco et al. [46], who used an STM tip to manipulate the orientation of the "legs" of Cu-tetra-3,5 di-tert-butyl-phenyl porphyrin (Cu-TBPP) molecules deposited on Cu(211). The conductance of the molecule where one of the legs is rotated was found to be higher than the flat molecule by approximately one order of magnitude. By performing lateral manipulation on this molecule using the STM tip, the molecule can be reversibly switched between the two configurations. The energy required for this switching procedure was determined using AFM measurements and molecular mechanics calculations to be of the order of 47zJ and 83zJ, respectively [47]. Mechanically controlled break junctions were used to investigate strain-induced conformational changes in hexanedithiol [48]. Two different peaks were observed in the conductance histogram obtained while repeatedly opening and closing the junction, which were due to the molecule switching between the trans and gauche conformations. The conductance of the trans conformation was approximately one order of magnitude higher because the current carrying orbitals are delocalized across the molecule. The use of a graphene sheet to apply strain to a magnetic molecule was investigated using DFT calculations with LSDA+U [49]. A Fe-porphyrin (FeP) molecule was placed on a graphene divacancy defect site, and the magnetic state of this molecule could be switched between $S = 2$ and $S = 4$ by the application of tensile and compressive strain. Applying tensile and compressive strain to a molecular junction can also alter the interaction between the molecule and the electrodes, which can change the conductance [50]. By stretching and compressing the junction formed by a bipyridine molecule bridging gold electrodes, the orientation of the molecule to the surfaces, and thus the coupling between the conducting LUMO and the electrodes could be altered. This resulting in the conductance switching between values of $1.6 \times 10^{-4} G_0$ and $6 \times 10^{-4} G_0$.

2.5 Atomic Contact-Induced Switching

As well as directly manipulating the position or structure of the atom or molecule itself, the properties of a single-molecule device can be altered by moving other

atoms into contact with it. This is typically done using a STM tip to manipulate adatoms on a substrate so that they come into contact and form chemical bonds with an adsorbed molecule. One of the first studies on the interaction of single atoms with individual molecules was on the formation of chemical bonds between Fe atoms and CO molecules on the Ag(110) substrate using STM [51]. This was followed by Nazin et al. [52] attaching chains of Au atoms to Cu-phthalocyanine (CuPc) molecules on a NiAl(110) substrate. These chains of atoms have the effect of shifting the lowest unoccupied CuPc orbital to lower energies, thus increasing the low bias conductance. Similar results were obtained by Yamachika et al. [53] who moved K atoms into contact with C_{60} molecules on a Ag(001) surface using a STM tip. This resulted in the K atoms transferring up to 0.6 electrons to the C_{60} molecule, and the lowest unoccupied orbitals of the C_{60} molecule shifted down in energy with each additional K atom that was moved into contact with it. A more complex interaction was described by Wegner et al. [54], who moved V atoms into contact with tetracyanoethylene (TCNE) on a Ag(100) substrate, resulting in a ferromagnetic coupling between the V atoms. By changing the arrangement of the TCNE molecule and the two V atoms, the Kondo effect could be switched on and off, resulting in significant changes in the low bias conductance. Investigations were performed on a thin film of NaCl on a Cu substrate involving moving Au atoms into contact with pentacene [55] and PTCDA [56]. For pentacene, the chemical bond was formed and broken through inelastic electron tunneling, while the Au-PTCDA complex was formed by using and applied bias of 1.5 V to remove one of the electrons from the negatively charge separate Au atom and PTCDA molecule. Again on the insulating NaCl substrate, Liljeroth et al. [57] used an STM to form complexes of dicyanoanthracene (DCA) molecules with Fe and Ni atoms. The metal atom strongly affected the spin state of the DCA molecules and the spatial symmetry of the molecular orbitals.

Localized molecular orbitals were individually successfully manipulated by using a STM tip to move single Cu atoms into contact with the terpyridine side groups of bis-terpyridine tetraphenyl ethylene (BTP-TPE) molecules on a Cu(111) substrate [58]. When a Cu atom was attached to only one end of the molecule, significant differences were observed in the STS measurements recorded at different ends of the molecule. The positioning of Au atoms with respect to two of the ends of a trinaphthylene molecule was used to produce a NOR logic gate [9]. The trinaphthylene molecule consists of three branches and was deposited on Au(111). Moving Au atoms into and out of contact with the ends of two of the branches altered the Rabi-like oscillation frequency. This could be detected by positioning the STM tip over the apex of the third branch of the molecule and measuring the tunneling current, which is proportional to the square of this oscillation frequency. This produced a NOR gate, so that a high tunneling current, corresponding to a logical "1", was obtained when both Au atoms were out of contact with the molecule (corresponding to logical "0" on the inputs), and a much lower tunneling current was observed when one or both Au atoms were in contact with the molecule.

Fig. 2 The azobenzene molecule can switch between (**a**) cis and (**b**) trans conformations, which have different conductance properties. Color code: C = black, N = orange, H = blue
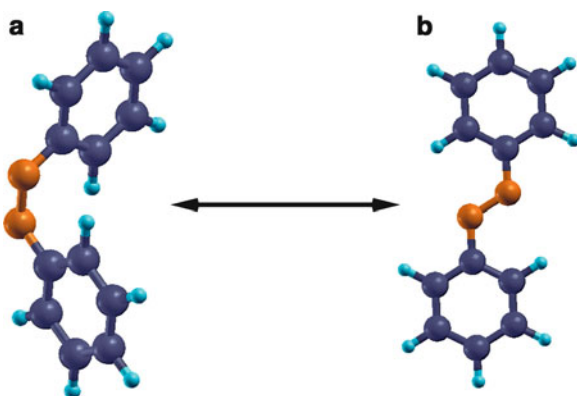
2.6 Light-Induced Switching

Electromagnetic radiation, typically in the ultraviolet part of the spectrum, can also be used to change the conformation and conductivity of molecular devices. One of the most commonly used light-activated molecular switches is azobenzene, which exists in cis and trans conformations, as shown in Fig. 2. DFT-based electronic transport calculations for molecular junctions formed from azobenzene molecules show different conductances for the two conformations [59–62], demonstrating that this molecule could operate as an electrical switch. Examples of other molecules which can operate as light-activated switches include diarylethene [63], carboxy-benzylideneaniline (CBA) [64], and molecular dyads consisting of a porphyrin chromophore and a C60 electron acceptor [65].

However, in order to use such molecules in devices, they first need to be attached to electrodes, and the interaction between the molecule and metal substrates can interfere with the switching process. This is due primarily to the shortened lifetimes of the photoexcited electrons, which tend to transfer from the excited state into the metallic substrate. To overcome this, methods to isolate the optically active part of the molecules from the substrate are used. For example, ligands are added to azobenzene molecules to form derivatives such as tetra-*tert*-butyl-azobenzene (TBA) [66, 67]. Another method is to trap the azobenzene derivatives in a physisorption well [68] so that it does not form a chemical bond with the substrate. Adding a thin insulating film, for example, a NaCl bilayer, on top of the metal electrode can isolate the molecule electronically from the metal electrode, thus allowing optically activated switching to take place [69].

There are several significant obstacles to using light-induced switching in logic circuits, however. Firstly, the experiments described above involved illuminating the entire substrate, whereas selectively illuminating a single molecule in a logic circuit would be much more difficult. Also, repeated exposure to ultraviolet light tends to degrade the molecule with time [63]. Nevertheless, light-induced switching could

have important applications for sensors, energy harvesting, communications, and data transfer. These experiments also demonstrate the importance of controlling the strength of the coupling with the metallic electrodes, as this interaction can interfere with the switching process.

2.7 Thermally Induced Switching

In several of the light-induced molecular switching measurements above, the switching process could be reversed by thermal annealing [64, 66]. There are also examples of molecular switches where the switching could only be induced by thermal isomerization, such as di-tert-butyl-(di-tert-butylbenzylidene)aniline (TBI) [70] and oligophenylenevinylene derivative (OPV3) [71]. However, it is difficult to selectively apply heat to individual molecule, so thermal switching is probably not very suitable as a basis for single-molecule logic.

2.8 Magnetic Molecules

Molecules with magnetic centers offer another degree of freedom which is susceptible to external manipulation: electron spin. There are two main types of switching effects in such molecules: either the net spin on the magnetic center is changed (spin crossover) or the magnetic interaction between different magnetic atoms is changed so that the overall magnetic moment of the molecule is changed. The spin-crossover effect can be induced on a single magnetic center using a number of physical mechanisms [72–74], including temperature, pressure, light, and applied electric fields, and examples of each are discussed in detail below. Single-molecule magnets consist of several transition metal atoms embedded in an organic framework. One commonly used family of single-molecule magnets are the Mn_{12} complexes. Another type are based on Fe_4 complexes, as investigated by Mannini et al. [75] on Au(111) using XMCD and STM, with applied magnetic fields of up to 3 T. The molecules consisted of 4 Fe(III) ions attached to 2-hydroxymethyl-1,3-propanediol ligands, and they exhibited magnetic hysteresis at 0.5 K but only showed paramagnetic behavior at 1.0 K.

The spin-crossover effect can be induced by a variety of different phenomena, including temperature, pressure, etc. From the point of view of single-molecule logic gates, the most interesting effect is the electrostatic spin-crossover effect, where the application of an external electric field changes the lowest energy spin configuration of the molecule. This works because the different spin configurations have either different permanent dipole moments or different polarizabilities. An example of an electrostatic spin crossover for a molecule with a permanent dipole moment was demonstrated by Baadji et al. [76] using a cobaltocene dimer (diCo) with a methoxy group attached. DFT calculations using the hybrid B3LYP

functional indicated the interaction between the two Co atoms should switch from antiferromagnetic to ferromagnetic upon the application of an electric field in excess of 1.5 V nm^{-1}. A similar ferromagnetic to antiferromagnetic transition was observed by Hao et al. [77] for the single-molecule magnet $Fe_2(acpypentO)(NCO)_3$ for an applied bias in the range of 0.4 V. The spin-crossover effect can also be observed in molecules which do not have a permanent dipole moment if the polarizabilities for the different spin states are different, as shown by Diefenbach et al. [78].

3   Conclusion

In this work, we have outlined many of the different switching mechanisms which can be used to alter the properties of a molecule and thus allow it to function as a logic device. However, not all of these mechanisms are suitable for use in logic circuits. Some of these mechanisms can degrade the molecules, or are suppressed by the interaction with a substrate. Other mechanisms are difficult to apply selectively to a single molecule, or are such that the output is in a different form than the input, complicating the linking together of several molecules to form a circuit.

One problem which is often encountered is that the switching properties of a molecule can be strongly affected by the interaction with metallic electrodes. This can be due, for example, to the shortening of the lifetime of an electron–hole pair required to activate the switching process. However, this problem can be overcome by attaching additional ligands to the molecule so as to electronically decouple it from the substrate.

Another limitation for practical commercial devices is that they should ideally be able to operate at ambient temperatures, as a requirement for sophisticated cooling would eliminate many of the cost and size advantages over conventional semiconductor electronics, although they may have applications for specialized very high performance devices.

For logic circuits, it is important that the output of one gate can be used as the input of another gate, to allow the performance of complex operations requiring multiple logic gates working in series. However, for the majority of the switching mechanisms described above, the input is a different property to the output, such as a photon inducing a change in the conductivity. Devices based on such mechanisms would require another conversion stage in order to work in logic circuits. For example, one could imagine using an electric current to move atoms in and out of contact with a molecule, changing its conductivity and thus providing another electric current, etc. However, this adds an extra level of complexity, reducing the speed of the logic operations and thus sacrificing some of the advantages over conventional semiconductor electronics. Such devices do however have a wide variety of very important applications including communications, sensors, energy harvesting, and interfaces to biological systems. They could even have important applications in advanced computational architectures: for example, light-activated

molecular switches could be very useful in data transfer applications, where information is converted into an optical form for transmission over relatively large distances (e.g., between the hard drive and the CPU). Nevertheless, devices based on such mechanisms are probably not very suitable for use as components in complex computer logic circuitry.

Therefore, the most promising molecules for use as logic gates are those in which both the input and output of the switching process are in the same form. From a practical point of view, this implies that the switching mechanism inputs should be electrical, that is, a finite bias, electric field, or current, and the output should be the same, that is, a change in the electronic conductance of the molecule. Devices which show hysteresis can also be used as memory elements, allowing for the combination of memory and logic functions within one circuit. Therefore, efforts to create single-molecule logic gates should probably focus on molecules which can be controlled using electrical inputs.

References

1. Joachim, C., Gimzewski, J.K., Aviram, A.: Electronics using hybrid-molecular and mono-molecular devices. Nature **408**, 541 (2000)
2. Joachim, C.: Bonding more atoms together for a single molecule computer. Nanotechnology **13**, R1 (2002)
3. Credi, A., Balzani, V., Langford, S.J., Fraser Stoddart, J.: Logic operations at the molecular level. An XOR gate based on a molecular machine. J. Am. Chem. Soc. **119**, 2679 (1997)
4. Prasanna de Silva, A., McClenaghan, N.D.: Proof-of-principle of molecular-scale arithmetic. J. Am. Chem. Soc. **122**, 3965 (2000)
5. Heinrich, A.J., Lutz, C.P., Gupta, J.A., Eigler, D.M.: Molecule cascades. Science **298**, 1381 (2002)
6. Ami, S., Hliwa, M., Joachim, C.: Molecular OR and AND logic gates integrated in a single molecule. Chem. Phys. Lett. **367**, 662 (2003)
7. Margulies, D., Melman, G., Shanzer, A.: A molecular full-adder and full-subtractor, an additional step toward a moleculator. J. Am. Chem. Soc. **128**, 4865 (2006)
8. Magri, D.C., Brown, G.J., McClean, G.D., Prasanna de Silva, A.: Communicating chemical congregation: a molecular and logic gate with three chemical inputs as a lab-on-a-molecule prototype. J. Am. Chem. Soc. **128**, 4950 (2006)
9. Soe, W.-H., Manzano, C., Renaud, N., de Mendoza, P., De Sarkar, A., Ample, F., Hliwa, M., Echavarren, A.M., Chandrasekhar, N., Joachim, C.: Manipulating molecular quantum states with classical metal atom inputs: demonstration of a single molecule NOR logic gate. ACS Nano **5**, 1436 (2011)
10. Soe, W.-H., Manzano, C., De Sarkar, A., Ample, F., Chandrasekhar, N., Renaud, N., de Mendoza, P., Echavarren, A.M., Hliwa, M., Joachim, C.: Demonstration of a NOR logic gate using a single molecule and two surface gold atoms to encode the logical input. Phys. Rev. B **83**, 155443 (2011)
11. van der Molen, S.J., Liljeroth, P.: Charge transport through molecular switches. J. Phys.: Condens. Matter **22**, 133001 (2010)

12. Montgomery, S.W., Holalkere, V.R.: Carbon nanotube thermal interface structures. US Patent No. 6965513 B2 (2005)
13. Eigler, D.M., Lutz, C.P., Rudge, W.E.: An atomic switch realized with the scanning tunnelling microscope. Nature **352**, 600 (1991)
14. Binnig, G., Rohrer, H., Gerber, Ch., Weibel, E.: Tunneling through a controllable vacuum gap. Appl. Phys. Lett. **40**, 178 (1982)
15. Binnig, G., Rohrer, H., Gerber, Ch., Weibel, E.: Surface studies by scanning tunneling microscopy. Phys. Rev. Lett. **49**, 57 (1982)
16. Gao, S., Persson, M., Lundqvist, B.I.: Theory of atom transfer with a scanning tunneling microscope. Phys. Rev. B **55**, 4825 (1997)
17. Sperl, A., Kröger, J., Berndt, R.: Direct observation of conductance fluctuations of a single-atom tunneling contact. Phys. Rev. B **81**, 035406 (2010)
18. Brumme, T., Neucheva, O.A., Toher, C., Gutiérrez, R., Weiss, C., Temirov, R., Greuling, A., Kaczmarski, M., Rohlfing, M., Tautz, F.S., Cuniberti, G.: Dynamical bistability of single-molecule junctions: a combined experimental and theoretical study of PTCDA on Ag(111). Phys. Rev. B **84**, 115449 (2011)
19. Tikhodeev, S.G., Ueba, H.: How vibrationally assisted tunneling with STM affects the motions and reactions of single adsorbates. Phys. Rev. Lett. **102**, 246101 (2009)
20. Kumagai, T., Kaizu, M., Hatta, S., Okuyama, H., Aruga, T., Direct observation of hydrogen-bond exchange within a single water dimer. Phys. Rev. Lett. **100**, 166101 (2008)
21. Henzl, J., Mehlhorn, M., Gawronski, H., Rieder, K.-H., Morgenstern, K.: Reversible cis-trans isomerization of a single azobenzene molecule. Angew. Chem. Int. Ed. **45**, 603 (2006)
22. Pavliček, N., Fleury, B., Neu, M., Niedenführ, J., Herranz-Lancho, C., Ruben, M., Repp, J.: Atomic force microscopy reveals bistable configurations of dibenzo[a,h]thianthrene and their interconversion pathway. Phys. Rev. Lett. **108**, 086101 (2012)
23. Liljeroth, P., Repp, J., Meyer, G.: Current-induced hydrogen tautomerization and conductance switching of naphthalocyanine molecules. Science **317**, 1203 (2007)
24. Auwärter, W., Seufert, K., Bischoff, F., Ecija, D., Vijayaraghavan, S., Joshi, S., Klappenberger, F., Samudrala, N., Barth, J.V.: A surface-anchored molecular four-level conductance switch based on single proton transfers. Nat. Nanotechnol. **7**, 41 (2011)
25. Ohmann, R., Vitali, L., Kern, K.: Actuated transitory metal-ligand bond as tunable electromechanical switch. Nano Lett. **10**, 2995 (2010)
26. Baadji, N., Kuck, S., Brede, J., Hoffmann, G., Wiesendanger, R., Sanvito, S.: Controlled sequential dehydrogenation of single molecules by scanning tunneling microscopy. Phys. Rev. B **82**, 115447 (2010)
27. Repp, J., Meyer, G., Olsson, F.E., Persson, M.: Controlling the charge state of individual gold adatoms. Science **305**, 493 (2004)
28. Olsson, F.E., Persson, M., Paavilainen, S., Repp, J., Meyer, G.: Multiple charge states of Ag atoms on ultrathin NaCl films. Phys. Rev. Lett. **98**, 176803 (2007)
29. Fernández-Torrente, I., Kreikemeyer-Lorenzo, D., Strózecka, A., Franke, K.J., Pascual, J.I.: Gating the charge state of single molecules by local electric fields. Phys. Rev. Lett. **108**, 036801 (2012)
30. Leoni, T., Guillermet, O., Walch, H., Langlais, V., Scheuermann, A., Bonvoisin, J., Gauthier, S.: Controlling the charge state of a single redox molecular switch. Phys. Rev. Lett. **106**, 216103 (2011)
31. Wu, S.W., Ogawa, N., Nazin, G.V., Ho, W.: Conductance hysteresis and switching in a single-molecule junction. J. Phys. Chem. C **112**, 5241 (2008)
32. Tao, N.J.: Probing potential-tuned resonant tunneling through redox molecules with scanning tunneling microscopy. Phys. Rev. Lett. **76**, 4066 (1996)
33. Park, J., Pasupathy, A.N., Goldsmith, J.I., Chang, C., Yaish, Y., Petta, J.R., Rinkoski, M., Sethna, J.P., Abruna, H.D., McEuen, P.L., Ralph, D.C.: Coulomb blockade and the Kondo effect in single-atom transistors. Nature **417**, 722 (2002)
34. Haiss, W., van Zalinge, H., Higgins, S.J., Bethell, D., Höbenreich, H., Schiffrin, D.J., Nichols, R.J.: Redox state dependence of single molecule conductivity. J. Am. Chem. Soc. **125**, 15294 (2003)

35. Li, X., Hihath, J., Chen, F., Masuda, T., Zang, L., Tao, N.: Thermally activated electron transport in single redox molecules. J. Am. Chem. Soc. **129**, 11535 (2007)
36. Simão, C., Mas-Torrent, M., Casado-Montenegro, J., Otón, F., Veciana, J., Rovira, C.: A three-state surface-confined molecular switch with multiple channel outputs. J. Am. Chem. Soc. **133**, 13256 (2011)
37. Osorio, E.A., O'Neill, K., Wegewijs, M., Stuhr-Hansen, N., Paaske, J., Bjørnholm, T., van der Zant, H.S.J.: Electronic excitations of a single molecule contacted in a three-terminal configuration. Nano Lett. **7**, 3336 (2007)
38. Osorio, E.A., O'Neill, K., Stuhr-Hansen, N., Nielsen, O.F., Bjørnholm, T., van der Zant, H.S.J.: Addition energies and vibrational fine structure measured in electromigrated single-molecule junctions based on an oligophenylenevinylene derivative. Adv. Mater. **19**, 281 (2007)
39. Fuechsle, M., Miwa, J.A., Mahapatra, S., Ryu, H., Lee, S., Warschkow, O., Hollenberg, L.C.L., Klimeck, G., Simmons, M.Y.: A single-atom transistor. Nat. Nanotechnol. **7**, 242 (2012)
40. Qiu, X.H., Nazin, G.V., Ho, W.: Mechanisms of reversible conformational transitions in a single molecule. Phys. Rev. Lett. **93**, 196806 (2004)
41. Alemani, M., Peters, M.V., Hecht, S., Rieder, K.H., Moresco, F., Grill, L.: Electric field-induced isomerization of azobenzene by STM. J. Am. Chem. Soc. **128**, 14446 (2006)
42. Harikumar, K.R., Polanyi, J.C., Sloan, P.A., Ayissi, S., Hofer, W.A.: Electronic switching of single silicon atoms by molecular field effects. J. Am. Chem. Soc. **128**, 16791 (2006)
43. Lörtscher, E., Ciszek, J.W., Tour, J., Riel, H.: Reversible and controllable switching of a single-molecule junction. Small **2**, 973 (2006)
44. Meded, V., Bagrets, A., Arnold, A., Evers, F.: Molecular switch controlled by pulsed bias voltages. Small **5**, 2218 (2009)
45. Grunder, S., Huber, R., Horhoiu, V., González, M.T., Schönenberger, C., Calame, M., Mayor, M.: New cruciform structures: toward coordination induced single molecule switches. J. Org. Chem. **72**, 8337 (2007)
46. Moresco, F., Meyer, G., Rieder, K.-H., Tang, H., Gourdon, A., Joachim, C.: Conformational changes of single molecules induced by scanning tunneling microscopy manipulation: a route to molecular switching. Phys. Rev. Lett. **86**, 672 (2001)
47. Loppacher, C., Guggisberg, M., Pfeiffer, O., Meyer, E., Bammerlin, M., Lüthi, R., Schlittler, R., Gimzewski, J.K., Tang, H., Joachim, C.: Direct determination of the energy required to operate a single molecule switch. Phys. Rev. Lett. **90**, 066107 (2003)
48. Kim, Y., Song, H., Strigl, F., Pernau, H.-F., Lee, T., Scheer, E.: Conductance and vibrational states of single-molecule junctions controlled by mechanical stretching and material variation. Phys. Rev. Lett. **106**, 196804 (2011)
49. Bhandary, S., Ghosh, S., Herper, H., Wende, H., Eriksson, O., Sanya, B.: Graphene as a reversible spin manipulator of molecular magnets. Phys. Rev. Lett. **107**, 257202 (2011)
50. Quek, S.Y., Kamenetska, M., Steigerwald, M.L., Choi, H.J., Louie, S.G., Hybertsen, M.S., Neaton, J.B., Venkataraman, L.: Mechanically controlled binary conductance switching of a single-molecule junction. Nat. Nanotechnol. **4**, 230 (2009)
51. Lee, H.J., Ho, W.: Single-bond formation and characterization with a scanning tunneling microscope. Science **286**, 1719 (1999)
52. Nazin, G.V., Qiu, X.H., Ho, W.: Visualization and spectroscopy of a metal-molecule-metal bridge. Science **302**, 77 (2003)
53. Yamachika, R., Grobis, M., Wachowiak, A., Crommie, M.F.: Visualization and spectroscopy of a metal-molecule-metal bridge. Science **304**, 281 (2004)
54. Wegner, D., Yamachika, R., Zhang, X., Wang, Y., Baruah, T., Pederson, M.R., Bartlett, B.M., Long, J.R., Crommie, M.F.: Tuning molecule-mediated spin coupling in bottom-up-fabricated vanadium-tetracyanoethylene nanostructures. Phys. Rev. Lett. **103**, 087205 (2009)
55. Repp, J., Meyer, G., Paavilainen, S., Olsson, F.E., Persson, M.: Imaging bond formation between a gold atom and pentacene on an insulating surface. Science **312**, 1196 (2006)
56. Mohn, F., Repp, J., Gross, L., Meyer, G., Dyer, M.S., Persson, M.: Reversible bond formation in a gold-atom organic-molecule complex as a molecular switch. Phys. Rev. Lett. **105**, 266102 (2010)

57. Liljeroth, P., Swart, I., Paavilainen, S., Repp, J., Meyer, G.: Single-molecule synthesis and characterization of metal-ligand complexes by low-temperature STM. Nano Lett. **10**, 2475 (2010)
58. Wang, W., Shi, X., Lin, C., Zhang, R.Q., Minot, C., Van Hove, M.A., Hong, Y., Tang, B.Z., Lin, N.: Manipulating localized molecular orbitals by single-atom contacts. Phys. Rev. Lett. **105**, 126801 (2010)
59. Zhang, C., Du, M.-H., Cheng, H.-P., Zhang, X.-G., Roitberg, A.E., Krause, J.L.: Coherent electron transport through an azobenzene molecule: a light-driven molecular switch. Phys. Rev. Lett. **92**, 158301 (2004)
60. Zhang, C., He, Y., Cheng, H.-P., Xue, Y., Ratner, M.A., Zhang, X.-G., Krstic, P.: Current voltage characteristics through a single light-sensitive molecule. Phys. Rev. B **73**, 125445 (2006)
61. del Valle, M., Gutierrez, R., Tejedor, C., Cuniberti, G.: Tuning the conductance of a molecular switch. Nat. Nanotechnol. **2**, 176 (2007)
62. Nozaki, D., Cuniberti, G.: Silicon-based molecular switch junctions. Nano Res. **2**, 648 (2009)
63. van der Molen, S.J., Liao, J., Kudernac, T., Agustsson, J.S., Bernard, L., Calame, M., van Wees, B.J., Feringa, B.L., Schönenberger, C.: Light-controlled conductance switching of ordered metal-molecule-metal devices. Nano Lett. **9**, 76 (2009)
64. Óvári, L., Luo, Y., Leyssner, F., Haag, R., Wolf, M., Tegeder, P.: Adsorption and switching properties of a N-benzylideneaniline based molecular switch on a Au(111) surface. J. Chem. Phys. **133**, 044707 (2010)
65. Battacharyya, S., Kibel, A., Kodis, G., Liddell, P.A., Gervaldo, M., Gust, D., Lindsay, S.A.: Optical modulation of molecular conductance. Nano Lett. **11**, 2709 (2011)
66. Hagen, S., Leyssner, F., Nandi, D., Wolf, M., Tegeder, P.: Reversible switching of tetra-tert-butyl-azobenzene on a Au(111) surface induced by light and thermal activation. Chem. Phys. Lett. **444**, 85 (2007)
67. Comstock, M.J., Levy, N., Kirakosian, A., Cho, J., Lauterwasser, F., Harvey, J.H., Strubbe, D.A., Fréchet, J.M.J., Trauner, D., Louie, S.G., Crommie, M.F.: Reversible photomechanical switching of individual engineered molecules at a metallic surface. Phys. Rev. Lett. **99**, 038301 (2007)
68. Bazarnik, M., Henzl, J., Czajka, R., Morgenstern, K.: Light driven reactions of single physisorbed azobenzenes. Chem. Comm. **47**, 7764 (2011)
69. Henzl, J., Puschnig, P., Ambrosch-Draxl, C., Schaate, A., Ufer, B., Behrens, P., Morgenstern, K.: Photoisomerization for a molecular switch in contact with a surface. Phys. Rev. B **85**, 035410 (2012)
70. Mielke, J., Leyssner, F., Koch, M., Meyer, S., Luo, Y., Selvanathan, S., Haag, R., Tegeder, P., Grill, L.: Imine Derivatives on Au(111): evidence for "inverted" thermal isomerization. ACS Nano **5**, 2090 (2011)
71. Danilov, A.V., Kubatkin, S.E., Kafanov, S.G., Flensberg, K., Bjørnholm, T.: Electron transfer dynamics of bistable single-molecule junctions. Nano Lett. **6**, 2184 (2006)
72. Gütlich, P., Hauser, A., Spiering, H.: Thermal and optical switching of iron(II) complexes. Angew. Chem. Int. Ed. **33**, 2024 (1994)
73. Real, J.A., Gaspar, A.B., Muñoz, M.C.: Thermal, pressure and light switchable spin-crossover materials. Dalton Trans. **34**, 2062 (2005)
74. Gamez, P., Sánchez Costa, J., Quesada, M., Aromi, G.: Iron spin-crossover compounds: from fundamental studies to practical applications. Dalton Trans. **38**, 7845 (2009)
75. Mannini, M., Pineider, F., Sainctavit, P., Danieli, C., Otero, E., Sciancalepore, C., Talarico, A.M., Arrio, M.-A., Cornia, A., Gatteschi, D., Sessoli, R.: Magnetic memory of a single-molecule quantum magnet wired to a gold surface. Nat. Mater. **8**, 194 (2009)
76. Baadji, N., Piacenza, M., Tugsuz, T., Della Sala, F., Maruccio, G., Sanvito, S.: Electrostatic spin crossover effect in polar magnetic molecules. Nat. Mater. **8**, 813 (2009)
77. Hao, H., Zheng, X., Song, L., Wang, R., Zeng, Z.: Electrostatic spin crossover in a molecular junction of a single-molecule magnet Fe_2. Phys. Rev. Lett. **108**, 017202 (2012)
78. Diefenbach, M., Kim, K.S.: Towards molecular magnetic switching with an electric bias. Angew. Chem. Int. Ed. **46**, 7640 (2007)

PTM Radicals for Molecular-Based Electronic Devices

Núria Crivillers, Marta Mas-Torrent, Cláudia Simão, Markos Paradinas, Carmen Munuera, Carmen Ocal, Stefan T. Bromley, Concepció Rovira, and Jaume Veciana

Abstract Self-assembled monolayers (SAMs) based on polychlorotrimethylphenyl (PTM) radicals have been prepared on different substrates showing great potential as platforms for the fabrication of molecular electronic devices. It is demonstrated that the intrinsic electrical, optical, and magnetic properties of these molecules can be used to prepare highly robust molecular switches.

1 Introduction

The increasing interest in miniaturizing electronic devices to achieve denser circuits is hindered by the growing limitations that current metal–oxide–semiconductor (CMOS) technology faces upon further device downscaling. The utilization of molecules as active components is an appealing alternative, and immobilization of these molecules on surfaces is compulsory for this purpose [1]. Preparation of self-assembled monolayers (SAMs) [2] of functional molecules that serve as or are part of an active device layer is an extensively used approach in molecular electronics

N. Crivillers · M. Mas-Torrent · C. Simão · C. Rovira (✉) · J. Veciana (✉)
Institut de Ciència de Materials de Barcelona (ICMAB-CSIC), Campus Universitari de Bellaterra, 08193 Bellaterra, Spain

Networking Research Center on Bioengineering, Biomaterials and Nanomedicine (CIBER-BBN) ICMAB-CSIC, Bellaterra, Spain
e-mail: cun@icmab.es; vecianaj@icmab.es

M. Paradinas · C. Munuera · C. Ocal
Institut de Ciència de Materials de Barcelona (ICMAB-CSIC), Campus Universitari de Bellaterra, 08193 Bellaterra, Spain

S.T. Bromley
Departament de Química Física & Institut de Química Teòrica i Computacional (IQTCUB), Universitat de Barcelona, 08028 Barcelona, Spain

Institució Catalana de Recerca i Estudis Avançats (ICREA), 08010 Barcelona, Spain

71

since it provides an easy route towards the immobilization of organic molecules containing grafting groups (i.e., –SH, –CN, –COOH, –NH$_2$, silanes, etc.) on selected metallic (Au, Ag, Pd, Pt, Hg, and HOPG) as well as semiconducting (Si, GaAs, indium tin oxide (ITO), etc.) surfaces [3, 4]. Over the last few years, a vast amount of research has been devoted to the fabrication and study of metal/molecule/metal junctions, based on either single molecules or SAMs coupled between two noble-metal electrodes, thus leading to well-defined molecular junctions, in which the transport through the layer is investigated [5–7]. In addition to that, if the grafted molecules are bistable systems, stimuli-responsive surfaces, also known as smart surfaces [8], can be prepared, which have potential applications in data storage, (bio)sensors, and (opto)electronic devices [9, 10]. These organic-based materials would also exhibit other interesting characteristics such as chemical versatility to tune the desired properties.

In this chapter, we report on the potential of SAMs based on polychloro-trimethylphenyl (PTM) radicals as suitable platforms for developing memory devices. PTM radicals are chemically and thermally persistent due to the fact that their open-shell centers are shielded by six bulky chlorine atoms [11]. In addition, they are bistable thanks to their electroactive character, as they can be easily and reversibly reduced to the carbanion form [12]. Importantly, it has been demonstrated that the intrinsic optical and magnetic properties of these radicals are preserved once immobilized on different substrates such as silicon oxide, quartz, and gold [13–15]. In such systems, the electrical properties have been exploited to characterize the SAMs and to trigger the surface properties.

2 Experiment and Results

2.1 Electrical Output from PTM SAMs

Since Aviram and Ratner's prediction in 1974 that a single molecule could behave as a rectifier [16], scientists from a variety of disciplines have been engaged in pursuing the understanding of transport mechanisms at the molecular level. There are three main critical factors that influence and could determine the conductivity in these junctions: the energy levels of the molecules relative to the Fermi levels of the contacts, the nature of the metal/molecule contacts, and the molecular and electronic structures of the molecule(s). Unfortunately, other aspects, such as sample preparation and measuring/characterization techniques, lack of good film quality, or uncontrolled details on the electrical contacts, can have a strong effect on the resulting transport measurements and might be at the origin of some non-reconciled results. An elegant way to circumvent these drawbacks and minimize the dependence of the results on the experimental boundary conditions is to rely on comparative transport measurements, in which individual molecular parameters are modified, rather than on absolute measurements. With this aim, the transport properties of two SAMs based on the radical (open-shell) and the closed-shell

form of a PTM derivative (SAM **S1(rad)** and **S1(αH)**, respectively) on gold were compared [15]. These two systems give rise to SAMs with no significant structural molecular variations, but with extremely different electronic structures. Transport measurements were performed by means of scanning force microscopy technique (SFM) and applying the so-called 3D modes [17]. This mode allows the simultaneous measurement of the normal force (F_n) and the electronic current (I) flowing between tip and surface as a function of the bias voltage (V) during a programmed tip–sample approaching determined by the piezo displacement (z). By combining the information extracted from the simultaneously acquired $F_n(V, z)$ and $I(V, z)$ images, the I–V characteristics at different applied loads and different tip–surface distances can be obtained. In such a way, it was possible to establish a comparison between conductivity measured for the same applied force on the different SAMs. The preparation of the PTM SAMs on Au(111) was achieved following a two-step strategy (Fig. 1). The gold substrate was first functionalized using 4-aminothiophenol (4-ATP), leading to an amino-terminated SAM that was used as a coupling layer to immobilize the PTM derivatives. In a second step, PTM derivatives functionalized with an acid chloride group were employed, since they react with the amino-terminated layer forming an amide group. The same strategy was followed for the PTM radical and non-radical (αH) leading to SAMs **S1(rad)** and **S1(αH),** respectively.

Diverse surface characterization techniques (X-ray photoelectron spectroscopy and water contact angle) demonstrated the successful formation of the SAMs. Importantly, cyclic voltammetry (CV) experiments using the functionalized gold surfaces as working electrodes showed that no-redox process takes place for the 4-ATP-SAM and SAM **S1(αH)** in the applied voltage range, as otherwise expected since they are not electroactive species. On the other hand, when the SAM **S1(rad)** was used, the CV revealed a redox wave corresponding to the reduction of the PTM radical to the anion species. An increase in the scan rate gave rise to a linear increase in the peak intensity, characteristic of a surface-confined electroactive species [18]. These CV results also demonstrate that the radical character is maintained after chemisorption on the surface.

Figure 2a shows the $F_n(V, z)$ image recorded on top of the SAM **S1(rad)**. The color scale is used to depict the normal force magnitude as a function of both the applied voltage (fast scan or horizontal axis), which is varied between ±2 V, and the total piezo movement (slow scan or vertical axis), which corresponds to a 20 nm travel in the present case. In our experimental setup, the piezo moves the sample toward the tip, that is, the tip–sample distance is reduced as z increases. From vertical profiles in $F_n(V, z)$, the force versus distance ($F - z$) curves are obtained for a specific tip voltage (e.g., $F_n(0, z)$ is shown in Fig. 2b), such that the applied load, at a given piezo displacement, can be estimated. The same analysis procedure was used in the case of the SAM **S1(αH)**. The $I(V, z)$ images acquired on both the αH (left) and radical (right) PTM SAMs are depicted in Fig. 2c, respectively. Horizontal profiles taken in the images are the I–V curves corresponding to each z, which, combined with the F–z, allows knowing the value of the applied load at which each I–V curve was obtained. The maximum current measured corresponds to the saturation of the current amplifier, fixed to 100 nA in the experimental setup
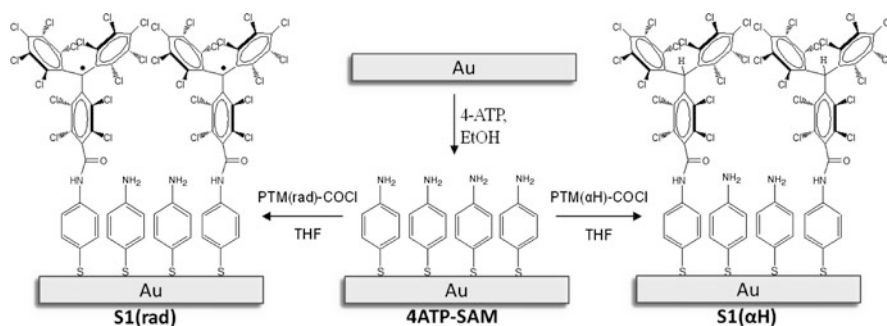
Fig. 1 Scheme of the strategy used to form the open-shell PTM radical SAM (**S1(rad)**) and closed-shell PTM derivative SAM (**S1(αH)**) (Reprinted from [15]. Copyright Wiley-VCH Verlag GmbH and Co 2009)

used. Straightforward comparison between $I-V$ characteristics at different applied loads for both PTM SAMs is therefore possible. Moreover, the simple observation of the appearance of the $I(V,z)$ images illustrates that changes appearing in the $I-V$ curves as the tip–sample distance decreases are clearly different for each SAM, reflecting different transport behaviors. After the jump into contact point, the central region (intermediate color) of the $I(V,z)$ image for SAM **S1(rad)** undergoes a continuous narrowing, leading to a triangular shape typical of a monotonous pseudogap reduction. Contrarily, for SAM **S1(αH)**, the image shows a region with non-distance-dependent changes producing a fairly constant gap width. This striking difference occurs in a wide range of tip–sample distances, indicating that it is intrinsically due to the distinct electronic characteristics of the two PTM SAMs. A series of $I-V$ curves for selected loads (in the attractive regime to avoid film indentation) have been extracted from the corresponding images and are shown in Fig. 2d. By increasing the applied load up to 15 nN (*black triangle*), this difference becomes more evident, and in particular, the conductivity through the SAM **S1(rad)** is much higher (note the nearly linear behavior) than for the SAM **S1(αH)**. By analyzing the zero-voltage region of the curves, it was found that the SAM **S1(rad)** shows a junction resistance (10–40 MΩ) one order of magnitude smaller than that of the SAM **S1(αH)** (200–300 MΩ), either for the same applied load or the same piezo displacement.

Density functional calculations were employed to gain further insight into the electronic structures of each molecule. In each case, the molecules were modeled by the PTM head group with an extended length of its attached linker chain [–(CO)–NH–Ph]. The results are summarized in Fig. 3. The PTM(αH) has a large energy gap (± 5 eV) between its closed-shell lowest unoccupied molecular orbital (LUMO) and the highest occupied molecular orbital (HOMO). The PTM(rad) has a singly occupied molecular orbital (SOMO) in the α spin, with a similar energy to the PTM(αH) HOMO but a significantly lower energy LUMO in the β spin compared to the LUMO of the PTM(αH). From the calculations, the LUMO-β of PTM(rad)
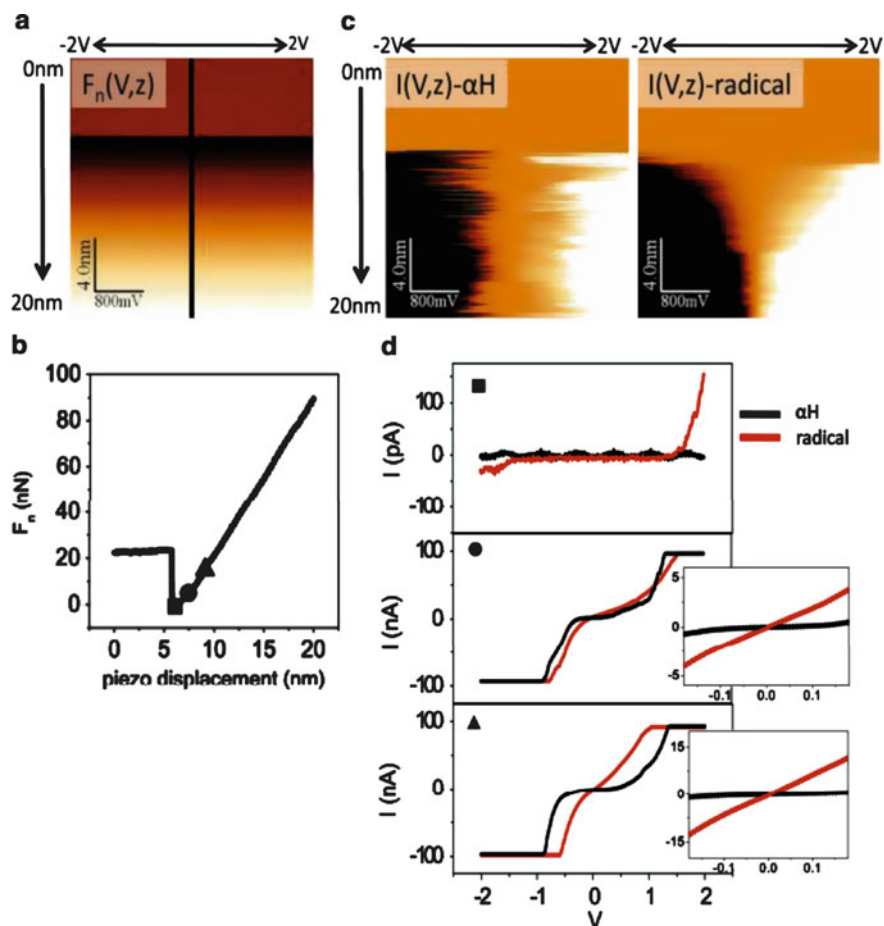
Fig. 2 (**a**) Normal force image, $F_n(V, z)$, acquired in 3D operation mode C-SFM for SAM **S1(rad)**. The voltage range is ± 2 V, and the total piezo displacement is $z = 20$ nm. (**b**) Line profile marked with a black line in (**a**) that corresponds to the F–z curve at $V = 0$ V. For convenience, zero force has been chosen as the jump into contact value. (**c**) Current image, $I(V, z)$, acquired on the αH (*left*) and radical (*right*) SAMs. The voltage range and total piezo displacement are the same as in (**a**). (**d**) Selected horizontal line profiles extracted from images in (**c**) at different applied loads. The symbols at the top left corner of the graphs have been used to mark the corresponding applied load in (**b**). Insets: linear region of the I–V curve (± 0.2 V), used to calculate the junction resistance. The values obtained are R(αH) $= 280 \pm 40$ MΩ and R(rad) $= 35 \pm 5$ MΩ in (*black circle*); R(αH) $= 200 \pm 40$ MV and R(rad) $= 12 \pm 5$ MΩ in (*black triangle*) (Reprinted from [15]. Copyright Wiley-VCH Verlag GmbH and Co 2009)

has an energy significantly closer to the Fermi levels of both Au and B-doped CVD diamond (used as a tip) than the LUMO in PTM(αH). This result suggests that the electronic differences between PTM(αH) and PTM(rad) with respect to their electron-accepting orbitals may play an important role in enhancing the conduction
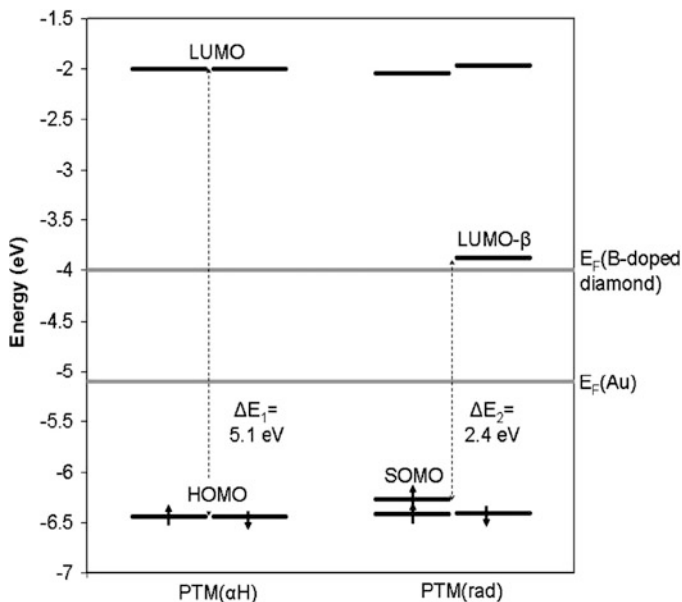
Fig. 3 Energy levels obtained from DFT calculations for PTM(αH) and PTM(rad) derivatives (Reprinted from [15]. Copyright Wiley-VCH Verlag GmbH and Co 2009)

in the SAM **S1(rad)**. It is generally agreed that the dominant transport mechanism in molecular junctions of alkanethiols, which have HOMO and LUMO levels far away from the Fermi level of the metal electrodes, is through a nonresonant and superexchange tunneling, that is, the interactions of the electron with the electronic structure of the molecule enhance the tunneling rate [19]. This is also probably the case of the SAM **S1(αH)**, since the Fermi level of the contacts employed lies in the large HOMO–LUMO gap (Fig. 3). However, the LUMO-β level of PTM(rad) approaches the values of the metal Fermi levels, and thus, other transport mechanisms may play a role. We believe that the experimental results strongly point toward a LUMO-assisted transport, and we suggest that for SAM **S1(rad)** either the tunnel barrier diminishes or, more probably, there might be some contribution of resonant tunneling, as stated by other authors for various redox molecules. Finally, we would also like to notice that the large energy difference between the SOMO and the LUMO-β of PTM(rad) opens the interesting possibility of whether this system could give rise to spin-polarized transport [20].

This study was later extended to the transport characterization of SAMs on gold based on the closed- and open-shell forms of a fully conjugated PTM derivative resulting in the formation of SAMs **S2(rad)** and **S2(αH)**, respectively (Fig. 4). Due to the molecular structure, there is a larger hybridization of the molecules with the metal [21].
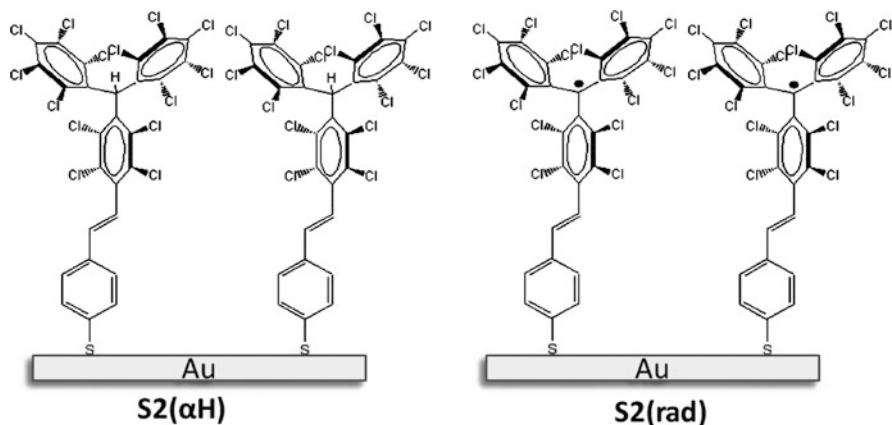
Fig. 4 Scheme of the two SAMs prepared, SAM **S2(αH)** and SAM **S2(rad)** (Reprinted from [21]. Copyright Royal Society of Chemistry 2011)

As in the previous case, the SFM 3D mode was also used for the electrical characterization at the nanoscale. Figure 5a and b depict a set of representative I–V curves for both SAMs at different applied loads. As in the measurements described before (Fig. 2), the current saturates at 100 nA. The force range shown is adjusted within each series to the most relevant conducting response of each SAM (lower resistance values), being from 0.75 to 1.25 nN and from 3.5 to 9 nN in the case of **S2(rad)** and **S2(αH)**, respectively. The junction resistance (R) was calculated from the low-voltage region (± 0.3 V) of the corresponding I–V characteristics revealing dramatic differences between these SAMs. The plot of R as a function of the applied force is depicted in Fig. 5c. As for the **S1** SAMs, R measured on the PTM radical SAM was significantly lower than the one obtained for the non-radical one. Moreover, we note that the ratio $R(\mathbf{S2(\alpha H)})/R(\mathbf{S2(rad)})$ obtained here is one order of magnitude larger than for the nonconjugated PTM SAMs, in agreement with the larger conductivity expected for the conjugated radical hybridized with the metal surface.

Though the sigmoidal-like shape of the curves persists around $V = 0$ during the whole load range shown, a negative differential resistance (NDR) feature emerges for both SAMs at negative voltage values close to -1.5 V. NDR devices undergo an increase in resistance when the voltage is increased in a specific bias range. This phenomenon has raised interest for their potential in numerous electronic applications. The NDR can be visualized as a switch in which the conductivity switches following an off/on/off trend in response to an increase in voltage [22]. In this way, the observed NDR can be exploited to store information using electrical signal as *output*. Moreover, as can be seen in the selected I–V curves (Fig. 5d), not only the position but also minimum to maximum current ratios in the NDR region were nearly identical for both SAMs if obtained at about 2 nN higher in **S2(αH)**
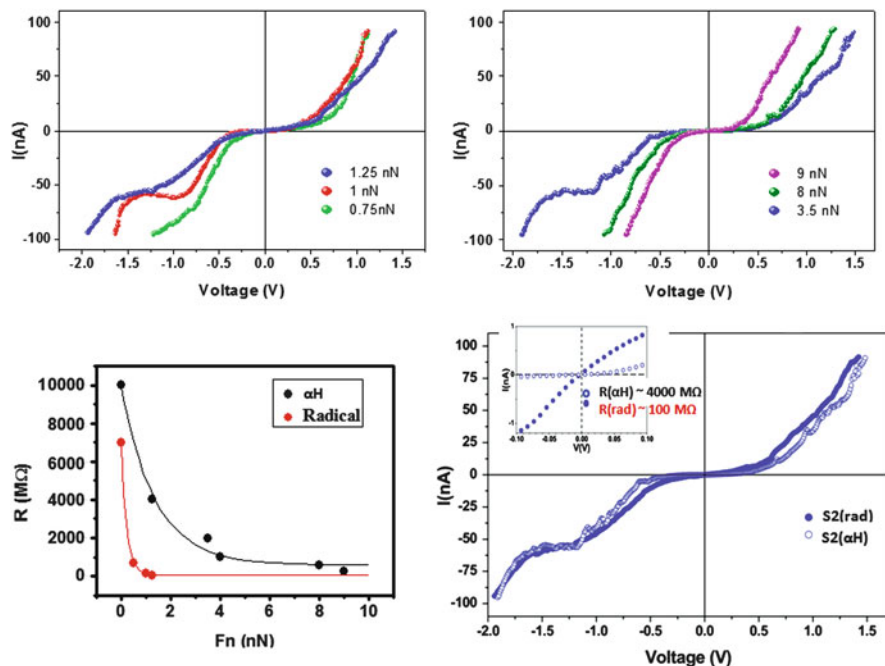
Fig. 5 Set of $I-V$ curves as a function of the applied load for the **S2(rad)** (**a**) and **S2(αH)** (**b**) SAMs. (**c**) Selected curves from the $I-V$ series on top for each SAM. Inset: magnification of the linear region at low voltages and junction-resistance values (R) (Reprinted from [21]. Copyright Royal Society of Chemistry 2011)

than for **S2(rad)**. This would be consistent with a slightly higher effective barrier in the case of **S2(αH)**.

Density functional calculations were employed to gain further insight into the origin of the NDR peaks. A similar energy-level picture is obtained here if compared to the one for the previous case (Fig. 6). The LUMO-β of PTM **S2(rad)** is very close in energy to the Fermi level of B-doped CVD diamond (used as a tip), and therefore, it is expected that the higher conductivity observed for this SAM is due to some resonant tunneling, while in the **S2(αH)** nonresonant tunneling must be the dominant transport mechanism that occurs. The fact that the LUMO energy level of **S2(αH)** is close (only slightly higher than) to the LUMO-α of **S2(rad)** suggests that if a high negative voltage is applied to the tip shifting upwards its work function, resonant conduction through these unoccupied orbitals could take place in both SAMs. Such an effect could account for the NDR peaks (slightly higher barrier for **S2(αH)**) observed in the $I-V$ curves. The results involve a statistical response, and molecules under the tip may present different structural conformations. Considering all the above, we believe that when a low bias is applied, the transport mechanisms dominating in both PTM SAMs are different (i.e., nonresonant tunneling for S2(alphaH) and resonant tunneling mediated by the
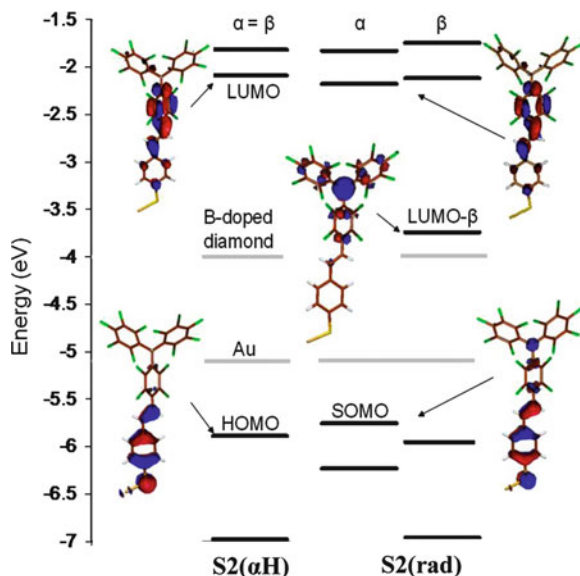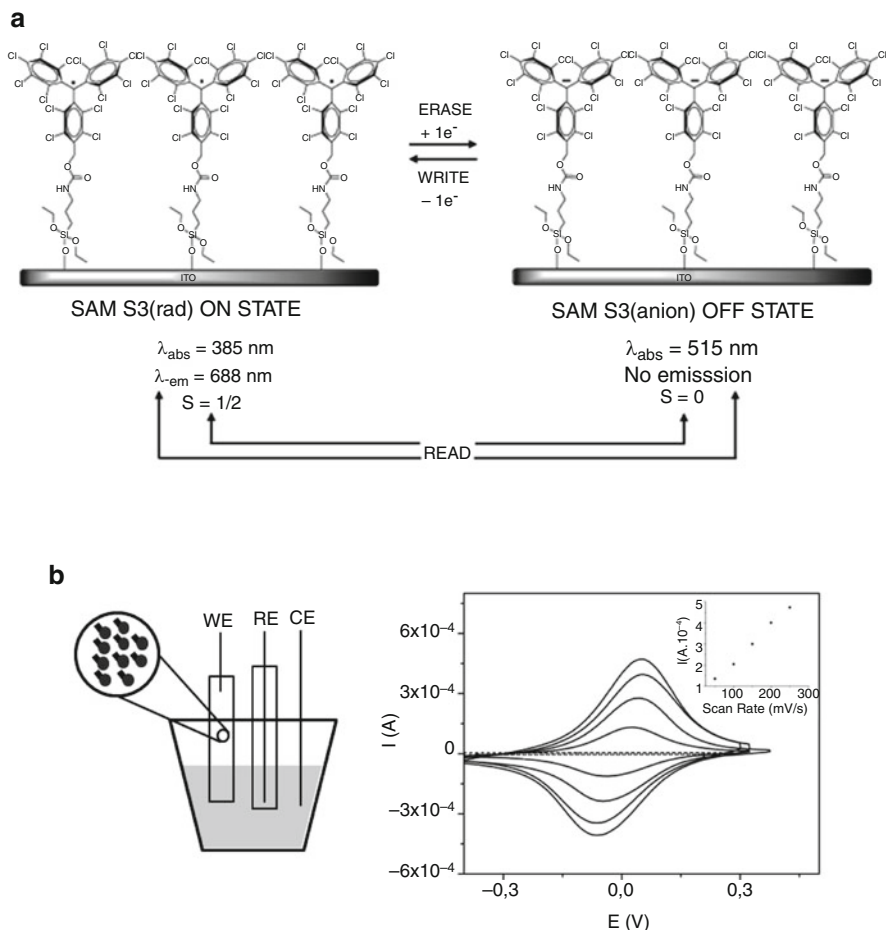
Fig. 6 Calculated most relevant orbital energy levels of **S2(αH)** and **S2(rad)**. The spatial localization of selected orbitals and the Fermi levels of gold and B-doped diamond contacts (*in gray*) are shown (Reprinted from [21]. Copyright Royal Society of Chemistry 2011)

LUMO-β in S2(rad)). However, at approximately −1.5 V, in both systems some resonant tunneling with the unoccupied orbitals occurs. Since the reduction potentials of **S2(rad)** and **S2(αH)** are completely different, we can affirm that in this reported example the redox character does not determine the NDR phenomena observed, and hence, molecular charging effects or polaron formation can be excluded as the NDR origin.

2.2 Electrical Input to Switch PTM Radical SAMs

Electrical signals can also be employed as *inputs* to switch the state of the PTM radical SAMs due to the electroactive character of the molecule. Recently, a highly robust surface-confined switch based on SAMs of a novel PTM radical silane on ITO was reported (Fig. 7a) [23]. The resulting functionalized substrate is labeled here as SAM **S3(rad)**. The ITO substrate was selected since it is conducting and transparent and, therefore, permits to simultaneously trigger electrochemically the state of the switch and to monitor the optical (absorbance and emission) and magnetic properties.

The electrochemical characteristics of SAM **S3(rad)** on ITO were investigated by CV. The experiments were carried out in a 0.02 M solution of tetrabutylammonium hexafluorophosphate in acetonitrile and using the functionalized substrate as working electrode (vs. Ag(s)). As it can be seen in Fig. 7b, the cyclic voltammogram

a

SAM S3(rad) ON STATE   SAM S3(anion) OFF STATE

λ_{abs} = 385 nm λ_{abs} = 515 nm
λ_{-em} = 688 nm   No emisssion
S = 1/2   S = 0

READ

b

Fig. 7 (**a**) Representation of the electrochemical bistability between SAM **S3(rad)** and **S3(anion)**. (**b**) *Left*. Setup employed for the CV experiments, where WE stands for working electrode; *RE*, reference electrode; and *CE*, counter electrode. *Right*. Cyclic voltammogram at different scan rates (50, 100, 150, 200 mV/s) of the SAM of (**a**) on ITO (*vs.* silver wire) in an electrolyte solution of 0.02 M tetrabutylammonium hexafluorophosphate in acetonitrile. *Inset*: plot of the anodic current *versus* scan rate (Reprinted from [23]. Copyright Nature Publishing Group 2011)

exhibits one reversible redox wave, corresponding to the redox process between the radical and the anionic form, with an oxidation peak at +53 mV and a reduction peak at −32 mV at a scan rate 100 mV/s. It was also observed that the current linearly increased with the scan rate, which is characteristic for surface-confined electroactive species (Fig. 7b inset). The stability of the two redox states, SAM **S3(rad)** and SAM **S3(anion)**, was confirmed by performing many consecutive voltage cycles, which resulted in completely identical redox waves without showing any sign of loss of current intensity, pointing out the excellent potential of these SAMs to work as extremely reversible and stable switches.

To achieve read/write memory devices, it is imperative to have a secondary physical signal to be able to read the state of the switch nondestructively. In this case, the optical absorption, optical emission, and magnetic responses were employed to read the state of this multichannel switch. In the three cases, the reversibility of the switch was explored while performing write–erase cycles, switching the SAM between the radical (on state) and the anion (off state) form.

Upon applying the switching cycles (+0.3 V (write) and −0.3 V (erase)), the absorption band characteristics of the two states changed simultaneously in opposite directions, following the profile of the applied voltages, in a completely reversible way and recovering completely the absorption intensity after each cycle (Fig. 8a). Outstandingly, the switch showed extremely high reversibility upon the application of hundreds of cycles and long-term stability since the same switching cycles are reproducible after three months. To further demonstrate the potential of this system to build nonvolatile memory devices, the switch response to a sequence of write–read–erase–read pulses was investigated. Short 5 s write (+0.3 V) and erase (−0.3 V) pulses were applied, while the reading of the state of the switch was performed for 30 s at 0 V. As it can be seen in Fig. 8b, both states of the switch were completely stable and reproducible after removal of the external stimuli. Also, similarly, the fluorescence emission was switched off/switched on when reduction and oxidation cycles were applied, which was followed employing a fluorescence microscope.

In turn, electron paramagnetic resonance (EPR) experiments demonstrated that the EPR signal, corresponding to the PTM radical immobilized on the surface, disappeared upon reduction to the anionic form and appeared again after further oxidation, corroborating that the magnetic output was also a suitable read-out tool to determine the state of the switch (Fig. 9).

More recently, the same optical and magnetic switching properties upon the application of an electrical external stimuli were found on a PTM-functionalized Au surface (SAM **S4(rad)**), when a very thin layer of gold was used [24]. In addition, it was also shown here that the switch could also be read following the surface wettability. Taking into account the high hydrophobicity of PTMs due to the chlorine groups, and that the reduced form of this SAM is an ionic species, the change of the surface-wetting properties in the switching process was followed by monitoring the water contact angle. SAM **S4(rad)** changed from an average contact angle value of $102 \pm 6°$ to $73 \pm 3°$ for the PTM anion SAM (SAM **S4(anion)**) (Fig. 10). This reversible difference ($\sim 29°$) in the contact angle is rather high for a self-assembled monolayer. Such systems, able to tune their wetting properties reversibly, are currently raising an increased interest for the development of self-cleaning surfaces, microfluidics, and (bio)sensors [25–29].

Considering all above, SAMs based on PTMs offer great perspectives to be used in binary logic gates [30–32]. We can consider the applied voltage as an input; that is to say, when we apply a positive voltage the SAM will be in the radical form (input = 1), while the applied voltage is negative, the SAM will be in the anionic state (input = 0). Further, five different outputs can be defined: the absorption band
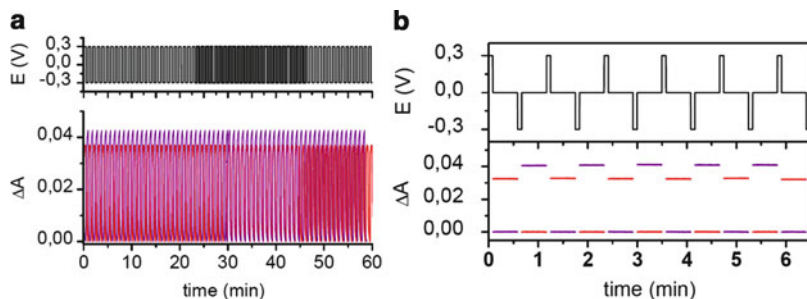
Fig. 8 Optical response along time during 65 consecutive write–erase cycles ($+0.3\,V/-0.3\,V$ *vs.* Ag(s)) applied to the SAM **S3(rad)** monitored at 385 nm (*red line*) and 515 nm (*purple line*). (**b**) Sequence of write–read–erase–read pulses ($+0.3\,V/0\,V/-0.3\,V/0\,V$ *vs.* Ag(s)) applied to the SAM (*top*) and optical response (*bottom*) monitored at 385 nm (*red line*) and 515 nm (*purple line*) during the reading processes (Reprinted from [23]. Copyright Nature Publishing Group 2011)
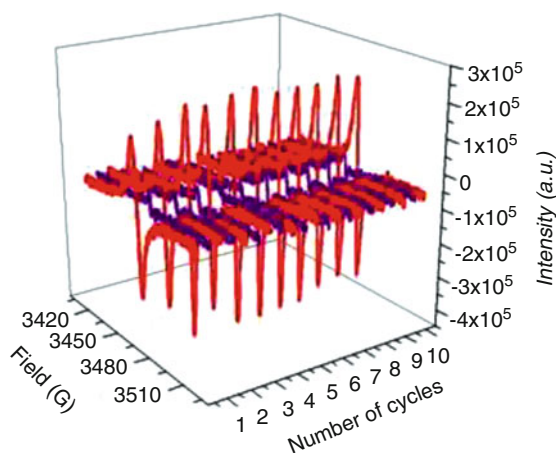
Fig. 9 EPR signal of the SAM **S3(rad)** on ITO in air upon application of ten *ex situ* electrochemical on/off switching cycles of $+0.3\,V$ (radical) and $-0.3\,V$ (anion) using a Ag wire as reference electrode, Pt wire as counter electrode and a electrolyte solution of 0.02 M tetrabutylammonium hexafluorophosphate in acetonitrile. *Red* corresponds to the on state (radical) and *purple* the off state (anion) (Reprinted from [23]. Copyright Nature Publishing Group 2011)

at $\lambda_{abs} = 385$ nm (output 1), the absorption band at $\lambda_{abs} = 515$ nm (output 2), the fluorescence emission at $\lambda_{em} = 688$ nm (output 3), the EPR signal (output 4), and the wetting properties reflected with the surface-water contact angle (output 5). Table 1 collects the truth table of this system. Since there are five different outputs for the same input, it is possible either to define five different logic gates or to combine the five outputs in one system.
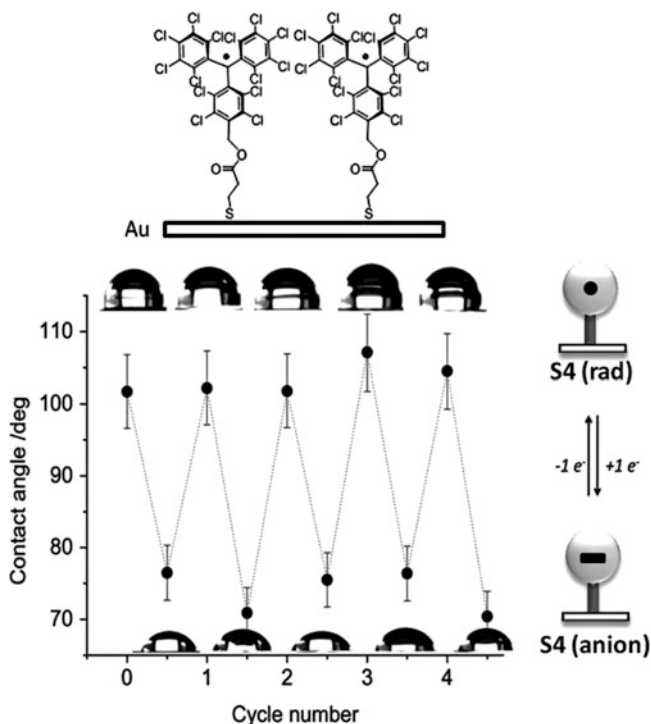
Fig. 10 SAM **S4(rad)** on gold (*top*) and its contact angle during the application of switching redox cycles (Reprinted from [24]. Copyright American Chemical Society 2011)

Table 1 Truth table for the binary logic functions for SAM of PTM

Input	Output 1 $\lambda_{abs} = 385\,nm$	Output 2 $\lambda_{abs} = 515\,nm$	Output 3 $\lambda_{em} = 688\,nm$	Output 4 EPR signal	Output 5 Contact angle
1 (radical)	1	0	1	1	1
0 (anion)	0	1	0	0	0

3 Summary

The preparation of SAMs based on PTM derivatives has been successfully achieved on different substrates, and the transport through PTM SAMs on Au(111) was studied. Both the radical and non-radical fully conjugated PTM derivatives (hybridized with the metal) showed NDR peaks, thus raising the possibility to use this electrical output for memory applications. Moreover, the contribution of the LUMO-β of the PTM radical on the transport points that they could act as spin filters in spintronic applications. Further, it has been demonstrated that the electroactive character of the PTM radical SAMs allows to reversibly interconvert the anchored molecules between two redox states performing as a highly robust, long-term stable, reversible,

and reproducible switch. Considering also that the operation voltage is very low, this system shows great potential for the development of nonvolatile memory devices.

References

1. Song, H., Reed, M.A., Lee, T.: Single molecule electronic devices. Adv. Mater. **23**(14), 1583–1608 (2011). doi:10.1002/adma.201004291
2. Ulman, A.: Formation and structure of self-assembled monolayers. Chem. Rev. **96**(4), 1533–1554 (1996). doi:10.1021/cr9502357
3. Chaki, N.K., Aslam, M., Sharma, J., Vijayamohanan, K.: Applications of self-assembled monolayers in materials chemistry. Proc. Indian Acad. Sci. Chem. Sci. **113**(5–6), 659–670 (2001)
4. Halik, M., Hirsch, A.: The potential of molecular self-assembled monolayers in organic electronic devices. Adv. Mater. **23**(22–23), 2689–2695 (2011). doi:10.1002/adma.201100337
5. Nitzan, A., Ratner, M.A.: Science **300**, 1384 (2003)
6. Chen, F., Hihath, J., Huang, Z.F., Li, X.L., Tao, N.J.: Annu. Rev. Phys. Chem. **58**, 535 (2007)
7. Haick, H., Cahen, D.: Prog. Surf. Sci. **83**, 217 (2008)
8. Mendes, P.M.: Stimuli-responsive surfaces for bio-applications. Chem. Soc. Rev. **37**(11), 2512–2529 (2008). doi:10.1039/b714635n
9. Kronemeijer, A.J., Akkerman, H.B., Kudernac, T., van Wees, B.J., Feringa, B.L., Blom, P.W.M., de Boer, B.: Reversible conductance switching in molecular devices. Adv. Mater. **20**(8), 1467 − + (2008). doi:10.1002/adma.200800053
10. Mativetsky, J.M., Pace, G., Elbing, M., Rampi, M.A., Mayor, M., Samori, P.: Azobenzenes as light-controlled molecular electronic switches in nanoscale metal-molecule-metal junctions. J. Am. Chem. Soc. **130**(29), 9192 − + (2008). doi:10.1021/ja8018093
11. Ballester, M., Riera, J., Castaner, J., Badia, C., Monso, J.M.: Inert carbon free radicals.1. Perchlorodiphenylmethyl and perchlorotriphenylmethyl radical series. J. Am. Chem. Soc. **93**(9), 2215-& (1971). doi:10.1021/ja00738a021
12. Sporer, C., Ratera, I., Ruiz-Molina, D., Zhao, Y.X., Vidal-Gancedo, J., Wurst, K., Jaitner, P., Clays, K., Persoons, A., Rovira, C., Veciana, J.: A molecular multiproperty switching array based on the redox behavior of a ferrocenyl polychlorotriphenyhnethyl radical. Angew. Chem. Int. Ed. **43**(39), 5266–5268 (2004). doi:10.1002/anie.200454150
13. Crivillers, N., Mas-Torrent, M., Perruchas, S., Roques, N., Vidal-Gancedo, J., Veciana, J., Rovira, C., Basabe-Desmonts, L., Ravoo, B.J., Crego-Calama, M., Reinhoudt, D.N.: Self-assembled monolayers of a multifunctional organic radical. Angew. Chem. Int. Ed. **46**(13), 2215–2219 (2007). doi:10.1002/anie.200603599
14. Crivillers, N., Mas-Torrent, M., Vidal-Gancedo, J., Veciana, J., Rovira, C.: Self-assembled monolayers of electroactive polychlorotriphenylmethyl radicals on Au(111). J. Am. Chem. Soc. **130**(16), 5499–5506 (2008). doi:10.1021/ja710845v
15. Crivillers, N., Munuera, C., Mas-Torrent, M., Simao, C., Bromley, S.T., Ocal, C., Rovira, C., Veciana, J.: Dramatic influence of the electronic structure on the conductivity through open- and closed-shell molecules. Adv. Mater. **21**(10–11), 1177–1181 (2009). doi:10.1002/adma.200801707

16. Aviram, A., Ratner, M.A.: Chem. Phys. Lett. **29**, 277 (1974)
17. Munuera, C., Barrena, E., Ocal, C.: Scanning force microscopy three-dimensional modes applied to conductivity measurements through linear-chain organic SAMs. Nanotechnology **18**(12), 125505 (2007). doi:12550510.1088/0957–4484/18/12/125505
18. Chidsey, C.E.D.: Free-energy and temperature-dependence of electron-transfer at the metal-electrolyte interface. Science **251**(4996), 919–922 (1991). doi:10.1126/science.251.4996.919
19. Salomon, A., Cahen, D., Lindsay, S., Tomfohr, J., Engelkes, V.B., Frisbie, C.D.: Comparison of electronic transport measurements on organic molecules. Adv. Mater. **15**(22), 1881–1890 (2003). doi:10.1002/adma.200306091
20. Mas-Torrent, M., Crivillers, N., Mugnaini, V., Ratera, I., Rovira, C., Veciana, J.: Organic radicals on surfaces: towards molecular spintronics. J. Mater. Chem. **19**(12), 1691–1695 (2009). doi:10.1039/b809875a
21. Crivillers, N., Paradinas, M., Mas-Torrent, M., Bromley, S.T., Rovira, C., Ocal, C., Veciana, J.: Negative differential resistance (NDR) in similar molecules with distinct redox behaviour. Chem. Commun. **47**(16), 4664–4666 (2011). doi:10.1039/c1cc10677e
22. Fuentes, N., Martin-Lasanta, A., Alvarez de Cienfuegos, L., Ribagorda, M., Parra, A., Cuerva, J.M.: Organic-based molecular switches for molecular electronics. Nanoscale **3**(10), 4003–4014 (2011). doi:10.1039/c1nr10536a
23. Simao, C., Mas-Torrent, M., Crivillers, N., Lloveras, V., Manuel Artes, J., Gorostiza, P., Veciana, J., Rovira, C.: A robust molecular platform for non-volatile memory devices with optical and magnetic responses. Nat. Chem. **3**(5), 359–364 (2011). doi:10.1038/nchem.1013
24. Simao, C., Mas-Torrent, M., Veciana, J., Rovira, C.: Multichannel molecular switch with a surface-confined electroactive radical exhibiting tunable wetting properties. Nano Lett. **11**(10), 4382–4385 (2011). doi:10.1021/nl2025097
25. Abbott, S., Ralston, J., Reynolds, G., Hayes, R.: Reversible wettability of photoresponsive pyrimidine-coated surfaces. Langmuir **15**(26), 8923–8928 (1999). doi:10.1021/la990558o
26. Artzy-Schnirman, A., Brod, E., Epel, M., Dines, M., Hammer, T., Benhar, I., Reiter, Y., Sivan, U.: A two-state electronic antigen and an antibody selected to discriminate between these states. Nano Lett. **8**(10), 3398–3403 (2008). doi:10.1021/nl8020895
27. Lahann, J., Mitragotri, S., Tran, T.N., Kaido, H., Sundaram, J., Choi, I.S., Hoffer, S., Somorjai, G.A., Langer, R.: A reversibly switching surface. Science **299**(5605), 371–374 (2003). doi:10.1126/science.1078933
28. Liu, Y., Mu, L., Liu, B.H., Zhang, S., Yang, P.Y., Kong, J.L.: Controlled protein assembly on a switchable surface. Chem. Commun. (10), 1194–1195 (2004). doi:10.1039/b400776j
29. Wieckowska, A., Braunschweig, A.B., Willner, I.: Electrochemical control of surface properties using a quinone-functionalized monolayer: effects of donor-acceptor complexes. Chem. Commun. (38), 3918–3920 (2007). doi:10.1039/b710540a
30. De Silva, A.P., James, M.R., McKinney, B.O.F., Pears, D.A., Weir, S.M.: Molecular computational elements encode large populations of small objects. Nat. Mater. **5**(10), 787–790 (2006). doi:10.1038/nmat1733
31. De Silva, A.P., Uchiyama, S.: Molecular logic and computing. Nat. Nanotechnol. **2**(7), 399–410 (2007). doi:10.1038/nnano.2007.188
32. Gupta, T., van der Boom, M.E.: Redox-active monolayers as a versatile platform for integrating Boolean logic gates. Angew. Chem. Int. Ed. **47**(29), 5322–5326 (2008). doi:10.1002/anie.200800830

Vibrational Heating in Single-Molecule Switches

Thomas Brumme, Rafael Gutiérrez, and Gianaurelio Cuniberti

Abstract It has been recently shown experimentally that the switching rate in single-molecule junctions sensitively depends on the applied bias voltage. Using a minimal model which describes the barrier crossing problem by multiple excitations of vibrations of the molecular junction and by taking into account the molecule specific nonconstant density of states, we are able to describe the complex, non-monotonic behavior of the switching process.

1 Introduction

A concept with promising potential applications is the creation of logic gates at the single-molecule level. For this, however, a microscopic understanding of the adsorption behavior of the molecules on surfaces as well as their behavior under applied bias should be achieved. Furthermore, an additional factor to be clarified in order to facilitate the performance of logic operations in single molecules is the physical mechanism responsible for conformational or electronic changes in the molecule, which could thus change the output of a molecular-based device.

The first molecular-scale device was already proposed in 1974 by Aviram and Ratner [1]; however, it took another two decades until significant breakthroughs were achieved [5, 14, 24, 25]. Different molecular-scale devices such as diodes, transistors, and switches have meanwhile been demonstrated and studied on the laboratory scale; see [17, 18] for comprehensive reviews. In order to create such molecular devices or even molecular logic gates, the molecule has to be studied with respect to very different properties. First, and most importantly, there is of

T. Brumme (✉) · R. Gutiérrez · G. Cuniberti
Institute for Materials Science and Max Bergmann Center of Biomaterials, TU Dresden, 01062 Dresden, Germany
e-mail: research@nano.tu-dresden.de

course its chemical composition and topology which determines the adsorption on surfaces. Secondly, due to this coupling to the substrate, the electronic structure of the molecule and also the dynamic behavior are altered.

In order to investigate the electronic properties of a single molecule, one can use different experimental techniques such as mechanically controllable break junctions or electromigration techniques. However, to really understand the adsorption and the dynamic behavior, the most important tool is probably the scanning tunneling microscope (STM) [2, 19]. The STM is a valuable and versatile tool for the study and manipulation of nanoscale structures, and just recently, the first single-molecule logic gate was built with the help of an STM [30]. Furthermore, one can use the STM to induce the switching between different stable states. A small overview over the different switching mechanisms and their experimental realization can be found in the chapter of Toher et al.

In this chapter, we will present a minimal model Hamiltonian approach to describe one important switching mechanism in typical single-molecule STM junctions—the vibrational heating mechanism [4, 8]. The model describes switching induced by the coupling of a tunneling charge to molecular vibrational degrees of freedom. The model we will review here was originally proposed by Gao et al. [8], and it was extended by us to include the influence of an energy-dependent electronic density of states around the Fermi level [3, 4].

2   Vibrational Heating in Single-Molecule Switches

In general, molecular switches can be classified depending on different aspects of the system. One scheme distinguishes between the physical mechanisms underlying the switching phenomenon [7, 18]. Different physical mechanisms have been proposed to explain the observed dependence of the switching rate on the different properties of molecular systems. One very important class of mechanisms is the current-induced switching, in which the switching is triggered by the inelastic scattering of the tunneling electrons in the molecular system [4–6, 8–13, 15, 16, 20–23, 26–29, 31–36]. If the electrons are inelastically scattered by vibrations of the molecule and multiple excitations in each of energy $\hbar\omega$ are needed to induce the switching, the mechanism is usually called vibrational heating, since the effective temperature of the junction is increased. In 1997 Gao et al. showed that the switching rate shows a power-law dependence on the applied bias voltage $R \propto V_{\text{bias}}^n$ [8], where n denotes the number of excitations needed to induce the switching. In the past the model has been extended several times in order to explain deviations of the measured switching rate from the power-law dependence [4, 20, 33–35], *for example,* by combining the vibrational heating with other switching mechanisms (*e.g.,* quantum tunneling [34]). Tikhodeev and Ueba extended the model of Gao et al. to include effects of a nonequilibrium phonon distribution in the leads and by modeling the vibrational density of states (DOS) of the molecule correctly
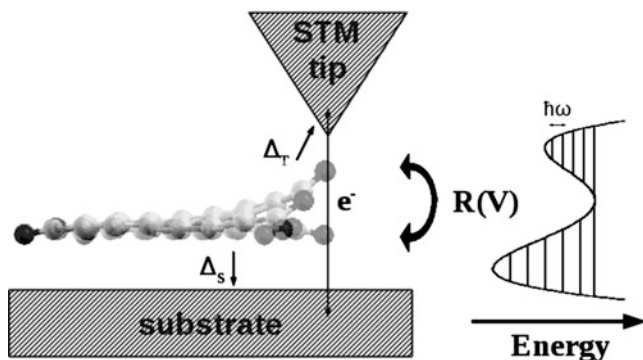
Fig. 1 Schematic representation of a single-molecule switch in an STM junction in which the molecule is asymmetrically coupled to the surface and the STM tip ($\Delta_s > \Delta_t$). The molecule gathers energy to overcome the potential barrier between the two stable positions by inelastic scattering of the tunneling electrons

(introducing a broadening due to the interaction with the substrate) [33]. This leads to a deviation from a simple power-law dependence of the switching rate on the bias voltage near the threshold voltage, $V_{bias} = \hbar\omega$. However, the authors still assumed that the adsorbate electronic DOS is constant over the relevant energy range, but in order to use molecules as logic gates, it is important that they have a nonconstant electronic DOS near the Fermi energy. As we will show below, this can lead to a dramatic change of the dependence of the switching rate on the bias voltage.

What all vibrational heating models have in common is that the molecule gathers enough energy to overcome the potential energy barrier between two stable states by multiple vibrational excitations. Each electron tunneling through the molecular junction has a certain probability of exciting vibrations of the molecule. The vibrational energy of the molecule dissipates at the same time into the leads mainly due to electron–hole pair creation.

In the following we will derive the excitation and relaxation rates of molecular vibrations due to inelastic scattering with tunneling electron and electron–hole pair creation in a typical STM molecular junction, in which the molecule is contacted by 2 leads; *cf.* Fig. 1. We will follow the derivation of [3, 4, 8]. The Hamiltonian of the STM molecule junction can be written as

$$H = \sum_{\alpha,k} \varepsilon_{\alpha,k}\, c^\dagger_{\alpha,k}\, c_{\alpha,k} \;+\; \varepsilon_m\, c^\dagger_m\, c_m + \sum_{\alpha,k} \left(T_{\alpha,k\,m}\, c^\dagger_{\alpha,k}\, c_m + \text{H.c.} \right) + \hbar\omega\, b^\dagger\, b, \quad (1)$$

where $c^\dagger_{\alpha,k}$ and $c^\dagger_m$ create an electron in the state $|k\rangle$ and $|m\rangle$ of the lead α (below, the lead α will be either the substrate s or the STM tip t) and the molecule, respectively, with the corresponding energies $\varepsilon_{\alpha,k}$ and ε_m. The hopping between the leads and the molecular level is described by the next term in (1) including $T_{\alpha,k\,m}$. The vibrational

system of the molecule is given by $\hbar\omega\, b^\dagger b$. Assuming that ε_m is a linear function of the vibrational coordinate q, $\varepsilon_m(q)$, the electron–vibron coupling can then be modeled by

$$H_{e-v} = \lambda_0 \left(b^\dagger + b\right)\left(c_m^\dagger c_m\right), \qquad (2)$$

where $\lambda_0 = \sqrt{\hbar/(2\,M\,\omega)}\,\varepsilon_m'$, with $\varepsilon_m' = \partial\varepsilon_m/\partial q$ at $q = 0$, ω is the frequency of the molecular vibration with the normal coordinate $q = \sqrt{\hbar/(2M\omega)}\,(b^\dagger + b)$ and mass M. For weak interaction between the vibrational system and the electronic system, the excitation and relaxation rates between the different vibrational levels can be expressed by the transition rates between the vibrational ground state and the first excited state (first-order perturbation theory). Using Fermi's golden rule, these rates can be calculated:

$$\Gamma_\uparrow = 2\tfrac{2\pi}{\hbar}\sum_{j,l} |\langle j, 1|H_{e-v}|l, 0\rangle|^2\; f_l\left(1 - f_j\right)\,\delta(\varepsilon_j - \varepsilon_l + \hbar\omega), \qquad (3)$$

$$\Gamma_\downarrow = 2\tfrac{2\pi}{\hbar}\sum_{j,l} |\langle j, 0|H_{e-v}|l, 1\rangle|^2\; f_l\left(1 - f_j\right)\,\delta(\varepsilon_j - \varepsilon_l - \hbar\omega) \qquad (4)$$

with 0 and 1 denoting the vibrational ground state and the first excited state respectively, while j and l denote any of the stationary one-electron states of the leads with corresponding Fermi–Dirac distributions $f_{j,l} = 1/\left\{1 + \exp\left[(\varepsilon - \mu_{j,l})/(k_B\,T)\right]\right\}$, and H_{e-v} denotes the electron-vibron interaction in (2). The overall rate can be decomposed into different terms $\Gamma_{\uparrow,\downarrow}^{ss}$, $\Gamma_{\uparrow,\downarrow}^{tt}$ and $\Gamma_{\uparrow,\downarrow}^{st}$, $\Gamma_{\uparrow,\downarrow}^{ts}$ depending on whether the final and initial state (first and second superscript) of the tunneling electron is in the substrate s or in the tip t. We model the electronic DOS of the combined STM tip–molecule–substrate system by a Lorentzian shape, *for example,*

$$\rho_m^s(E) = \Sigma_\kappa |\langle\kappa|m\rangle|^2\delta(\varepsilon - \varepsilon_\kappa) = \Delta_s/(\pi((E - \varepsilon_m)^2 + \Delta^2)), \qquad (5)$$

where κ labels the stationary one-electron states $|\kappa\rangle$ in the leads and $\Delta = \Delta_s + \Delta_t$, with Δ_s and Δ_t describing the electronic coupling between the molecular level and the substrate and STM tip, respectively. For low temperature, the excitation and relaxation rates can be calculated analytically by approximating the Fermi functions with Heaviside step functions. The terms $\Gamma_\downarrow^{ss}$ and $\Gamma_\downarrow^{tt}$ are similar, and we will evaluate only $\Gamma_\downarrow^{ss}$:

$$
\begin{aligned}
\Gamma_\downarrow^{ss} &= 2\frac{2\pi\lambda_0^2}{\hbar}\sum_{\alpha',\alpha}\left|\langle\alpha'|m\rangle\langle m|\alpha\rangle\right|^2 [1 - f_s(\varepsilon_{\alpha'})]\; f_s(\varepsilon_\alpha)\,\delta(\varepsilon_{\alpha'} - \varepsilon_\alpha - \hbar\omega) \\[2mm]
&= 2\frac{2\pi\lambda_0^2}{\hbar}\int d\varepsilon\,\rho_m^s(\varepsilon)\,\rho_m^s(\varepsilon + \hbar\omega)\,[1 - f_s(\varepsilon + \hbar\omega)]\; f_s(\varepsilon) \\[2mm]
&= 2\frac{2\pi\Delta_s^2\lambda_0^2}{\hbar}\int d\varepsilon\,\frac{1}{[\varepsilon - \varepsilon_m]^2 + \Delta^2}\frac{1}{[\varepsilon + \hbar\omega - \varepsilon_m]^2 + \Delta^2} \\[2mm]
&\quad\times [1 - f_s(\varepsilon + \hbar\omega)]\; f_s(\varepsilon)
\end{aligned}
$$

$$
\approx 2 \frac{2\pi \Delta_s^2 \lambda_0^2}{\hbar} \int d\varepsilon \, \frac{1}{[\varepsilon - \varepsilon_m]^2 + \Delta^2} \frac{1}{[\varepsilon + \hbar\omega - \varepsilon_m]^2 + \Delta^2}
$$

$$
\times [1 - \Theta(\varepsilon_{Fs} - \hbar\omega - \varepsilon)] \, \Theta(\varepsilon_{Fs} - \varepsilon)
$$

$$
= 2 \frac{2\pi \Delta_s^2 \lambda_0^2}{\hbar} \int_{\varepsilon_{Fs} - \hbar\omega}^{\varepsilon_{Fs}} d\varepsilon \, \frac{1}{[\varepsilon - \varepsilon_m]^2 + \Delta^2} \frac{1}{[\varepsilon + \hbar\omega - \varepsilon_m]^2 + \Delta^2}
$$

$$
= \frac{4\Delta_s^2 \lambda_0^2}{\pi \Delta \hbar^2 \omega \, (4\Delta^2 + \hbar^2\omega^2)} \left\{ \hbar\omega \left(\tan^{-1} \left[\frac{\varepsilon_m - \varepsilon_{Fs} + \hbar\omega}{\Delta} \right] \right.\right.
$$

$$
\left. - \tan^{-1} \left[\frac{\varepsilon_m - \varepsilon_{Fs} - \hbar\omega}{\Delta} \right] \right) + \Delta \left(\log \left[\Delta^2 + (\varepsilon_m - \varepsilon_{Fs} + \hbar\omega)^2 \right] \right.
$$

$$
\left.\left. + \log \left[\Delta^2 + (\varepsilon_m - \varepsilon_{Fs} - \hbar\omega)^2 \right] - 2 \log \left[\Delta^2 + (\varepsilon_m - \varepsilon_{Fs})^2 \right] \right) \right\}. \quad (6)
$$

In the first two steps, we replaced the sum over states with an integral over ε by introducing the electronic DOS, $\rho_m^s(\varepsilon)$, of the combined system as defined in (5). In the next step, the low-temperature approximation was used. This leads to a change of the limits of the integral from $+\infty$ and $-\infty$ to ε_{Fs} or $\varepsilon_{Fs} - \hbar\omega$, respectively. An applied bias voltage shifts the Fermi level of the surface $\varepsilon_{Fs} = \varepsilon_{Fs}^0 + eV$, with ε_{Fs}^0 being the Fermi energy of the surface at $V = 0$. The excitation rates $\Gamma_\uparrow^{ss,tt}$ become zero in the low temperature, because of the Pauli exclusion principle.

The Pauli exclusion principle also reduces the number of transition rates $\Gamma_{\uparrow,\downarrow}^{st,ts}$ one has to calculate, since the electrons can only tunnel from the higher to the lower chemical potential. The transition rates $\Gamma_{\uparrow,\downarrow}^{st}$ (for positive bias) can be written as

$$
f_\pm(E) = \frac{4\lambda_0^2}{\pi \, \Delta \, \hbar^2 \, \omega \, (4\Delta^2 + \hbar^2 \, \omega^2)}
$$

$$
\times \left(\hbar\omega \, \tan^{-1} \left[\frac{E - \varepsilon_m}{\Delta} \right] \pm \Delta \, \log \left[\Delta^2 + (E - \varepsilon_m)^2 \right] \right), \quad (7)
$$

$$
\Gamma_\downarrow^{st} = \Delta_s \, \Delta_t \, (f_+(\mu_t + \hbar\omega) - f_+(\mu_s) + f_-(\mu_t) - f_-(\mu_s - \hbar\omega)), \quad (8)
$$

$$
\Gamma_\uparrow^{st} = \Delta_s \, \Delta_t \, (f_+(\mu_t) - f_+(\mu_s + \hbar\omega) + f_-(\mu_t - \hbar\omega) - f_-(\mu_s)), \quad (9)
$$

where $\mu_s = \varepsilon_{F_s} - |V_{bias}|$ and $\mu_t = \varepsilon_{F_t}$ (i.e., bias is applied to the substrate) and the excitation rate $\Gamma_\uparrow^{st}$ is only nonzero for $|\mu_t - \mu_s| \geq \hbar\omega$. In an analogous manner one can find the rates $\Gamma_{\uparrow,\downarrow}^{ts}$ for negative bias.

The transfer between the two wells of a double well, as shown in Fig. 1, can in general involve various processes. The vibrationally assisted tunneling [34] can have an especially great impact on the switching rate below and near the threshold voltage, $V_{bias} = \hbar\omega$. However, for clarification and to highlight the changes due
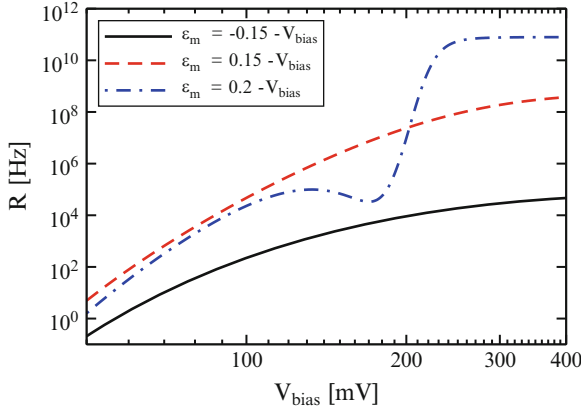
**Fig. 2** Calculated transfer rate R for different orbitals through which the electrons tunnel. The *black (solid)* and *red (dashed) line* is for an occupied and an unoccupied orbital, respectively, whose position is coupled to the chemical potential of the surface (parameter: $\Delta_s = 0.2\,\text{eV}$, $\Delta_t = 0.1\Delta_s$, $\hbar\omega = 20\,\text{meV}$, $n = 10$, $\lambda_0 = 1\,\text{meV}$). The *blue (dash-dotted) line* represents the transfer rate if the molecule is coupled weakly to the substrate as, for example, on a NaCl film (parameter: $\Delta_s = 0.025\,\text{eV}$, $\Delta_t = 0.1\Delta_s$, $\hbar\omega = 20\,\text{meV}$, $n = 10$, $\lambda_0 = 1\,\text{meV}$)

to the nonconstant electronic DOS, we use a simple truncated harmonic oscillator potential to describe the transfer between two stable configurations and assume that the vibrational heating is the only relevant process which can induce the switching. The transfer rate R can then be expressed as a product of the transition into level n from $(n - 1)$ and an effective Boltzmann factor (with temperature $T_{\text{eff}} = \hbar\omega/(k_B \ln[\Gamma_\downarrow/\Gamma_\uparrow])$) describing the probability to arrive at the subcritical level $(n - 1)$ [8]:

$$R \simeq n\,\Gamma_\uparrow \exp\left[\frac{(n-1)\,\hbar\omega}{k_B\,T_{\text{eff}}}\right] = n\,\Gamma_\uparrow \left(\frac{\Gamma_\uparrow}{\Gamma_\downarrow}\right)^{n-1} . \tag{10}$$

Figure 2 shows the dependence of the transfer rate, (10), on different values for the substrate–molecule coupling Δ_s and on different positions of the molecular level with respect to the Fermi energy. For positive bias and electrons tunneling mainly through the lowest unoccupied orbital (LUMO) of the molecule, the transfer rate is always larger than if the level is just below the Fermi energy. This is due to the fact that the LUMO shifts with the applied bias voltage, and, thus, the DOS in the bias window increases constantly. In contrast, the highest occupied orbital always stays below the bias window if a positive bias is applied. Thus, also the number of tunneling channels (the DOS in the bias window) changes only slightly. The opposite is the case for negative voltages. In general, if the molecule is coupled strongly to the surface (*i.e.,* Δ_s is in the order of $100\,\text{meV}$), the transfer rate shows a power-law behavior as already described by Gao et al. [8]. The main difference is that for large applied bias voltage, the rate becomes constant. The limit of the

Fig. 3 Calculated transition rates Γ for the *blue (dash-dotted) curve* in Fig. 2
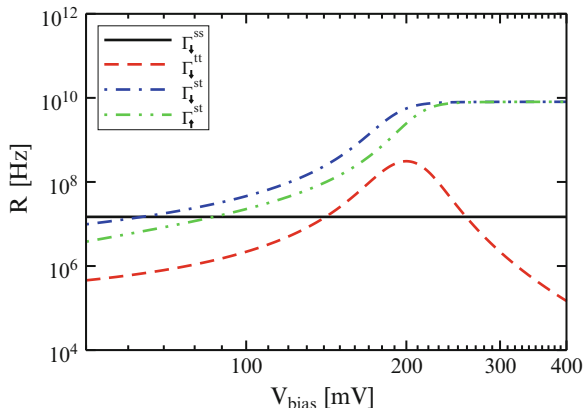
transfer rate can be calculated analytically, and it depends strongly on the electronic coupling of the molecular level to the leads Δ and on the barrier height $n\,\hbar\omega$. Furthermore, in an STM junction, because of the asymmetric coupling to the leads, the limit also depends on the position of the molecular level relative to Fermi energy of the lead to which it is coupled more strongly.

For less strongly coupled molecules, *for example,* on a NaCl film, the transfer rate can deviate from the power-law dependence on the applied bias voltage as shown in Fig. 2 as blue, dashed-dotted curve. The moment the molecular level enters into resonance with the Fermi energy of the STM tip, the transfer rate can show a constant behavior for a certain bias range or even decrease. The origin of this behavior can be identified by having a closer look at the different transition rates, $\Gamma_{\downarrow}^{ss,tt}$ and $\Gamma_{\uparrow,\downarrow}^{st}$ in Fig. 3. While the rates $\Gamma_{\uparrow,\downarrow}^{st}$ increase until the molecular level is completely within the bias window, the transition rate $\Gamma_{\downarrow}^{ss}$ is constant since the position of the molecular level relative to the chemical potential of the surface does not change. The excitation rate, $\Gamma_{\uparrow}^{st}$, and relaxation rate, $\Gamma_{\downarrow}^{st}$, due to electrons tunneling from the STM tip to the surface, are shifted relative to each other, and this shift is related to the vibrational energy $\hbar\omega$, *cf.* Equations (6)–(9). The rate $\Gamma_{\downarrow}^{tt}$ has a maximum when the molecular level is in resonance with the Fermi energy of the tip, as shown in Fig. 3. These different behaviors lead to the strong deviation from the power-law dependence on the applied bias voltage as shown in Fig. 2, and they have a clear physical meaning. As soon as the vibrationally excited molecular level, $\varepsilon_m + \hbar\omega$, enters the bias window, a new transport channel opens. Electrons can now tunnel through the molecule by relaxing vibrations on it, thus increasing the dissipation of vibrational energy into the leads which results in cooling of the molecular junction. An experimental verification of this cooling is in general very demanding since the transfer rate has to be analyzed with respect to many different parameters. Furthermore, the coupling to both the surface and the STM tip need to be weak so that the cooling can be effective and a saturation or decrease in the transfer rate can be seen. One possible example can be seen in Fig. 4 for a PTCDA molecule switching between an STM tip and a Ag(111) surface.

Fig. 4 Transfer rates for a PTCDA molecule switching between the STM tip and a Ag(111) surface for different tip–surface separations. Measured rate for the transfer from the surface to the tip is indicated by small symbols. Solid lines display the fitted theoretical transfer rate. Redrawn from [4]; Copyright (2011) by the American Physical Society
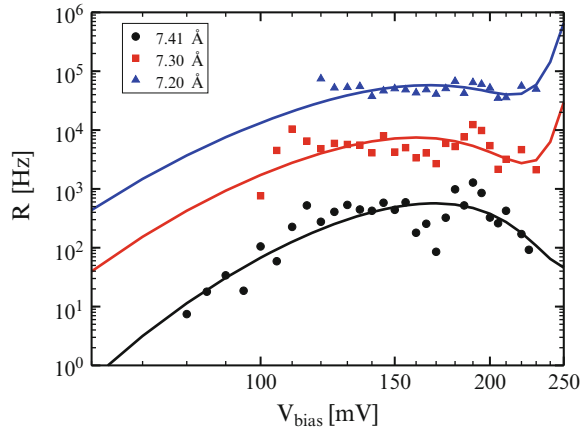
3 Summary

Recently, it has been shown experimentally that the switching rate in molecular junctions can deviate strongly from the simple power-law dependence on the applied bias as proposed by Gao et al. [4, 22]. By including an energy-dependent electronic DOS near the Fermi energy, one can qualitatively explain the saturation and the decrease in the switching rate. This can be related to an enhanced cooling as soon as molecular level, which is coupled weakly to the leads, enters the relevant bias window. Our results show that by including an energy dependence of the DOS around the Fermi energy, a complex and rich behavior of the switching rate can be described. However, one has always to be aware of the approximations behind this model; $k_B T \approx 0$, $|V_{bias}| \gg \hbar\omega$, $\Gamma_{\uparrow,\downarrow} \ll \hbar\omega$, and $\lambda_0/\Delta < 1$ (weak inelasticity).

References

1. Aviram, A., Ratner, M.: Molecular rectifiers. Chem. Phys. Lett. **29**(2), 277–283 (1974)
2. Binnig, G., Rohrer, H., Gerber, C., Weibel, E.: Surface studies by scanning tunneling microscopy. Phys. Rev. Lett. **49**, 57–61 (1982)

3. Brumme, T., Gutiérrez, R., Cuniberti, G.: Vibrational induced switching in single-molecule junctions: influence of an energy dependent density of states. to appear in J. Phys.: Condens. Matter **23**, 394003 (2012)

4. Brumme, T., Neucheva, O.A., Toher, C., Gutiérrez, R., Weiss, C., Temirov, R., Greuling, A., Kaczmarski, M., Rohlfing, M., Tautz, F.S., Cuniberti, G.: Dynamical bistability of single-molecule junctions: a combined experimental and theoretical study of ptcda on ag(111). Phys. Rev. B **84**, 115449 (2011)

5. Eigler, D., Lutz, C., Rudge, W.: An atomic switch realized with the scanning tunnelling microscope. Nature **352**, 600–603 (1991)

6. Elste, F., Weick, G., Timm, C., von Oppen, F.: Current-induced conformational switching in single-molecule junctions. Appl. Phys. A: Mater. Sci. Process. **93**, 345–354 (2008)

7. Feringa, B.: The art of building small: from molecular switches to molecular motors. J. Org. Chem. **72**(18), 6635–6652 (2007)

8. Gao, S., Persson, M., Lundqvist, B.I.: Theory of atom transfer with a scanning tunneling microscope. Phys. Rev. B **55**(7), 4825–4836 (1997)

9. Hahn, J., Ho, W.: Vibrational mode specific bond dissociation in a single molecule. J. Chem. Phys. **131**(4), 044706 (2009)

10. Henningsen, N., Franke, K.J., Torrente, I.F., Schulze, G., Priewisch, B., Rack-Braun, K., Dokia, J., Klamroth, T., Saalfrank, P., Pascual, J.I.: Inducing the rotation of a single phenyl ring with tunneling electrons. J. Phys. Chem. C **111**(40), 14,843–14,848 (2007)

11. Iancu, V., Deshpande, A., Hla, S.W.: Manipulating kondo temperature via single molecule switching. Nano Lett. **6**(4), 820–823 (2006)

12. Iancu, V., Hla, S.W.: Realization of a four-step molecular switch in scanning tunneling microscope manipulation of single chlorophyll-a molecules. PNAS **103**(37), 13,718–13,721 (2006)

13. Jorn, R., Seideman, T.: Competition between current-induced excitation and bath-induced decoherence in molecular junctions. J. Chem. Phys. **131**(24), 244114 (2009)

14. Kulzer, F., Kummer, S., Matzke, R., Brauchle, C., Basche´, T.: Single-molecule optical switching of terrylene in p-terphenyl. Nature **387**, 688–691 (1997)

15. Lauhon, L., Ho, W.: Direct observation of the quantum tunneling of single hydrogen atoms with a scanning tunneling microscope. Phys. Rev. Lett. **85**(21), 4566–4569 (2000)

16. Liu, K., Gao, S.: Excitation of frustrated translation and nonadiabatic adatom hopping induced by inelastic tunneling. Phys. Rev. Lett. **95**(22), 226102 (2005)

17. Metzger, R.M.: Unimolecular electronics. J. Mater. Chem. **18**, 4364–4396 (2008)

18. van der Molen, S., Liljeroth, P.: Charge transport through molecular switches. J. Phys.: Condens. Matter **22**(13), 133001 (2010)

19. Moresco, F.: Manipulation of large molecules by low-temperature stm: model systems for molecular electronics. Phys. Rep. **399**(4), 175–225 (2004)

20. Motobayashi, K., Kim, Y., Ueba, H., Kawai, M.: Insight into action spectroscopy for single-molecule motion and reactions through inelastic electron tunneling. Phys. Rev. Lett. **105**(7), 076101 (2010)

21. Nacci, C., Lagoute, J., Liu, X., Fölsch, S.: Conformational switching of single 1,5-cyclooctadiene molecules on si(001) induced by inelastic electron tunneling. Phys. Rev. B **77**(12), 121405 (2008)

22. Néel, N., Kröger, J., Berndt, R.: Two-level conductance fluctuations of a single-molecule junction. Nano Lett. **11**(9), 3593–3596 (2011)

23. Ohmann, R., Vitali, L., Kern, K.: Actuated transitory metalligand bond as tunable electromechanical switch. Nano Lett. **10**(8), 2995–3000 (2010)

24. Pascual, J., Méndez, J., Gómez-Herrero, J., Baró, A., Garcia, N., Landman, U., Luedtke, W., Bogachek, E., Cheng, H.P.: Properties of metallic nanowires: From conductance quantization to localization. Science **267**(5205), 1793–1795 (1995)

25. Reed, M., Zhou, C., Muller, C., Burgin, T., Tour, J.: Conductance of a molecular junction. Science **278**(5336), 252–254 (1997)

26. Safiei, A., Henzl, J., Morgenstern, K.: Isomerization of an azobenzene derivative on a thin insulating layer by inelastically tunneling electrons. Phys. Rev. Lett. **104**(21), 216102 (2010)

27. Seideman, T. (ed.): Current-Driven Phenomena in NANOELECTRONICS. Pan Stanford Publishing Pte. Ltd. (Singapore, 2011)

28. Simic-Milosevic, V., Mehlhorn, M., Rieder, K.H., Meyer, J., Morgenstern, K.: Electron induced ortho-meta isomerization of single molecules. Phys. Rev. Lett. **98**(11), 116102 (2007)

29. Smit, R., Noat, Y., Untiedt, C., Lang, N., van Hemert, M., van Ruitenbeek, J.: Measurement of the conductance of a hydrogen molecule. Nature **419**, 906–909 (2002)

30. Soe, W.H., Manzano, C., De Sarkar, A., Ample, F., Chandrasekhar, N., Renaud, N., de Mendoza, P., Echavarren, A.M., Hliwa, M., Joachim, C.: Demonstration of a nor logic gate using a single molecule and two surface gold atoms to encode the logical input. Phys. Rev. B **83**, 155443 (2011)

31. Stroscio, J., Celotta, R.: Controlling the dynamics of a single atom in lateral atom manipulation. Science **306**(5694), 242–247 (2004)

32. Stroscio, J., Tavazza, F., Crain, J., Celotta, R., Chaka, A.: Electronically induced atom motion in engineered cocu$_n$ nanostructures. Science **313**(5789), 948–951 (2006)

33. Tikhodeev, S., Ueba, H.: Relation between inelastic electron tunneling and vibrational excitation of single adsorbates on metal surfaces. Phys. Rev. B **70**(12), 125414 (2004)

34. Tikhodeev, S.G., Ueba, H.: How vibrationally assisted tunneling with stm affects the motions and reactions of single adsorbates. Phys. Rev. Lett. **102**(24), 246101 (2009)

35. Ueba, H., Mii, T., Lorente, N., Persson, B.N.J.: Adsorbate motions induced by inelastic-tunneling current: theoretical scenarios of two-electron processes. J. Chem. Phys. **123**(8), 084707 (2005)

36. Wang, Y., Kröger, J., Berndt, R., Hofer, W.: Pushing and pulling a sn ion through an adsorbed phthalocyanine molecule. J. Am. Chem. Soc. **131**(10), 3639–3643 (2009)

Heat Dissipation in Molecular Junctions: Linking Molecules to Macroscopic Contacts

Alessandro Pecchia

Abstract Multiscale and hierarchical methods are becoming a paradigm for the understanding of complex physical phenomena. The concept can be applied to modern nanoelectronic devices where charge and thermal transport phenomena span a broad range of scales from nanometers up to millimeters, sometimes tightly interconnected as in the case of heat dissipation. This demand for the development of new stimulation tools that can cope with microscopic and macroscopic scales coupling different physical models.

In this work progresses towards the realization of such integration schemes are presented. At the microscopic scale, the system is described using empirical or density-functional tight-binding descriptions (DFTB). Transport calculations are obtained using nonequilibrium Green's functions methods that allow for calculations of coherent and incoherent transport and heat dissipation. At larger scales, effective medium equations are represented on finite-element meshes (FEM) to describe electronic and heat-transport phenomena with drift-diffusion or Fourier equations. Atomistic/FEM models are coupled imposing energy/current flux continuity at the boundaries. In this chapter an application of this scheme for the calculation of heat dissipation in molecular junctions is presented.

1 Introduction

Nanoelectronic devices—and to their extreme-end single-molecule electronics—always require coupling the active units characterized by nanoscale dimensions to contacts, wires, and packaging, characterized by much larger scales. However, the behavior of the whole device is determined by the interplay of different transport

A. Pecchia
CNR-ISMN Via Salaria km 29.300, 00017 Monterotondo Stazione, Rome, Italy
e-mail: alessandro.pecchia@ismn.cnr.it

mechanisms occurring at different length scales. The typical approach in charge transport is to concentrate on the nanoscale devices with accurate simulations and then treat the contacts and the environment as effective circuit components within a SPICE-like approach. There are problems, however, that cannot be easily decoupled in such a simple way. In molecular electronics, small changes of local potentials can have large effects on the electronic and transport properties of the system, and for this reason, accurate density-functional tools have been developed in the last decade in order to describe charge-transport mechanisms in molecules when transport is dominated by quantum coherence. However, computational limitations prevent treating substantial parts of the contacting leads at the same level of accuracy. The only practical solution is to tackle the problem in a pragmatic cutting-and-sewing approach in which the molecular transport is treated using quantum-transport methods and the contacting leads and surrounding environment is described as a continuous medium using semiclassical models.

Heat dissipation, and more in general energy transport, is another important example of nonlinear coupling between the nano-world and its environment. Miniaturization obviously increases the power density of heat generation, making heat management one of the key issues that needs to be addressed in order to improve the stability and reliability of nanodevices. Heat dissipation depends on the transport property at all scales, and careful simulations are crucial in order to predict and control the working temperatures reached in the device.

The wide span of length scales and transport phenomena requires the development of new tools of multiscale character. A general a priori methodology for such a multiscale coupling has not been established to date, especially when quantum- and classical-charge-transport models are sewed together. Most of the solutions must be guided by physical intuition, requirement of consistency, and continuity equations. The situation is similar to the practical needs that have guided the developments of sophisticated QM/MM coupling schemes and have proven quite useful in molecular dynamics simulations in order to understand a wide range of physical phenomena, from structural properties to excitation dynamics and mass transport.

In this work an example towards the development of quantum-classical multiscale coupling for charge and heat transport is presented and applied to the problem of heating of a benzo-di-pyridine molecule adsorbed on a Cu substrate when current is driven across by an STM measurement.

2   Coupling Quantum with Semiclassical Transport Models

Nonequilibrium Green's functions (NEGF) have become a standard tool to analyze transport in nanodevices [1] when quantum coherence plays a relevant role. Yet, the evaluation of NEGF is numerically very expensive, especially when scattering is included. In general the microscopic domain in which quantum effects need to be fully taken into account is restricted to the molecular scale and/or its close

surroundings. The molecular region is embedded within a macroscopic domain, where simpler phenomenological transport equations can be solved. A multiscale/multiphysics approach is therefore necessary in order to efficiently compute transport in the whole system. To this end we have developed a coupling scheme between drift-diffusion (DD) and NEGF transport models which are solved on different subdomains. These are coupled via boundary conditions: the macroscale models providing boundary conditions in terms of electrochemical potentials, whereas the microscale models provide flux boundary conditions to the macro domains. In order to ensure continuity conditions on current, the two models are coupled self-consistently with an iteration scheme that starts with a guess solution. This method goes under the name of bridge multiscale approach [2, 3]. In the same way, heat dissipation at the molecular scale is coupled to a Fourier heat-transport model at larger scales by imposing temperature boundary conditions and heat flux. A problem in this coupling scheme is that molecular transport needs to be simulated using atomistic approaches, whereas macroscopic scales are treated as effective continuous media and the differential equations are discretized on meshes. Sewing the two models requires appropriate interpolations and embracing schemes of the electronic charge density and currents at the interfaces between atoms and finite elements.

3 FEM and Atomistic Model of the Tip/Molecule/Substrate

The first step is to build a realistic model of the STM tip, which is typically tungsten-made ultrasharp objects fabricated using electromigration processes [4].

Figure 1 shows a micrograph of one of such tips [5]. Based on available SEM/TEM images, a model comprising $2\,\mu m$ of the tip ending has been built. This is considered sufficient for the purposes of the subsequent computations, especially heat transport along the tip. The tip is still reduced to an idealized model having a conical shape with a termination assumed as an ideal hemisphere of 3 nm in diameter, as shown in Fig. 2. A flat substrate is also included in the model.

The next step is to introduce an adequate atomistic description of the tip/molecule/Cu substrate. This is obtained in a three-step procedure. The first step consists in filling with atoms the mesh regions at the tip apex and substrate, which is done assuming a [111]Cu orientation and imposing the same atomistic Cu geometry within the tip. The reason for doing this is justified by the fact that in most STM/STS experiments, the tip is dipped on the substrate before imaging, and after this procedure, it is likely to pick up a substantial fraction of substrate atoms.

The following step is to insert a pre-relaxed benzene-di-pyridine molecule within the tip/substrate gap, including two extra Cu atoms which are bonded to the nitrogen atoms of the molecule and to the tip and substrate, respectively. This is done following the indication that these kinds of molecules tend to bind to Cu adatoms [6]. Finally the geometry is relaxed, including the two Cu atoms, keeping fixed the substrate and tip. A relaxed geometry for tip-substrate distance of 1.2 nm is shown

Fig. 1 SEM image of an electrochemically etched ultrasharp STM tip made of tungsten
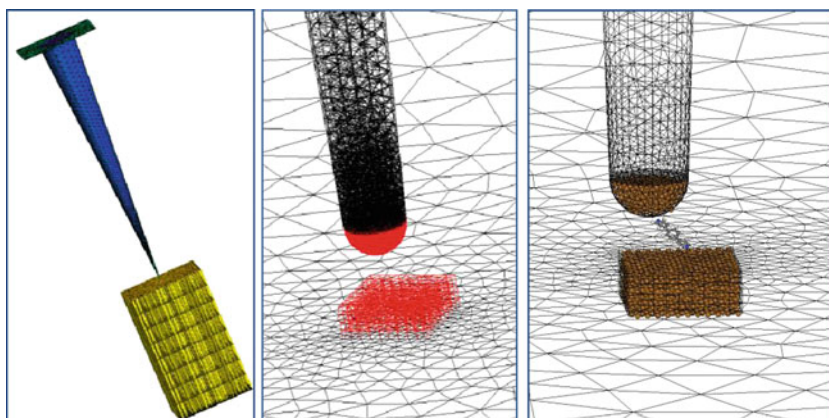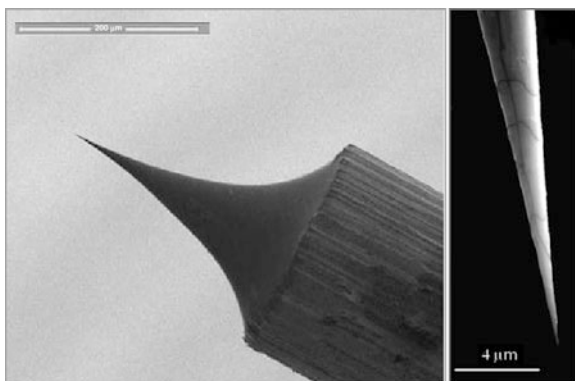
Fig. 2 (*Right*) FEM model of tip apex including $2\,\mu m$ of tip and substrate. (*Center*) Zoom in of the tip/molecule/substrate mesh before atoms are added and (*left*) atomistic model

in Fig. 3. All DFT calculations in this work have been performed using the density-functional tight-binding (DFTB) approach and its extensions to transport. For an extended review of the method, see [7, 8].

4 Electron–Phonon Coupling and IETS Spectrum

Once the final geometry has been obtained, the vibrational modes of the molecule and the electron–vibron (localized phonon) coupling matrices are computed at the bias $V = 0$ [9, 10]. A good insight of the electron–phonon scattering can be obtained looking at the inelastic electron tunneling spectroscopy (IETS) [11], which is proportional to d^2I/dV^2 in order to enhance the onset of inelastic vibronic excitations by the tunneling electrons.
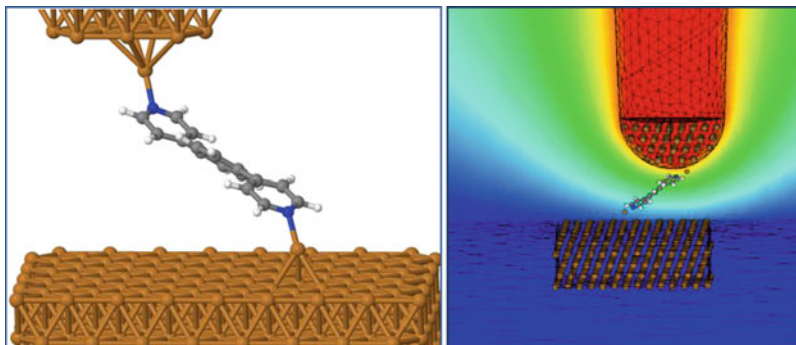
Fig. 3 (*Left*) A view of the relaxed geometry of the tip/molecule/substrate system and (*right*) potential profile computed at a bias of 1.0 V

The simulated IETS spectrum is shown in Fig. 4 and reveals few dominant peaks corresponding to specific vibrational modes of the pyridine and benzene cages. The most important peak, at $1,810\,\text{cm}^{-1}$, actually originates from a combination of two modes with even and odd symmetry with respect to the molecular reflection plane. In Fig. 4, only the mode with odd symmetry is shown. The IETS signal is computed and measured at low temperatures ($T = 4.2\,\text{K}$) and low bias ($V \sim 400\,\text{mV}$) in order to reduce noise. When large biases are applied, the molecule heats up and the vibronic population becomes strongly a nonequilibrium distribution, and it is not obvious that these modes are still dominating.

5 Nonequilibrium Phonon Distributions and Molecular Heating

The nonequilibrium phonon population can be computed by setting a self-consistent calculation in which the average occupation of each vibrational mode is computed following a simple rate equation whose linearized solution is [12]

$$N_q = \frac{n_q(T_0)J_q + E_q}{J_q + A_q - E_q} \tag{1}$$

where J_q is the rate of phonon dissipated in the contacts, A_q and E_q are the rates of phonon absorbed and emitted in the molecule, and $n_q(T_0)$ is the equilibrium Bose–Einstein phonon distribution in the reservoirs. Expressions for A_q and E_q can be derived from the NEGF theory and can be found in [9]. Figure 5 shows the nonequilibrium distribution of quanta in all vibrational modes for different applied bias voltages. Solid lines are best distribution estimators assuming a Bose–Einstein
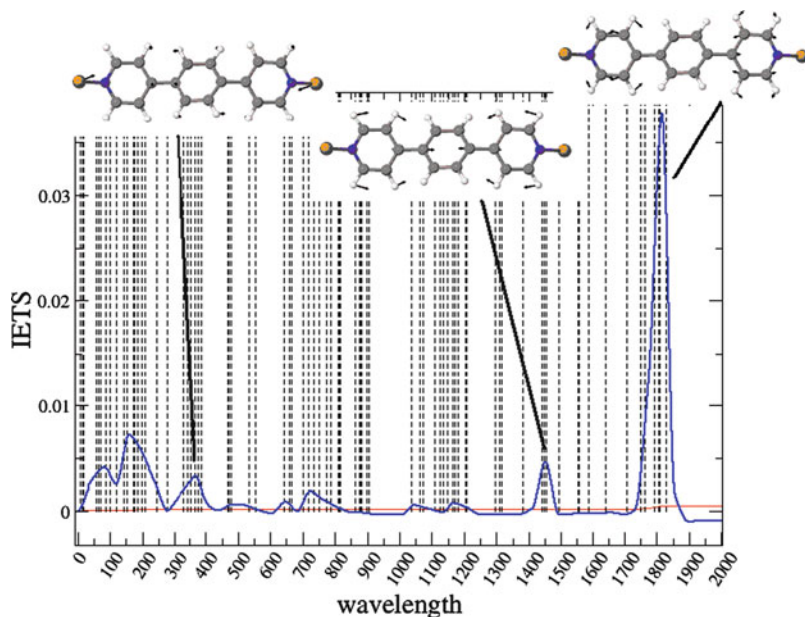
Fig. 4 Simulated IETS signal of the molecule and vibrational modes giving the largest signal

form and give an effective molecular temperature. The estimator is defined such that the total energy stored in the vibrational modes is conserved, namely,

$$U = \sum_q \hbar\omega_q N_q = \sum_q \hbar\omega_q n_q(T_{mol}) \qquad (2)$$

It is possible to observe that low-energy modes tend to be less populated with respect to the equilibrium distribution, whereas high-energy modes are much more populated. This effect is due to the fact that the electron–phonon coupling occurs mainly with the high-energy modes which couple very weakly to the reservoirs due to a strong band mismatch. It should be noted, however, that these calculations neglect anharmonicity eventually responsible for phonon decays from high to low energies. This redistribution is expected to give a final population that is much closer to an equilibrium distribution, characterized by an effective temperature, especially when internal relaxations are much faster than dissipation into the reservoirs. The equilibrium distribution that conserves total energy, as computed and shown in Fig. 5, is therefore realistic. It is also worth to observe that in these calculations it is not simply possible to just retain those few modes giving the largest IETS signal, but to the contrary, all vibrational modes must be included. This is because the actual equilibrium population depends on the delicate ratio between emission and absorption given by Eq. (1) in which the denominator can be small or the ratio can approach unity.
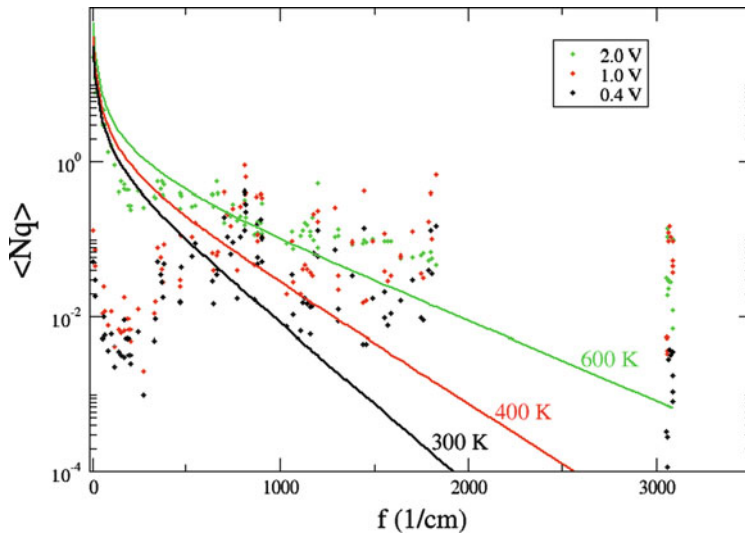
Fig. 5 Average number of vibrational quanta in each molecular mode and temperature fit using a Bose–Einstein distribution

The calculation of the coherent and incoherent current across the molecule includes a self-consistent calculation of the potential profile. In order to properly consider the tip shape, a large portion of the latter is included in the calculation at the level of an effective medium drift-diffusion model. This is necessary since a complete atomistic simulation of the tip would be computationally too demanding. An example of potential profile is shown in the right panel of Fig. 3, obtained by coupling the DFTB-NEGF charge density and potential solution [8] to the drift-diffusion solution, as explained in Sect. 1. The metallic contacts efficiently screen the applied bias and, as expected, the potential drops almost entirely across the tip/molecule/substrate junction due to its large resistance.

6 Coupling to Fourier Thermal Transport and Tip Heating

The knowledge of the temperature profile of the STM tip under bias is a relevant problem in order to understand tip-induced excitations and tip degradation and helps to disentangle the tip signal from molecular electroluminescence. In order to study this problem, the molecular heat dissipation is coupled to the tip and substrate where a simpler Fourier thermal transport model is used. This is done because the size of the contact makes rapidly intractable the problem of electron–phonon coupling and thermal transport at the atomistic level.

It turns out that the heat released in the molecule is only a small fraction of the total available power, $P = I \cdot V$, from the applied bias. For instance, at the applied bias of 1.0 V, only about 1 nW is released in the molecule, whereas for

a typical tunneling current of $1\,\mu$A, the power supplied is $1\,\mu$W, i.e., about three orders of magnitude larger. This does not immediately imply that electron–phonon scattering events are rare. In fact comparing the tunneling rate of $\sim 10^{13}\ e/s$ with the total absorption and emission rates of $\sim 10^{12}1/s$, we conclude that one electron in ten suffers an incoherent scattering. The net rate of phonon emitted is the result of the close balance between absorption and emission rates which tend to cancel each other.

Ultimately the electric power has to be released somewhere as heat. We assume that the hot electrons release their energy within a mean free path in the tip and the substrate that can be estimated to be about 5–10 nm. Consequently we assume that all the electronic energy is converted into heat within this distance.

In order to simulate how this energy is transported away along the tip and in the substrate, we couple the microscopic heat dissipation to a Fourier heat-transport equation. This phenomenological model requires as input the thermal conductivity of the materials, a quantity taken from database values that also depends on temperature. Thermal conductance is also strongly affected by size effects due to surface roughness scattering at the boundaries. Typically, the thermal conductance shows a Fuchs-Sondheimer behavior that scales with the inverse of the wire cross section. Metallic nanowires with 10-nm cross section can exhibit an increase of thermal resistance up to one order of magnitude with respect to bulk values. This is expected to play a crucial role near the tip apex, where the diameter can reach few nanometers. The size effect has been included in a phenomenological way, using the results of [13]. The thermal conductance of the vacuum gap between tip and substrate is assumed to be zero, although this may lead to a small error since it neglects radiative effects. The simulation is performed assuming an environment temperature of liquid Helium of 4.2 K as in low temperature STM [6]. In our simulations, however, we cannot simply assume fixed temperature boundary conditions since we are still simulating only a subpart of the whole system (2 μm of tip length rather than the whole tip of Fig. 1). Consequently a fixed thermal surface conductance is imposed on the outer boundaries of the tip and substrate cross sections, simulating an effective heat flux with bulk thermal conductivities. This is the same as assuming that the system is embedded in a material with constant thermal resistance and reaches the equilibrium thermostat temperature only far away from the tunneling junction.

The results of the nonequilibrium temperature profiles computed at a substrate bias of 1 V are shown in Fig. 6. The right and left diagrams show the temperature map in the tip and substrate, respectively. It is possible to appreciate how the size effect strongly influences the tip thermal conductance, hence the temperature map. Temperatures as high as 145 K can be found near the tip apex, where the hot tunneling electrons release their extra energy. On the other hand, the substrate that does not suffer size effects does not show noticeable heating.

The temperature map depends on the heat-transport properties in the nanoscale tip which are lumped here into an effective thermal conductivity. A Fourier heat-transport model taking into account for size effects in a phenomenological way can be seen as a first approximation to the problem. Simulations based on the
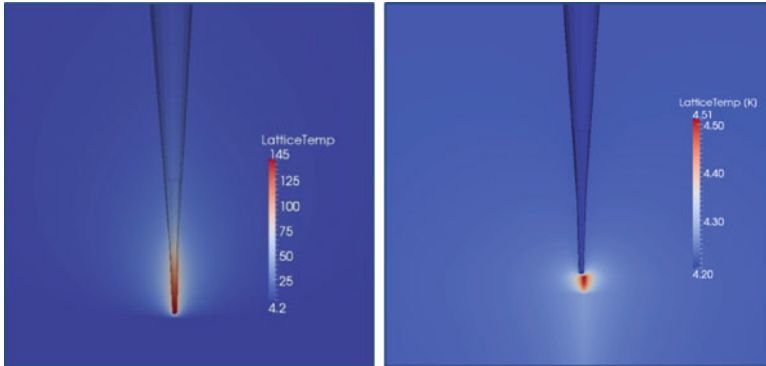
Fig. 6 Temperature profiles of the STM tip (*right*) and substrate (*left*)

Boltzmann transport equation or atomistic phonon transport models including surface roughness and phonon–phonon scattering may be necessary in order to account for realistic density of states and nonequilibrium phonon transport, improving the accuracy of these predictions.

7 Conclusions

Density-functional tight-binding calculations and NEGF have been applied to the electron–phonon scattering and heat dissipation problem in a molecular junction. The calculations performed at atomistic scales serve as boundary condition to a drift-diffusion/Fourier model of charge and heat transport in the mesoscopic STM tip. The method can be seen as a first step towards a multiscale/multiphysics modeling of electrothermal coupling between molecular transport and heat dissipation in mesoscale continuum media. The calculations show that even at moderate applied biases, the STM tip apex can reach temperatures much larger than the environment. The model can be useful in future applications of molecular electronics devices.

References

1. Pecchia, A., Di Carlo, A.: Transport in nanoscale and molecular devices. Rep. Prog. Phys. **67**, 1497 (2004)
2. Auf der Maur, M., Penazzi, G., Romano, G., Sacconi, F., Pecchia, A., Di Carlo, A.: The multiscale paradigm in electronic device simulation. IEEE Trans. Elect. Dev. **58**, 1425 (2011)

3. Auf der Maur, M., Sacconi, F., Penazzi, G., Povolotskyi, M., Romano, G., Pecchia, A., Di Carlo, A.: Coupling atomistic and finite element approaches for the simulation of opto-electronic devices. Opt. Quant. Electron. **41** 671-679 (2010)

4. Ibe, J.P., Bey Jr., P.O., Brandow, S.L., Brizzolara, R.A., Burnham, N.A., Di Lella, D.P., Lee, K.P., Marrian, C.R.K., Colton, R.J.: On the electrochemical etching of tips for scanning tunneling microscopy. J. Vac. Sci. Technol. **A 8**, 3570 (1990)

5. Setvín, M., Javorský, J., Turčinková, D., Matolínová, I., Sobotík, P., Kocán, P., Ošt'ádal, I.: Ultrasharp tungsten tips, characterization and non destructive cleaning. Ultramicroscopy **113**, 152 (2012)

6. Gunnar Schulze, Elementary processes in single molecule devices: electronic transport and molecular isomerization. Doctoral Thesis (2009)

7. Elstner, M., Frauenheim, T., McKelvey, J., Seifert, G. (ed.): Special section: DFTB symposium - density functional tight binding: contributions from the American Chemical Society Symposium. J. Phys. Chem. A **111**, 5607–5944 (2007)

8. Pecchia, A., Penazzi, G., Salvucci, L., Di Carlo, A.: Non-equilibrium Green's functions in density functional tight binding: method and applications. New J. Phys. **10**, 065022 (2010)

9. Pecchia, A., Romano, G., Di Carlo, A.: Theory of heat dissipation in molecular electronics. Phys. Rev. B **75**(3), 035401 (2007)

10. Gagliardi, A., Romano, G., Pecchia, A., Di Carlo, A.: Simulation of inelastic scattering in molecular junctions: application to inelastic electron tunneling spectroscopy and dissipation effects. J. Comput. Theor. Nanosci. **7**, 2512–2526 (2010)

11. Jaklevic, R.C., Lambe, J.: Molecular vibration spectra by electron tunneling. Phys. Rev. Lett. **17,** 1139 (1966)

12. Romano, G., Gagliardi, A., Pecchia, A., Di Carlo, A.: Heating and cooling mechanisms in single-molecule junctions. Phys. Rev. B **81**, 115438 (2010)

13. Lü, X.: Thermal conductivity modeling of copper and tungsten damascene structures. J. Appl. Phys. **105**, 094301 (2009)

Part II
Molecule-Circuits

Classical Logic in a Single Molecule

Mohamed Hliwa and Christian Joachim

Abstract The mesh and node circuit rules required to design an intramolecular electronic circuit are discussed. Adapting a standard diode logic circuit structure, OR, AND and XOR unimolecular logic gates are designed. The full multichannel electronic scattering matrix of those molecule circuits are calculated using our EHMO-NESQC technique [1] in accordance with those new quantum circuit superposition rules [2] and taking into account the chemisorption of the molecule on the contacting pads at the end of the input branches. For a Molecule-XOR gate to work, a non-linear transduction effect was introduced using a semiclassical model [10, 11] to describe the inelastic coupling between the electron transfer process through the molecule-XOR and the soft molecule conformation mode used to generate the XOR truth table. The calculated logic surface is very close to the ideal XOR Boolean truth table. We also report another application of our node and mesh intramolecular circuit laws [2] in balancing a 4-branch molecule Wheatstone bridge.

M. Hliwa (✉)
Faculty of Sciences Ben M'Sik, University Hassan II-Mohammedia-Casablanca, BP 7955-Sidi Othman, Casablanca, Maroc. Nanoscience Groupe and MANA Satellite, CEMES/CNRS, 29 rue Jeanne Marvig, 31055, Toulouse, France
e-mail: hliwa@cemes.fr

C. Joachim
Nanoscience Groupe and MANA Satellite, CEMES/CNRS, 29 rue Jeanne Marvig, 31055, Toulouse, France
e-mail: joachim@cemes.fr

1   Introduction

The concept of hybrid molecular electronics was introduced by Aviram and Ratner [5] in the mid-1970s. In their approach, a Boolean logic circuit can be constructed by interconnecting together molecular devices such as molecular diodes, molecular switches or molecular transistors. By a molecular device, we mean here an electronic device made of one (or a small number) of molecules or macromolecules interacting with metallic nano-pads. The hardware which may result from this network of molecules and metallic nano-wires circuits was called "hybrid" because of the material difference between the organic molecules and the metal of the interconnections. To design those hybrid circuits, meshes and nodes electrical circuit, Kirchhoff laws are applicable when the length of each interconnect is larger than a few tens of nanometres, that is, when the phase of the electron wave functions circulating in the circuit is lost in between the molecular devices. This condition prohibits the development of hybrid molecular circuits whose dimensions are below a few nanometres per interconnects.

To circumvent this miniaturisation problem, Carter [7] suggested to incorporate the full circuit in a single molecule suppressing all the metallic wiring and interconnections. Since then, numerous monomolecular electronic circuits have been proposed reaching the large single-molecule Boolean binary adder [9]. These intramolecular circuits were designed assuming the validity of the Kirchhoff laws for the bonding in series and in parallel of molecular groups to form the intramolecular circuit. However, the standard electrical circuit Kirchhoff laws are not directly applicable along a single molecule [3]. To design intramolecular electronic circuits, we have first established the intramolecular circuit laws to be used [2] and then developed a new intramolecular circuit simulator software N-electrodes Elastic Scattering Quantum Chemistry (N-ESQC) [1] respecting the quantum physics laws driving the serial and parallel bonding of molecular chemical groups in an intramolecular circuit and of their valence electronic structures [2]. The primary purpose of our N-ESQC circuit simulator was to describe the tunnelling electron transport through the various branches of a monomolecular circuit connected externally to several metallic nano-pads. Using N-ESQC in its semiempirical EHMO version, simple prototype of molecule logic gates like "AND", "OR" and "XOR" were presented in [1, 10, 13, 14]. N-ESQC can also be used for the design of more complex electronic circuits such as a digital "half-Adder" or a "full-adder" integrated in a single molecule. The supporting surface of the full molecule circuit and its contacting metallic nano-pads can now be also described to take into account the surface leakage current [4].

In Sect. 2, the new intramolecular meshes and nodes circuit laws are recalled. Monomolecular circuits using a single intramolecular node and a variety of elementary Boolean molecule-logic gates built from them are discussed in Sect. 3. In Sect. 4, we present an application of those new circuit rules to balance a molecule 4-branch Wheatstone bridge which contains one mesh and four nodes.

2 Intramolecular Mesh and Node Circuit Rules

At low bias voltage and for any of the Fig. 1 molecule circuits, electrons are transferred through the molecular orbital tunnel paths offered by the conjugated branches of those intramolecular circuits. To a good approximation [12], the tunnel current intensity measured by an external macroscopic circuit connected to any combination of two electrodes i and j on the circuit is proportional to $\mid V_{ij} \mid^2$. This electronic coupling V_{ij} is introduced by the molecule itself between the selected i and j electrodes. With a molecule in the junction, V_{ij} is generally much larger than the direct through space electronic coupling between those i and j electrodes but with no molecules in this (i, j) tunnel junction. In some cases, a molecule can introduce specific electronic interference effects by its specific topology, chemical composition or molecular orbital structure. This will reduce the low voltage conductance of the tunnel junction as compared with its conductance with no molecule in the junction.

Let us now consider two molecular wires M_1 and M_2. Each one is able to introduce, respectively, an electronic coupling V_{ij_1} and V_{ij_2} when jumping over the $i - j$ tunnel junction (Fig. 2a). At small coupling, that is, for an electronic transparency of each individual molecular wire much lower than unity, the electronic coupling introduced between the i and j electrodes by the "in series" molecular wire $M_1 - M_2$ is $V_{ij,\text{series}} = k.V_{ij_1}.V_{ij_2}$ with k a normalisation factor (Fig. 1a). For two molecular wires bond in parallel, there are two different cases. When the nodes are on the metallic electrodes, each molecular wire brings its independent V_{ij} contribution to the inter-electrode electronic coupling (Fig. 1d). When the two nodes are part of the molecule and by using two other auxiliary molecular groups L_1 and L_2 connected each side to an electrode, the final electronic coupling to consider is the one introduced by the new molecule $L_1 - M_1 \parallel M_2 - L_2$. This new molecule creates two different tunnel paths: the $L_1 - M_1 - L_2$ path accounting for a V_{ij_1} electronic coupling and the $L_1 - M_2 - L_2$ path accounting for another V_{ij_2} electronic coupling between the two electrodes (Fig. 1b). In this case, the electronic coupling between electrodes i and j introduced by the complete $L_1 - M_1 \parallel M_2 - L_2$ molecule is simply $V_{ij,\text{para}} = V_{ij_1} + V_{ij_2}$ (Fig. 1b).

Starting from these three ways of superposing electronic couplings through molecule(s) and at small electronic coupling, the conductance G of a metal–molecule–metal tunnel junction is easily deduced from the proportionality between the current intensity and the square of the electronic coupling [12]. In series, for the $M_1 - M_2$ molecule, it comes $G \propto G_1.G_2$ with G_1 and G_2, respectively, the conductance of M_1 and M_2 groups measured separately. When two molecules M_1 and M_2 are connected in parallel to the two electrodes of the junction (Fig. 1c), the standard $G = G_1 + G_2$ resumes with some corrections depending on the adsorption distance between the two molecular wires M_1 and M_2 on the surface of the electrodes [16]. With a $L - M_1 \parallel M_2$ molecule where only the L to $M_1 \parallel M_2$ node belongs to the molecule (Fig. 1d), the standard $G = G_1 + G_2$ resumes taking into account each electron transfer path independently. Each path
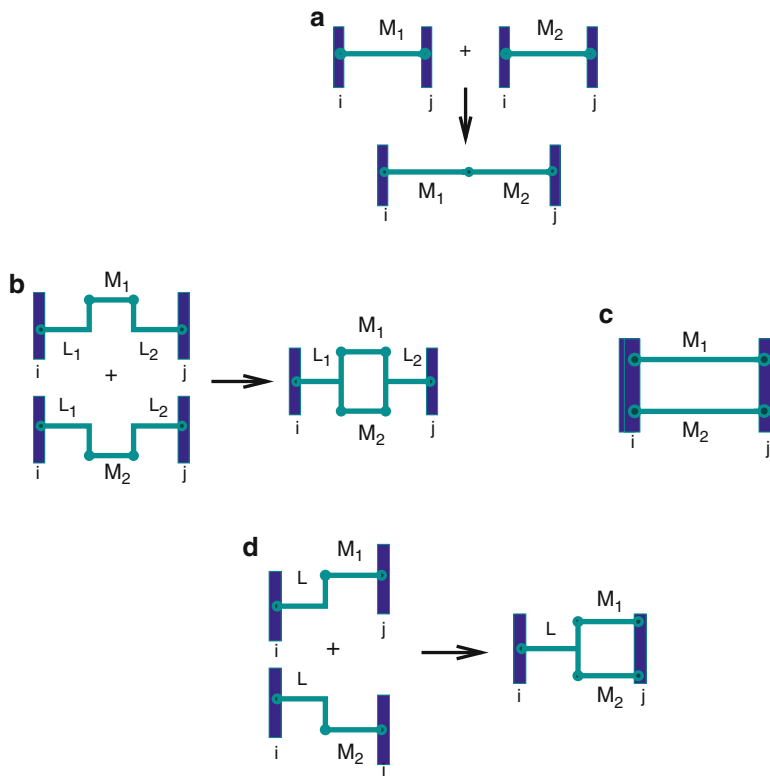
Fig. 1 Simple circuit diagrams of the different series and parallel association of molecular wires M_1 and M_2 discussed in the text. The two molecular wires are (**a**) bonded in series, (**b**) forming a single molecule with 2 intramolecular nodes, (**c**) connected in parallel on the metallic pads and (**d**) forming a single molecule with one intramolecular node

leads already a product of two conductances according to the series circuit law given above. There is here again a possible renormalisation depending on the adsorption distance between the two molecular wires M_1 and M_2 on the surface of the electrodes [1,3]. Finally, with a single $L_1 - M_1 \parallel M_2 - L_2$ molecule (Fig. 1b) where the two nodes L_1 to $M_1 \parallel M_2$ and $M_1 \parallel M_2$ to L_2 belong to the molecule, $G = G_1 + G_2 + 2\sqrt{G_1.G_2}$ with G_1 and G_2 the conductance of the $L_1 - M_1 - L_2$ and $L_1 - M_2 - L_2$ molecule taken separately [16]. This results comes from the fact that at low coupling, $G \propto | V_{ij,para} |^2 = | V_{ij_1} |^2 + | V_{ij_2} |^2 + 2V_{ij_1}V_{ij_2}$.

One interesting and simple example is the molecule circuit presented in Fig. 2 that is made of five molecular branches and interconnected only to two metallic electrodes. Its 2-terminal conductance can be calculated using the $N = 2$ version of EHMO N-ESQC [1]. As expected, there is a pronounced interference effect in the middle of the HOMO-LUMO gap of this 5-branch molecule (Fig. 2c). The overall electronic conductance of this molecule circuit can be calculated by decomposing
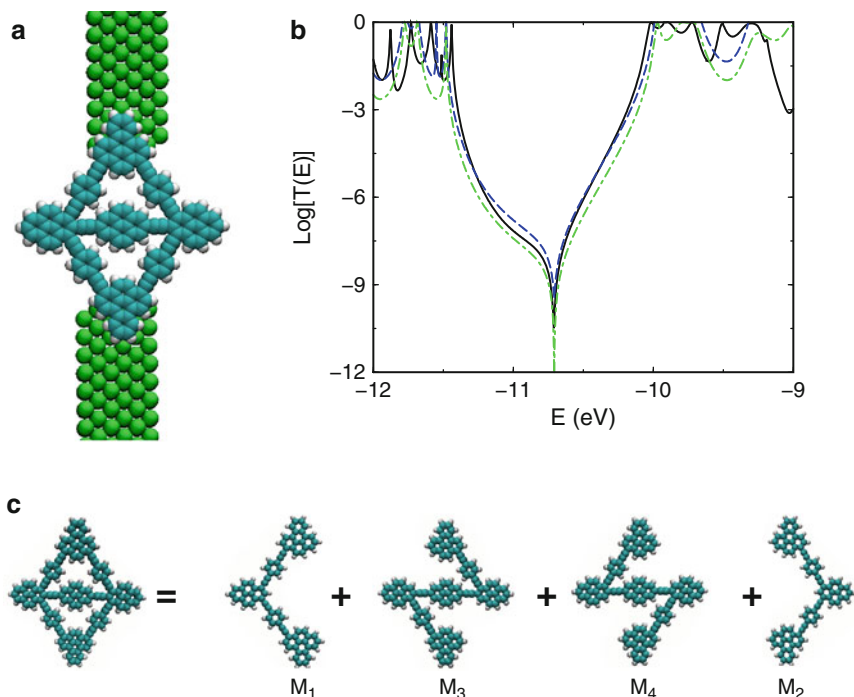
Fig. 2 The scattering properties of a 5 branches-4 electrodes molecular bridge. (**a**) The detail atomic structure of the molecule. A central perylene branch was included to mimic an internal measurement branch. (**b**) (Plain) is the EHMO-ESQC calculated $T_{12}(E)$ transmission coefficient and (*dashed*) the predicted $T_{12}(E)$ applying the intramolecular circuit rules discussed in this section for the 4 molecular fragments given in (**c**). (*Dash/point*) is the $T_{12}(E)$ variation for the single molecular branch as presented in the insert to show the origin of the destructive interference. (**c**) The (**a**) intramolecular circuit can be decomposed in 4 tunnelling paths to apply the parallel superposition rule and predict the transmission coefficient through the molecule in (**a**) and (**b**). Molecules 1 and 2 are for the contribution of two short tunnel paths and molecules 3 and 4 for the contribution of the two longer paths through the central perylene wire

this circuit in 4 molecular branches M_1, M_2, M_3 and M_4 (see Fig. 2) and by applying the intramolecular circuit rules given above to this decomposition. From nano-pad 1 to nano-pad 2, there are two left M_1 and right M_2 lateral branches with, respectively, a conductance G_1 and G_2 with $G_1 = G_2$ for a planar conformation. There are also two zigzag left M_4 and right M_3 branches via the central perylene molecular wires. They bring to the circuit, respectively, a conductance with $G_3 = G_4$ in a planar conformation. The conductance of each branch is calculated after its interconnection to the Fig. 2 metallic nano-pads using benzoperylene end groups for the chemisorption on each nano-pad. According to our circuit rules, one has to sum up the conductance of each branches to get the total conductance of this circuit. But the application of the series law indicates that G_4 and G_3 are much smaller than G_1 and G_2. Therefore, and as presented in Fig. 2b, the conductance of

this molecule circuit is simply $G_1 + G_2$ since the nodes of the superposition are in the electrodes. Using the $N = 2$ EHMO-ESQC technique, the energy dependent transmission coefficients $T(E)$ deduced from this rule are compared with the one of the complete molecule. There is almost no difference in the HOMO-LUMO gap of the different molecule paths. The destructive interference predicted for the total molecule circuit is still present with only the M_1 and M_2 branches in the junction. This discussion will be generalised below for the balancing rules of a single-molecule Wheatstone bridge.

## 3 Intramolecular Logic Circuit with Only One Node

The next step in intramolecular circuit theory is to connect a single-molecule circuit to three metallic nano-pads with a central molecular node where the three molecular branches M_1, M_2 and M_3 are converging and chemically bonded (see Fig. 3). A simple circuit is when those three branches are chemically the same using also a symmetric central node chemical group. In this case, the charge conservation occurs for the tunnelling transport resulting in an identical conductance for all the two terminal molecular tunnel junction that can be defined in the 3-terminal circuit [3] presented in Fig. 3. Of course, each elementary conductance depends on the chemical composition of the third branch.

3.1 Three-Branch Molecular Device

A very good example of a single-node three-branch molecule circuit is the dianthranaphtacene starphene molecule presented in Fig. 3 interacting with three metallic nano-pads. The Fig. 3c EHMO N-ESQC $T(E)$ transmission spectrum per tunnel junction looks like a standard conjugated molecule $T(E)$ with well identified tunnelling resonances. In the Fig. 3 circuit, the $T(E)$ spectra are all identical. One can notice a small deviation after the LUMO resonance due to a little asymmetry in the adsorption site between the three branches on the nano-pads [14].

3.2 Elementary Molecule Logic Gates

According to the Carter [7] and Mitre Corporation suggestions [9], Boolean logic functions may be embedded in a molecule circuit. It remains to apply the molecule circuit laws discussed above to design the corresponding molecules. From a topological point of view, a symmetric 2 input-1 output OR Boolean logic gate can be implemented by a 3-branch molecule circuit where each branch is connected to a common central node. Two branches must be chemically equivalent for the
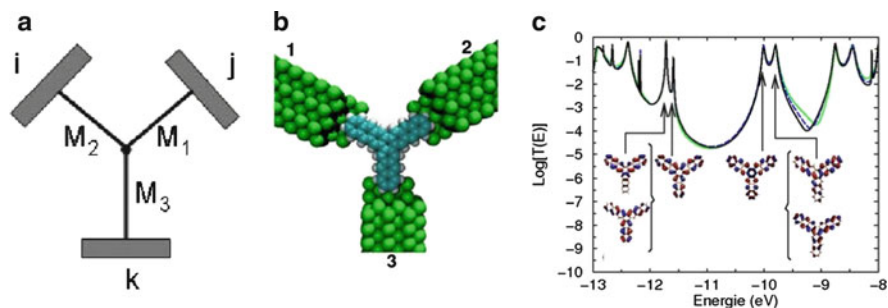
Fig. 3 The simple circuit diagram of a central molecular node connected to three nano-pads i, j and k. The three M_1, M_2, M_3 branches are forming with the central node a single molecule. (**a**) Schematic one-node circuit, (**b**) the 3-branch dianthra[a,c]naphthacene molecule circuit of D_{3h} symmetry formed by three anthracene fragments equivalently bond to a central phenyl node. The molecule is adsorbed by the 3-branch-ending phenyls above the Au nano-pads. (**b**) A semilogarithmic plot of the $T_{ij}(E)$ EHMO-NESQC electron transmission spectra (in valence energy range) per pair of branches. The presented frontier MOs show how the valence Π electrons are delocalized on the molecule. At resonances, this provides a good electronic conductance through each pair of molecular branches, almost one quantum of conductance

input channels of the gate and the third branch used for output measurement. This is exactly the Fig. 3 molecule circuit topology discussed above. Applying input voltages ($V_{\text{input}(1)}$, $V_{\text{input}(2)}$), a strong condition for an OR gate to work is that the tunnelling current coming from one of the input branch does not back flow through the other input branch. This condition imposes that the resistance from one-input branch to the other be larger than the circuit resistance from one input to the output. Since the 1950s, one design practice for Boolean diode logic is to insert a rectifier along each input branch as recalled in Fig. 1a. Such a circuit design is well-adapted to realise an "OR" gate with semiconductor devices where the input rectifiers are p-n junction diodes. The situation is different for a molecule circuit. In this case, quantum phenomena come into play. Consequently, the rectification effects provided by a single molecular diode, for example, a donor-acceptor-like molecule interconnected to 2 metallic nano-pads is strongly dependent on the chemical bond of this molecule with the others in the molecule circuit. The molecular diode characteristics, electronic states energy position and molecular orbital spatial expansion can be transformed by this chemical bonding through the central node chemical bond.

Of course, many authors [8, 9, 15, 17] have proposed molecular diodes based on the initial Aviram and Ratner design [5]. Here, the molecular diode is made by chemically bonding an electron-donor and an electron-acceptor fragments through an aliphatic organic chain essential to preserve the electronic structure of both partners. Recently, we have studied the conductance and the rectification properties of the Ratner-Aviram molecular rectifiers [1] and proposed shorter molecular diodes more adapted for the design of OR, AND and XOR Boolean logic gates molecule circuits [13].
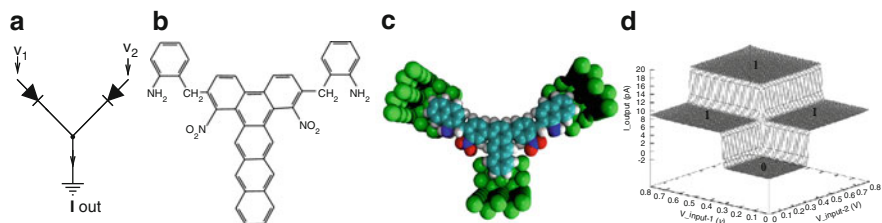
Fig. 4 Molecule-OR. (**a**) Schematic diode-based classical OR logic device, (**b**) chemical representation of a molecule-OR, (**c**) the equivalent 3-terminal monomolecular OR logic gate and (**d**) the corresponding $I_{\text{out}}(V_1, V_2)$ logic surface
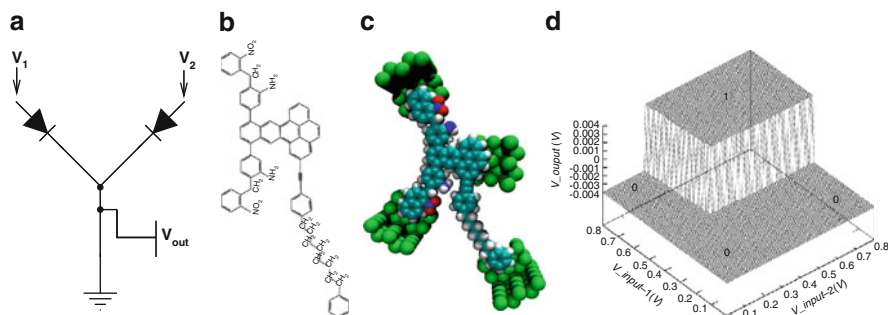
Fig. 5 Molecule-AND. (**a**) Schematic diode-based classical AND logic device, (**b**) chemical representation of a molecule-AND, (**c**) the equivalent 3-terminal monomolecular AND logic gate and (**d**) the corresponding $V_{\text{out}}(V_1, V_2)$ logic surface

The main results of these studies are, respectively, summarised in Figs. 4–6. In all those cases, the tunnelling electron transmission spectra between each pair of electrodes were calculated using EHMO N-ESQC technique. The output current intensity (or voltage) of each gate was calculated from the electron transmission spectra by using the multichannel Landauer-B*ü*ttiker formula [6] generalised to N-electrodes [3].

The rectifier based molecule-OR logic gate proposed in Fig. 4 contains a molecule-rectifier fragment per input branch composed of aminophenyl and nitro-phenyl groups bonded together by a methylene fragment ($C_6H_5NH_2 - CH_2 - C_6H_5NO_2$). Each rectifier end is interacting with an input metallic pad via a phenyl ring Π-chemisorbed 2.3 Å in height on the Au pad. The output branch of this gate is composed of an anthracene group. As presented in Fig. 4d, the superposition law of the tunnelling current through this molecule works perfectly as compared to an ideal OR logic surface. But from inside the molecule, there is no means to equalise the logical output level "1" resulting from one-input set at 0.3 V or two-input set also at 0.3 V. Such logical level equalisation will have to be performed outside the molecule-OR circuit.
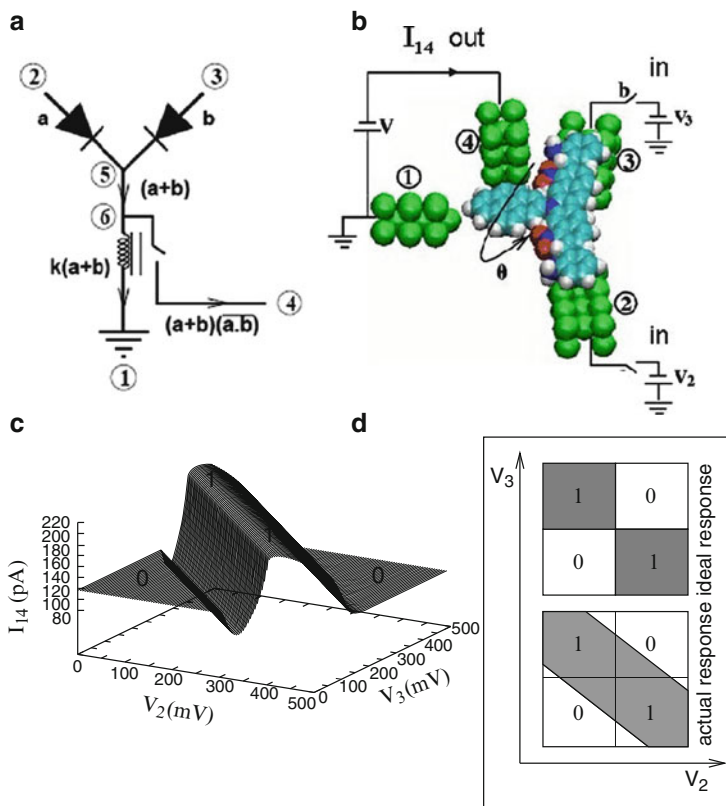
Fig. 6 (**a**) Schematic diode-based classical XOR logic device, (**b**) the equivalent 4-terminal molecule XOR logic gate, (**c**) the corresponding $I_{out}(V_1, V_2)$ logic surface and (**d**) a top point of view of ideal XOR logic response compared to the N-ESQC calculated one

The standard electrical circuit design of an AND logic gate uses also two semiconductor diodes, and a voltage drop is normally used to limit the current and stabilise the output voltage. For this purpose, and as presented in Fig. 5, those diodes are reverse connected in a classical AND logic circuit as compared to an OR circuit. But along a molecule circuit, there is no voltage drop defined. Fortunately, along a molecule logic gate circuit, the rectification does not depend on the spatial orientation of the molecular rectifier chemical groups but on the detail location of their HOMO and LUMO relative to the electrode Fermi level. For this reason, the input rectifier branches of the molecule-AND circuit (Fig. 5) have the same orientation as compared with the molecule-OR circuit (Fig. 4). With such a design, our molecule-AND gate works only in a voltage mode. Therefore, a fourth branch was added as compared to the molecule-OR for measuring the output potential relative to the grounded third branch. This lateral branch is composed of a long alkane chain embedded between two phenyl rings. The resulting molecule-AND $V_{out}(V_1, V_2)$ logic surface is close to the ideal one coming from a very precise tuning of the alkane chain length.
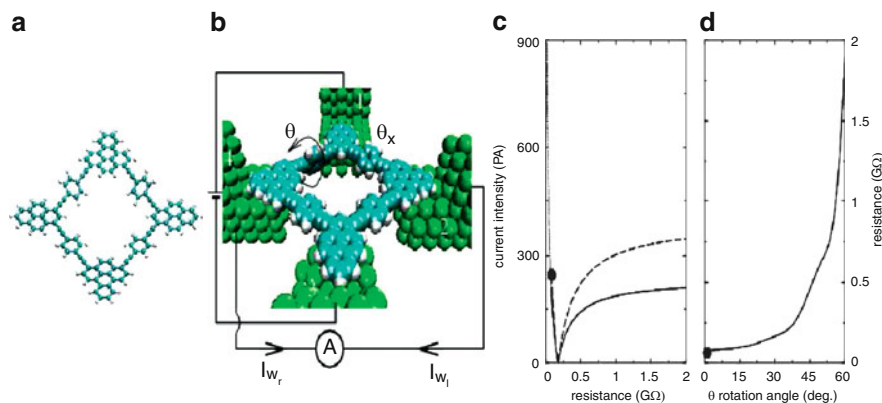
The Fig. 6b molecule performs a Boolean XOR function. In this design, the output circuit between the electrodes connected to the molecule-XOR branches 1 and 4 is independant of the molecule-OR like part of this molecule circuit which includes the two-input branches. Under an intramolecular tunnel inelastic effect, the conformation of this molecule-OR part is changing. This change is detected by the fourth lateral electrode external circuit because of the rotation of the pyrene group induced by the inelastic effect acting of the soft mode of this conformation change. A semiclassical model can be used to describe this intramolecular transduction effect between the electron transferred through the molecule and its conformation change [10, 11]. The full multichannel scattering matrix of the molecule-XOR was calculated taking into account the chemisorption of the device at the end of the input branches and the detail mechanics of the conformation change of this molecule. It results a non-linear transduction effect between the inputs and the output current for a range of tunnel current intensity of interest to monomolecular electronics. The "0" logical output is corresponding to an I_{14} current around 100 pA for an output circuit bias voltage of $V = 100$ mV. The "1" logical output plateau is large enough to stabilise a I_{14} current around 220 pA also for $V = 100$ mV. The difference between the "0" and "1" is large enough to be detectable. But as presented in the Fig. 6d, our design deforms the ideal XOR response logic surface in a way that the noise immunity of the molecule-XOR gate can compromise the viability of our design, especially for the "0" inputs.

4   Balancing 4-Branch Wheatstone Bridge

One of the interesting applications of the mesh and node intramolecular circuit rules is the well-known problem in electrical circuit theory of balancing a Wheatstone bridge. In Fig. 7, a molecule-Wheatstone bridge circuit is presented composed of a loop of 4 tolane molecular wires bonded via benzopyrene end groups to the metallic nano-pads 1 and 3 and via pyrene end group to the metallic nano-pads 2 and 4. This 4-electrode and 4-branch molecule circuit is connected to a voltage source V and to an amperemeter A.

Like in any Wheatstone bridge problem, one phenyl of the tolane molecular bridge is rotated by an angle $\theta_x = 30$. It plays the role of the unknown resistance to be determined after a good balancing of the bridge. In Fig. 7, this phenyl rotation corresponds to a branch resistance of $R_x = 175 M\Omega$ [2]. Here, all the resistance are defined by the junction resistances: R_x for the 1-2 molecular wire tunnel junction, R_{23} for the 2-3 one, R_{34} for the 3-4 one and R_θ for the 4-1 one. Notice that for the chosen Fig. 7 molecule circuit, the R_{23} and R_{34} minimum value is 78 $M\Omega$ while keeping their planar phenyl conformation.

By definition, the molecule Wheatstone bridge is balanced when the tunnelling current intensity I_w measured by the amperemeter A in Fig. 7b reaches zero. For the supposed unknown θ_x value, the balancing will be obtained by rotating another

Fig. 7 (**a**) A 4-branch Wheatstone bridge molecule. (**c**) The variation of the balancing tunnelling current of the 4-branch-4-electrode molecule Wheatstone bridge connected as presented in (**b**). In (**c**), (*dashed*) is for the current intensity I_w (in absolute value) measured by the amperemeter A and deduced from the standard Kirchhoff laws calculating each molecular wire tunnelling junction resistance of the bridge one after the other from the EHMO-ESQC technique. In (**c**), (plain) is the same tunnel current intensity but obtained with the new intramolecular circuit rules discussed in Sect. 2. (**d**) is the resistance of the branch used to balance the bridge as a function of its rotation angle. The minimum accessible resistance by rotation is 78 $M\Omega$ for the short tolane molecular wire used here (**b**)

phenyl of the molecule bridge by an angle θ. Following the standard Kirchhoff mesh and node laws, this balancing would be reached respecting the *"balancing equality"*: $R_\theta.R_{23} = R_x.R_{34}$.[2]. Following this standard electrical circuit calculations, the I_w variations as a function of R_θ are obtained using the standard expression of the central branch current intensity of a Wheatstone bridge with no resistance in this branch [2]. On Fig. 7b, this corresponds to the external amperemeter branch. The result is presented in Fig. 7c, and the balancing of the bridge would be obtained when $R_\theta = R_x$.

But the basic behind the above-mentioned *"balancing equality"* and behind the standard calculation for I_w is that, for example, two resistances in series add up as given by the standard Kirchhoff law. But as discussed above, this is not the case in a molecule circuit where now two resistances in series multiply up. Therefore, the current intensity from electrode 1 to electrode 3 is too small as compared to the one from electrode 1 to electrode 4. As a consequence and since I_w is measured outside the molecule bridge by the classical amperemeter A, I_w is simply the superposition of 2 tunnel currents I_{wl} and I_{wr} with $I_w = I_{wl} - I_{wr}$. Because the molecular junctions 1-4 and 2-3 are connected in series via a metallic wire under a Boltzmann regime of transport, it comes $I_{wl} = V/(R_\theta + R_{23})$ and also $I_{wr} = V/(R_x + R_{34})$.

Therefore, the balancing condition of the bridge becomes $R_\theta + R_{23} = R_x + R_{34}$. Interestingly, our molecule bridge is still balanced for $R_\theta = R_x$. But as presented in Fig. 7d, the I_w variations as a function of R_θ are different with our molecule circuit

rules as compared to the Kirchhoff circuit laws. Notice also that the conformation variations used to balance our molecule bridge do not permit to explore R_θ values below the planar conformation one. This restricts the exploration of the possible I_w intensity as presented in Fig. 7.

5   Conclusion

Different from the well-known G. Kirchhoff electrical circuit laws, the mesh and node laws for molecule circuits have been discussed. On simple examples, we have demonstrated how those laws are well-adapted for intramolecular tunnelling electronic circuits design like Boolean molecule logic gate circuits. Those molecule circuits are smaller than the ones proposed by many authors in the past [5,7,9,17]. Furthermore, we can now design molecule logic gates where the output current intensity is of order of a few ten of nA for input bias voltage of 100 mV. However, this improvement is not sufficient for integrating elementary logic gates inside a more complex molecule logic circuit with the objective to obtain again measurable output current intensities. Inside a molecule logic circuit, an electronic functional molecular group (resistance, rectifier, elementary logic gate, etc.) can play its assigned role when it is electronically relatively decoupled from the others of the same circuit. This can be achieved by inserting saturated aliphatic chains in between these functional groups or by twisting the different part of the molecule circuit. But this electronic separation goes against the necessity of a selective delocalization among the different branches of the molecule circuit to obtain a very large output current intensity. The electronic interactions between the molecular orbitals localised on the various parts (rectifiers, branches, etc.) of the molecule circuit lead to interference phenomena, resonances and transmission peak overlapping in the valence molecular orbital region of the electronic spectrum associated to the global circuit. This modifies in a drastic way the electronic behaviour of the individual functional group in the molecule circuit. Finally, the intensity of the output current does not only depend on properties of neighbourhood and on the electron cloud overlapping in between the individual functional groups. It also depends on the electronic interaction of the total molecule circuit with its multiple contacting metallic nano-pads and on the interactions of this molecule circuit with the supporting surface.

References

1. Ami, S., Hliwa, M., Joachim, C.: Molecular OR and AND logic gates integrated in a single molecule. Chem. Phys. Lett. **367**, 662 (2003a)
2. Ami, S., Hliwa, M., Joachim, C.: Balancing a four branch-single-molecule nanoscale Wheatstone bridge. Nanotechnology **14**, 283 (2003b)
3. Ami, S., Joachim, C.: Intramolecular circuits connected to N electrodes using a scattering matrix approach. Phys. Rev. B **65**, 155419 (2002)

4. Ample, F., Duchemin, I., Hliwa, M., Joachim, C.: Single OR-molecule and OR atomic circuit logic gates interconnected on Si(100)H surface. J. Phys. Condens. Matter. **23**, 125303 (2011)
5. Aviram, A., Ratner, M.A.: Molecular rectifiers. Chem. Phys. Lett. **29**, 277 (1974)
6. Büttiker, M., Imry, Y., Landauer, R., Pinhas, S.: Generalized many channel conductance formula with application to small rings. Phys. Rev. B **31**, 6207 (1985)
7. Carter, F.L.: The molecular device computer: point of departure for large scale cellular automata. Physica D **10**, 175 (1984)
8. Chen, J., Wang, W., Reed, M.A., Rawlett, A.M., Price, D.W., Tour, J.M.: Room-temperature negative differential resistance in nanoscale molecular junctions. Appl. Phys. Lett. **77**, 1224 (2000)
9. Ellenbogen, J.C., Love, J.C.: Architectures for molecular electronic computers. I. Logic structures and an adder designed from molecular electronic diodes. IEEE **88**, 386 (2000)
10. Hliwa, M., Ami, S., Joachim, C.: A 3-terminal single molecule nanoscale amperometer. Chem. Phys. Lett. **425**, 356 (2006)
11. Hliwa, M., Joachim, C.: Tunnel heating of a single Xe adsorbate. Phys. Rev. B **65**, 085406 (2002)
12. Joachim, C., Gimzewski, J.K., Aviram, A.: Electronics using hybrid-molecular and mono-molecular devices. Nature **408**, 541 (2000)
13. Jlidat, N., Hliwa, M., Joachim, C.: A semi-classical XOR logic gate integrated in a single molecule. Chem. Phys. Lett. **451**, 270 (2008)
14. Jlidat, N., Hliwa, M., Joachim, C.: A molecule OR logic gate with no molecular rectifier. Chem. Phys. Lett. **470**, 275 (2009)
15. Krzeminski, C., Delerue, C., Allan, G., Vuillaume, D., Metzger, R.M.: Theory of rectification in molecular monolayer. Phys. Rev. B **64**, 085405 (2001)
16. Magoga, M., Joachim, C.: Conductance of molecular wires connected or bonded in parallel. Phys. Rev. B **59**, 16011 (1999)
17. Metzger, R.M., Xu, T., Peterson, I.R.: Electrical rectification by a monolayer of hexade-cylquinolinium tricyanoquinodimethanide measured between macroscopic Gold electrodes. J. Phys. Chem. B **105**, 7280 (2001)

Modeling and Simulation of Electron Transport at the Nanoscale: Illustrations in Low-Dimensional Carbon Nanostructures

Vincent Meunier, Eduardo Costa Girão, and Bobby G. Sumpter

Abstract This chapter showcases selected illustrations of various manifestations of nanoscale and molecular electronic effects as investigated by quantum mechanical methods. The examples include results demonstrating (1) how graphitic nanoribbons can be assembled into multiterminal networks and the influence on electron transport; (2) how the position of a single embedded molecule can be modified to change the overall conduction state of a nanowire; (3) how carbon nanotubes can be assembled into complex covalent arrays and how these can be obtained experimentally; (4) how quantum interference can be understood as emerging from the presence of multiple levels of confinements in carbon nanorings; (5) how new functionality emerges at the nanoscale due to the interplay of magnetic, electronic, and structural properties of individual graphitic nanoribbons assembled into wiggle-like structures; and (6) how quantum chemical modeling can lead to the design of electrodes with enhanced interfaces for molecular coupling.

1 Introduction

The unification of scalable mathematical algorithms, novel electronic structure methods, advanced computing tools, and petascale computational performance have enabled the development of predictive tools for the discovery of novel phenomena

V. Meunier (✉)
Rensselaer Polytechnic Institute, Troy, NY, USA
e-mail: meuniv@rpi.edu

E.C. Girão
Departamento de Física, Universidade Federal do Piauí, CEP 64049-550, Teresina, Piauí, Brazil
e-mail: edu@fisica.ufc.br

B.G. Sumpter
Oak Ridge National Laboratory, Oak Ridge, TN, USA
e-mail: sumpterbg@ornl.gov

and principles for the design of new molecular electronics with breakthrough properties. Theoretical methods have now evolved to a point where the properties of materials can be successfully predicted based essentially on their atomic structure and with limited or no experimental input. As a consequence, computational sciences capabilities can substantially speed up the search for novel materials and devices, especially when theoretical work proceeds in parallel and in collaboration with strong experimental efforts. In this chapter we review our recent progress in describing electron transport at the nanoscale and how this work provides unique physicochemical insight that is applicable to the development of novel materials and devices. Indeed, detailed understanding of how quantum mechanical effects impact electron transport and other electronic processes within nanostructures and across interfaces is critical for enabling new innovations.

2 Electronic Transport at the Nanoscale

When describing electronic transport at the nanoscale, the device's size is smaller than the phase coherence length and quantum interference effects become prominent, demanding a full departure from the macroscopic description of Ohm's law. In a perfect crystalline system such as a pristine nanotube, for instance, electrons do not suffer phase-breaking collisions, thereby marking the onset of ballistic transport. When we relax the defect-free assumption, electrons traveling through the system experience scattering events, thereby increasing the probability for electrons to not be transmitted. These quantum mechanical aspects are captured by the Landauer formalism, which states the following for the conductance between two terminals n and m in the low bias and zero temperature limits [4]:

$$G^{n \to m} = \frac{2e^2}{h} T^{n \to m}. \tag{1}$$

This result expresses the essence of the formalism, namely, "conductance G is transmission probability T." Landauer's theory is frequently used for computing electronic transport properties of nanoscale systems within the framework of Green's function (GF) formalism.

The basic system under consideration in the problem of electronic transport at the nanoscale is the one composed by a central scattering region ($\mathscr{C}$) in contact with a number (N) of semi-infinite terminals ($\mathscr{L}_l, l = 1, 2, \ldots, N$) as depicted in Fig. 1. Each terminal is built from the repetition of a characteristic unit along a specific (periodic) direction. In practice, it is typical to employ the tight-binding approach where the principal layer (PL) of each electrode is defined so as to interact only with the first-neighbor cells. This allows one to write the problem in a convenient, numerically solvable way. Even though the Hamiltonian of any extended open system is infinite and nonperiodic, we can still treat the conductor's GF (G_C) in terms of a modified Hamiltonian representing the central conductor:

Fig. 1 Basic system for electronic transport calculations. A central scattering region $\mathscr{C}$ coupled to the semi-infinite terminals $\mathscr{L}_1, \mathscr{L}_2, \mathscr{L}_3, \mathscr{L}_4, \ldots, \mathscr{L}_N$
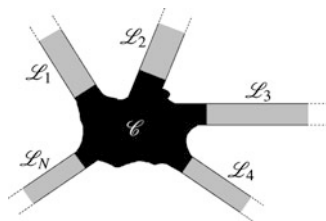
$$G_C = \left((E \pm i\eta)I_C - H_C - \sum_l \Sigma_l \right)^{-1}, \quad \Sigma_l = h_{Cl} g_l h_{lC}, \quad g_l = (\epsilon I_l - H_l)^{-1},$$

(2)

where $\eta \to 0^+$ is a small complex number added to (subtracted from) the energy to avoid singularities in the calculation of the retarded (advanced) GF. Here, H_C (H_l) [h_{Cl} and h_{lC}] is the tight-binding Hamiltonian describing $\mathscr{C}$ ($\mathscr{L}_l$) [the interaction between $\mathscr{C}$ and $\mathscr{L}_l$], and the so-called self-energy matrices (Σ_l) can be interpreted as effective potentials which formally describe the effects of the semi-infinite terminals on $\mathscr{C}$. In other words, the sum of the H_C Hamiltonian with the self-energies represents a finite central conductor satisfying the boundary conditions corresponding to the extended system [4]. Even though the Σ_l terms still depend on infinite matrices, we can write them in terms of finite matrices describing the interface between $\mathscr{C}$ and the first PL from $\mathscr{L}_l$ and determine them by recursive methods [14]. Finally, the quantum transmission is obtained by [4]

$$T^{n \to m} = \text{Tr}(\Gamma_n G_C^r \Gamma_m G_C^a), \quad \Gamma_l = i(\Sigma_l - \Sigma_l^\dagger).$$

(3)

3 Applications

Exploration of how electrons are transported through materials at the nanoscale and the influence of quantum confinement, defects, and interfacial interactions are critical for developing the next generation of materials and electronic devices. Indeed this general topic was recently identified as one of the five basic grand challenges for science and engineering [7]. Below, we highlight some recent examples of calculations showing novel results and promising behaviors.

3.1 Multiterminal GNR Junctions (Fig. 2)

The system in Fig. 2a is a 60° in-plane junction between two zigzag-edged nanoribbons [1]. The asymmetry brought about by the antiferromagnetic ground
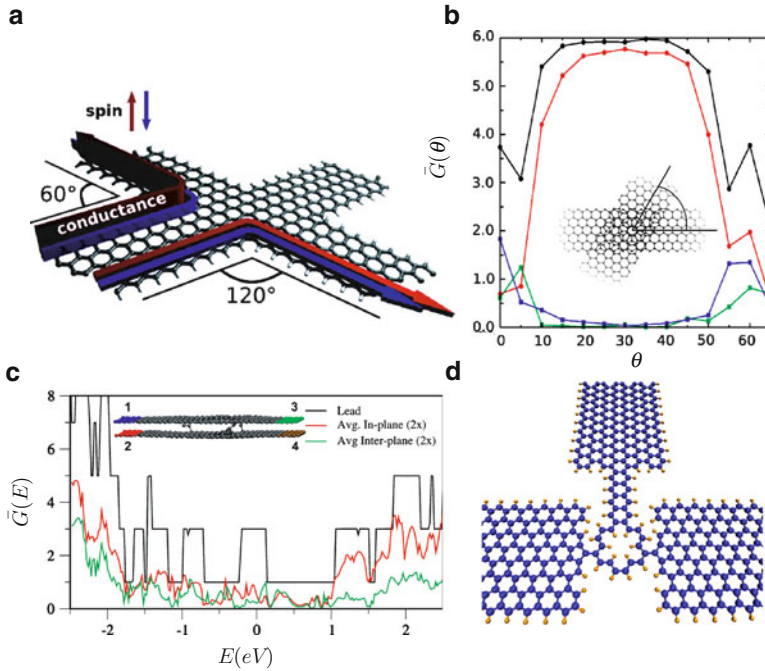
Fig. 2 Four different ways to create multiple graphitic nanoribbon (GNR) junctions

state in the zigzag GNR leads the spin channels to proceed in different directions along the arms of the junction. The plot reproduced in Fig. 2b is the result of a tight-binding calculation showing electron transmission in an out-of-plane junction between 15 nm wide armchair and zigzag nanoribbons. The two structures are bound by weak van der Waals interactions, making it possible for the device to operate as a switch or rheostat. The black (red) curve corresponds to the in-plane transmission probability measured at 0.5 (−0.5) V. The blue (green) curve represents the conductance across the junction at 0.5 (−0.5) V. The significant conductance difference could be exploited for switching applications [1]. Figure 2c is a representation of a covalent junction between two parallel zigzag GNRs. The cross-links are induced by electronic irradiations such as those experienced by carbon nanostructures observed under a high-resolution transmission electron microscope. The irreversible transformation is shown to cause significant out-of-plane electron transmission, indicating possible applications for stable information storage [3]. Three-terminal GNR arrangements where cross-linking is ensured by small carbon-rich chains are shown in Fig. 2d. This setup is well-suited for the investigation of electronic interference effects between wave packets originating from two different electrodes and collected at the third [13].

Fig. 3 Carbon
nanotube-based nonvolatile
memory elements
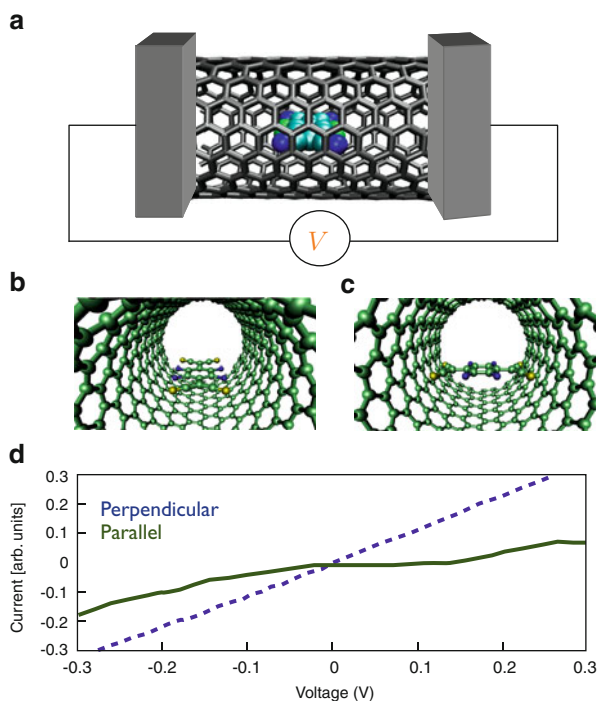
3.2 Nonvolatile Memory Elements (Fig. 3)

Carbon nanotubes have been shown to allow for the facile absorption of small organic molecules inside their inner core, and the resulting self-assembly of basic low-dimensional structures can lead to interesting nanotechnological applications. Figure 3a is a schematic representation of a nonvolatile memory device design where single bits of information are stored in the position of a single molecule (TCNQ) relative to the host nanotube container. Large-scale quantum chemistry calculations were employed to demonstrate that when a molecule is associated with a carbon nanotube of appropriate diameter, the flat molecule can assume a number of metastable positions relative to the nanotube walls. Here, Fig. 3b, c represent parallel and perpendicular arrangements corresponding to two local minima on the absorption energy surface of the system. The converged Fock matrix expressed in the localized basis employed in the quantum chemistry calculations is recast into an open-system configuration, allowing for computing transport properties, shown in Fig. 3d. The important result here is that the two stable positions depicted in Fig. 3b, c have very distinct conductivity, thereby leading to a way to *read* the ON and OFF states. Writing information can be achieved by a number of electromechanical approaches, such as the application of time-dependent electric field or by applying a radial strain to the nanotube wall [9].
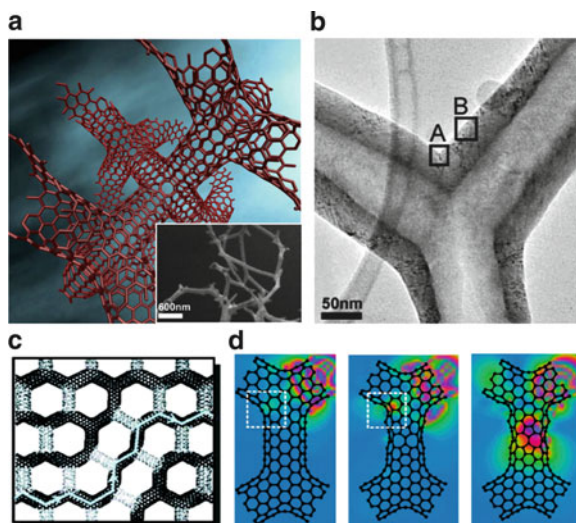
3.3 Carbon Nanotube Covalent Networks (Fig. 4)

Figure 4a is a ball-and-sticks representation of a super-diamond three-dimensional crystal structure where each carbon nanotube is crystallographically equivalent to a C–C bond in the conventional diamond structure [11]. The resulting system possesses a large number of pores, corresponding to a topological structure with a large genus. The high genus can be accounted for by the insertion of heptagonal and octagonal carbon nanorings, located at the junction. The insert of panel a in Fig. 4 shows the experimental evidence of a possible method to create such complex networks during growth using a small amount of sulfur in the precursor to induce the formation of multiple junctions [10]. The close-up view of sulfur-induced junction in Fig. 4b shows a three-terminal carbon fiber. Such networks have high potential for nanocircuit design, including logical operations and memory storage. Figure 4c shows that structural changes (bond rotations) within the branches of this type of network (a two-dimensional super-graphene network is illustrated here) control the electronic flow along predetermined paths [12]. This concept was demonstrated theoretically using a tight-binding based scattering approach (Fig. 4d) where an incoming electronic wave packet is found to bounce on the defects and, instead of being reflected back into the source (top right), is reinjected along a different path (top left).

3.4 Nanotori: From Two Dimensions to Zero Dimension (Fig. 5)

Figure 5a illustrates the different levels of quantum confinements from two dimensions (graphene) to zero dimension (nanotorus) in carbon nanostructures.

Fig. 5 Quantum mechanical
interferences in carbon
nanotori
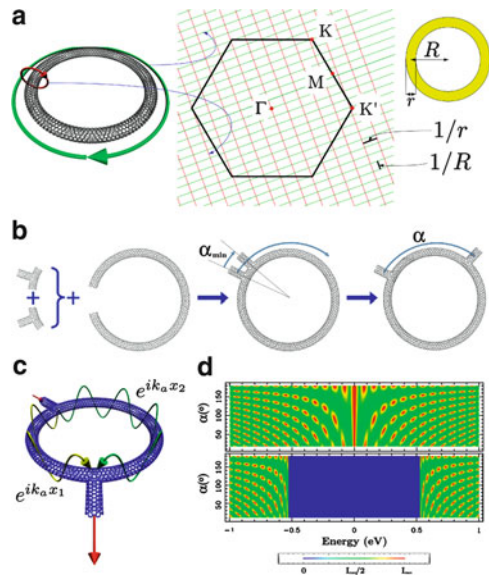
The confinement is best illustrated on its effect in the Brillouin zone (central panel) where we show cutting lines induced by cyclic boundary conditions imposed by wrapping graphene along a chiral vector to form a carbon nanotube (separation $\sim 1/r$) and a carbon nanotorus (separation $\sim 1/R$) where r and R are the nanotube and torus radii, respectively. Note that $R >> r$ and the relative separations between the two sets of lines are not at scale. Figure 5b shows how electrodes are inserted into the carbon nanoring to effectively create an interface between the nanotube system and external electrodes. The relative angle α is in principle arbitrary, as long as the electrode can be inserted into the nanoring lattice and can be quasi-continuously varied around the torus [6]. In order to guarantee that each carbon atom remains connected to three other carbon atoms, heptagonal and pentagonal defects are included at the joints. Note that the system shown here has a genus $g = 2$, therefore requiring the presence of a total of 12 more heptagons than pentagons, all located at the junction with the electrodes (similar effects can be achieved with higher order rings, such as octagons). Figures 5c, d show the interference patterns due to the electronic wave traveling along the two nonequivalent paths of the torus (i.e., clockwise and counterclockwise), as illustrated in Fig. 5c by green and yellow wavy lines, respectively. Figure 5d shows the resulting interference pattern in the conductance for a metallic system (top) and semiconducting one (bottom). The latter is marked by a ~ 1 eV gap around the Fermi energy located at $E = 0$.

3.5 Graphitic Nanowiggles, GNWs (Fig. 6)

GNWs can be obtained by regularly combining GNRs of different edge geometries, leading to possible armchair–armchair (AA), armchair–zigzag (AZ),

Fig. 6 Seamless junctions between graphitic nanoribbons assembled into ordered one-dimensional systems: the case of graphitic nanowiggles (GNWs)

	AFM	TAFM	LAFM	FM	PM
Δ_{min}^{AZ} (meV)	183	22	7	0	0
Δ_{max}^{AZ} (meV)	446	396	428	347	393
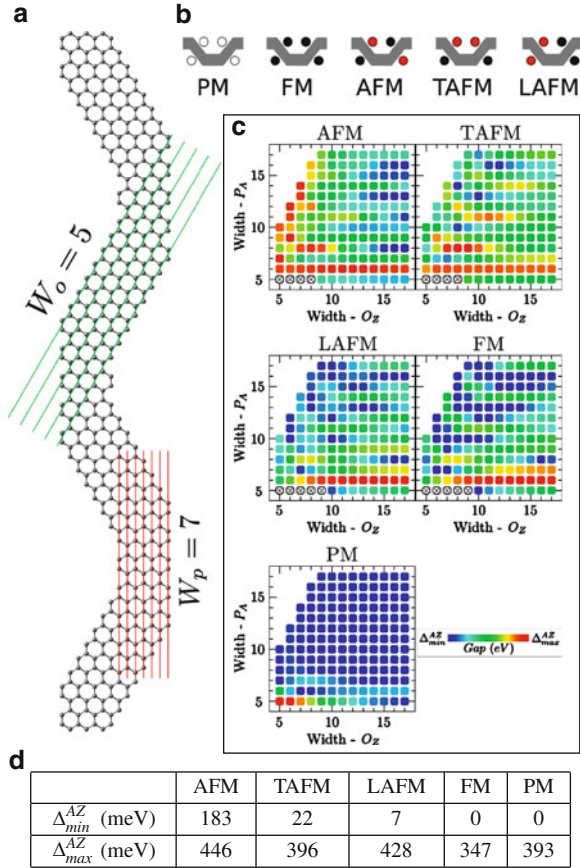
zigzag-armchair (ZA), and zigzag–zigzag (ZZ) systems with atypical electronic, structural, and magnetic properties [2]. Figure 6 illustrates the unusual physics of the AZ nanowiggles. A sketch of the $(7, 5)_{AZ}$ is shown in Fig. 6a, where the numbers used to determine the geometry correspond to the number of parallel (W_p) and oblique (W_o) lines with respect to the periodic direction. Figure 6b illustrates the possible magnetic states that such a multi-domain system can assume (the red and black dots represent spin up and down, respectively). The magnetic properties are dominated by spin distributions located essentially at the zigzag edges. The spins organize in a ferromagnetic manner along the edge of a given domain. However, similar to zigzag GNRs, the electronic ground state corresponds to an AFM arrangement where spins in opposite edges are flipped with respect to one another. Using a tight-binding + Hubbard model (parametrized on DFT calculations) [15], we established a systematic relationship between the electronic bandgap and the atomic structure for a series of structures in their various metastable magnetic states (Fig. 6c, with the range of color scales provided in Fig. 6d). The bandgap of the
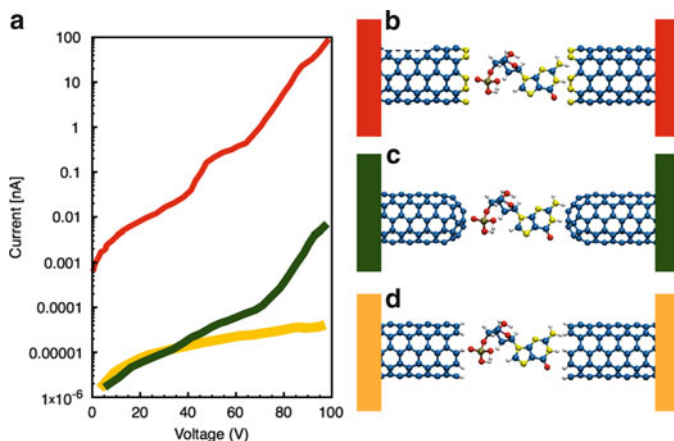
Fig. 7 Example of electronic transport calculations using quantum chemistry calculations to determine the Hamiltonian matrices required to recast a finite-size problem into an open system, within density functional theory

structure is found to vary over a wide range, indicating the possibility of devising optoelectronic and spintronic devices with tailored properties [5].

3.6 Transport Measurements in Modified Molecular Interfaces (Fig. 7)

The objective of the study depicted in Fig. 7 is to demonstrate that molecule-electrode coupling can be enhanced by a proper choice of chemical environment at the interface. Shown in Fig. 7a are the I–V curves for a Guanine molecule sandwiched between three types of carbon nanotube-based electrodes. Ball-and-sticks representations in Fig. 7b–d correspond to nitrogen-terminated, carbon-capped, and hydrogen-terminated end saturations. Here, carbon, nitrogen, oxygen, hydrogen, and phosphorus are shown in blue, yellow, red, white, and gold, respectively. The presence of nitrogen greatly enhances the signal measurable in such a setup as a result of better matched electronic molecular states at the interface. Similar results were found for adenine, thymine, and cytosine [8].

4 Conclusions

Modern theoretical and computational science provides opportunities to explore physics and chemistry at the length and time scales where the material properties and behavior are controlled and is thereby a "key" to performing predictive design.

In this chapter we have reviewed recent work in nanoscale electron transport that has delivered new understanding that can be useful for novel electronic devices and mesoscale materials design, such as nonvolatile memory at the single molecule level (Fig. 3), spin filters, spintronics and magnetics (Figs. 2 and 6), smart networks (Figs. 4 and 5), and DNA sequencing (Fig. 7).

References

1. Botello-Mendez, A.R., Cruz-Silva, E., Romo-Herrera, J.M., Lopez-Urias, F., Terrones, M., Sumpter, B.G., Terrones, H., Charlier, J.C., Meunier, V.: Quantum transport in graphene nanonetworks. Nano Lett. **11**(8), 3058–3064 (2011)
2. Cai, J., Ruffieux, P., Jaafar, R., Bieri, M., Braun, T., Blankenburg, S., Muoth, M., Seitsonen, A.P., Saleh, M., Feng, X., Muellen, K., Fasel, R.: Atomically precise bottom-up fabrication of graphene nanoribbons. Nature **466**(7305), 470–473 (2010)
3. Cruz-Silva, E., Botello-Mendez, A.R., Barnett, Z.M., Jia, X., Dresselhaus, M.S., Terrones, H., Terrones, M., Sumpter, B.G., Meunier, V.: Controlling edge morphology in graphene layers using electron irradiation: from sharp atomic edges to coalesced layers forming loops. Phys. Rev. Lett. **105**(4) (2010). DOI 10.1103/PhysRevLett.105.045501
4. Datta, S.: Quantum Transport: Atom to Transistor. Cambridge University Press, Cambridge (2005)
5. Girão, E.C., Liang, L., Cruz-Silva, E., Souza Filho, A.G., Meunier, V.: Emergence of atypical properties in assembled graphene nanoribbons. Phys. Rev. Lett. **107**, 135501 (2011)
6. Girao, E.C., Souza Filho, A.G., Meunier, V.: Electronic transmission selectivity in multiterminal graphitic nanorings. Appl. Phys. Lett. **98**(11), 112111 (2011)
7. Hemminger, J., Fleming, G., Ratner, M.: Directing matter and energy: five challenges for science and the imagination; US-DOE (2007). DOI 10.21727935427
8. Meunier, V., Krstic, P.S.: Enhancement of the transverse conductance in DNA nucleotides. J. Chem. Phys. **128**(4) (2008)(2008). DOI 10.1063/1.2835350
9. Meunier, V., Kalinin, S.V., Sumpter, B.G.: Nonvolatile memory elements based on the intercalation of organic molecules inside carbon nanotubes. Phys. Rev. Lett. **98**(5) (2007). DOI 10.1103/PhysRevLett.98.056401
10. Romo-Herrera, J.M., Sumpter, B.G., Cullen, D.A., Terrones, H., Cruz-Silva, E., Smith, D.J., Meunier, V., Terrones, M.: An atomistic branching mechanism for carbon nanotubes: sulfur as the triggering agent. Ang. Chem. Int. Ed. **47**(16), 2948–2953 (2008). DOI 10.1002/anie.200705053
11. Romo-Herrera, J.M., Terrones, M., Terrones, H., Dag, S., Meunier, V.: Covalent 2d and 3d networks from 1D nanostructures: designing new materials. Nano Lett. **7**(3), 570–576 (2007)
12. Romo-Herrera, J.M., Terrones, M., Terrones, H., Meunier, V.: Guiding electrical current in nanotube circuits using structural defects. ACS Nano **2**(12), 2585 (2008)

13. Saha, K.K., Nikolic, B.K., Meunier, V., Lu, W., Bernholc, J.: Quantum-interference-controlled three-terminal molecular transistors based on a single ring-shaped molecule connected to graphene nanoribbon electrodes. Phys. Rev. Lett. **105**(23) (2010). DOI 10.1103/PhysRevLett. 105.236803
14. Sancho, M.P.L., Sancho, J.M.L., Rubio, J.: Highly convergent schemes for the calculation of bulk and surface green-functions. J. Phys. F-Met. Phys. **15**(4), 851–858 (1985)
15. Yazyev, O.V.: Emergence of magnetism in graphene materials and nanostructures. Rep. Prog. Phys. **73**(5), 056501 (2010)

Part III
Surface Dangling Bond Circuits

First-Principles Simulations of Electronic Transport in Dangling-Bond Wires

M. Kepenekian, R. Robles, and N. Lorente

Abstract It has recently become possible to calculate at an ab initio level electronic transport in atomic and molecular systems connected to semi-infinite electrodes under an applied bias. In this chapter, we show how electronic structure calculations based on the density functional theory (DFT), followed by the use of nonequilibrium Green's functions (NEGF), allow one to simulate the electronic transport in various systems. This method is apply to the problem of electronic transport in dangling-bond wires built on the Si(100) surface.

1 Introduction

In the past few years it has become possible to measure charge transport across many different types of nanoscale systems such as molecules [1–3], nanowires [4, 5], or carbon nanotubes [6]. The development of such systems is of prime importance for molecular electronics [7, 8], which constitutes the best chance to overcome the physical limits in the miniaturization of electronic devices [9, 10].

There is no doubt today that electronic structure calculations constitute an important tool to scrutinize the physics of new materials. For many years, parametrized approaches have furnished an elegant and efficient way to deal with large systems. However, they are now more and more often replaced by ab initio methods that are conducted without having to introduce system-dependent parameters. In particular, the advent of density functional theory (DFT) [11, 12] has led to calculations offering quantitative agreement with experiments in a number of various problems such as spectroscopy or catalysis. Even if it suffers from a number of important flaws, there are careful studies that show static DFT to be a good quantitative

M. Kepenekian (✉) · R. Robles · N. Lorente
Centro de Investigación en Nanociencia y Nanotecnología, CSIC-ICN,
E-08193 Bellaterra, Spain

choice to study electron transport in many interesting situations [13–15]. Hence, DFT remains the proper choice to reach the best level of accuracy at the lowest computational cost.

In the setup described above, the system is neither isolated nor periodic and one cannot use the normal periodic boundary conditions which are a standard ingredient in electronic structure calculations. This situation can be addressed within DFT by calculating the exact scattering states [16]. Another popular approach is to use nonequilibrium Green's functions (NEGF) [17, 18]. As with the scattering approach, the NEGF method permits us to obtain electronic currents, densities, and potentials at a finite applied voltage. Several working implementations of transport calculations based on DFT and NEGF are available. We mention here two because they are related to the approach we are going to briefly present. These are the TRANSIESTA code [19] and the SMEAGOL one [20]. Both are based on strictly localized electronic basis set which permit us to clearly separate the different spatial regions of a transport problem in electrodes and the contact or the device region.

The purpose of this chapter is to give a brief introduction to the DFT-based NEGF method to calculate electronic transport in materials. As an illustration, the problem of electronic transport in dangling-bond wires built on the Si(100) surface is treated.

2 The DFT-NEGF Method

In its Kohn–Sham formulation [12], density functional theory is a mean-field theory [21]. This means that it treats a one-particle like Schrödinger equation with some effective potential, the exchange and correlation potential. These particles actually solve the Kohn–Sham equations, and they are no more than an approximation to actual electrons. One should keep in mind this point when comparing electronic levels, electronic wave functions, and eventually transport properties computed for Kohn–Sham particles.

Nowadays, a large type of potentials exists to obtain the Kohn–Sham equations. Typically, these potentials are local and semi-local, losing information on nonlocal interactions between electrons. Thus, the usual approximations of DFT, *i.e.*, the local density approximation (LDA) and the generalized gradient approximation (GGA), fail to describe properly effects such as van der Waals interactions.

As in any quantum chemistry code, DFT implementations use an electronic basis set to express the Hamiltonian. The typical basis sets are either local, usually atomic strictly localized basis sets [22], as in the case of SIESTA [23, 24] (TRANSIESTA and SMEAGOL for the transport implementations [19, 20]), or extended, typically plane waves as in the case of VASP [25]. Local basis sets are particularly suited for insulators and molecules, where electrons are localized, while plane waves are more suited for metals.

DFT-based calculations usually give reliable and predictive results for properties such as structural geometries, vibrational frequencies, or energy barriers. Besides, in the particular frame of a setup consisting in right and left leads and a contact

Fig. 1 Schematic picture of the division of the system into a central contact (C) and left (L) and right (R) electrode regions. The z axis corresponds to the transport direction

region, DFT is probably the only scheme offering the opportunity to describe with appreciable accuracy the whole system on the same footing given the large amount of atoms, as described next.

We consider the following situation (see Fig. 1): a left semi-infinite electrode (L), a contact region (C), and a right semi-infinite electrode (R). We use an atomic orbital basis set with a finite range as implemented in the SIESTA DFT code [23,24]. This basis enables us to split the space into these regions. Let us note that these basis set is not orthogonal, and thus, the overlap $\langle \phi_\alpha | \phi_\beta \rangle = \mathbf{S}_{\alpha,\beta}$ has to be taken into account. This specific problem does not affect the fundamental ideas and has been previously thoroughly treated [19], so it is not discussed here.

The electrode regions L and R are chosen to have a perfect layer structure with a potential converging to the bulk values. That is to say that all the disturbances in the C region are assumed to be screened out before the electrodes. This assumption can be tested by including a larger fraction of the electrodes in the central region. In this way, there is no overlap between the L and R regions. Thus, the matrix takes the following form:

$$\mathscr{H} = \begin{pmatrix} \mathbf{H}_L & \mathbf{V}_L & 0 \\ \mathbf{V}_L^\dagger & \mathbf{H}_C & \mathbf{V}_R \\ 0 & \mathbf{V}_R^\dagger & \mathbf{H}_R \end{pmatrix} \tag{1}$$

where $\mathbf{H}_L$ and $\mathbf{H}_R$ are semi-infinite tri-diagonal matrices,

$$\mathbf{H}_L = \begin{pmatrix} \mathbf{h}_L & \mathbf{v}_L & 0 & \cdots & \\ \mathbf{v}_L^\dagger & \mathbf{h}_L & \mathbf{v}_L & 0 & \cdots \\ 0 & \mathbf{v}_L^\dagger & \mathbf{h}_L & \mathbf{v}_L & \ddots \\ \vdots & \ddots & \ddots & \ddots & \ddots \end{pmatrix} \tag{2}$$

The intralayer ($\mathbf{h}$) and interlayer ($\mathbf{v}$) Hamiltonians are identical to the corresponding Hamiltonian for the semi-infinitely repeated layer structure for the L or R electrodes and can be calculated once and for all using periodic boundary conditions. The electron density, $n(\mathbf{r})$, is then obtained via the density matrix $\mathbf{D}_{\alpha\beta}$:

$$n(\mathbf{r}) = \sum_{\alpha,\beta} \phi_\alpha(\mathbf{r})\mathbf{D}_{\alpha\beta}\phi_\beta(\mathbf{r}). \tag{3}$$

The latter can be obtained from the retarded Green's function matrix $\mathbf{G}$ (as defined by (4)):

$$\mathbf{G}(E) = (E + \mathrm{i}\delta - \mathscr{H})^{-1} \tag{4}$$

$$\mathbf{D} = \int \frac{\mathrm{d}E}{2\pi} n_\mathrm{F}(E - E_\mathrm{F})\,\mathrm{i}\left[\mathbf{G}(E) - \mathbf{G}^\dagger(E)\right] \tag{5}$$

where E_F is the Fermi energy, $n_\mathrm{F}(E)$ is the Fermi distribution function, and δ is a positive infinitesimal.

Equation (5) is only true in equilibrium, *i.e.*, when no bias voltage is applied between the left and right electrodes. In principle the Green's function matrix $\mathbf{G}$ involves the inversion of an infinite matrix corresponding to the infinite system. However, we are only interested in what takes place within the contact, C-region. Then, we limit ourselves to the inversion of the finite matrix by taking the effect of the electrodes in effective "optical" potentials also called "self-energies":

$$\mathbf{G}_{CC}(E) = (E + \mathrm{i}\delta - \mathbf{H}_C - \Sigma_L(E) - \Sigma_R(E))^{-1} \tag{6}$$

where the so-called (one-electron) self-energies, $\Sigma_{L,R}$, fully take into account the coupling of C to L and R. Thanks to the perfect semi-infinite layer structure of the electrodes, the self-energies can be calculated exactly using recursion-like methods ("decimation" in TRANSIESTA or exact identities with Green's functions in SMEAGOL). We can write

$$\mathbf{H}_L = \begin{pmatrix} \mathbf{h}_L & \mathbf{v}_L \\ \mathbf{v}_L^\dagger & \mathbf{H}_L \end{pmatrix} \tag{7}$$

The inverse $\mathbf{g}_L$ (respectively, $\mathbf{g}_R$) of $\mathbf{H}_L$ (respectively, $\mathbf{H}_R$) restricted to L (resp. R) is obtained. We can then solve (4) and (6) and find

$$\Sigma_L(E) = \mathbf{V}_L^\dagger \mathbf{g}_L \mathbf{V}_L \tag{8}$$

$$\Sigma_R(E) = \mathbf{V}_R^\dagger \mathbf{g}_R \mathbf{V}_R \tag{9}$$

Roughly speaking, the real part of $\Sigma_{L,R}$ describes the change in energy levels in region C due to the bond formation with the L, R electrodes, whereas the imaginary part describes the decay (inverse lifetime) of electronic states located inside the C-region.

Defining $\Gamma_{L,R}(E)$ related to the imaginary part of the corresponding self-energies and hence to the inverse lifetimes of electronic states in the C-region (see (10)), we can write the density matrix, which is related to the density inside region C resolved in electronic states:

$$\Gamma_L(E) = i\left(\Sigma_L(E) - \Sigma_L^\dagger(E)\right) \tag{10}$$

$$\mathbf{D} = \int \frac{dE}{2\pi} n_F(E - E_F)\left[\mathbf{G}\Gamma_L\mathbf{G}^\dagger(E) + \mathbf{G}\Gamma_R\mathbf{G}^\dagger(E)\right] \tag{11}$$

where we have assumed that all the matrix elements are restricted to the C-region and thus discarded the CC label.

One can show [19] that the first (resp., second) term of (11) corresponds to the electron density in C due to the filling of scattering states originating in the left (resp. right) electrodes. In equilibrium, these scattering states are filled up to the common Fermi level $E_F^L = E_F^R = E_F$. The situation is different out of equilibrium. In this case, there is a voltage drop and a difference in the filling of the scattering states, and the two terms in (11) acquire different Fermi functions:

$$\mathbf{D} = \int \frac{dE}{2\pi}\left(n_F(E - E_F^L)\left[\mathbf{G}\Gamma_L\mathbf{G}^\dagger(E)\right] + n_F(E - E_F^R)\left[\mathbf{G}\Gamma_R\mathbf{G}^\dagger(E)\right]\right) \tag{12}$$

which can also be written in terms of the lesser Green's function [17],

$$\mathbf{D} = \int \frac{dE}{2\pi}\left(-i\mathbf{G}^<(E)\right) \tag{13}$$

The latter equation describes how the charge density in C responds to the voltage V making the chemical potentials differ in electrodes left and right, *i.e.*, $E_F^L - E_F^R = eV$. The two electrodes are still described by their bulk quantities except for a constant shift in the Kohn and Sham potential for electrons and in the electrode's Fermi energy. Thus, it is assumed that the current has spread out and the change in electron density due to the nonequilibrium situation is totally screened in L and R.

In the DFT approach, we calculate the electronic density and potential in a self-consistent cycle solving the Kohn–Sham and Poisson equations but now using the expression in (12) for the electron density inside C. This enables us to calculate the voltage drop in a current-carrying device, which is a nontrivial quantity. Plus, the nonequilibrium situation changes the electron density in the atomic bonds and will lead to forces and structural changes.

In the case of elastic electron transport, the conductance G can eventually be calculated following a Landauer-Büttiker-like formula [18]:

$$G = G_0 \int dE\left(n_F(E - E_F^L) - n_F(E - E_F^R)\right)\mathrm{Tr}[\mathbf{t}^\dagger\mathbf{t}](E) \tag{14}$$

where G_0 is the quantum of conductance $G_0 = 2e^2/h$ and the transmission amplitude matrix, $\mathbf{t}$, involves the decay rates to the left and right electrodes and the matrix elements of the retarded Green's function between orbitals connecting L and R [26],

$$\mathbf{t} = (\Gamma_R)^{1/2}\,G\,(\Gamma_L)^{1/2} \tag{15}$$

The transmission itself depends on the applied voltage through the change in the self-consistent potential landscape in the C region (*i.e.*, the change in $\mathbf{H}_C$ in (1) with applied voltage) and the rigid potential shifts of the electrodes relative to each other. An equivalent way to write the conductance is

$$G = G_0 \int \mathrm{d}E \left(n_\mathrm{F}(E - E_\mathrm{F}^L) - n_\mathrm{F}(E - E_\mathrm{F}^R) \right) \mathrm{Tr}[\Gamma_R \mathbf{G} \Gamma_L \mathbf{G}^*] \qquad (16)$$

The total transmission, $T_{\mathrm{tot}}(E) = \mathrm{Tr}[\mathbf{t}^\dagger \mathbf{t}](E)$, can take values greater than 1 corresponding to several transmitting channels. This can be investigated using the so-called transmission eigenchannels [27, 28]:

$$T_{\mathrm{tot}}(E) = \sum_n |\tau_n(E)|^2 \qquad (17)$$

which corresponds to a basis change to scattering states so that $\mathbf{t}$ becomes diagonal with values $0 \leq |\tau_n| \leq 1$ in the diagonal. By plotting the corresponding scattering states at a particular energy, one can get information on what orbitals contribute to the conduction.

An illustration of the use of all these tools is presented in the next section in the particular case of Si dangling-bond wires.

3 Application to Si Dangling-Bond Wires

In the mid-1970s, it was proposed that a single molecule could perform the same basic functions of electronics than traditional silicon-based technologies [7, 8]. One remaining challenge is to create a frame, at atomic scale, where a number of these "molecular processors" could be (1) assessed and (2) interconnected to construct a complete circuit. It has been shown that such structures can be obtained using the scanning tunneling microscope (STM), which can selectively remove atoms on the surface of semiconductors to construct lines [29–35]. The dangling bonds (DBs) created by the removal of atoms introduce then states in the band gap of the semiconductor. An important example of such fabrication is the DB wire produced by the selective removal of hydrogen atoms from an H-passivated Si(001) surface along the Si dimer row (see Fig. 2). This DB wire has a single dangling bond per Si atom, offering a 1D metallic band within the gap (see Fig. 2c). The transport of such a wire has been previously inspected by extended Hückel calculations and a tight-binding model [36,37]. Here, we use first-principles calculations based on density functional theory (DFT) as implemented in SIESTA [23, 24]. Calculations have been carried out with the GGA functional in the PBE form [38], Troullier–Martins pseudopotentials [39], and a basis set of finite-range numerical pseudoatomic orbitals for the valence wave functions [22]. Structures have been relaxed using a double-ζ polarized basis sets [22], while the conductance has been computed,
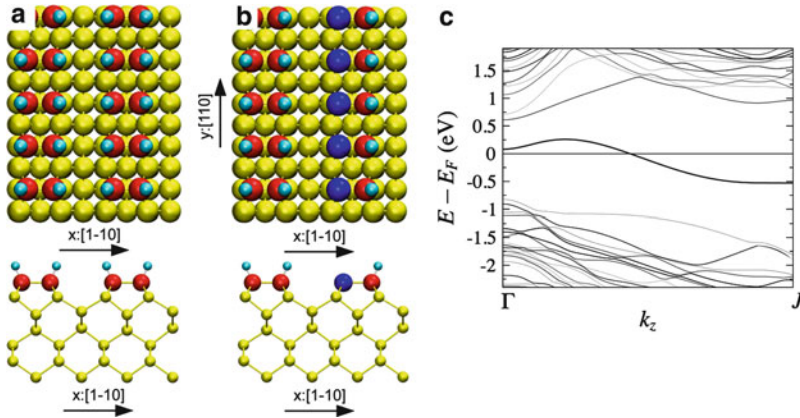
Fig. 2 Atomic structure of (**a**) the Si(100)-(2x1)-H surface and (**b**) the infinite ideal wire drawn along the y direction. H atoms are depicted in cyan, while Si atoms are depicted in *red* (surface dimers), *yellow* (others), and *blue* when holding a dangling bond. (**c**) Band structure of the ideal wire along the direction of the wire
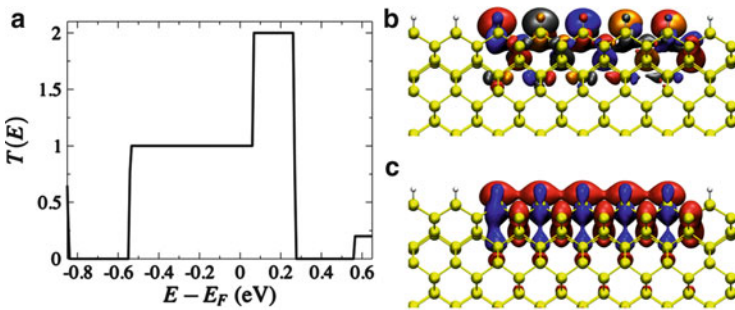
Fig. 3 (**a**) Transmission as a function of energy through the ideal wire (*black solid line*). (**b**) and (**c**) display the channels 1 and 2 at $E - E_F = 1.0$ eV, respectively. Color code: real, positive in *blue*; real, negative in *red*; imaginary, positive in *silver*; imaginary, negative in *orange*

using a single-ζ polarized basis set, by means of the TRANSIESTA code [19]. In all cases, an energy cutoff of 200 Ry for the real-space mesh size has been used.

Figure 3a shows the transmission of an infinite ideal wire. As expected from the band structure, the transmission exhibits clear steps featuring the existence of two channels between 0.08 eV and 0.26 eV above the Fermi energy, with only one remaining for $E - E_F$ taken between -0.53 and 0.08 eV. This result differs from the one previously obtained by Kawai et al. [37] from tight-binding calculations, where the one-channel domain is as large as the two-channel one (~ 0.4 eV).

An intuitive picture of the transmission through these wires would be that it arises from the direct coupling between DBs. However, the substrate is thought to play an important role in the transport [37]. This can be seen by computing the transmission eigenchannels. Indeed, it is clear from Fig. 3b, c that channels imply not only the

orbital corresponding to the DB but also orbitals from the sublayers. Another point is that there are no two distinct paths corresponding to each channel, but a modulation of phase corresponding to k vectors with values of $k_1 \sim -\pi/(2a)$ and $k_2 \sim 0$ (where a is the distance between two DBs).

Unfortunately, the configuration of the ideal DB wire is not stable, and a Peierls distortion takes place, involving a metal–insulator transition. The unstable DB wire can also relax in two magnetic forms resulting from the antiferromagnetic (AFM) and ferromagnetic (FM) coupling of adjacent DBs, respectively. The description of these different states has been the subject of intense activity with DFT-based calculations [40–48]. In particular the magnetic solutions appear to be more stable than the distorted structure, referred to as the nonmagnetic (NM) wire, when dealing with finite-size wires [46, 48]. Although these relaxed periodic structures break the metallicity of the DB wire by opening a gap, it does not preclude us from finding transport through a finite wire of DB, and ab initio calculations can predict the transport properties of the NM, AFM, and FM wires.

As presented in the previous section, the system is divided into left and right electrodes (L and R) and a central scattering region (C), in our case the different possible wires (Ideal, NM, AFM, and FM). In order to avoid the sensitive problem of the description of the interface between realistic electrodes and the DB wires, we choose to take advantage of the metallic behavior of ideal wires and use them as the source for injecting electrons into the scattering region. Thus, in our calculations, the role of right and left electrodes are performed by semi-infinite ideal wires. In order to have a physical stable system, the C-region is taken as the studied wire (NM, AFM, or FM) and the interface between the ideal wire and the finite wire is a passivated DB by a Hydrogen atom. The C-region then contains a finite wire, two pieces of infinite ideal wires, separated by two passivated DB one in each extreme of the finite wire. Only in this way, a relaxed, self-consistent solution could be found.

In the case of a finite-size DB wire, we observe a confinement of the DB-wire states, thus a particle in a box-like behavior. If instead of using the open boundary conditions, one uses periodic conditions, these confined states will appear as essentially flat bands within the bulk gap as can be seen on Fig. 4a on the example of a 5 DB AFM wire. The corresponding transmission exhibits peaks and dips that can be understood by examining the confined states. As can be seen on Fig. 4b, the states confined appear to be a sum of orbitals similar to the one observed in the eigenchannels, underlining the major role played by the substrate in the transport properties of the DB wires. Let us stress that the general shape of the wire's states corresponds to those obtained from a particle in a box problem, with an increasing number of nodes when going to states of higher energies. The behavior is similar for Ideal, NM, and FM wires.

Such figures of the transmission do not allow one to easily foresee what would be the result of current measurements for any DB wire. In order to average the effect of these peaks and dips, we can compute the current following (14). Figure 5 shows the computed I–V curves for 5-DB wires in the ideal, NM, AFM, and FM configuration. As can be seen, the relaxation from ideal to nonmagnetic (distorted) or magnetic solution causes the loss of one order of magnitude in the current. This trend is
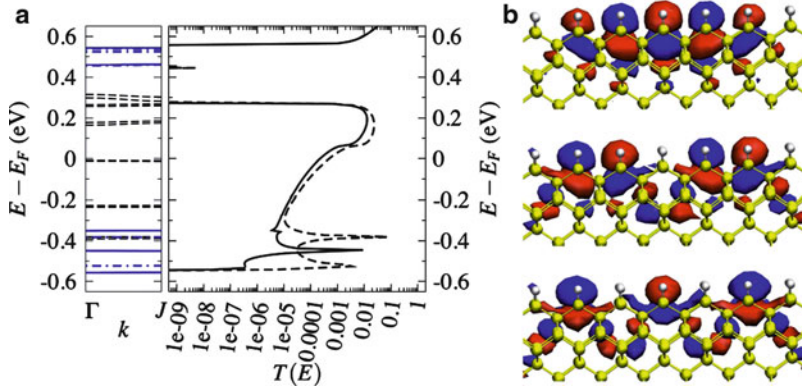
Fig. 4 (**a**) Band structure (*left*) and transmission $T(E)$ (*right*) of the 5-DB AFM wire. The states localized on the wire are depicted in *blue* (*solid and dashed lines* for majority and minority spins, respectively). States of the electrodes are depicted in *black dashed lines*. The bands of the electrodes appear shifted due to the periodic boundary conditions used to calculate the band structures. (**b**) Plot of the three wave functions of lower energy of the 5-DB AFM wire at Γ
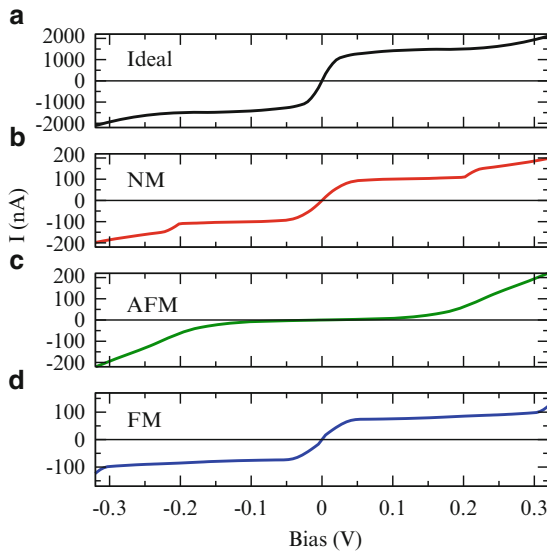
Fig. 5 Calculated current (nA) with respect to the bias (V) for 5-DB wires. Ideal, NM, AFM and FM wires are displayed top to bottom

much more pronounced in the case of the AFM wire at small bias. Thus, I–V curves depend strongly from the type of DB wire. In particular, the behaviors of AFM and NM wires—so close in energy [48]—are so different, that I–V measurements would allow one to identify the ground state beyond the shadow of a doubt.

4 Summary and Conclusions

In this chapter, we have succinctly reviewed the technique of nonequilibrium Green's functions (NEGF) for electronic transport calculations, based on density functional theory (DFT). This permits us to attain good accuracy in the atomistic description of nanoscale devices while taking into account the full nonequilibrium regime of electron transport. The method consists in interfacing DFT and NEGF through the density matrix. To achieve this, a careful partitioning of the device has to be performed in order to have well-defined asymptotic-like electrodes and the device or contact region where the bias drop takes place.

We have briefly illustrated a NEGF-DFT calculation by evaluating electron transport between two semi-infinite ideal dangling-bond (DB) wires of an otherwise passivated Si(100)-H surface. Between the two semi-infinite wires, a realistic DB wire, solution of the DFT equations has been placed. In order to achieve a physical solution of the full problem, electrodes (semi-infinite ideal wires) and contact (realistic finite DB wire) are partially decoupled by two passivated DB with an H atom each. Hence, NEGF-DFT takes into account the full problem of stability and transport. The calculations permit us to show distinct I–V characteristics for each of the possible solutions found by DFT for finite-size DB wires, furnishing a way to determine the structure of DB wires via transport measurements.

References

1. Ruben, M., Landa, A., Lörtscher, E., Riel, H., Mayor, M., Görls, H., Weber, H.B., Arnold, A., Evers, F.: Small **4**(12), 2229 (2008)
2. Martin, C.A., Smit, R.H.M., van Egmond, R., van der Zant, H.S.J., van Ruitenbeek, J.M.: Rev. Scientif. Instrum. **82**(5), 053907 (2011)
3. Schull, G., Frederiksen, T., Arnau, A., Sanchez-Portal, D., Berndt, R.: Nature Nanotechnol. **6**(12), 23 (2011)
4. Pascual, J.I., Mendez, J., Gomez-Herrero, J., Baro, A.M., Garcia, N., Binh, V.: Phys. Rev. Lett. **71**, 1852 (1993)
5. Agrait, N., Untiedt, C., Rubio-Bollinger, G., Vieira, S.: Phys. Rev. Lett. **88**, 216803 (2002)
6. Charlier, J.C., Blase, X., Roche, S.: Rev. Mod. Phys. **79**, 677 (2007)
7. Aviram, A., Ratner, M.A.: Chem. Phys. Lett. **29**, 277 (1974)
8. Joachim, C., Gimzewski, J.K., Aviram, A.: Nature **408**, 541 (2000)
9. Muller, D.A., Sorsch, T., Moccio, S., Baumann, F.H., Evans-Lutterodt, K., Timp, G.: Nature **399**, 758 (1999)
10. Meindl, J.D., Chen, Q., Davis, J.A.: Science **293**, 2044 (2001)
11. Hohenberg, P., Kohn, W.: Phys. Rev. B **136**, 864 (1964)
12. Kohn, W., Sham, L.J.: Phys. Rev. A **140**, 1133 (1965)
13. Schmitteckert, P., Evers, F.: Phys. Rev. Lett. **100**, 086401 (2008)
14. Mera, H., Niquet, Y.M.: Phys. Rev. Lett. **105**, 216408 (2010)
15. Bergfield, J.P., Liu, Z.F., Burke, K., Stafford, C.A.: Phys. Rev. Lett. **108**, 066801 (2012)

16. Lang, N.D.: Phys. Rev. Lett. **55**, 230 (1985)
17. Economou, E.N.: Green's Functions in Quantum Physics. Springer, Berlin (2005)
18. Datta, S.: Electronic Transport in Mesoscopic Systems. Cambridge University Press, Cambridge (2007)
19. Brandbyge, M., Mozos, J.L., Ordejón, P., Taylor, J., Stokbro, K.: Phys. Rev. B **65**, 165401 (2002)
20. Rocha, A.R., García-Suárez, V.M., Bailey, S., Lambert, C., Ferrer, J., Sanvito, S.: Phys. Rev. B **73**, 085414 (2006)
21. Koch, W., Holthausen, M.C.: A Chemist's Guide to Density Functional Theory. Wiley-VCH Verlag GmbH, Weinheim (2001)
22. Artacho, E., Sánchez-Portal, D., Ordejón, P., García, A., Soler, J.M.: Phys. Stat. Sol. (B) **215**, 809 (1999)
23. Soler, J.M., Artacho, E., Gale, J.D., García, A., Junquera, J., Ordejón, P., Sánchez-Portal, D.: J. Phys.: Condens. Matter **14**, 2745 (2002)
24. Artacho, E., Anglada, E., Diéguez, O., Gale, J.D., García, A., Junquera, J., Martin, R.M., Ordejón, P., Pruneda, J.M., Sánchez-Portal, D., Soler, J.M.: J. Phys.: Condens. Matter **20**, 064208 (2008)
25. Kresse, G., Furthmüller, J.: Comput. Mater. Sci. **6**, 15 (1996)
26. Cuevas, J.C., Levy Yeyati, A., Martín-Rodero, A.: Phys. Rev. Lett. **80**, 1066 (1998)
27. Martin, T., Landauer, R.: Phys. Rev. B **45**, 1742 (1992)
28. Brandbyge, M., Sørensen, M.R., Jacobsen, K.W.: Phys. Rev. B **56**, 14956 (1997)
29. Shen, T.C., Wang, C., Abeln, G.C., Tucker, J.R., Lyding, J.W., Avouris, P., Walkup, R.E.: Science **268**, 1590 (1995)
30. Hosaka, S., Hosoki, S., Hasegawa, T., Koyanagi, H., Shintani, T., Miyamoto, M.: J. Vac. Sci. Technol. B **13**, 2813 (1995)
31. Hitosugi, T., Heike, S., Onogi, T., Hashizume, T., Watanabe, S., Li, Z.Q., Ohno, K., Kawazoe, Y., Hasegawa, T., Kitazawa, K.: Phys. Rev. Lett. **82**, 4034 (1999)
32. Soukiassian, L., Mayne, A.J., Carbone, M., Dujardin, G.: Surf. Sci. **528**, 121 (2003)
33. Hallam, T., Reusch, T.C.G., Oberbeck, L., Curson, N.J., Simmons, M.Y.: J. Appl. Phys. **101**, 034305 (2007)
34. Haider, M.B., Pitters, J.L., DiLabio, G.A., Livadaru, L., Mutus, J.Y., Wolkow, R.A.: Phys. Rev. Lett. **102**, 046805 (2009)
35. Pitters, J.L., Livadaru, L., Haider, M.B., Wolkow, R.A.: J. Chem. Phys. **134**, 064712 (2011)
36. Doumergue, P., Pizzagalli, L., Joachim, C., Altibelli, A., Baratoff, A.: Phys. Rev. B **59**, 15910 (1999)
37. Kawai, H., Yeo, Y.K., Saeys, M., Joachim, C.: Phys. Rev. B **81**, 195316 (2010)
38. Perdew, J.P., Burke, K., Ernzerhof, M.: Phys. Rev. Lett. **77**, 3865 (1996)
39. Troullier, N., Martins, J.L.: Phys. Rev. B **43**, 1993 (1991)
40. Watanabe, S., Ono, Y.A., Hashizume, T., Wada, Y.: Phys. Rev. B **54**, R17308 (1996)
41. Watanabe, S., Ono, Y.A., Hashizume, T., Wada, Y.: Surf. Sci. **386**, 340 (1997)
42. Cho, J.H., Kleinman, L.: Phys. Rev. B **66**, 235405 (2002)
43. Bird, C.F., Bowler, D.R.: Surf. Sci. **531**, L351 (2003)
44. Çakmak, M., Srivastava, G.P.: Surf. Sci. **532–535**, 556 (2003)
45. Lee, J.Y., Choi, J.H., Cho, J.H.: Phys. Rev. B **78**, 081303 (2008)
46. Lee, J.Y., Cho, J.H., Zhang, Z.: Phys. Rev. B **80**, 155329 (2009)
47. Lee, J.H., Cho, J.H.: Surf. Sci. **605**, L13 (2011)
48. Robles, R., Kepenekian, M., Monturet, S., Joachim, C., Lorente, N.: J. Phys.: Condens. Matter 24, 445004 (2012)

Dangling-Bond Logic: Designing Boolean Logic Gates on a Si(001)-(2x1):H Surface

Hiroyo Kawai, Francisco Ample, Christian Joachim, and Mark Saeys

Abstract Atomic-scale dangling-bond Boolean logic gates with two inputs and one output are designed on a Si(001)-(2x1):H surface. The dangling-bond logic gates are connected to the macroscopic scale by metallic nano-electrodes physisorbed on the Si(100)-(2x1):H surface. The logic inputs are provided by saturating and unsaturating surface Si dangling bonds, which can, for example, be achieved by adding and extracting two hydrogen atoms per input. Quantum-transport calculations were used to investigate the operation of the proposed dangling-bond logic gates interconnected to the metallic nano-electrodes by surface dangling-bond wires. Our calculations indicate that the proposed dangling-bond logic devices can reach ON/OFF ratios up to 2000.

H. Kawai (✉) · F. Ample
Institute of Materials Research and Engineering, 3 Research Link, Singapore 117602
e-mail: kawaih@imre.a-star.edu.sg; navarrofa@imre.a-star.edu.sg

C. Joachim
Institute of Materials Research and Engineering, 3 Research Link, Singapore 117602

Nanosciences Group & MANA Satellite, CEMES-CNRS, 29 rue Jeanne Marvig,
F-31055 Toulouse, France
e-mail: joachim@cemes.fr

M. Saeys
Institute of Materials Research and Engineering, 3 Research Link, Singapore 117602

Department of Chemical and Biomolecular Engineering, National University of Singapore,
4 Engineering Drive 4, Singapore 117576
e-mail: saeys@nus.edu.sg

1   Introduction

As the semiconductor industry races towards the atomic scale, it becomes imperative to investigate how many atoms it takes to construct functional devices. The controlled desorption of hydrogen atoms from the hydrogen-passivated Si(001)-(2x1):H surface with the scanning tunnelling microscope (STM) tip creates surface dangling bonds (DBs), which introduce states in the Si(001)-(2x1):H surface band gap [1–4]. We illustrate how these surface DB states can be coupled and manipulated to construct atomic-scale switches and logic devices.

In this chapter, atomic-scale switches and Boolean logic gates (AND, NOR, NAND, OR) are created on a Si(001)-(2x1):H surface and analysed using quantum-transport calculations with the elastic-scattering quantum chemistry (ESQC) method [5]. In Sect. 1, the DB state introduced by the removal of a hydrogen atom from the Si(001)-(2x1):H surface is discussed, followed by an illustration of the bands derived from an infinite line of DBs running either parallel or perpendicular to the dimer reconstruction rows on the Si(001)-(2x1):H surface. In Sect. 2, a DB wire running along the dimer rows is analysed, and the effect of the introduction of a H-tunnelling junction along the wire is described. In Sect. 3, the designs of two atomic-scale DB switches and their electron transport properties are presented, followed by the designs of the four Boolean dangling-bond logic gates.

2   Dangling Bonds on Semiconductor Surfaces

Modern STM technology allows the controllable atom-by-atom removal of passivating H atoms from the Si(001)-(2x1):H semiconductor surface, as illustrated schematically in Fig. 1a [3,4]. Removing one H atom creates one DB state. This state is mainly composed of the p_z orbital of the unpassivated Si but mixes substantially with subsurface and neighbouring Si orbitals, as observed in the molecular orbital image of a Si(001)-(2x1):H surface with one isolated DB (Fig. 1b). The DB state lies within the surface band gap of the fully passivated Si(001)-(2x1):H slab. The band structures of a fully passivated five-layer Si(001)-(2x1):H slab and a surface with an isolated DB are shown in Fig. 1c and d, respectively. The DB-derived state can be found near the centre of the band gap and is isolated from other bands (Fig. 1d).

A line of DBs can be created by removing a row of H atoms either along the dimer reconstruction rows (Fig. 2a) or perpendicular to the dimer reconstruction rows (Fig. 2b and c). In both cases, the DB states are introduced within the band gap, but the couplings between the DBs are different. When the DB wire runs parallel to the dimer rows, there is a significant through-space and through-lattice coupling between the DBs, which results in a large dispersion of a DB wire band (Fig. 2a). On the other hand, the bands derived from the DB wire perpendicular to the dimer rows have very small dispersions, indicating that the coupling between the DB dimers is small (Fig. 2b and c). The two DB-derived bands for the perpendicular
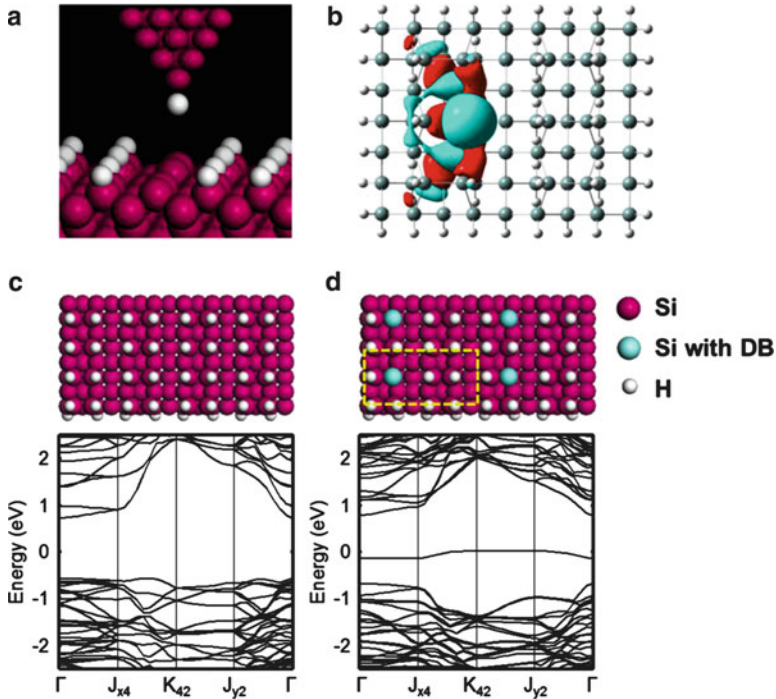
Fig. 1 (**a**) Schematic illustration of the selective removal of a hydrogen atom from a H-passivated Si(001)-(2x1):H surface using the tip of an STM. (**b**) Top view of a DB orbital, calculated using DFT PBE/6–31G(d,p), as implemented in Gaussian 03 [6]. Atomic structures and corresponding band structures for a H-passivated Si(001)-(2x1):H surface slab (**c**) and a H-passivated Si(001)-(2x1):H surface with an isolated DB (**d**), calculated using DFT-PBE [7] as implemented in VASP [8]. The band structure was calculated along the symmetry lines indicated on the atomic structure

wire (one above and one below the Fermi level) correspond to the so-called π and π^* bands. The DB dimers in the DB wire perpendicular to the dimer rows can be either unbuckled (Fig. 2b) or buckled (Fig. 2c). When the DB dimers are buckled (Fig. 2c), which is known to be a more stable surface configuration for an infinite DB wire [9], the gap between the π and π^* band increases. However, the two bands still appear within the Si(001)-(2x1):H surface band gap and are separated from the bulk and surface bands.

3   H-Tunnelling Junction Created Along a DB Wire Parallel to the Dimer Rows

It is apparent from the band structure that the DB wire running along the dimer rows has a higher conductance compared to the perpendicular wire, and it can act as a 1D quasi-ballistic wire. To characterise the electron transport properties of this
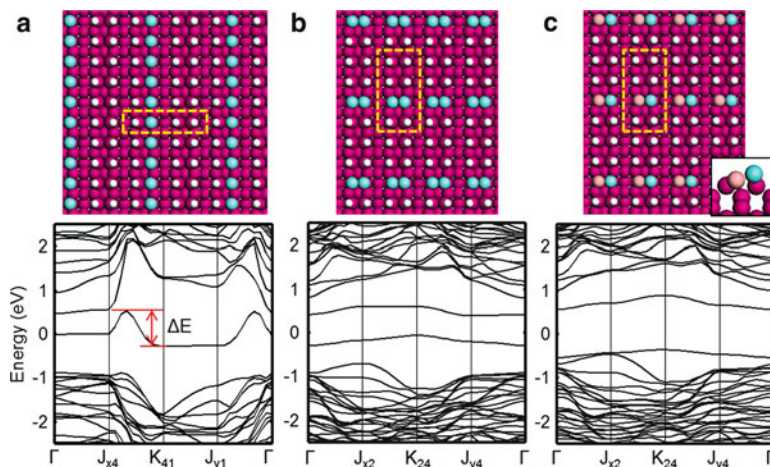
Fig. 2 Atomic and surface band structures of a H-passivated Si(001)-(2x1):H surface slab with
(**a**) a DB wire running parallel to the dimer rows, with a DB wire band dispersion, ΔE, of 0.81 eV,
(**b**) a DB wire running perpendicular to the dimer rows, where the DB dimers are not buckled, and
(**c**) DB wire perpendicular to the dimer rows, where DB dimers are buckled in-phase (down-up-
down-up)
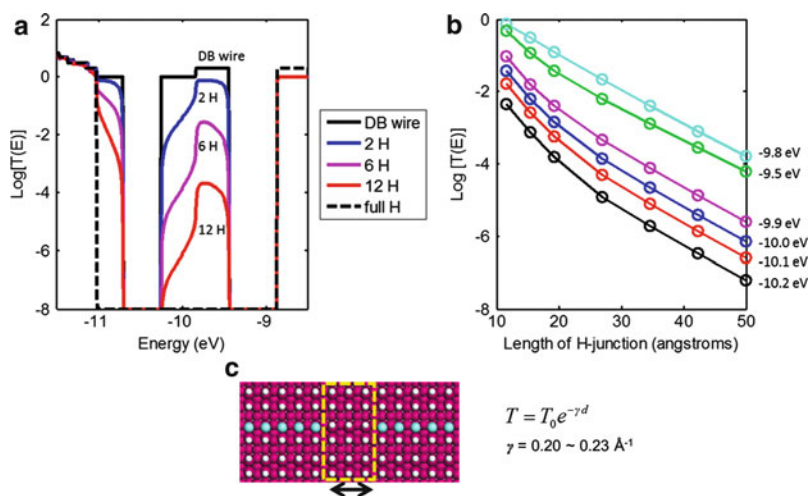
Fig. 3 (**a**) Transmission spectra for a H-tunnelling junction (2, 6, and 12 H) contacted by semi-
infinite DB wires running parallel to the dimer rows. (**b**) Semilogarithmic plots of the transmission
decay with increasing H-junction length at different energies. At the Fermi energy (-9.9 eV), the
$T(E)$ decreases exponentially with an inverse decay length, γ, of 0.22 Å^{-1} for junctions longer
than 25 Å. (**c**) Atomic structure of the H-junction

DB wire in more detail, its transmission spectrum, $T(E)$, was calculated using the
ESQC method. The extended Hückel molecular orbital (EHMO) approximation [10]
was fitted to accurate DFT band structures and used to construct the Hamiltonian of
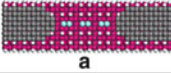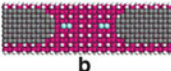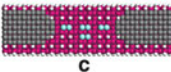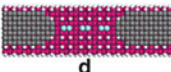
the system. As shown in Fig. 3a (black solid line), the *infinite* DB wire along the dimer rows introduces transport channels around the Fermi level, corresponding to the DB wire-derived band between –10.2 and –9.4 eV (Fig. 2a). Next, each end of a *finite*-length DB wire was contacted by metal nano-electrodes physisorbed on the H-passivated Si(001)-(2x1):H surface to connect the wire to the macroscopic scale. In this case, resonance peaks resulting from the individual DB states appear within the energy range of the infinite wire band (not shown).

To evaluate the effect of the introduction of a H-tunnelling junction into the DB wire on the electron transport along the wire, the $T(E)$ spectra for different widths of the H-junction were calculated (Fig. 3a). The structure of the junction is shown in Fig. 3c. The $T(E)$ in the range of the DB wire-derived channels decreases with increasing width of H-junction, approaching the $T(E)$ spectrum of the fully hydrogenated Si(100)-(2x1):H surface *with* a full band gap (dashed line). A semilogarithmic plot of $T(E)$ shows an exponential decay with the width of the H-junction, with an inverse decay length, γ, of about 0.20–0.23 Å^{-1}. Thus, a H-junction must be at least 30 Å (6 H atoms) wide to significantly weaken the electronic coupling between the two contacting DB wires and to decrease the $T(E)$ by two orders of magnitude. In other words, a H-tunnelling junction is not a very effective insulating barrier [11].

4 Switches and Boolean DB Logic Gates Created on the Si(001)-(2x1):H Surface

Although the DB wire perpendicular to the dimer rows is not effective as a conducting wire due to the smaller coupling between the DB dimers, electron transport along the wire in this direction is very sensitive to neighbouring DB configurations or to changes in the electronic properties or the geometry of the DB dimers. This property can be exploited to design atomic-scale DB switches and logic devices [12].

One possible design of the atomic-scale switches consists of 3 DB dimers perpendicular to the dimer rows on a Si(001)-(2x1):H surface, where each end of this short DB wire is contacted by a physisorbed surface Au nano-electrode (Fig. 4). The DB dimers are assumed to be unbuckled, but the buckling of the Si dimers only slightly increases the $\pi-\pi^*$ gap and does not significantly change electron tunnelling transport through the DB wire [13]. Switching between 'ON' and 'OFF' states is controlled by the addition or removal of two H atoms either on the central dimer or on a DB dimer adjacent to the central dimer (Fig. 4). The addition of two H atoms is defined as a logic input '1', and removal/absence of the H atoms is defined as a logic input '0'. The addition of H atoms to the central DB dimer in Fig. 4a turns the switch 'OFF' (Fig. 4b), resulting in an inverter switch. The addition of two H atoms to the DB dimer adjacent to the central DB dimer in Fig. 4c turns the switch 'ON', resulting in a follower switch. The equivalent electromechanical structure is also shown for each switch (Fig. 4).

Fig. 4 Atomic structures for the two proposed DB switches created on a Si(001)-(2x1):H surface. In the inverter, the addition of 2 H atoms to the central dimer in (**a**) encodes a logic input '1', which turns the switch 'OFF' (**b**). In the follower, the addition of 2 H atoms to the dimer adjacent to the central dimer in (**c**) encodes a logic input '1', which turns the switch 'ON' (**d**). The equivalent electromechanical circuit for each structure is also shown
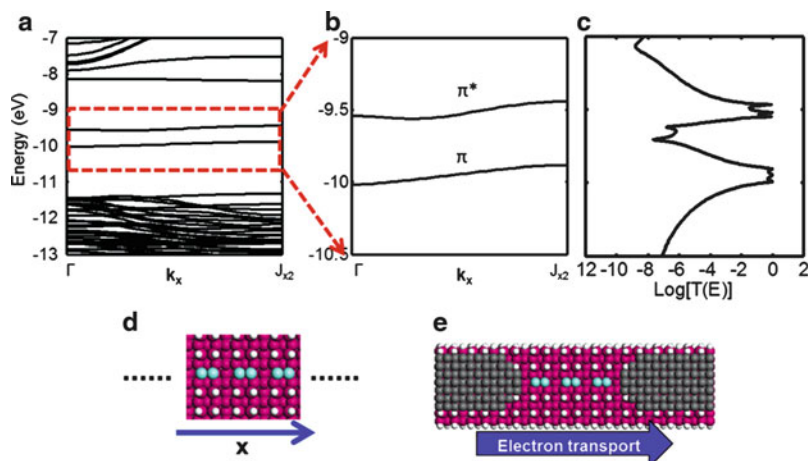
Fig. 5 (**a**) EHMO band structure of an infinite DB wire perpendicular to the dimer rows on a Si(001)-(2x1):H surface. The atomic structure for an infinite DB wire is shown in (**d**). (**b**) Zoom in of the band structure in (**a**), focused on the two DB wire-derived bands. (**c**) $T(E)$ spectrum for a short three-DB wire contacted by Au nano-electrodes. The atomic structure of the short DB wire is shown in (**e**)

How do these switches work? Electron transport through the short 3 DB dimer wire results from the π and π^* states introduced by the DBs within the Si(001)-(2x1):H surface band gap, as shown in Fig. 5. π and π^* states fall below and above the Fermi energy, respectively, and the corresponding $T(E)$ resonance peaks appear in that energy range (Fig. 5c). There are three π and three π^* peaks in the $T(E)$ spectrum, and the $T(E)$ near the peaks is about seven orders of magnitude higher
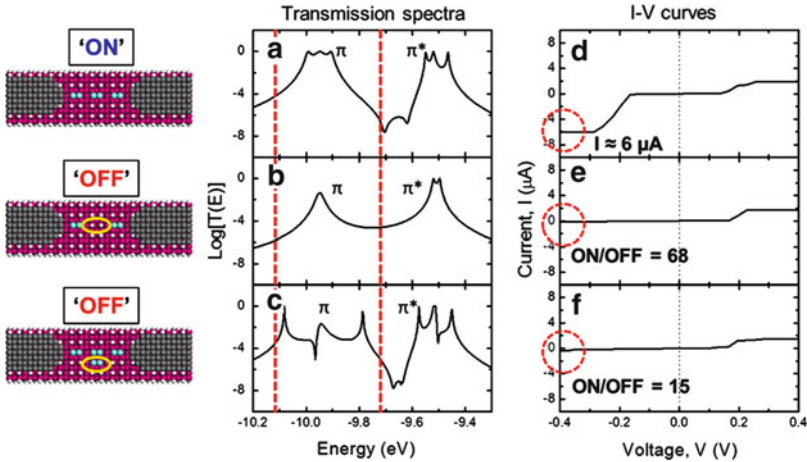
Fig. 6 $T(E)$ spectra for (**a**) the inverter and follower in their 'ON' state, (**b**) the inverter in its 'OFF' state, and (**c**) the follower in its 'OFF' state. The atomic structure of each configuration is shown in the left column. Corresponding I–V curves are shown in (**d**)–(**f**). The current and ON/OFF ratio at –0.4 V are calculated by integrating the $T(E)$ spectra between the *dashed lines* indicated in (**a**)–(**c**)

than in the gap between the π and π^* states. A tunnelling current, I, passes through the DB wire when a bias voltage, V, is applied to the junction. The π and π^* $T(E)$ resonance peaks are affected by the DB configuration, which results in a switching in the tunnelling current. The π states were used for the switches (corresponding to a negative bias voltage) because the π states are more sensitive to neighbouring DB configurations than the π^* states. The $T(E)$ and I–V characteristics for each DB configuration are plotted in Fig. 6.

The inverter in Fig. 4a is turned 'OFF' by passivating the central Si dimer with two H atoms (Fig. 4b), and the corresponding $T(E)$ spectrum is shown in Fig. 6b. In the 'OFF' state, there are two π and two π^* peaks, compared to three peaks each in the 'ON' state. Note that only one resonance is observed in the π region (Fig. 6b) because the two $T(E)$ peaks largely overlap. The passivation of two central DBs shifts one π and one π^* peak to higher energies, outside the energy range considered in Fig. 6b. As a result, the overall width of the π resonances decreases, leading to a smaller current. At a bias voltage of –0.4 V, the current is $0.09\,\mu A$, much smaller than the tunnelling current of $6\,\mu A$ in the 'ON' state, and the ON/OFF ratio for the inverter is about 68 (Fig. 6e). The current in the 'ON' state is close to the current obtained for a perfect ballistic wire with the width of the π band, about 0.1 eV.

The follower device in Fig. 4c is turned 'OFF' when two H atoms are removed from the DB dimer adjacent to the central dimer because the adjacent DB dimer introduces a new surface tunnelling path, causing a phase shift in the corresponding electron Bloch wave. The corresponding $T(E)$ (Fig. 6c) has four π and four π^* peaks and two destructive interferences, one in the π and one in the π^* range,

Fig. 7 $T(E)$ spectra and I–V curves for the inverter and follower DB switches contacted to the Au nano-electrodes by DB wires paral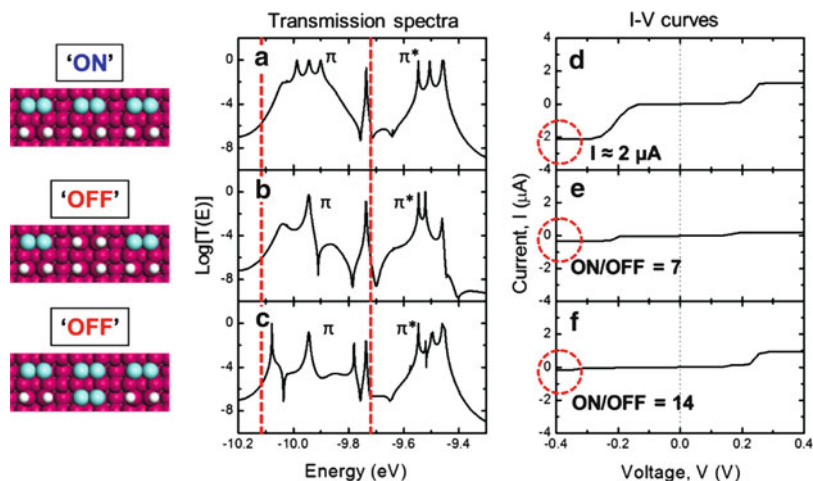lel to the dimer rows, as shown in Fig. 8b. $T(E)$ spectra of (**a**) the inverter and follower in their 'ON' state, (**b**) the inverter in its 'OFF' state, and (**c**) the follower in its 'OFF' state. The atomic structure of each configuration is shown in the left column. Corresponding I–V curves are shown in (**d**)–(**f**). The tunnelling current and the ON/OFF ratio at –0.4 V are calculated by integrating the $T(E)$ between the *dashed lines* indicated in (**a**)–(**c**)

because of the introduction of a second tunnelling path. The plot shows only three peaks each because the central two peaks overlap. The two groups of $T(E)$ resonances resulting from the π and π^* dimer states are wider than those in Fig. 6a or b due to the stronger electronic interactions between the two central dimers along the dimer row, which causes the electronic states to split and decreases the current through the wire. In the 'OFF' state, the current through the follower is $0.4\,\mu A$ for a bias voltage of –0.4 V, leading to an ON/OFF ratio of about 15 (Fig. 6f).

To incorporate the atomic-scale DB switching devices into atomic-scale DB logic circuits, a larger flexibility is required to position the nano-electrodes on the surface. In addition, it is important to increase the interelectrode distance to minimise surface leakage currents when the devices are in the 'OFF' state. It was found that the interelectrode distance could be increased both parallel and perpendicular to the dimer rows without affecting the ON/OFF ratio of the devices significantly. Indeed, as an example, the electron transport through a DB inverter and follower switch contacted by DB wires parallel to the dimer rows (Fig. 8b) was calculated. $T(E)$ spectra and I–V curves for the 'ON' and the 'OFF' state of each device are shown in Fig. 7. The additional resonance peak near the Fermi level originates from electronic interactions at the corners between the first DB state of the DB wire parallel to the dimer rows and the outermost DB dimer of the DB switching device. Since this resonance is sharp, it does not contribute significantly to the tunnelling current. The π and π^* resonance peaks become sharper than for a DB switch contacted directly by the nano-electrodes (Fig. 6) because the coupling between the central DB switch

Fig. 8 Atomic structures of (**a**) three-DB-dimer switching device contacted directly by Au nano-electrodes, (**b**) three-DB switching device contacted to the Au nano-electrodes by DB wires running along the dimer rows, (**c**) series circuit where the DB switching devices are connected in series by a central Au nano-island, (**d**) series circuit where the DB switching devices are connected directly, (**e**) circuit where the series DB logic gate is connected to the Au nano-electrodes by DB wires running along the dimer rows, (**f**) parallel circuit where the DB switching devices are connected by wide Au nano-electrodes, and (**g**) circuit where the DB switching devices are connected in parallel by DB wires running along the dimer rows

Switches (Inverter, Follower)

Series circuits (AND, NOR)

Parallel circuits (NAND, OR)
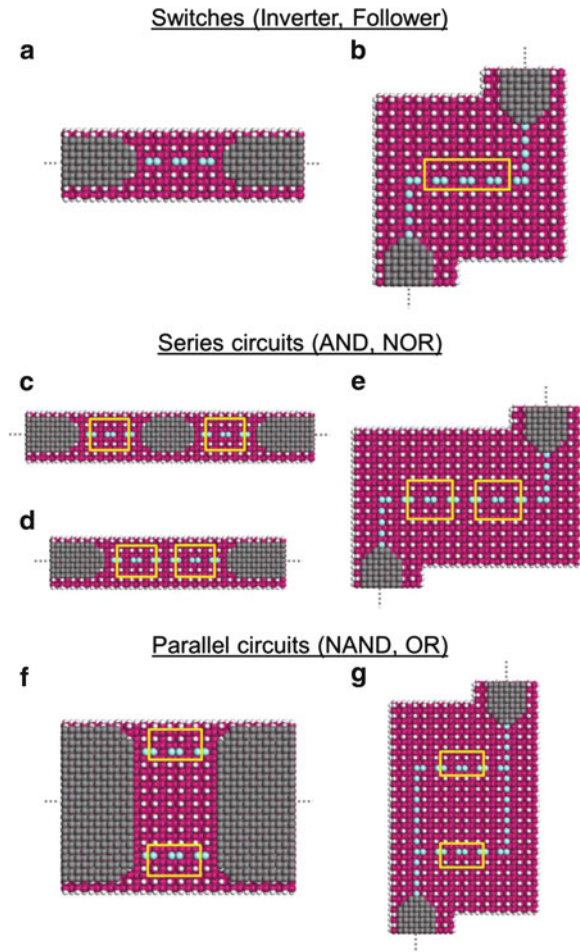
and the Au nano-electrodes through the parallel DB wires is weaker. Due to these differences, the 'ON' current and ON/OFF ratios are reduced compared to the DB switches in Fig. 4, but remain close to ten.

Four Boolean logic gates with two inputs and one output (AND, NOR, NAND, OR) can be constructed by interconnecting the atomic-scale inverter or follower devices in series or in parallel. The AND (NOR) gate is created by connecting two followers (inverters) in series, and the NAND (OR) gate is created by connecting two inverters (followers) in parallel. There are several ways to interconnect two DB switching devices, as shown in Fig. 8. In a series circuit, two DB switching devices can be connected through a central Au nano-island (Fig. 8c) or directly (Fig. 8d). The circuit can also be contacted with DB wires parallel to the dimer rows (Fig. 8e),

similar to the DB switch shown in Fig. 8b, to increase the distance between the nano-electrodes. In a parallel circuit, two DB switching devices can be connected in parallel by a wider Au nano-electrode at each end of the switching devices (Fig. 8f) or by DB wires parallel to the dimer rows (Fig. 8g). Although the ON/OFF ratio of each DB logic gate depends on how the switches are connected, this difference does not affect its logic function. The truth tables and atomic structures for the four DB logic gates are shown in Fig. 9. The equivalent classical structures are also shown to help visualise the circuits. $T(E)$ spectra and $I–V$ curves are shown for the AND and the NAND gate.

The $T(E)$ spectra and the corresponding $I–V$ curves for the three different input configurations ('11', '01', '00') for the AND DB logic gate circuit in Fig. 8d are shown in Fig. 10. For the '11' configuration (Fig. 10a), a six-dimer DB wire is contacted by Au nano-electrodes at each end. The $T(E)$ spectrum hence shows six π and six π^* resonances, twice the number observed for the '1' configuration of follower DB switch (Fig. 6a). More peaks and interferences are observed in the $T(E)$ spectra of the '00' and the '01' configurations (Fig. 10b and c), when compared to the spectra of the follower switch in Fig. 6. This is because there are more DB states involved in the AND device. In addition, there are at least four different tunnelling paths through the DB logic circuit for the '00' configuration, compared to two paths for the follower switch in the 'OFF' state, and therefore, more destructive interferences are expected in the series circuit. The $I–V$ curves for the three input configurations (Fig. 10d–f) clearly show a large change in the output current intensity between the 'ON' and the 'OFF' states. At a bias voltage of –0.4 V, the ON/OFF ratios for the '11'/'01' and the '11'/'00' configurations are 620 and 17, respectively.

The $T(E)$ spectra and the corresponding $I–V$ characteristics for the three different input configurations ('11', '01', '00') of the NAND DB logic gate in Fig. 8f are shown in Fig. 11. For the NAND gate, it is important that the distance between the inverter DB switches is sufficiently large to reduce their interaction through the Si(100)-(2x1):H surface, as shown for the H-tunnelling junction (Fig. 3) [11]. The spectra for the '00' and the '11' input configurations resemble the spectra for the 'ON' and the 'OFF' states of the inverter (Fig. 6a and b), showing that the $T(E)$ for this circuit is essentially the superposition of the $T(E)$ spectra for two independent inverters. Additional π^* peaks are observed for the NAND gate compared to the inverter because the two inverters in the NAND gate are not completely decoupled. The small through-lattice interaction between the two inverters causes some of the states to split. At a bias voltage of –0.4 V, the $I–V$ curves in Fig. 11d–f show ON/OFF ratios of 21 and 41 for the '01' and for the '00' input configurations, respectively, and therefore, the DB logic device functions as a NAND gate in this bias voltage range.
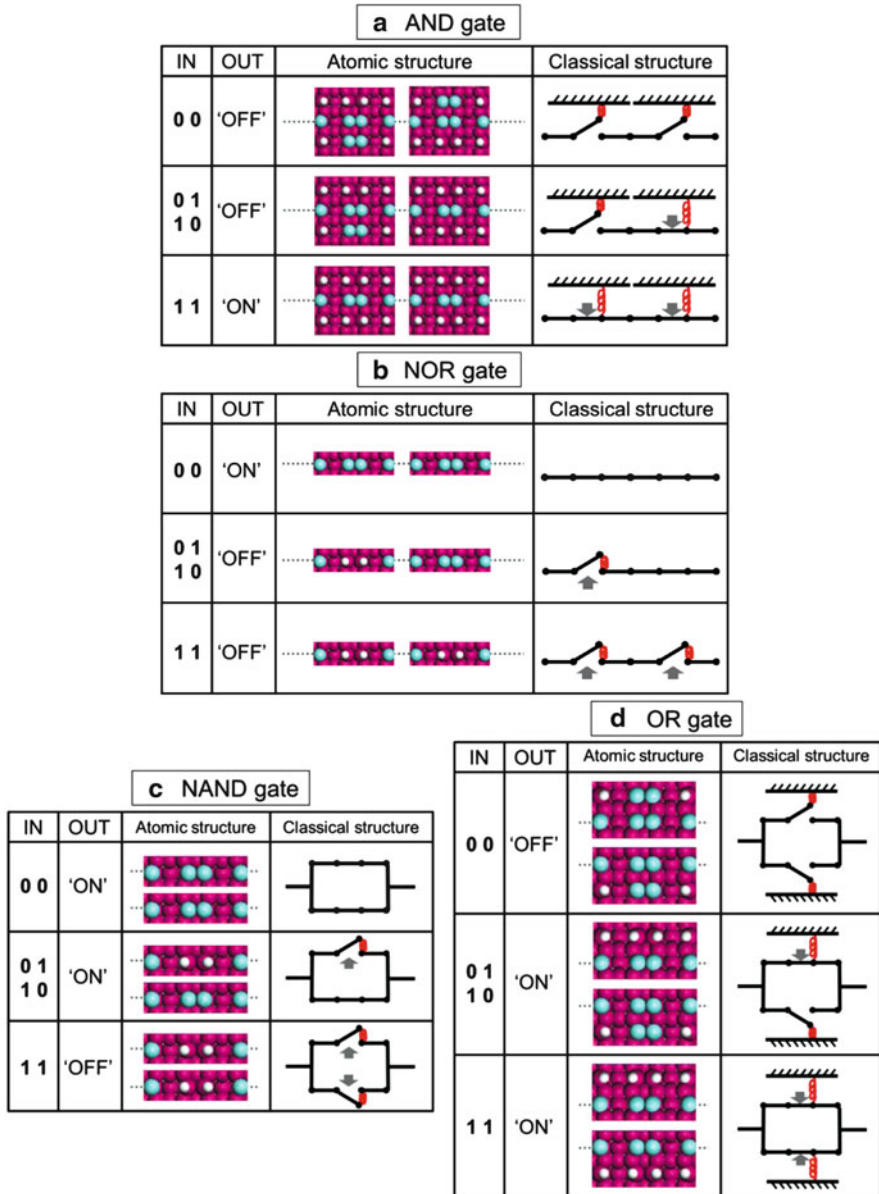
Fig. 9 Truth tables and atomic structures for (**a**) AND, (**b**) NOR, (**c**) NAND, and (**d**) OR gates. The equivalent classical structure is shown for each atomic configuration
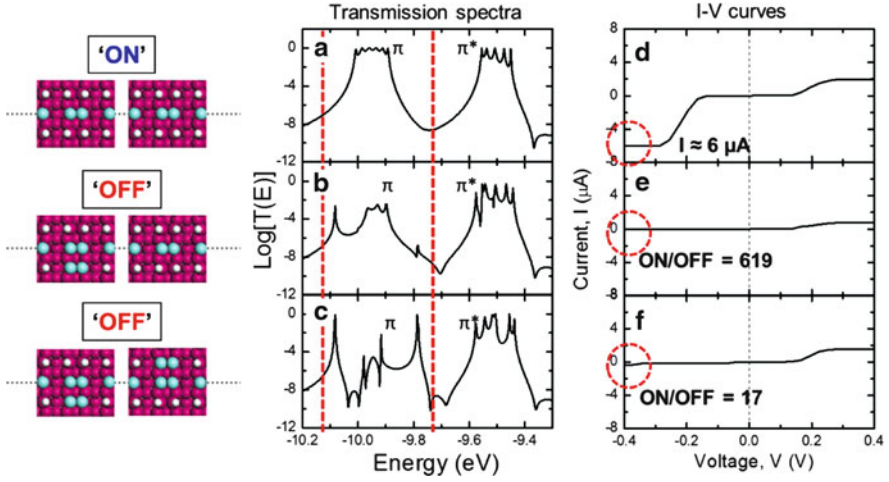
Fig. 10 $T(E)$ spectra for (**a**) '11' ('ON'), (**b**) '01' ('OFF'), and (**c**) '00' ('OFF') input configurations for the AND DB logic gate in Fig. 8d, where two followers are connected directly in series. The corresponding I–V curves are shown in (**d**)–(**f**)
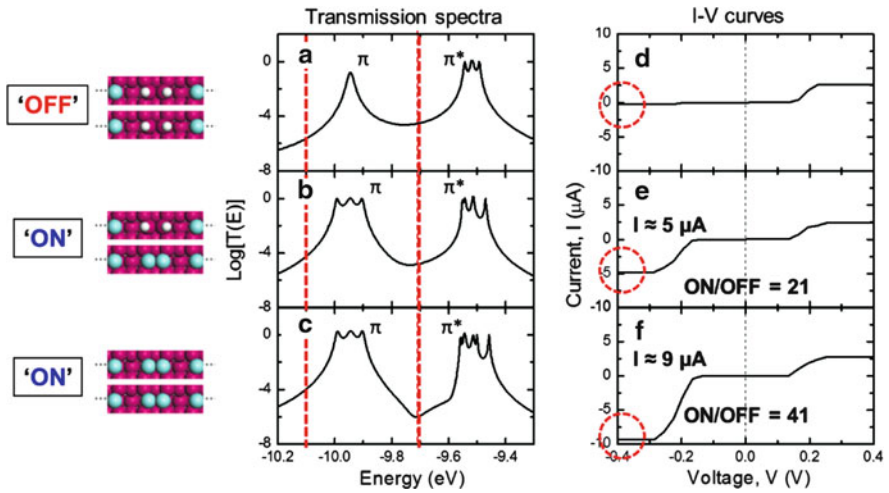
Fig. 11 $T(E)$ spectra for (**a**) '11' ('OFF'), (**b**) '01' ('ON'), and (**c**) '00' ('ON') input configurations for the NAND DB logic gate in Fig. 8f, where two inverters are connected in parallel by wide Au nano-electrodes. The corresponding I–V curves are shown in (**d**)–(**f**)

5 Summary

Four Boolean DB logic gates with two inputs and one output were designed by interconnecting follower and inverter DB switches in series or in parallel on a Si(001)-(2x1):H surface. The $I-V$ characteristics of the circuits were calculated using the ESQC quantum-transport approach and the EHMO Hamiltonian for the full atomic-scale circuits. The input strategy used in the simulations for the follower and inverter DB switches is very simple, namely, the reversible saturation and desaturation of the two DBs of a single Si dimer by adding or removing two H atoms. This concept can be tested using dI/dV tunnelling spectroscopy with a LT-UHV STM. However, more practical ways to provide the digital input to the logic gates are required. Future efforts will therefore focus on the design of more complex atomic-scale DB logic circuits and on more effective switching strategies.

References

1. Lyding, J.W., Shen, T.-C., Hubacek, J.S., Tucker, J.R., Abeln, G.C.: Nanoscale patterning and oxidation of H-passivated Si(100)-2x1 surfaces with an ultrahigh vacuum scanning tunneling microscope. Appl. Phys. Lett. **64,** 2010 (1994). doi: 0003–6951/94/64(15)/2010/3
2. Hallam, T., Reusch, T.C.G., Oberbeck, L., Curson N.J., Simmons, M.Y.: Scanning tunneling microscope based fabrication of nano- and atomic scale dopant devices in silicon: The crucial step of hydrogen removal. J. Appl. Phys. **101,** 034305 (2007). doi: 10.1063/1.2433138
3. Hitosugi, T., Hashizume, T., Heike, S., Wada, Y., Watanabe, S., Hasegawa, T., Kitazawa, K.: Appl. Phys. A **66,** S695 (1998). doi: 10.1007/s003390051224
4. Soukiassian, L., Mayne, A.J., Carbone, M., Dujardin, G.: Atomic wire fabrication by STM induced hydrogen desorption. Surf. Sci. **528,** 121 (2003). doi: 10.1016/S0039–6028(02)02620–1
5. Sautet, P., Joachim, C.: Electronic transmission coefficient for the single-impurity problem in the scattering-matrix approach. Phys. Rev. B **38,** 12238 (1988). doi: 10.1103/PhysRevB.38.12238
6. Frisch, M.J. et al.: GAUSSIAN03, Revision C.02, Gaussian, Inc., Wallingford, Connecticut (2004)
7. Perdew, J.P., Burke, K., Ernzerhof, M.: Generalized gradient approximation made simple. Phys. Rev. Lett. **77,** 3865 (1996). doi: 10.1103/PhysRevLett.77.3865
8. Kresse, G., Hafner, J.: Ab initio molecular dynamics for liquid metals. Phys. Rev. B **47,** 558 (1993). doi: 10.1103/PhysRevB.47.558
9. Wolkow, R.A.: Direct observation of an increase in buckled dimers on Si(001) at low temperature. Phys. Rev. Lett. **68,** 2636 (1992). doi: 10.1103/PhysRevLett.68.2636
10. Hoffmann, R.: An extended Hückel theory. I. Hydrocarbons. J. Chem. Phys. **39,** 1397 (1963). doi: 10.1063/1.1734456

11. Kawai, H., Yeo, Y.K., Saeys, M., Joachim, C.: Conductance decay of a surface hydrogen tunneling junction fabricated along a Si(001)-(2x1)-H atomic wire. Phys. Rev. B **81,** 195316 (2010). doi: 10.1103/PhysRevB.81.195316

12. Kawai, H., Ample, F., Wang, Q., Yeo, Y.K., Saeys, M., Joachim, C.: Dangling-bond logic gates on a Si(100)-(2x1)-H surface. J. Phys. Condens. Matter **24,** 095011 (2012). doi: 10.1088/0953–8984/24/9/095011

13. Ample, F., Duchemin, I., Hliwa, M., Joachim, C.: Single OR molecule and OR atomic circuit logic gates interconnected on a Si(100)H surface. J. Phys. Condens. Matter **23,** 125303 (2011). doi: 10.1088/0953–8984/23/12/125303

Dangling-Bond Wire Circuits on a Si(001)-(2x1):H Surface with Their Contacting Nanopads

**Francisco Ample, Hiroyo Kawai, Kian Soon Yong, Mark Saeys,
Kuan Eng Johnson Goh, and Christian Joachim**

Abstract Electron transport through atomic-scale circuits made of dangling-bond (DB) wires is discussed using the N-ESQC technique taking also into account the contacting nanopads on the circuits. The band structure of the Si(001)-(2x1):H surface is analyzed together with the ones with infinite dangling-bond wires. The exponential decay in the conductance when tunneling between two atomic wires through the hydrogenated Si(001) surface shows two different rates depending of the tunneling direction. Taking advantage of this difference in the decay rate, an efficient OR DB logic gate is presented. When the DB is connected to metallic nanopads, the circuit is behaving like a quantum box with states resonating as captured by its electronic transmission spectrum. The through-surface leakage current between the nanopads is also evaluated. Finally and in the tunneling regime, the DB electronic circuit rules are discussed using series and parallel surface circuits.

1 Introduction

The microelectronic technology has progressively miniaturized the electronic devices in the last decades because miniaturization makes the devices faster,

F. Ample (✉) · H. Kawai · K.S. Yong · K.E.J. Goh
Institute of Materials Research and Engineering, 3 Research Link, Singapore 117602
e-mail: navarrofa@imre.a-star.edu.sg

M. Saeys
Institute of Materials Research and Engineering, 3 Research Link, Singapore 117602

Department of Chemical and Biomolecular Engineering, National University of Singapore,
4 Engineering Drive, Singapore 117576

C. Joachim
Institute of Materials Research and Engineering, 3 Research Link, Singapore 117602

Nanosciences Group & MANA Satellite, CEMES-CNRS, 29 rue Jeanne Marvig,
F-31055 Toulouse, France

cheaper, and lighter or less energy consuming. Now, miniaturization is approaching the atomic scale with devices of few nanometers in dimension [1]. At this atomic scale, quantum effects will shape the physical behaviors of any devices making mandatory to respect quantum physics and even use it for the design and the running of the future atomic-scale devices and circuits. Here, a full understanding of the electronic properties of circuits and components at the atomic scale is needed.

In this chapter, we study theoretically atomic-scale circuits made by dangling-bond (DB) atomic wires and their interconnections to the external world by metallic nanopads. The hydrogen-passivated Si(001) surface was selected as a supporting surface because DB wires can be constructed by removing one by one surface H atoms by vertical scanning tunneling microscopy (STM) manipulation. Also, metallic nanopads can be transfer printed on a semiconductor surface [2] and STM manipulated individually with a precision better than 1 nm to form any multi-pads interconnection configurations at the nanoscale [3].

Electron-transport calculations were carried out using the N-ESQC general-ization of the elastic-scattering quantum chemistry (ESQC) technique [4]. The calculations were performed at the semiempirical extended Hückel molecular orbital (EHMO) level of approximation because it would demand an enormous computational power for a self-consistent method to calculate the corresponding full scattering matrix of the presented DB circuits involving thousands of atoms. But the EHMO parameters were optimized to have a good description of the electronic band structure compared to density functional theory (DFT) keeping the simple valence orbital-like structure of the semiempirical technique, so convenient for the implementation of a spatial propagator technique [5]. Electronic transmission spectra were obtained per pair of electrodes after calculating the full scattering matrix of the multi-pads multichannels tunnel junction taking into account in the central defect: the full valence electronic structure of the dangling-bond wires, the Si(100)H substrate, and their electronic interaction with the interconnecting nanopads. Electron–electron and electron–phonon interactions, inelastic scattering, and finite-temperature effects were not included. In the following, the hydrogenated Si(001) surface was modeled as a five-layer silicon slab. For simplicity, no surface relaxation leading to the well-known surface dimer buckling was considered. A buckled DB atomic wire will open a small gap in its surface electronic band structure introducing a few hundred meV nonlinearity in the corresponding current–voltage (I–V) characteristics [6] which does not alter the conclusion of this chapter.

2 Dangling-Bond Atomic Wires on a Si(001)–H Surface

An accurate description of the electronic band structure of the supporting substrate of the DB circuit is needed to characterize the electron-transport properties. Figure 1a is presenting the electronic band structure of a Si(001)-(2x1)–H surface calculated using the DFT re-parameterized EHMO Hamiltonian. An electronic band gap of 1.9 eV is obtained for the hydrogenated Si(001)-(2x1)–H surface to
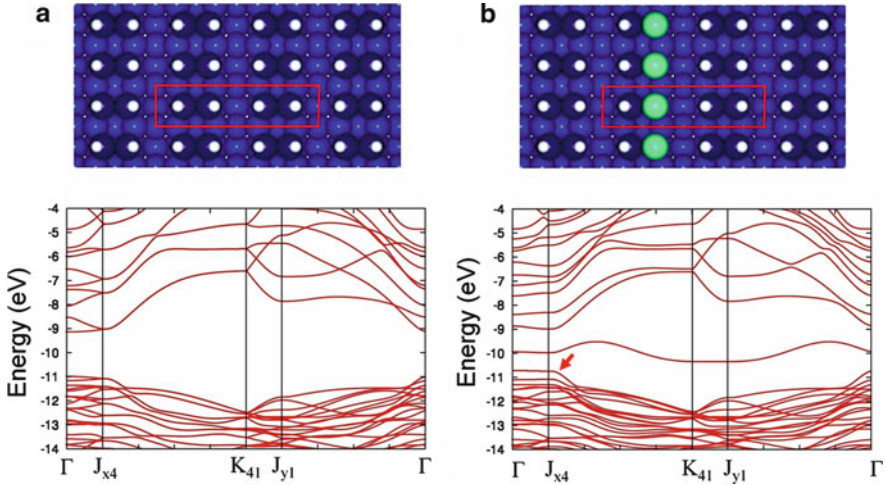
Fig. 1 The surface atomic structures and corresponding band structures for a H-passivated Si(001)-(2x1) surface slab (**a**) and a H-passivated Si(001)-(2x1) surface with an infinite dangling-bond wire (**b**). The *red rectangle* indicates the periodic unit cell used to calculate the band structure. The *small arrow* in (**b**) indicates the band which is creating the edge resonance in Fig. 6

be compared with the experimental surface gap of about 2.0 eV [7]. The detail comparison between the EHMO re-parameterized and exact DFT band structures is available in [5].

Removing individual H atoms on a H-passivated Si(100) surface by using a vertical STM manipulation mode [7] introduces electronic states in the Si(100)–H-surface band gap. If an infinite line of such dangling bonds is created, then a metallic band appears in the middle of the Si(100)–H-surface electronic band gap [6, 8]. Dangling-bond wires can be created parallel or perpendicular to the surface dimer rows direction. When an infinite H line is constructed parallel to the dimer rows, the dispersion of the band appearing in the middle of the Si(100)–H-surface gap is 0.8 eV (see Fig. 1b). The band structure of such an atomic wire cannot be described by a simple through-space coupling between the now dangling Si surface pz orbitals [5]. The through-lattice electronic coupling via the Si px subsurface orbitals plays here a major role in shaping the surface electronic band structure. As a consequence, there are two conduction channels between –9.9 and –9.5 eV and one conduction channel between –10.3 and –9.9 eV. The number of conductive channels can be counted from Fig. 2 $T(E)$ electronic transmission spectra because the DB wire is fully periodic. Then, $T(E)$ is equal to the number of ballistic channels. When two H infinite lines are removed from the same dimer row, the width of the central surface band increases to reach 1.2 eV as presented in Fig. 2c. In this case, the number of conductive channels reaches four in the central part of the transmission spectrum. Finally, if an infinite line of H is removed in a direction perpendicular to a dimer row as presented in Fig. 2d, two very narrow 0.1 eV in width bands are created as
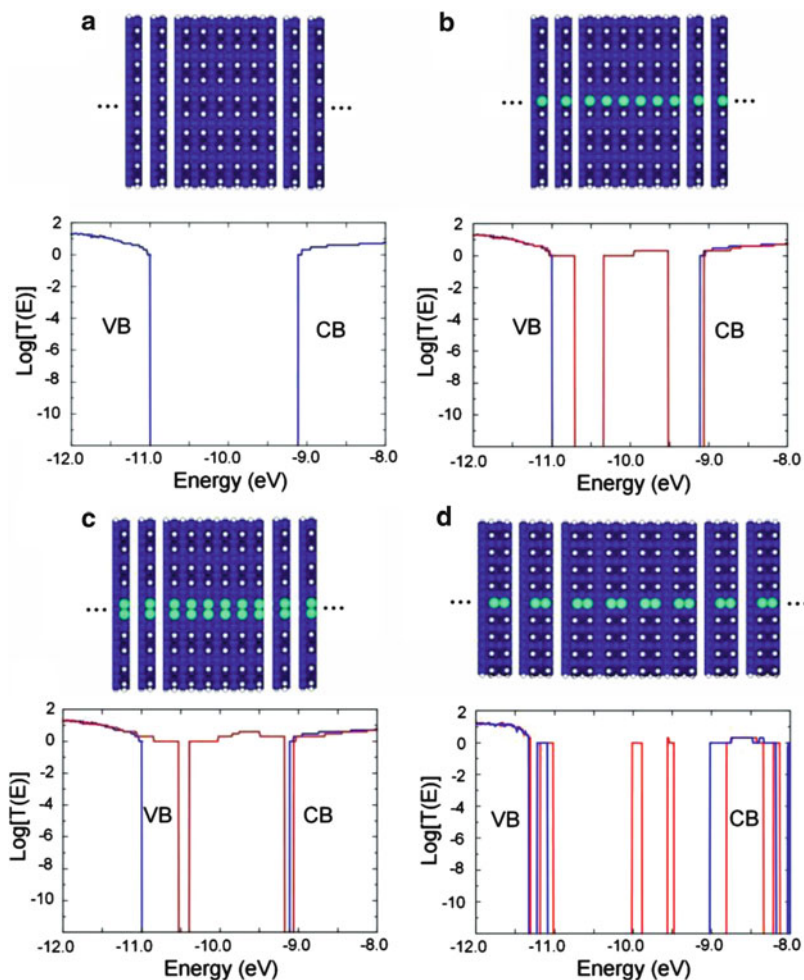
Fig. 2 Electronic transmission spectra $T(E)$ for a fully hydrogenated Si(001)-(2×1) surface in (**a**) with (**b**) an infinite line of H vacancies constructed in the dimer row direction, with (**c**) two infinite lines of H vacancies on the same dimer and also in the dimer row direction, and (**d**) an infinite line of H vacancies in a perpendicular direction to the dimer rows. *Blue line* corresponds to fully hydrogenated Si(001)–H $T(E)$. The corresponding surface atomic structures are also presented with the periodic cells (2 left and right) used for the scattering matrix calculations

indicated by Fig. 2d $T(E)$. The small interaction between two dimers along the wire in the perpendicular direction preserves a gap of 0.25 eV gap between those two DB bands of the Si(100)–H surface.

From the above analysis, we can conclude that DB atomic wires in the dimer row direction must be used when a large current intensity through the circuit is awaited. DB atomic wires in the perpendicular direction are also very interesting for

the construction of DB-surface Boolean logic gates as demonstrated in [9] because the current can be more easily controlled in intensity due to the smaller interaction between dimers.

3 An Atomic Scale OR Gate with Semi-infinite Dangling-Bond Wires

Surface H-junctions [5] can be created between dangling-bond atomic wires (see Fig. 3). The rupture of the periodicity between two semi-infinite wires created by such a junction acts as a surface potential energy barrier for the ballistic electrons transported along the atomic wire. In this case, the conductance between the two DB atomic wires playing the role of the input electrodes decreases exponentially with an increase of their interatomic distance [10, 11]:

$$G(d) = G_0 e^{-\beta d} \tag{1}$$

The inverse decay rate of this surface tunneling effect is smaller when tunneling in a dimer direction $\beta = 0.23\,\text{Å}^{-1}$ (Fig. 3a) as compared to $\beta = 0.38\,\text{Å}^{-1}$ for a surface tunneling perpendicular to the dimer rows (Fig. 3b) [10]. This is due to the small surface band gap in the dimer row direction and to the more rigid band structure in the perpendicular to the dimer row direction leading to a bigger effective mass [12]. By playing with this asymmetry in the tunneling decay between the two surface directions, it is possible to design an efficient surface atomic-scale OR gate.

Figure 4 is presenting a Boolean DB OR gate constructed using two convergent DB wires corresponding to the two logical inputs (electrodes 1 and 2) and one output (electrode 3). An efficient OR gate must operate with a large electronic transmission between the input–output electrodes and a very low transmission between the two input electrodes via the surface. As presented in Fig. 4, the two input DB wires were brought as close as possible in distance to the input atomic wire edges to compensate for the conductance decay as a function of the separation of the two atomic wires. As presented in Fig. 4b, the input–output transmission spectrum is two orders of magnitude larger than the input–input one in the energy range of the atomic wire conduction band. This surface DB circuit acts like an OR gate as confirmed by the $I–V$ characteristics of this device presented in Fig. 4c. For a 0.4-V input bias voltage, the output tunneling current reaches $4\,\mu\text{A}$ with a negligible input–input surface leakage current of $0.08\,\mu\text{A}$.

For a 0.4-V bias voltage, the maximum ballistic current which can pass through one quantum channel is around $30\,\mu\text{A}$. A 4-μA tunneling current intensity can appear quite large relative to the mechanical stability of a surface dangling-bond atomic wire. But here, the size of the atomic circuit is much smaller than the mean free path of an electron in silicon [13]. Since there is no energy loss due to inelastic scattering in a ballistic transport, the dissipation will occur mainly in the contacting nanopads.
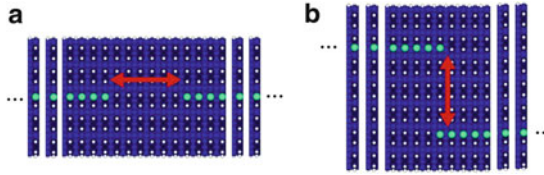
Fig. 3 Atomic structure of an H-junction constructed along dangling-bond wires (**a**) in the dimer row direction and (**b**) in the perpendicular direction. The 2 first unit cells of the semi-infinite DB wires used as contacting pads for the scattering matrix calculations are also represented
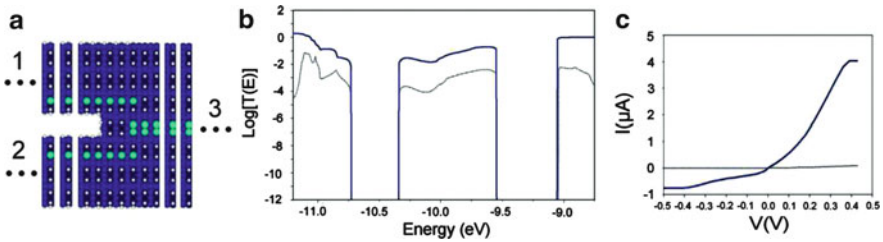
Fig. 4 (**a**) An optimized OR gate made by two convergent dangling-bond wires on the Si(100)–H surface. Electrodes 1 and 2 correspond to inputs, while electrode 3 corresponds to the output. (**b**) The corresponding $T(E)$ electron transmission spectra and (**c**) the current–voltage I–V characteristics as a function of the bias voltage. The $T(E)$ and current between atomic wires 1–3 and 1–2 are plotted with continuous and dashed lines, respectively

4 Leakage Current Between Au Nanopads Adsorbed on a Si(100)–H Surface

One way to connect our atomic scale circuits to the external world in a planar configuration is by using surface metallic nanopads since Au nanopads can be UHV transfer printed on a semiconductor surface [2] and step-by-step manipulated individually with a precision better than 0.1 nm using STM [3]

Theoretically, when the metallic contact nanopads are adsorbed on a Si(100)–H surface, a significant leakage tunneling current appears between them through the surface in its valence–conduction band gap [6]. Like in any tunneling process, the resulting junction surface conductance decreases exponentially as a function of the distance between the nanopads. In the dimer row direction, the surface conductance exponential decay with a variation of the electrode–electrode distance is characterized by a $\beta = 0.20\,\text{Å}^{-1}$ tunnel inverse decay length. As in Sect. 2, this decay rate is much bigger when tunneling through the direction perpendicular to the dimer row with $\beta = 0.42\,\text{Å}^{-1}$ [10]. This was calculated using an exceptionally long nanopads surface separation (as presented in Fig. 5) resulting from a new optimization of the N-ESQC code able to take into account thousands of surface atoms in the prospect of creating a true atomic-scale circuit simulator. In both

Fig. 5 (**a**) The atomic structure of a H-passivated Si(001) surface with 2 physisorbed Au nanopads separated by 22.7 nm. The junction is composed by 4,797 atoms. The periodicity of the semi-infinite electrodes both side of the junction is also presented. (**b**) The corresponding transmission spectrum for different electrode–electrode distances: 4.2, 8.1, 12.7, 17.3, and 22.7 nm
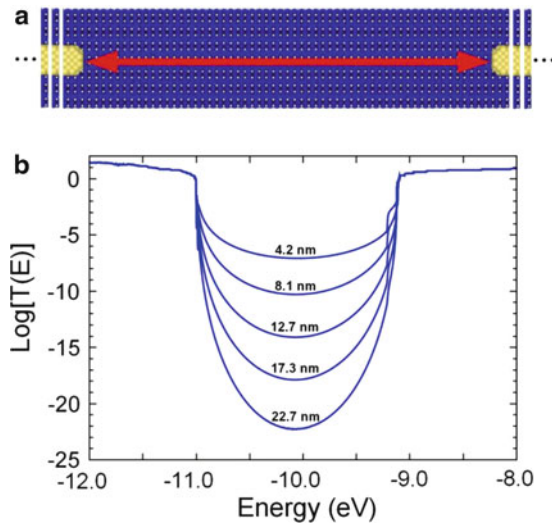
directions, the exponential decay of the conductance is much smaller with length as compared to a tunneling through vacuum: $\beta = 2.1\,\text{Å}^{-1}$. This demonstrates how the material electronic structure and the tunneling direction influence the tunneling leakage current. The design of an atomic-scale circuit must take into account this leakage current to avoid being short-circuited by the surface tunnel conductance.

The G_0 junction contact conductance can also be deduced from Eq. (1). The calculated value for a direction parallel to the dimer row is $G_0 = 31.23\,\text{nS}$ and $G_0 = 1.22\,\text{nS}$ in the perpendicular direction. These are typical values for van der Waals like contacts with no hybridization between the Au nanopads and the Si(100)–H-surface states.

5   Au Nanopads Connecting Dangling-Bond Wires

Finite Si DB wires can be connected to the external world via metallic nanopads, as presented in Fig. 6. In this case, a metallic nanopad can overlap from the top with the end of one DB wire. In this conformation, the 6s like Au atomic orbitals of a nanopad are in a good position to overlap from the top with the DB pz-like surface states. Compared with Fig. 2 junction atomic structure where the electronic contact was achieved via DB wires, the electronic homogeneity between the DB wire and its interconnection is suppressed. As a consequence, an effective energy potential barrier will appear for the ballistic electrons willing to propagate from the metallic nanopads to a DB atomic wire. The central DB wire is now like a leaky quantum box. The resulting 2-ESQC-calculated Fig. 6 $T(E)$ spectrum provides a detailed electronic spectrum of this quantum box. The tunneling resonance peaks
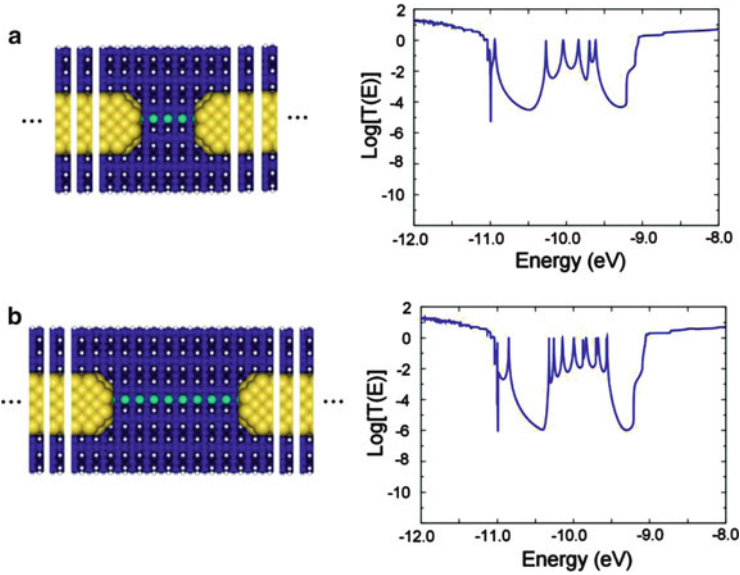
Fig. 6 Top view of a finite dangling wire connect by Au two nanopads with it corresponding surface $T(E)$ electronic transmission spectrum. Finite wire in (**a**) is composed by 5 Si dangling bonds (note that one dangling bond below each nanopad is partially obscured from view). Wire in (**b**) is composed by 10 dangling bonds. There is one peak for each dangling bond in electronic transmission spectrum for the range energy of the metallic wire band. Resonance appearing near the valence band is due to the building up of the band selected with an arrow in Fig. 1b

appear from the DB states within the energy range of the metallic wire band. There is a peak for each Si dangling bond. The metallic band of the DB wire obtained in Fig. 2 is recovered as the length of the DB wire between the two nanopads is increased toward infinity. Since there is only one conducting channel between –10.3 and –9.9 eV and two conducting channels between –9.9 and –9.5 eV, the number of resonances is bigger in the two channel range. In addition to the peaks in the wire band region, a single resonance peak also appears at the top of the valence-band edge. This resonance results from the building up of the band indicated with an arrow at the top of the valence band in Fig. 1b.

6 Circuit Rules in the Tunneling Regime

According to the Kirchhoff law, the conductance of an electrical circuit consisting of two resistances G_1 and G_2 interconnected in series is given by

$$G_{\text{series}} = \frac{G_1 G_2}{G_1 + G_2} \tag{2}$$

But Kirchhoff laws do not apply at the tunneling regime [14, 15] due to the preservation of the electronic coherence along the circuit each time one electron is transferred indicating that there are no inelastic interactions nor decoherence along this circuit. In the tunneling transport regime, the overall electronic transmission of two quantum electronic pathways with transmission coefficient $T_1(E)$ and $T_2(E)$ interconnected in series is given by [15]:

$$T_{\text{series}}(E) = T_1(E)T_2(E) \tag{3}$$

In this equation, the final electronic transmission is being filtered by each unit of the series meaning that (1) is a direct consequence of the tunnel series law (3) applied for a regular and identical network of tunneling barrier connected in series [10]. Applying (3) for the case of DB wires interconnected using metallic nano-pads, Fig. 7c is presenting the surface atomic structure of two short DB wires connected in series via a central Au nano-island also physisorbed on Si(100)–H. For the complete "Au-nanopad to Au-nanopad surface" tunnel junction and including the central Au nano-island in the scattering matrix calculations, the calculated Fig. 7c transmission spectrum is similar to the one obtained by applying (3). Some differences appear because (a) the central Au nano-island is coupling more DB wire states together than a direct DB wire–DB wire interaction and because (b) the H-tunnel junction underneath the central Au nano-island is quite short which favors the through-surface leakage current. There are also additional tunneling resonances coming from the Au central nano-island itself, for example, around –10.4 eV in energy.

When the DB wires are connected in parallel using a common metallic nanopad per interconnection node, the parallel superposition law giving the overall transmission through the circuit is

$$T_{\text{parallel}}(E) = T_1(E) + T_2(E) \tag{4}$$

In this case, the parallel Kirchhoff circuit law is preserved because for a ballistic regime in the nanopads, the incident electronic Bloch waves splits into two normalized waves before being scattered through the two tunnel paths. After the scattering events, the superposition of the two tunnels paths happens after only in the nanopad because the two tunneling paths are independent. The limitation of (4) occurs when the elementary tunneling paths have each a large $T(E)$ in such a way that the sum of the two saturates to unity. This is, for example, the case at each tunnel resonance which cannot go further than unity. The DB circuit presented in Fig. 8 follows this superposition rule (4) because the surface DB wires are directly in interactions with the metallic nanopads and also maintained far away enough to avoid any lateral electronic interactions between the 2 DB wires through the surface.

The superposition rule (4) is not valid when the two tunneling paths to be superposed are interconnected directly in the tunnel junction and away from the metallic nanopads. In this case, a third term must be added to (4) because it is now
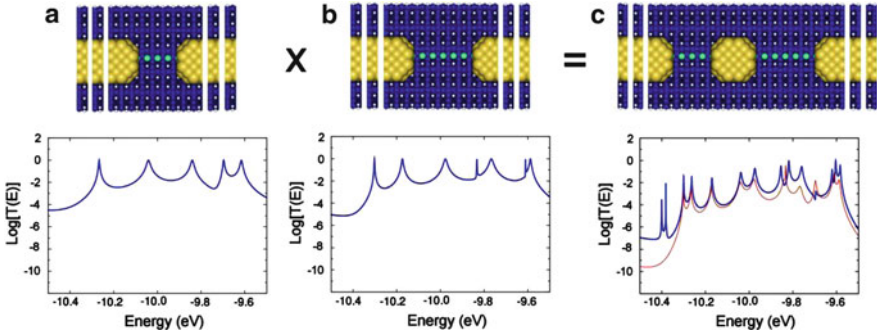
Fig. 7 The atomic structures with their corresponding transmission spectra for a finite wire of 5 dangling bonds in (**a**), 7 dangling bonds in (**b**), and the corresponding circuit interconnected in series in (**c**). Note that one dangling bond below each nanopad is partially obscured by this top view. *Blue line* corresponds to the original transmission spectrum, while *red line* corresponds to the resulting transmission spectrum when the rule of Eq. (3) is applied. Structure in (**c**) is composed by 1,786 atoms
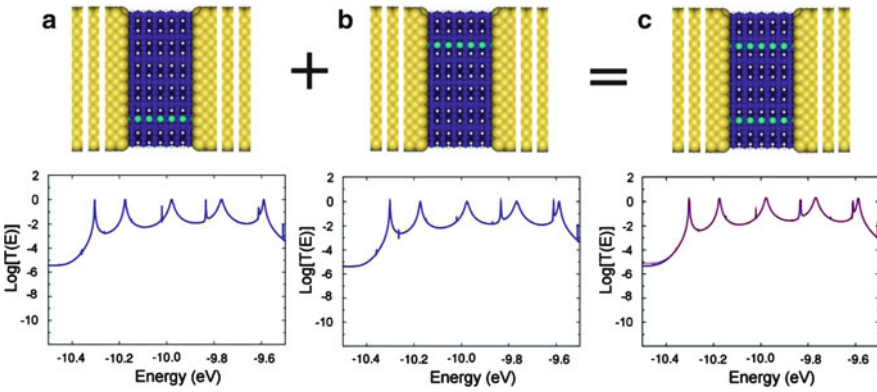
Fig. 8 Circuit configurations with their corresponding transmission spectra for a finite wire of 7 dangling bonds in (**a**) and (**b**) and the corresponding circuit connected in parallel in (**c**). Note that one dangling bond below each nanopad is partially obscured from view. *Blue line* corresponds to the original transmission spectrum, while *red line* corresponds to the resulting transmission spectrum when the rule of Eq. (4) is applied

the electronic coupling between the two nanopads introduced by each tunneling path and not the transmission which must be superposed [15]. A third term must be added as follows:

$$T_{\text{parallel}}(E) = T_1(E) + T_2(E) + 2\sqrt{T_1(E)T_2(E)} \tag{5}$$

A circuit of 2 DB wires connected in parallel in the tunneling region is presented in Fig. 9. Since the two tunneling paths are here identical and according to (5), the overall transmission spectrum must be four times the one of each path. This is
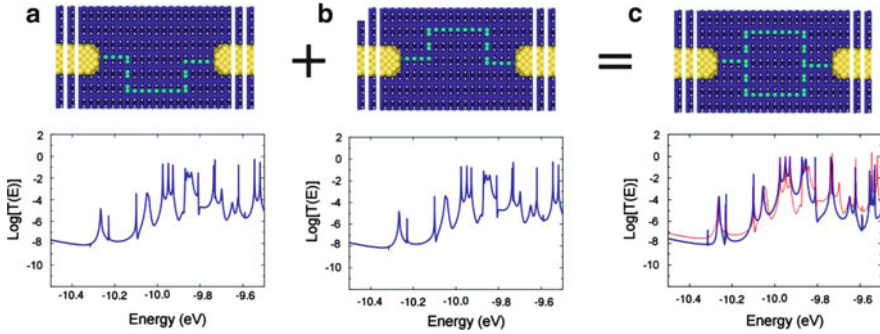
Fig. 9 Atomic-scale circuits with their corresponding transmission spectra for different quantum electronic pathways (**a**) and (**b**) and the two electronic pathways connected in parallel (**c**) sharing two nodes inside the scattering zone. *Blue line* corresponds to the original transmission spectrum, while *red line* corresponds to the resulting transmission spectrum when the rule of Eq. (5) is applied. Structure in (**c**) is composed by 2,583 atoms

presented in Fig. 9 where the overall 2-ESQC-calculated $T(E)$ spectrum matches quite well the superposition of the two independently calculated $T(E)$, one per tunneling branch.

7   Conclusions

The design of a DB circuit must take into account the full electronic structure as a whole in a complete multielectrode multichannel scattering approach. All the parts on the DB circuit that is the supporting surface, the DB atomic wires, and the nanopads are not independent of each other and must all be taken into account in the design of circuit. For example, as shown in Sect. 4, the interactions of the DB wires with the metallic nanopads perturb the entire transmission spectrum, and the functionality of the circuit can be significantly altered [10].

The design of a DB atomic-scale circuit must also consider the leakage current through the supporting surface to avoid being short-circuited. As shown in Sects. 2 and 3, the leakage current can be different depending of the propagation direction. An appropriate spacing and routing on the surface must be selected to reach the desired circuit function.

Kirchhoff classical laws are not applicable in the tunneling regime, and new circuit rules must be considered when designing a surface DB circuit. Kirchhoff classical law remains if the node of connection is in the ballistic region, but if the node of connection is in the scattering region, then circuit rules in the tunneling region must be applied.

The DB atomic-scale circuits presented here are involving thousands of atoms. The calculation of the multichannel scattering matrix in a self-consistent method

would demand an enormous computational power. At the semiempirical level, the N-ESQC approach is able to deliver reliable prediction on the circuit electronic behavior of such large surface circuits. The parameters of the semiempirical Hamiltonian used to describe this circuit can now be optimized using DFT or more sophisticated quantum chemistry approaches and transferred to the semiempirical Hamiltonian without changing the exact scattering matrix calculation performed in N-ESQC.

References

1. The international Technology Roadmap for Semiconductors: 2011 Update: http://www.itrs.net/Links/2011ITRS/Home2011.htm
2. Deng, J., Troadec, C., Kim, H.H., Joachim, C.: J. Vac. Sci. Technol. B **28**, 484 (2010)
3. Yang, J., Deng, J., Chandrasekhar, N., Joachim, C.: J. Vac. Sci. Technol. B **25**, 1694 (2007)
4. Ami, S., Hliwa, M., Joachim, C.: Chem. Phys. Lett. **367**, 662 (2003)
5. Kawai, H., Yeo, Y.K., Saeys, M., Joachim, C.: Phys. Rev. B **81**, 195316 (2010)
6. Doumergue, P., Pizzagalli, L., Joachim, C., Altibelli, A., Baratoff, A.: Phys. Rev. B **59,** 159100 (1999)
7. Soukiassian, L., Mayne, A.J., Carbone, M., Dujardin, G.: Surf. Sci. **528**, 121 (2003)
8. Watanabe, S., Ono, Y.A., Hashizume, T., Wada, Y.: Phys. Rev. B **54**, R17308 (1996)
9. Kawai, H., Ample, F., Wang, Q., Yeo, Y.K., Saeys, M., Joachim, C.: J. Phys. Condens. Matter **24**, 095011 (2012)
10. Ample, F., Duchemin, I., Hliwa, M., Joachim, C.: J. Phys. Condens. Matter **23**, 125303 (2011)
11. Lafferentz, L., Ample, F., Yu, H., Hecht, S., Joachim, C., Grill, L.: Science **323**, 1193 (2010)
12. Joachim, C., Magoga, M.: Chem. Phys. **281**, 347 (2002)
13. Lundstrom, M.: Fundamentals of Carrier Transport, 2nd edn, Chap. 8. Cambridge University Press, Cambridge (2000)
14. Magoga, M., Joachim, C.: Phys. Rev. B **59**, 16011 (1999)
15. Ami, S., Joachim, C.: Phys. Rev. B **65**, 155419 (2002)

Theory of Inelastic Transport Through Atomic Surface Wires

Serge Monturet and Christian Joachim

Abstract With the help of state-of-the-art local probe microscopy together with the capability of synthetic chemistry to produce a wide swathe of molecules, the functionalization of adsorbed species on surfaces can be achieved; they can notably play the role of logic gates[1, 2]. To contact them, nanoscale wires have been studied both experimentally [3] and theoretically [4, 5] regarding their structural and electronic properties. However, the role that inelastic effects may play during the transport through these wires is still an open question. The aim of this chapter is to give an overview of the theoretical methods that can be set up to elucidate the problem of mechanical heating of the surface atomic wires by conduction electrons.

1 Prologue: Nonadiabatic Effects During the Transport

When dealing with electronic currents passing through a single quantum object to probe either their electronic or vibrational structure or simply to transport electrons, one can imagine two sorts of interconnect configurations: firstly, a tip-molecule-surface experiment, corresponding to a "vertical" situation, where, for a low bias voltage, electrons tunnel through the molecule, and secondly, a "planar" situation, as in the case of surface supported atomic dangling bond wires connected to metallic surface nano-pads. The first case is generally a tunneling transport regime and the second a pseudo-ballistic transport regime. It cannot be a fully ballistic since, in general, the interconnection metallic pads are not made out of the same materials as the atomic wire. This results in a quantum box effect even when the electronic coupling between the metallic pads and the surface atomic wire is large enough for the average conductance over the bias voltage range to be close to a quantum of conductance.

S. Monturet (✉) · C. Joachim
CEMES/CNRS, 29 rue Jeanne Marvig, 31055, Toulouse, France
e-mail: monturet@cemes.fr; joachim@cemes.fr

A quasi-1D conductor can be built using a hydrogen-passivated silicon surface by desorbing H atoms in a row with the help of the tip of a scanning tunneling microscope. A line of constructed dangling bonds plays the role of an atomic-scale wire at the surface, and a current can flow through it when the line is voltage biased. From this starting point, several questions arise: What is the maximum value of the current? What happens if the electrons heat up the wire during transport? Due to the supporting surface, is the wire mechanically stable enough to support current intensities as large as a few microamps? These questions indicate the need for calculating the electronic transport taking into account the inelastic interactions of the electrons transferring through a surface atomic wire and the nuclei of the surface structure.

The basic problem one encounters when exploring the correlated motion of electrons and ions is the breakdown of the Born–Oppenheimer approximation. When the electronic and vibrational degrees of freedom are separated in the Schrödinger equation, the nuclei move in a potential energy surface that is given by the electronic Schrödinger equation, solved for the electronic coordinate and considering the ionic one as a parameter. Physically, this approximation takes advantage of the important mass difference between a typical nucleus and an electron and assumes that the electrons, because they are faster than nuclei, will immediately and adiabatically reorganize and follow the movement of the ion cores. Mathematically, the Schrödinger equation is not analytically solvable, even for small systems, but the Born–Oppenheimer approximation leads to a dramatic simplification that permits numerical solving, analysis, and interpretation of a great variety of physical phenomena.

However, nonadiabatic phenomena are ubiquitous. For instance, one can consider cases where ions are light and move fast enough so that their velocity is to a certain extent comparable to that of the electrons. Additionally, in the Born–Oppenheimer picture, the movement of the nuclei cannot induce electronic transitions, this process can occur especially when the electronic energy levels are particularly close to each other. This case is naturally found in condensed matter physics: one can consider a metal for instance. Given its characteristic band structure, around the Fermi level, an arbitrarily small amount of energy given to the electronic degrees of freedom by, say, an adsorbed vibrator can lead to an electronic excitation, *i.e.*, the creation of an electron-hole pair.

In the case of atomic surface wires, our approach is based on a time-dependent perspective on heating. Most methods addressing the problem of electron transport with interactions at the nanoscale are based on energy-dependent (time-independent) Green's functions. Under certain approximations, the electron-vibration interaction can be diagrammatically solved using Dyson's equation. Several perturbative techniques leading to the calculation of transmission probabilities as well as currents include the first Born approximation and the self-consistent Born approximation [6, 7] (or alternatively the lowest order expansion [8]). Among them, only the latter is particularly suitable for treating transport properties because it guarantees the conservation of the current. Note that heating at the nanoscale has also been treated using first-principles calculations using other techniques to obtain the forces and the current [9–11].

To explore these quantum inelastic effects, a harmonic oscillator will be considered and discussed when an electron transfer event takes place through this system. In the first section of this chapter, a time-dependent calculation, based on the mixed classical/quantum Ehrenfest approximation, is presented. In the second section, a simple valence-bond-like model is presented in order to treat the electron-vibration interaction form a complete quantum perspective, exploring the new transition rules in the tunneling transport regime.

2 Mixed Quantum/Classical Ehrenfest Dynamics

In the Ehrenfest approach, we take advantage of the time-dependent perspective to analyze the dynamics of a coupled electron-vibrator system. Moreover, in contrast with the approaches mentioned above, this mixed quantum/classical method is non-perturbative regarding the electron-vibration coupling. Hereafter, the descriptions of the method and model are first presented in detail; then, some results are shown and discussed. Finally, the possible extensions of this work will be mentioned.

2.1 Tight-Binding Model Hamiltonian

Consider a three-state tight-binding model where a particular site, here the central site, is coupled to a vibration. The Hamiltonian reads:

$$h(R) = \begin{pmatrix} 0 & t & 0 \\ t & E(R) & t \\ 0 & t & 0 \end{pmatrix} \tag{1}$$

where R is the coordinate of a nucleus and E is the on-site energy on the central site (the other being set to zero). The basis set used to define the h(R) matrix elements is not the eigenbasis set of the system. It is built to describe the interaction of the left and right states with contacting nano-pads. The electronic coupling between these states is labeled t. $E(R)$ is the sum of the on-site energy e of this particular site and the potential energy of the vibrator, described as a classical harmonic oscillator. It can be written as

$$E(R) = e + \frac{1}{2} K (R - R_{eq})^2 \tag{2}$$

where K is the spring constant of the oscillator and R_{eq} its equilibrium position.

The method consists in propagating an electron wave packet through the system, initializing it on the fist site and letting it evolve according to the time-dependent Schrödinger equation as $E(R)$ takes different values depending on the position of the oscillator. The wave packet preparation is supposed to be provided by a left

Fig. 1 Displacement and
velocities of the nucleus
calculated using Ehrenfest
dynamics. The main figure
represents the time-dependent
evolution; in the inset, the
same quantities are given as
phase diagram
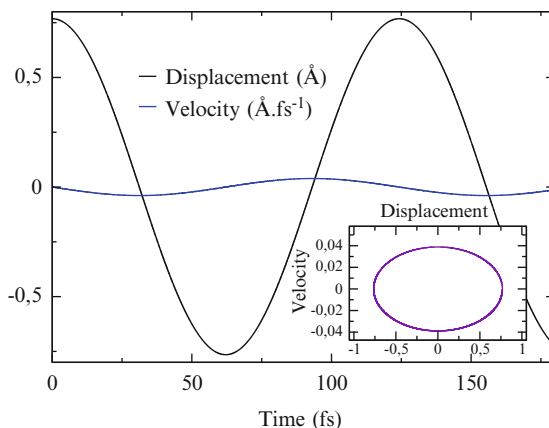
metallic nano-pad. The tunneling current intensity passing through the vibrator can
always be evaluated by taking the effective Rabi oscillation frequency through this
vibrator [12]. Notice that the detail of the wave packet preparation process is not of
interest here. At the same time steps, Newton equation is solved for R. The forces
applied on the nucleus are, first, the force of the oscillator itself, that maintains the
vibrator around its equilibrium position, and second, a quantum force due to the
presence of an electronic population in the central site.

It is important to comment here on the nature of the interplay between the
electron and the nucleus. On the one hand, the Hamiltonian evolution of the
electronic wave packet is modified at each time step because $E(R)$ takes different
values depending on the movement of the ion. The Hamiltonian is actually redefined
at each time step by the new value of R—and thus of $E(R)$—leading to a new set
of eigenvalues and eigenvectors. The Hamiltonian is explicitly dependent on R,
therefore implicitly dependent on time. On the other hand, the motion of the nuclei
is governed by the force that electrons exert on it. An example of ion dynamics is
presented in Fig. 1, where positions and velocities are given as a function of time
and as a phase diagram in the inset.

2.2 Numerical Results

The forces that drive the oscillator are depicted in Fig. 2a for different values of
the e parameter, which corresponds to an on-site energy shift. The low-frequency
oscillation is due to the harmonic potential felt by the nucleus, while the high-
frequency signal is the signature of the forces exerted by the electron. Clearly, a
change in the frequency is observed between the red and black curves as a function
of e. As can be seen in Fig. 2b, for a different value of e, the electronic populations
in the vibrating site show different behaviors in amplitude as well as in frequency.
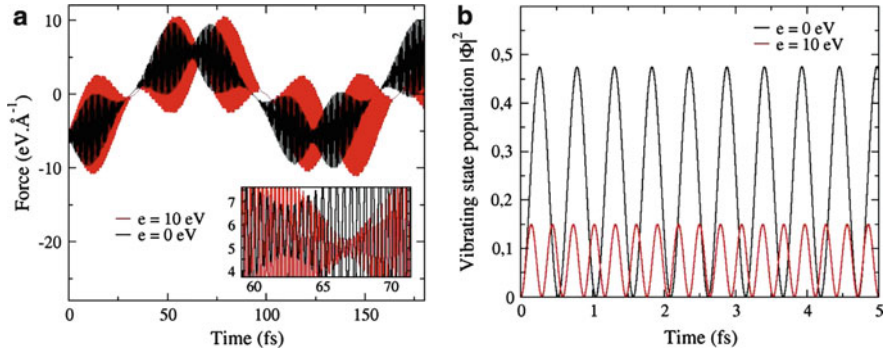
Fig. 2 (a) Time evolution of the total force applied on the nucleus. The two curves correspond to two different values of the parameter e and (b) electronic population on the vibrating site.
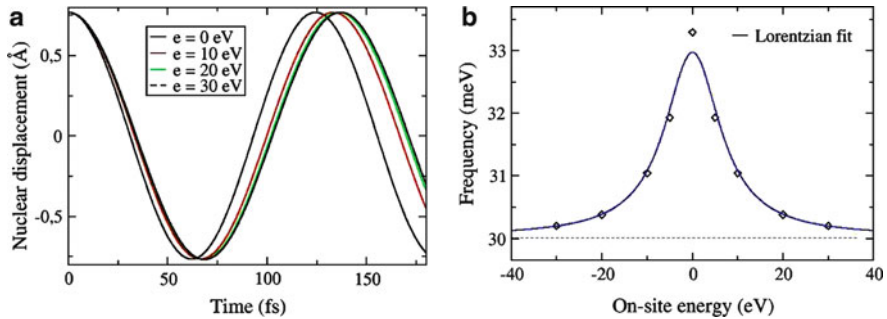
Fig. 3 (a) Different nuclear displacements as a function of the e parameter and (b) the effect of the value of e on the frequency of the ionic vibration. The Lorentzian fit is a guide to the eye

We interpret the e-dependent change in frequency of the ionic vibration as the renormalization of the spring constant K due to the additional force exerted on the nucleus by the electron.

An example of different nuclear oscillations as a function of e are presented in Fig. 3a. The effect of the value of e is better shown thanks to the plot of the frequency of the oscillation versus e in Fig. 3b. When e has a rather big value, the central site is barely populated; then the forces applied on the nucleus are small, and its motion is essentially governed by the spring constant. It is found therefore that the frequency of the oscillator is the one given by the spring alone, 30 meV in the case of Fig. 3b as shown by the dotted base line. When e vanishes, the population becomes important in the vibrating site, and the forces acting on the nucleus add up to the force of the spring, producing a shift in frequency. This effect and the fact that the system is symmetric for positive and negative values of e explain the shape of the curve depicted in Fig. 3b. Note that the Lorentzian fit (blue curve) is merely a guide to the eye.

Fig. 4 Forces applied to each nuclei as a function of time. The low-frequency oscillation is due to the harmonic potential felt by each nucleus, while the high-frequency signal is the signature of the forces exerted by the electron
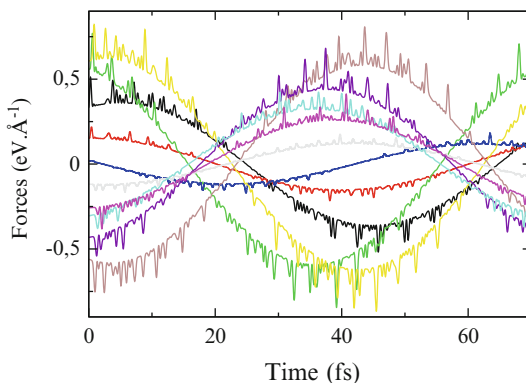
Fig. 5 Energy conservation diagram. The *black* and *blue* curves represent the kinetic energy of the nuclei, respectively, the *violet* curve is the electronic energy, and the *red* one is the total energy, clearly conserved throughout the propagation
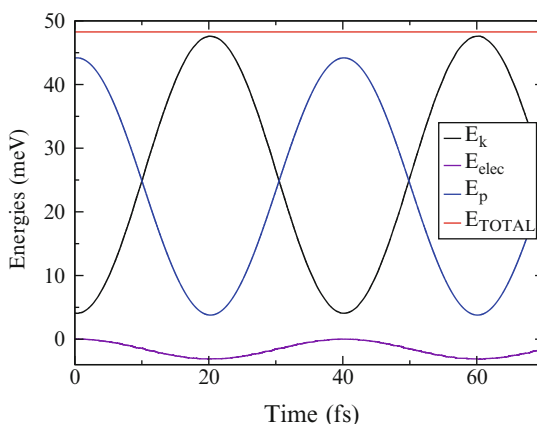
This model can now be easily generalized to several oscillators in series representing the vibrating structure of a surface atomic wire. The nuclear dynamics of a chain of ten harmonic oscillators is shown in Fig. 4, where the total force on each nuclei is represented versus time. Interestingly enough, one can observe that the kicks the electron gives to the ions are correlated to the position of the ion at that particular time. When a nucleus is in the region of positive displacement, the kicks appear like peaks, while when the displacement is negative, the kicks are rather dips.

Finally, an important result regarding the accuracy of the Ehrenfest dynamics code is the plot showing the conservation of the total energy at all times. The Fig. 5 convincingly illustrates that the extra kinetic energy (black curve) given to the ions by the electrons through the mechanism described above is compensated by a change in the electronic energy (violet curve). In this case, the electronic energy becomes negative to compensate an increase in kinetic energy relative to potential energy (blue curve); see, e.g., the behavior of the curves around 20 fs. The red curve corresponds to the total energy and is the sum of the other three.

As seen in Fig. 5, the kinetic energy of the full chain oscillates with time but always recovers its maximal value. The effective temperature is therefore expected

to be conserved. Although the Ehrenfest dynamics has the ability to go beyond the Born–Oppenheimer approximation, this technique does not capture the whole nonadiabatic effects [13]. To calculate accurately the heating of the nuclei, one needs to go beyond the Ehrenfest picture. Pursuing the task of improving the model can thus be achieved by considering that when, from the many-body general Schrödinger equation, we render classical the movement of the ions, an imaginary term comes into the electronic Schrödinger equation. This term is responsible for relaxation. On the other hand, in Newton equation, an additional force appears that can play the role of a friction force in the case of vibrational relaxation or an excitation in the case of nuclear heating [14]. Very similar approaches have also been developed with the help of the Liouville-von Neumann formalism [15, 16]. In references [17, 18], the use of the so-called "small amplitude moment expansion" leads to correlated electron-ion dynamics (CEID) capable of describing the heating of vibrations under steady current.

3 Quantum Dynamics for Inelastic Transport

In the previous section, the nuclei were treated classically. Consider now the quantification of the vibrational degrees of freedom with the electron transfer process treated as a quantum superexchange process. In such a case, the probability to excite the vibration must be triggered by the motion of the electronic wave packet through the system. To explore this vibrational transition driven by an electron transfer process, a simple six-state quantum system has been considered (see the inset in Fig. 6). The canonical basis set used to describe this process is simply the tensor product of the electronic quantum states (labeled $|n\rangle$) used in the previous section times the two ground and first excited states of the central quantum vibrator (label $|m\rangle$). This central vibrator was simply a classical harmonic oscillator in the above section. The vibrational coupling α, the electronic coupling q, the vibrational quantum $\Delta\omega$, and the on-site energies are the parameters to be explored in such a toy Hamiltonian. On the canonical basis set $|n, m\rangle$, it reads

$$H = \begin{pmatrix} 0 & q & 0 & 0 & 0 & 0 \\ q & e & q & 0 & \alpha & 0 \\ 0 & q & 0 & 0 & 0 & 0 \\ 0 & 0 & 0 & \Delta\omega & q & 0 \\ 0 & \alpha & 0 & q & e + \Delta\omega & q \\ 0 & 0 & 0 & 0 & q & \Delta\omega \end{pmatrix} \tag{3}$$

Starting at time $t = 0$ on the state $|1, 0\rangle$, *i.e.*, with an electron located on the left electronic state and the vibrator in its ground state, the time-dependent Schrödinger equation was solved numerically, looking for a resonant evolution between this initial state and the $|3, 1\rangle$ target state defined by the electron transferred to the

Fig. 6 Transition probability as a function of the energy shift e for various values of the vibrational coupling α and the vibrational quantum $\Delta\omega$. The electronic coupling has been set to $q = 10$ meV. The inserted scheme represents the six-state model used in the calculation
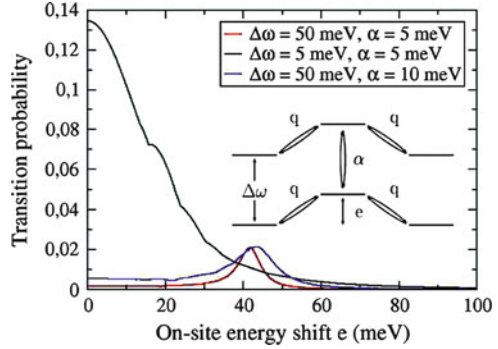
right electronic state with the vibrator in its first excited state. Such a transition depends on the resonant characteristics of the electron transfer process between the left and the right electronic states as presented in Fig. 6. For a given q, $e = 0$ is characteristic of a resonant evolution through the intermediate vibrating state and a large resonance can be observed. For nonzero values of e, the Rabi oscillations represent a tunnel evolution, *i.e.*, the occupation probability of the intermediate states $|\,2,0\rangle$, and $|\,2,1\rangle$ is very small, but a resonance can still be observed. This demonstrates that even in a tunneling regime there is a resonance condition for a vibrational transition to occur on the central quantum vibrator depending on the frequencies of the Rabi-like time-dependent quantum evolution between the left and the right electronic states.

To explore this effect and identify which characteristic frequency of the Rabi evolution controls the vibrational transition, an exhaustive examination of the behavior of the transition probability $|\,\langle 3,1\,|\,e^{-iHt}\,|\,1,0\rangle\,|^2$ can be performed versus all the parameters of the six-state quantum system. For this purpose, we have first to consider the standard example of the time-dependent Rabi oscillations of our system forced to remain in its ground vibrational state. In this case, the quantum state space can be reduced to a simple three-state subsystem described by the following Hamiltonian h:

$$h = \begin{pmatrix} 0 & q & 0 \\ q & e & q \\ 0 & q & 0 \end{pmatrix} \qquad (4)$$

Describing the transition probability $|\,\langle 3,1\,|\,e^{-iHt}\,|\,1,0\rangle\,|^2$ in terms of the frequencies obtained by analytically solving time-dependent Schrödinger equation for h is sensible because the vibrational coupling α is small compared to the electronic coupling q.

Let us initialize the wave function in the first site $|\,a\rangle$ and calculate the time-dependent coefficient of the wave function $\Psi(t)$ on the central site $|\,\Phi\rangle$ writing in atomic units:
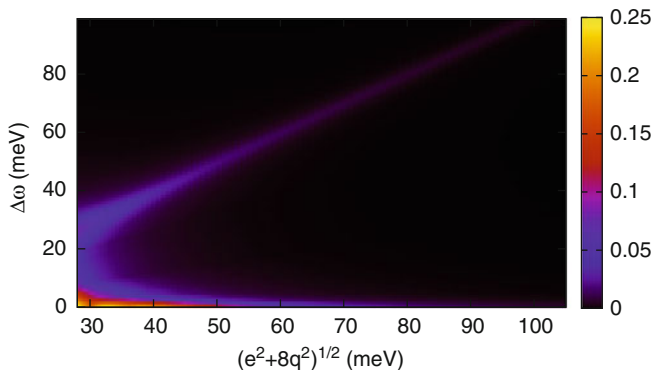
Fig. 7 Transition probability as a function of the driving frequency $\sqrt{e^2 + 8q^2}$ and of the quantum of vibration. The parameters for this calculations are $q = 10$ meV and $\alpha = 5$ meV. e takes values in the interval $[0, 100]$ meV

$$C_\phi(t) = \langle \phi \mid \Psi(t) \rangle = \langle \phi \mid e^{-iht} \mid a \rangle \tag{5}$$

The squared modulus of this coefficient gives the population of the central state:

$$\mid C_\phi(t) \mid^2 = \frac{2q^2}{e^2 + 8q^2}(1 - \cos(\sqrt{e^2 + 8q^2}t)) \tag{6}$$

where the frequency in the cosine is the variable considered in the following.

The transition probability shown in Fig. 7 is plotted as a function of the quantum of vibration and the oscillation frequency of the population of the electronic central state as calculated in (6). The higher values of the transition are of course obtained for $\Delta\omega = 0$, *i.e.*, when the levels are degenerate. But there is also a full range of possible values of $\Delta\omega$ for a transition to occur when e is nonzero, *i.e.*, in a pure nonresonant tunneling electron transfer regime. This gives the linear behavior of the maxima across the color plot of the Fig. 7 (in violet). This nonresonant excitation of the vibration is generally not considered in tunneling inelastic effects. Therefore, to obtain some population transfer to the higher levels of the central oscillator, one has to fulfill the following condition:

$$\Delta\omega = \sqrt{e^2 + 8q^2}. \tag{7}$$

This new transition rule indicates that the excitation of the transition from the ground to the first excited state of the central vibrator is due to the oscillation of the population of the central electronic state. This oscillation is the quantum analog of an electromagnetic field triggering the transition from the ground to an excited state of a two-state quantum system in interaction with this electromagnetic field [19]. There is no relation between this intrinsic quantum excitation and the alignment of the initial $\mid 1, 0 \rangle$ or the target $\mid 3, 1 \rangle$ states with $\Delta\omega$. The time-independent

prefactor in (6) also plays a role since for large values of e relative to q, this prefactor decreases in amplitude, lowering the transition probability as seen in Fig. 7. This new transition rule has now to be extended to a chain of quantum oscillators excited by a tunneling electron transfer process.

4   Epilogue

In this chapter, some methods employed for calculating the electronic transport taking into account the interactions with the nuclei have been presented. In particular, a simple model of a vibrator coupled to an electron transfer process has been presented in a mixed quantum/classical way. Although the Ehrenfest dynamics is capable of describing nonadiabatic phenomena, the heating is not correctly captured within this approach. Further developments are necessary to introduce irreversibility in the way the electronic and the nuclear degrees of freedom interact.

A second approach has been presented, where the electronic and the vibrational degrees of freedom of the problem are treated in the same quantum way. Here, it is the oscillation frequency of the population of the central intermediate electronic state which is driving the vibrational transition. This frequency is the quantum analog of the classical formula of the transition probability for a two-state quantum system interacting with an electromagnetic field. Of course, other time-dependent one electron studies have been developed in the context of transport with interactions with the nuclei [12, 20]. The novelty of the present study relies on the fact that the perspective used focuses on the effect of the intrinsic quantum process frequency of the system. The details of the influence of the amplitude of these intrinsic oscillation coefficients ought to be checked in future developments especially for a chain of quantum oscillators representing a surface atomic wire.

References

1. Soukiassian, L., Mayne, A.J., Carbone, M., Dujardin, G.: Atomic wire fabrication by STM induced hydrogen desorption. Surf. Sci. **528**, 121 (2003)
2. Ample, F., Duchemin, I., Hliwa, M., Joachim, C.: Single OR molecule and OR atomic circuit logic gates interconnected on a Si(100)H surface. J. Phys.: Condens. Matter **23**, 125303 (2011)
3. Hitosugi, T., Heike, S., Onogi, T., Hashizume, T., Watanabe, S., Li, Z.-Q., Ohno, K., Kawazoe, Y., Kitazawa, K.: Jahn-Teller distortion in dangling-bond linear chains fabricated on a hydrogen-terminated Si(100)-2x1 surface. Phys. Rev. Lett. **82**, 4034 (1999)
4. Cho, J.-H., Kleinman, L.: Nature of lattice distortion in one-dimensional dangling-bond wires on Si and C. Phys. Rev. B **66**, 235405 (2002)

5. Kawai, H., Yeo, Y.K., Saeys, M., Joachim, C.: Conductance decay of a surface hydrogen tunneling junction fabricated along a Si(001)-(2x1)-H atomic wire. Phys. Rev. B **81**, 195316 (2010)
6. Frederiksen, T., Brandbyge, M., Lorente, N., Jauho, A.-P.: Inelastic scattering and local heating in atomic gold wires. Phys. Rev. Lett. **93**, 256601 (2004)
7. Frederiksen, T., Brandbyge, M., Jauho, A.-P.: Inelastic transport theory from first principles: methodology and application to nanoscale devices. Phys. Rev. B **75**, 205413 (2007)
8. Paulsson, M., Frederiksen, T., Brandbyge, M.: Modeling inelastic phonon scattering in atomic- and molecular-wire junctions. Phys. Rev. B **72**, 201101(R) (2005)
9. Di Ventra, M., Lang, N.D.: Transport in nanoscale conductors form first principles. Phys. Rev. B **65**, 045402 (2001)
10. Chen, Y.-C., Zwolak, M., Di Ventra, M.: Local heating in nanoscale conductors. Nano Lett. **3**, 1691 (2003)
11. Brandbyge, M., Stokbro, K., Taylor, J., Mozos, J.-L., Ordejon, P.: Origin of current-induced forces in an atomic gold wire: a first-principles study. Phys. Rev. B **67**, 193104 (2003)
12. Renaud, N., Ratner, M.A., Joachim, C.: A time-dependent approach to electronic transmission in model molecular junctions. J. Phys. Chem. B **115**, 5582 (2011)
13. Horsefield, A.P., Bowler, D.R., Fisher, A.J.: Open-boundary Ehrenfest molecular dynamics: towards a model of current induced heating in nanowires. J. Phys.: Condens. Matter **16**, L65 (2004)
14. Joachim, C.: H_2 intramolecular evolution: non-adiabatic quasi-classical local analysis. Mol. Phys. **52**, 1191 (1984)
15. Berkelbach, T.C., Reichman, D.R., Markland, T.E.: Reduced density matrix hybrid approach: an efficient and accurate method for adiabatic and non-adiabatic quantum dynamics. arXiv:1110.0490v1 [cond-mat.stat-mech]
16. McEniry, E.J., Bowler, D.R., Dundas, D., Horsfield, A.P., Sánchez, C.G., Todorov, T.N.: Dynamical simulation of inelastic quantum transport. J. Phys.: Condens. Matter **19**, 196201 (2007)
17. McEniry, E.J., Wang, Y., Dundas, D., Todorov, T.N., Stella, L., Miranda, R.P., Fisher, A.J., Horsfield, A.P., Race, C.P., Mason, D.R., Foulkes, W.M.C., Sutton, A.P.: Modelling non-adiabatic processes using correlated electron-ion dynamics. Eur. Phys. J. B **77**, 305 (2010)
18. Horsefield, A.P., Bowler, D.R., Fisher, A.J., Todorov, T.N., Sánchez, C.G.: Correlated electron-ion dynamics: the excitation of atomic motion by energetic electrons. J. Phys.: Condens. Matter **17**, 4793 (2005)
19. Rabi, I.I.: Space quantization in a graying magnetic field. Phys. Rev. **51**, 652 (1937)
20. Monturet, S., Lorente, N.: Inelastic effects in electron transport studied with wave packet propagation. Phys. Rev. B **78**, 035445 (2008)

Part IV
Quantum Controlled Logic Gates

Single Molecule Can Calculate 1,000 Times Faster than Supercomputers

Kenji Ohmori

Abstract This short account summarizes our recent achievements in coherent control and its applications to information processing with molecular wavefunctions. A combination of designed femtosecond laser pulses and wave-packet interferometry implements ultrafast Fourier transform executed in 145 fs.

1 Introduction

The wavefunctions of electrically neutral systems can replace electric charges of the present Si-based circuits, whose further downsizing will soon reach its limit where current leakage will cause heat and errors with insulators thinned to atomic levels. Atoms and molecules are promising candidates for these neutral systems, in which the population and phase of each eigenstate serve as carriers of information. A shaped ultrashort laser pulse can access many eigenstates simultaneously within a single atom or molecule, manipulating the amplitude and phase of each eigenstate individually to write more than one million distinct binary codes in the angstrom space [1–3]. Molecules in particular are now expected to be promising components to develop scalable quantum computers [4]. The development of I/O and logic gates with molecules should be meaningful for us to be prepared for such a future scalable system. It is therefore important to study information processing with molecular eigenstates for both high-density classical information processing and quantum information processing. Here we demonstrate a logic gate based on the temporal evolution of a wavefunction. An optically tailored vibrational wave packet in the iodine molecule implements four- and eight-element discrete Fourier transforms [2]. Our ultrahigh-precision wave-packet interferometry [5–9] has retrieved complete

K. Ohmori

Institute for Molecular Science, National Institutes of Natural Sciences, Myodaiji, Okazaki 444-8585, Japan
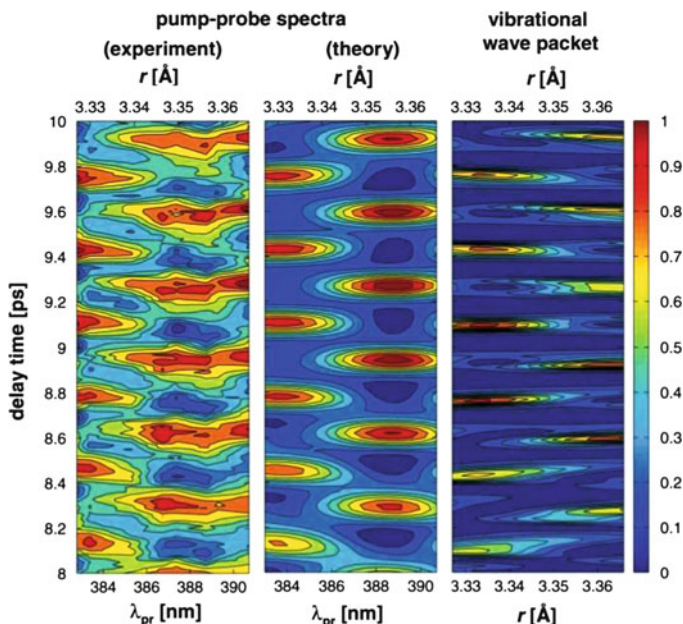
Fig. 1 Spatiotemporal images of the interference of vibrational wave packets in the iodine molecule visualized experimentally (*left column*) and the theoretical simulation of the experimental signal (*middle column*) and the wave packets (*right column*). λ_{pr} and r denote the wavelength of the probe pulse and the internuclear distance, respectively. Reprinted figure with permission from [7]

sets of amplitude and phase information stored in the input and output states, verifying the transform has been securely executed with arbitrary real and imaginary inputs. The evolution time is 145 fs, which is shorter than the typical clock period of the current fastest Si-based computers by 3 orders of magnitudes.[1] We have also developed another class of logic gates based on quantum interference among different molecular eigenstates induced by a strong nonresonant femtosecond laser pulse, which is referred to as strong-laser-induced quantum interference [3].

2   Ultrahigh-Precision Wave-Packet Interferometry

We have developed high-precision wave-packet interferometry to be utilized to implement logic gates with molecular wavefunctions. Figure 1 shows the spatiotemporal images of the interference of two vibrational wave packets in the iodine molecule that we have visualized [7]. It is seen that we have succeeded in visualizing

---

[1] The maximum clock rate of IBM Power 6 is 5.0 GHz, giving its clock period to be 200 ps.

Fig. 2 Spatiotemporal images of the wave-packet interference measured (*left*) and simulated (*right*) with the relative phases of the two laser pulses to be (**a**) $0°$, (**b**) $90°$, (**c**) $180°$, and (**d**) $270°$. The color scaling is common within each set of measured or simulated images; the maxima of those two sets have the same color. Reprinted figure with permission from [9]. Copyright 2009 by the American Physical Society
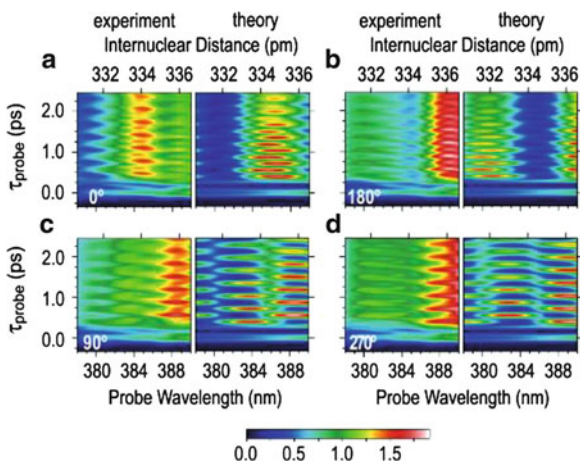
the spatiotemporal images with precisions on the picometer spatial and femtosecond temporal scales. Theory predicts that the spatiotemporal images of the wave-packet interference could be actively designed by tuning the timing of two femtosecond laser pulses that produce the wave packets. We have developed our homemade optical interferometer, referred to as an "attosecond phase modulator (APM)," that produces a pair of two femtosecond laser pulses whose interpulse delay is tuned and stabilized on the attosecond timescale [5, 6, 8, 9]. This APM has allowed us to actively design the spatiotemporal images by tuning the relative phase of the two femtosecond laser pulses in steps of $90°$ [9]. Those actively tailored spatiotemporal images are shown in Fig. 2. It is seen that we have succeeded in tailoring the spatiotemporal images on the picometer and femtosecond scales.

3   Ultrafast Fourier Transform with a Femtosecond Laser-Driven Molecule

We have utilized this high-precision wave-packet interferometry to develop a molecular computer in which a single molecule can calculate faster than the current fastest supercomputer [2]. Figure 3 shows a scheme of this ultrafast computing. Four- or eight-element inputs have been encoded with a shaped femtosecond laser pulse into the complex coefficients of vibrational eigenstates of the iodine molecule. The temporal evolution of the superposition of those vibrational eigenstates has executed discrete Fourier transform. The output of the transform has been retrieved with our high-precision wave-packet interferometry. The evolution time is 145 fs, which is shorter than one clock period of IBM Power 6 by three orders of magnitude (see Footnote 1).
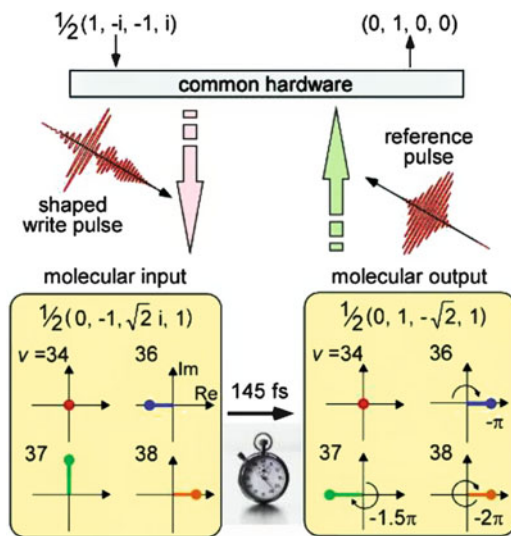
Fig. 3 Schematic of the ultrafast Fourier transform. The common transform matrices could be operated for any arbitrary inputs and outputs, respectively, by the indicated hardware. Reprinted figure with permission from [2]. Copyright 2010 by the American Physical Society

4 Strong-Laser-Induced Quantum Interference

The molecular computer described above is indebted to the spontaneous temporal evolution of the molecule, so that the performance of the computer is dominated by the molecular property which we are unable to control actively. In order to implement universal logic gates, it is necessary to develop a method to actively modify the codes input to the complex coefficients of molecular eigenstates. We have recently discovered a new phenomenon referred to as "strong-laser-induced quantum interference" in which multiple vibrational eigenstates of the iodine molecule are coherently mixed by a strong nonresonant femtosecond laser pulse in the near-infrared region, as is schematically illustrated in Fig. 4 [3]. This mixing induces the interference of those different eigenstates, so that their complex coefficients are actively modified. The strong-laser-induced quantum interference that we have discovered is not specific to vibrational eigenstates of a molecule, but universal to the superposition of any eigenstates of a variety of quantum systems, being a new tool for quantum logic gates and providing a new method to manipulate wave packets with femtosecond laser pulses in general applications of coherent control.
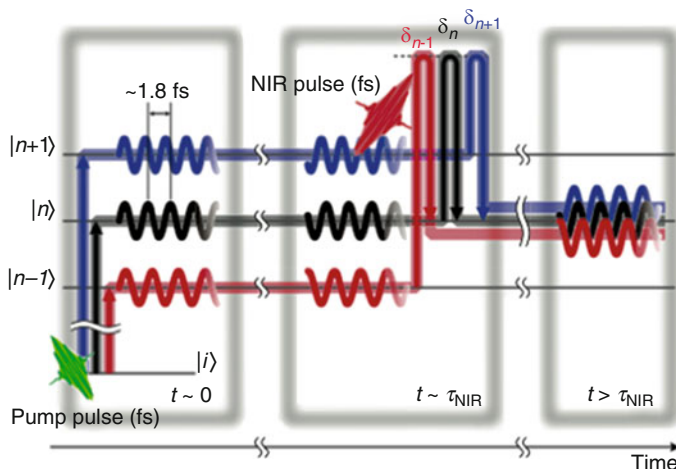
Fig. 4 Schematic of the strong-laser-induced quantum interference. Starting from a common initial state i, there are multiple pathways to the final state n. Those multiple pathways interfere with each other. Reprinted figure with permission from [3]

References

1. Ohmori, K.: Wave-packet and coherent control dynamics. Annu. Rev. Phys. Chem. **60**, 487–511 (2009). doi:10.1146/annurev.physchem.59.032607.093818

2. Hosaka, K., Shimada, H., Chiba, H., Katsuki, H., Teranishi, Y., Ohtsuki, Y., Ohmori, K.: Ultrafast Fourier transform with a femtosecond-laser-driven molecule. Phys. Rev. Lett.**104**, 180501 (2010). doi:10.1103/PhysRevLett.104.180501

3. Goto, H., Katsuki, H., Ibrahim, H., Chiba, H., Ohmori, K.: Strong-laser-induced quantum interference. Nat. Phys. **7**, 383–385 (2011). doi:10.1038/nphys1960

4. DeMille, D.: Quantum computation with trapped polar molecules. Phys. Rev. Lett. **88**, 067901 (2002). doi:10.1103/PhysRevLett.88.067901

5. Ohmori, K., Sato, Y., Nikitin, E.E., Rice, S.A.: High-precision wave-packet interferometry with HgAr dimers. Phys. Rev. Lett. **91**, 243003 (2003). doi:10.1103/PhysRevLett.91.243003

6. Ohmori, K., Katsuki, H., Chiba, H,. Honda, M., Hagihara, Y., Fujiwara, K., Sato, Y., Ueda, K.: Real-time observation of phase-controlled molecular wave-packet interference. Phys. Rev. Lett. **96**, 093002 (2006). doi:10.1103/PhysRevLett.96.093002

7. Katsuki, H., Chiba, H., Girard, B., Meier, C., Ohmori, K.: Visualizing picometric quantum ripples of ultrafast wave-packet interference. Science **311**, 1589–1592 (2006). doi:10.1126/science.1121240

8. Katsuki, H., Hosaka, K., Chiba, H., Ohmori, K.: Read and write amplitude and phase information by using high-precision molecular wave-packet interferometry. Phys. Rev. A **76**, 013403 (2007). doi:10.1103/PhysRevA.76.013403

9. Katsuki, H., Chiba, H., Meier, C., Girard, B., Ohmori, K.: Actively tailored spatiotemporal images of quantum interference on the picometer and femtosecond scales. Phys. Rev. Lett. **102**, 103602 (2009). doi:10.1103/PhysRevLett.102.103602

Realization of Complex Logic Operations at the Nanoscale

R.D. Levine and F. Remacle

Abstract The principles underlying the implementation of complex logic operations at the molecular scale are outlined. Different types of logic machines can be implemented. The simplest ones are combinational circuits, in which logic gates are connected in order to compute a logic function. We discuss several physical realizations of combinational circuits operating on Boolean or multivalued variables, as well as cascade thereof, implemented in a solid state or in a biochemical environment. The next level of complexity in logic machines is that of finite-state machines, which, in addition to a combinational unit, possess a memory unit so that the outputs depend not only on the inputs but also on the state of the memory. They therefore offer the possibility to implement parallel logic operations. Physical realizations of electrically and optically addressed finite-state machines are discussed. Special emphasis is given to electrical addressing which is currently able to implement logic on a single atom and even to concatenate.

R.D. Levine
The Fritz Haber Research Center for Molecular Dynamics, The Institute of Chemistry,
The Hebrew University of Jerusalem, Jerusalem 91904, Israel

Departments of Chemistry and Biochemistry and of Molecular and Medical Pharmacology
and the Crump Institute for Molecular Imaging, University of California, Los Angeles, CA 90095
e-mail: rafi@fh.huji.ac.il

F. Remacle (✉)
The Fritz Haber Research Center for Molecular Dynamics, The Institute of Chemistry,
The Hebrew University of Jerusalem, Jerusalem 91904, Israel

Department of Chemistry, University of Liège, B4000 Liège, Belgium
e-mail: fremacle@ulg.ac.be

195

1 Introduction

Molecules, nanosystems, dopants in bulk material, etc., exhibit multiple (quasi)stationary discrete energy states by virtue of their confined size. Electrical charge is also discrete. So is spin that we will not discuss further here. We provide examples where the ability to selectively address and probe the discrete states allows implementing complex logic operations at the nanoscale. In our approach, the nanosystem itself acts as a logic combinational circuit or a finite-state machine, and the logic is implemented at the hardware level [1, 2]. Information processing is executed by exploiting the specific time evolution of the system induced by the inputs. The outputs are the final states selectively reached as a response to the inputs. We therefore make an advantage of the nanoscale, which is imposed by the cardinal technological need to reduce the size of the circuit. We not only perform logic at the nanoscale but our devices can and do perform much more complex operations that a switch. So we not only go beyond the switching paradigm but we also intrinsically increase the complexity of the logic that is for us implemented at the hardware level.

The most straightforward way to go beyond the switching paradigm is to implement Boolean combinational circuits directly on states of the confined system that response selectively to perturbations and produce a readable output. Since the early work of de Silva [3, 4], there were numerous demonstrations of logic gates operating at the molecular scale; for reviews, see [5–10]. Typically, the inputs are provided chemically and/or optically or electrochemically to chromophoric or electroactive systems in solution or organized as a monolayer on surfaces. This mode of operation, while well suited for monitoring and intelligent sensing, does not provide a direct mean of scaling down the size of the device; typically an ensemble of several thousands or millions of molecules are responding, nor does it allow to easily address the need to concatenate the devices, that is, to cascade the output of one device as an input to the next one. In the field of DNA computing [11–20], addressing biosystems based on artificial DNA or RNA systems does solve the problem of the cascade: one DNA strand can be released from a DNAzyme complex acting as a device and serve as an input to the next device [21]. Another recent example of cascade is based on electrochemical addressing [22].

Logic gates and combinational circuits can also be implemented at the nanoscale by electrically addressing molecules or nanoparticles trapped in well-defined nanogaps [23–28]. While this approach truly allows to downsize the devices and to address fewer molecular complexes, ideally a single one, it often suffers from a lack of reproducibility, as it is a challenge to produce identical devices at the nanoscale. Here too, the problem of the cascade and of scalability has not yet received practical solutions.

One route that we explored and on which we report below is that of a molecular solid-state approach, based on single-atom transistor (SAT) [29–31]. In that approach [32–35], the logic gates are implemented by addressing electrically

the electronic levels of a single-dopant atom embedded in a transistor. These devices are fully CMOS compatible, stable, and reproducible and can be concatenated. We show below that one can use the CMOS machinery to cascade the output of a SAT as an input voltage for the next one. This approach is also scalable.

Optical addressing is a very promising route for selectively exciting the discrete states of a system and probing the outputs in order to realize gates and combinational circuits [36–38]. When implemented using short to ultrashort pulses, it can lead to very fast rates of information processing. The recent developments in the synthesis of attopulses [39–41] in particular offer the promise to be able to selectively excite and probe directly electron dynamics with a petahertz rate of information processing before dissipation due to the onset of the motion of the nuclei takes place [42]. It remains however a challenge to immobilize the molecular systems and move to solid-state optically addressed devices. A promising route in that direction is that of coherently exciting transitions of dopant atoms in solid. This approach combines the advantages of atoms in the gas phase (i.e., spectrally narrow transitions) and solids (i.e., large storage density and scalability). It has mainly been developed for data storage [43, 44] but recently applied to the realization of logic gates [45].

Beyond Boolean combinational circuits, the complexity of logic operations can be further increased in different ways. One is to depart from Boolean logic and move to multivalued logic, which allows the processing of more information per logic operation. The molecular scale is particularly well suited to do so because several discrete states can typically be addressed and probed. However, the price is to be able to physically distinguish between more than two possibilities and to design more complex logic gates than in binary logic, that is, a two-ternary-input logic gate has nine possible outputs. We will discuss below examples of multivalued logic gates and circuits, mainly ternary logic circuits. Base 3 was shown to be the best compromise between the exponential increase in information processing and storage and the assumed linearly increasing cost in physical resources to be able to do so [46].

Another promising route to higher throughput is to operate simultaneously on several states, thereby achieving parallelism at the molecular scale. For implementing parallelism, we rely on the model of finite-state machines [47,48], which possess a memory unit where the states of the machine are stored and a combinational circuit that processes inputs and the states of the machine to produce new states and outputs; see Fig. 1. When the memory of the finite-state machine consists of several states, they are all addressed in parallel to produce a new set of states for the next operation. The logic is processed by the time evolution of the system that has to be described at the quantum level because of the size of the system. However, the parallelism that we propose is quasi-classical [49,50] and does not rely on encoding information in the phase of the wave function. As such it is less prone to noise than quantum information processing [51].

Fig. 1 A schematic
representation of a finite-state
machine
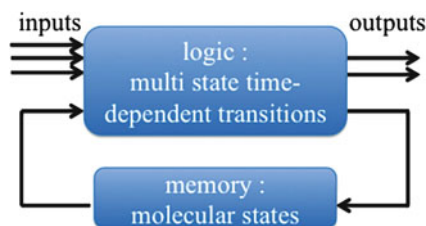
2 Cascade of Logic Devices

To be efficient and scalable, the cascade of logic devices must be such that the
physical nature of the output of one device can be transmitted to the next device
as an input. For scalability to be possible, one needs to be able to achieve gain,
that is, to amplify the signal when going from one device to the next. We review in
this section two very different schemes that satisfy these requirements: a full adder
implemented by cascading two single-atom transistors [33] and cascades of gates
realized on DNAzyme systems [21]. Both examples use Boolean logic and can be
generalized to multivalued logic. The devices operate in different environments and
on different time scales but share the common features of implementing directly
the gates at the hardware level and being able to sustain cascade because there is a
possibility to restore the signal with gain. In the SAT, gain is achieved using a load
resistor, while in the biodevice, gain is achieved by amplifying the DNA strands that
serve as input/output. A noteworthy aspect is that the SAT is literally a single-atom
device.

The cascade of full adders implemented on SATs is fully CMOS compatible and
uses in an essential way the ability to electrically address severable electronic states
of the dopant atom in the SAT; see Fig. 2. In addition to the ground state (GS), the
dopant in its neutral state has two exited electronic states that can be resolved in a
current map [29, 30]. There are several ways to implement a full addition, either by
concatenation of two half adders [37, 38, 52, 53] or by directly mapping the truth
table of the full addition on the level structure of the system [54].

A full adder has three inputs [55], the two digits to be added, x and y, and the
carry in, C_{in}, from the previous addition cycle and two outputs, the sum out that
needs to be read and the carry out. To cascade two full adders, one needs to transmit
the carry out of one addition as a carry in to the next device. The SAT is used to
perform the addition of the two input numbers, x and y, as shown in Fig. 3. One
important point in the design of the scheme is that the SAT performs an arithmetic
addition, as is shown in Fig. 3c; see also the truth table, Table 1. The two inputs are
encoded in the values of the two voltages, V_b, the applied bias and V_G, the gate
voltage. The values are chosen so that the measured current is zero for the (0,0)
input since for these values of V_b and V_G, the system is in the Coulomb blockade
region, I_1 for the (1,0) and (0,1) inputs (one level, the GS, contributes to the current)
and $I_2 = 2I_1$ for the (1,1) input (two levels, the GS and the first ES contribute to
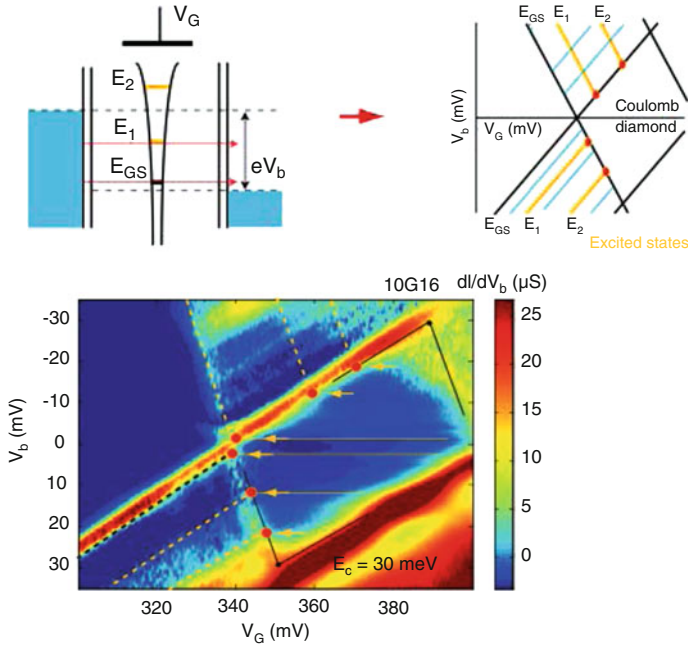
Fig. 2 (**a**) Energy scheme for the addressing of the electronic levels of a dopant atom in by a source drain (V_b) and a gate voltage (V_G) in a transistor configuration. (**b**) The corresponding scheme for the Coulomb map and (**c**) the measured Coulomb map [29] for a single As dopant atom in a FinFET transistor

the current). The carry in is provided through a carry-in buffer (CIB, see Fig. 4) which consists in a FET with a load resistor that lets current through only when the arithmetic sum (a.s. in Table 1) is larger than one. The carry-in FET and the SAT are placed in parallel, so that the total current out of the unit is the arithmetic sum, $x + y + C_{in}$. The FET and the SAT are sufficient to perform the full addition with gain. The arithmetic sum, a.s., is then decoded into a binary number to get the sum out by applying the voltage corresponding to the a.s., V_i, to a SET with a Coulomb blockade periodicity such that current goes through only when the voltage V_i corresponds to the a.s. of 1 or 3. As shown in Fig. 4, in total, four transistors, a SAT, a SET for decoding the sum out, the CIB, and a load resistor for gain and providing the carry in, are needed to perform a full addition. These are to be compared to the 28 needed for the best CMOS implementation [56]. See [33] for the experimental demonstration of a cascade of two full adders.

We next illustrate the implementation of a cascade in a completely different context, using a biosystem based on DNAzymes [21]. This system presents the necessary requirements for concatenation too: the output of one gate can serve as an input for the next gate because inputs and outputs are of the same chemical nature, a DNA strand. This is what is usually very difficult to achieve in

Fig. 3 Scheme for the implementation of the full adder showing which levels of the dopant atom contribute to the current for the different pairs of inputs. Adapted from [33]
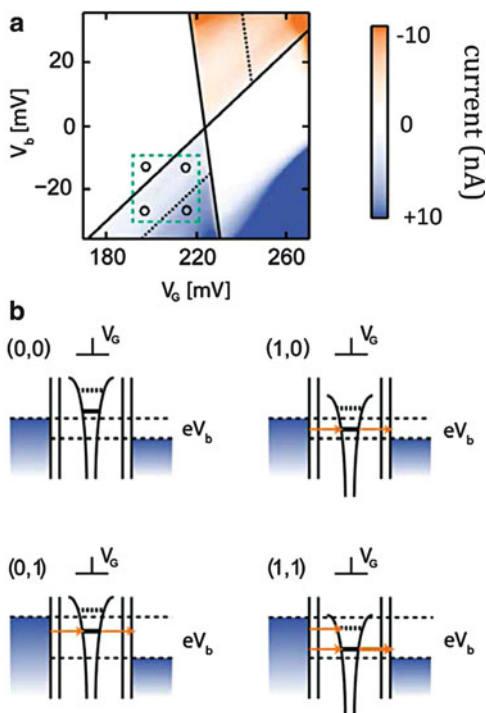
Table 1 Truth table of a full adder

X	y	C_{in}	a.s.	C_{out}	S_{out}
0	0	0	0	0	0
1	0	0	1	0	1
0	1	0	1	0	1
1	1	0	2	1	0
0	0	1	1	0	1
1	0	1	2	1	0
0	1	1	2	1	0
1	1	1	3	1	1

The three inputs are the two binary numbers x and y and the carry in, C_{in}. The next column is the arithmetic sum, a.s. The measure of the current of the SAT gives the arithmetic sum which is encoded in base 4. The next two columns are the two binary outputs of a full adder, the carry out, C_{out}, and the sum out, S_{out}. Note that the binary number (C_{out}, S_{out}) is the arithmetic sum. The part shaded in gray corresponds to the entries for which the C_{in} is 1

optical/chemically addressed molecular logic systems. Moreover, because it is possible to amplify DNA, the DNAzyme-based devices show gain. While the previous example based on single-atom transistors can be integrated in CMOS architectures, cascades of DNAzyme gates offer prospects of applications in bioengineering and nanomedicine [57].

Fig. 4 The circuit of 4 transistors that performs the full addition. The SAT_i, FET_i and RL_i (part **a**, encircled in blue dashes) are sufficient to perform a full addition in base 4, transmit the C_{in} for the next addition, and have gain. The SET_i (part **b**, encircled in orange dots) is necessary only if one needs to decode the a.s. into a binary number. Adapted from [33]
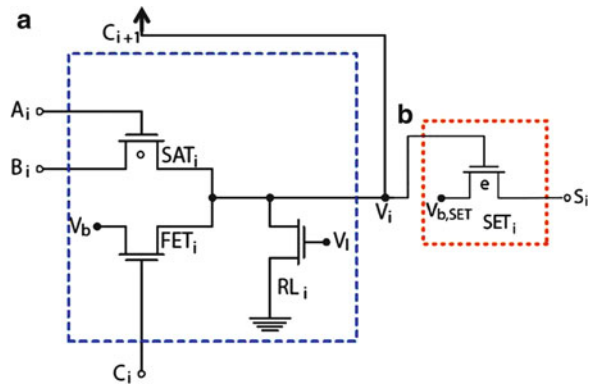
Fig. 5 Schematic representation of a DNAzyme computational module. The modularity is achieved by building a library of DNAzyme subunits based on the Mg^{2+}-dependent E6 DNAzyme [61] and a library of substrates. The addition of the input leads to the self-assembly of the DNAzyme and the cleavage of the substrate that releases the output. The output release is monitored by fluorescence. Adapted from [21]
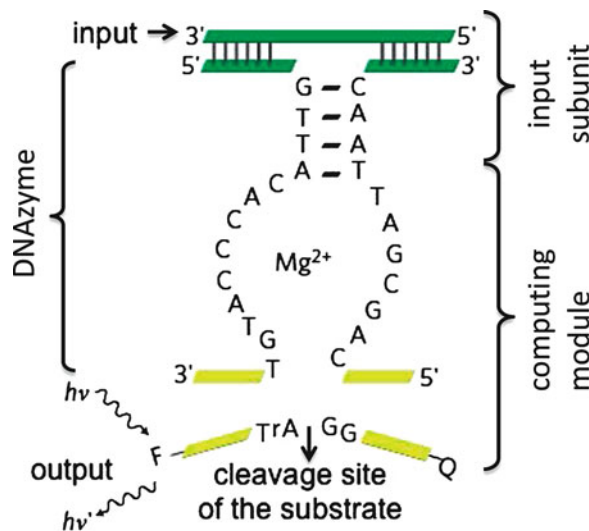
DNAzymes are catalytic nucleic acids that can self-assemble in the presence of metallic ions and cleave a substrate, a DNA strand containing a ribonuclease (rA); see Fig. 5. They have been extensively used for building automaton [16] and realizing complex logic operations [18–20, 58]. In most cases, DNAzyme gates are used to implement single-use gates [16, 18–20, 57, 58] and may require the presence of additional enzymes for their operation. The design that we report on here is modular and protein-free. It can also be used to build automata [59] and reconfigurable gates [60]. Moreover, the operation of the gates does not destroy their building components. Upon receiving the inputs, the logic gates self-assemble from a library of subunits of DNAzymes and a library of substrates that the DNAzymes can cleave, thereby releasing the output. The computational module is built of a processing and an input subunits; see Fig. 5. The catalytic DNAzyme core binds to the substrate subunit to form the processing subunit. The inputs are nucleic acid strands that can combine selectively with predesigned recognizing arms of
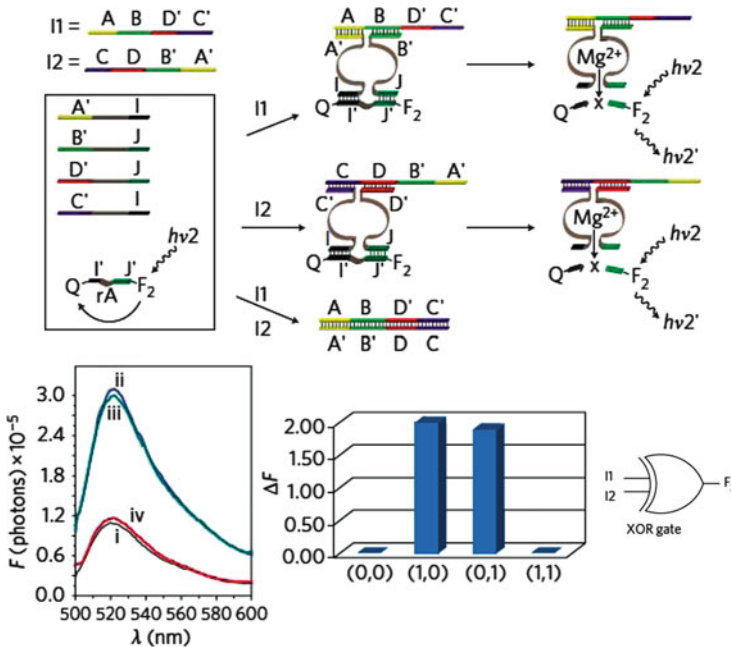
Fig. 6 Implementation of an XOR gate using the self-assembly of a DNAzyme computational module. Adapted from [21]

DNAzyme subunits to form the input subunit. Upon assembly of the computational module by addition of the input, the DNAzyme cleaves the substrate and the output is released. For simple binary gates, the monitoring of the outputs is through detection of a fluorescence signal. The substrate is tagged by a fluorophore and a quencher. The fluorescence is quenched as long as the substrate is bound to the DNAzyme. Upon cleavage, the fluorophore is separated from the quencher and a fluorescence signal is monitored. With this design, one can implement all important two-input binary gates (AND, OR, XOR, INH, NAND, NOR) as well as the one input gates NOT and FAN OUT. One therefore has access to a complete set of gates. We give in Fig. 6 the details of the implementation of the XOR gate. The DNAzyme is acting on the same substrate, but its recognizing arms can bind to two different sequences of DNA, either AB or CD. The input strands I_1 and I_2 are respectively ABC'D' and A'B'CD where an X' indicates the complementary sequence of X. If either I_1 or I_2 is present, the DNAzyme self-assembles and the substrate is cleaved, leading to a fluorescence signal. When both inputs are present simultaneously, a DNA duplex is formed that is more stable than the DNAzyme, and no fluorescence signal is observed. See [21] for more details. Circuits of gates acting in parallel can be built using this design by directing the assembly of DNAzyme modules acting on different substrates through the assembly by the inputs. Each substrate can be tagged by a specific fluorophore that allows monitoring the output of a given gate. The pair
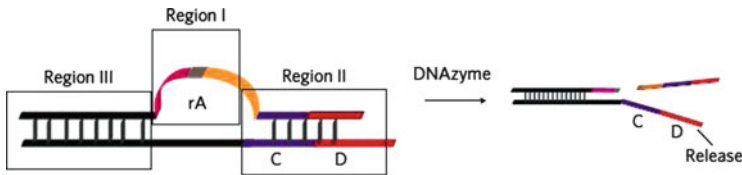
Fig. 7 Protected substrate used for implementing a cascade of gates as shown in Fig. 8
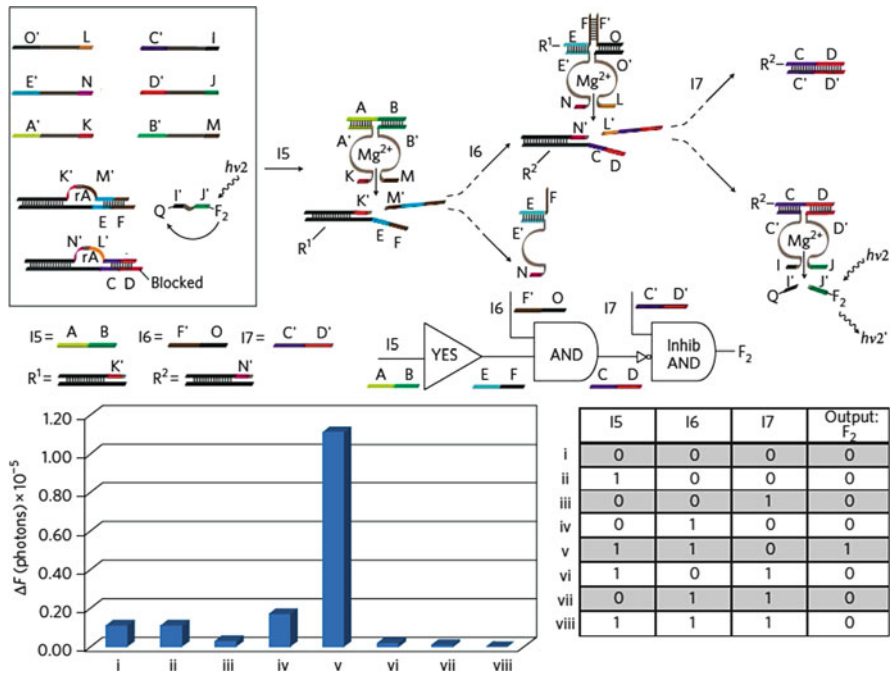
Fig. 8 Three-layer cascade implemented by using protected substrate for the first two layers of the circuit. Adapted from [21]

of inputs is common to all DNAzyme computational modules. A circuit showing an INH, XOR, and AND gates acting in parallel has been designed [21]. This circuit realizes simultaneously a half adder (XOR and AND) and a half subtractor (XOR and INH).

In the circuit shown in Fig. 6, the output signal is read by fluorescence which prevents for cascading the output of one gate as the input to the next gate. Cascade can however be easily achieved when the cleaved DNA strand can serve as an input for the next DNAzyme computational module, that is, when the inputs and the outputs are of the same physical nature. The price for doing so is to use a more complex substrate where the ribonuclease DNA strand is partially hybridized in region II and III by a complementary DNA strand that when released will serve as an input for the next DNAzyme gate (see Fig. 7). To achieve a multilayer circuit, the

relative stabilities of the different DNA duplexes and DNAzyme complexes must be carefully engineered. The protected DNA sequence complex of the first layer must be more stable than the DNAzyme computing unit of the second layer and so forth. The substrate for the last layer is a simple one as used for the one-layer circuits discussed above and is tagged by a fluorophore. Reference [21] shows that it is possible to build a three-layer circuit that is a cascade of a YES-AND-INH gates (see Fig. 8). Using this design, one can also build a fan out and amplify the signal.

3   Multivalued Circuits

Contemporary classical and quantal binary gates are built on Boolean logic that deals with variables that can take one of two values, 1 or 0. Nanoscale-confined systems typically possess several discrete states that can be selectively excited and probed. Executing logic operations in a basis larger than base 2 allows taking full advantage of this inherent complexity to increase the amount of information processed by the gates, thereby opening the way to reducing the size and power consumption of logic devices. However, the implementation of multivalued logic operations at the nanoscale is very demanding because the gates are complex and the number of possible inputs and outputs increases exponentially with the radix of the base used. For a given radix p and number of logic variables n, there are p^n possible inputs and p^{p^n} possible functions. For this reason, most implementations are in base 3 [62–66]. In base 3, the logic variables are three valued. An integer in base 10 is written in base 3 as $I = \sum^{n} t, 3^i$. In base 3, there are 27 unary functions, while there are only 4 in base 2. The number of functions of 2 ternary variables is 19,683, while there are only 16 functions of 2 bits. Balanced ternary variables take the values -1, 0, or 1, while the values of unbalanced ternary variables are 0, 1, and 2. There are very few implementations of base 3 logic gates at the hardware level [34, 35, 67]. Most of the implementations are based on CMOS transistors and use base 2 at the hardware level.

Charge states are systems of choice for implementing ternary variables because they can be positive, neutral, or negative. For example, we have used the charge states of a metallic quantum dot [68] to implement a complete set of ternary gates [69, 70]. One possible complete set of ternary gates comprises two two-variable gates, the MIN operation that is a generalization of the AND gate in binary variables and the MAX operation that is a generalization of the OR gate in binary. For a ternary variable, the negation is not unique. In addition to MIN and MAX, three negation gates are needed to build a complete set of gates, the simple ternary inverter, STI, and the positive (PTI) and negative (NTI) ternary inverters [70]. The truth tables of these 5 gates are given in Table 2. Figure 9 shows the results of a realistic simulation of an electrical device operating as a ternary logic gate where the possible values of the variables are -1, 0, and 1 [68]. The device consists in an array of three gated coupled quantum dots. It accepts two ternary inputs (the two

Table 2 Truth tables of the ternary logic gates MIN and MAX and of the negation gates STI, PIT, and NTI

MIN	−1	0	1
−1	−1	−1	−1
0	−1	0	0
1	−1	0	1
MAX	−1	0	1
−1	−1	0	1
0	0	0	1
1	1	1	1
Input	STI	PTI	NTI
−1	1	1	1
0	0	1	−1
1	−1	−1	−1
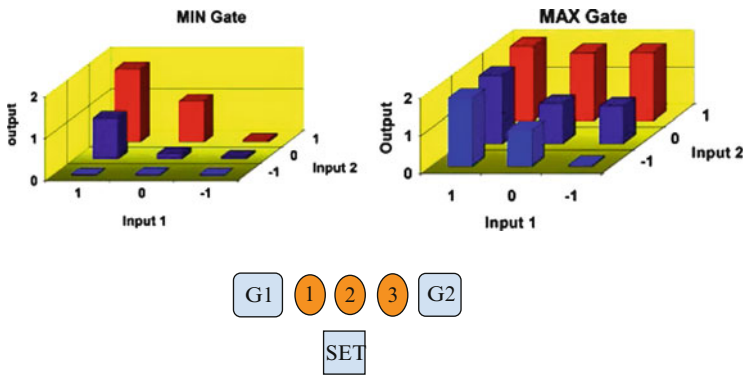
Fig. 9 *Top*: Computed output of a min and a max logic operation in ternary variables for which the inputs are the gate voltages G1 and G2. The charge on the middle dot is detected by a capacitive coupling to a SET [68]. *Bottom*: Schematic view of the device

gate voltages applied to the two end QD that can either be lowered or raised or left unchanged) and produces an output that is the minimum or the maximum of the two input values depending on the number of electrons on the device. The output is encoded in the charge (negative, neutral, or positive) of the middle quantum, as detected by a SET. The processing of the logic takes advantage of Coulomb blockade in a many-electron device. The electronic dynamics induced by the rising of the gate voltages $G1$ and $G2$ on a ns time scale was simulated at the many-electron quantum level using a Hubbard Hamiltonian [71, 72].

The MIN and the MAX operations do not require the introduction of a carry bit, for example, the case for an addition. Another operation for which no carry bit is needed is the multiplication of balanced ternary variables. This scheme allows in principle for the multiplication of a rather long number made of several digits by a constant, where each digit multiplication can be treated by a separate unit, without any need to transfer information from one unit to the next. We have proposed two

Fig. 10 An EFM experimental output for balanced ternary multiplication. The two inputs are the charge on the NP and on the tip. The readout is the sign of the force with a key as shown on the right. Adapted from [67]
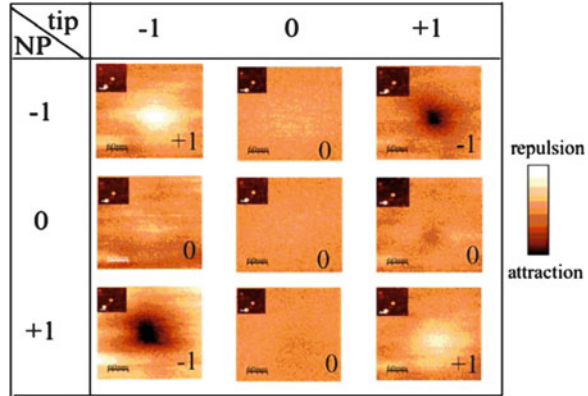
Table 3 Operation of the first half adder

Initial state = Carry in	Voltage pulse = x	Intermediate state = intermediate sum = output of XOR	Output of AND operation (C_1) = charge on right dopant R at F_{max}
L^+R (0)	0	L^+R (0)	0
L^+R (0)	1	LR^+ (1)	0
LR^+ (1)	0	LR^+ (1)	0
LR^+ (1)	1	L^+R (0)	1

The "carry in" is stored in the initial state, left column. The first digit is encoded in a pulse of voltage that is applied (0) or not (1). The intermediate sum is the output of the XOR operation. The charge on the left or on the right dopant is measured at the plateau of the field strength where the field is maximal. For a half addition, the charge on the dopant on the right gives the intermediate carry C_1

physical realizations, also based on the charge states of a confined nanosystem electrically addressed, a SAT [34] and a SiO_2 NP encapsulated in an insulating protein [67].

We discuss here the latter implementation. One of the numbers to be multiplied is encoded into the charging of the NP by a conductive AFM tip. The charging can be positive (value $+1$), negative (value -1), or no charging (value 0). After the encoding of the first number in the NP, the second number is encoded in the charge of the tip that can also be negative (-1), neutral (0), or positive ($+1$). The output is read by electrostatic force microscopy (EFM), which probes the electrostatic repulsion or attraction between the NP and the tip, according to their respective charge; see Fig. 10. This scheme can be generalized to the multiplication of an n-digit ternary number by a constant and operates at room temperature [67].

We conclude this section on the physical realization of multivalued devices by the implementation of a full ternary adder on gated silicon nanowire [35]. The truth tables of a ternary addition are shown in Table 3. Like the binary addition discussed
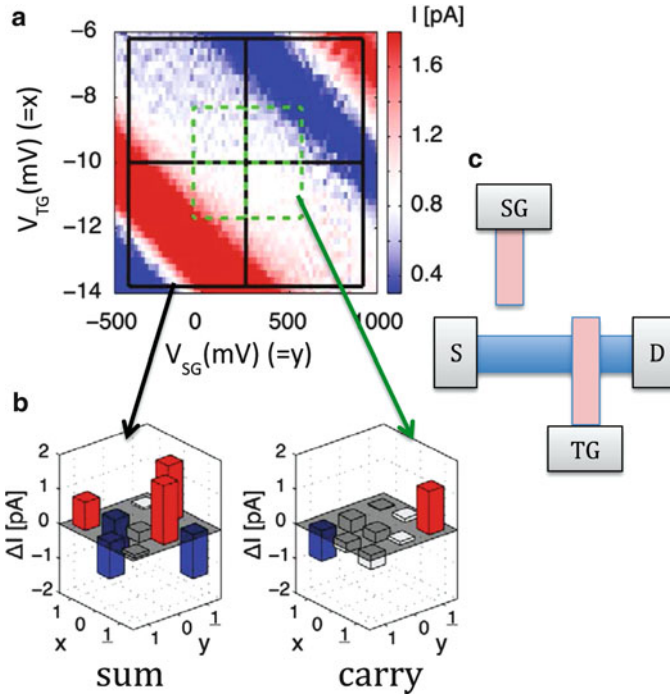
Fig. 11 Ternary addition implemented on a MOSSET. (**a**): Current maps as a function of the top and side gates (see panel c) for an AC bias of 1.7 mV. (**b**): the values of the sum-out and the carry-out current for a carry in $= 0$, (**c**): schematic of the device. For more details, see [35]

above, a ternary addition has two outputs, the sum out that is the output of the addition modulo 3 of the two numbers, x and y, to be added and the carry out that needs to be cascaded to the next addition. The sum and the carry out can be defined from the value of the integer, s, that is the arithmetic sum of two ternary numbers to be added, as the two ternary numbers t_0 and t_1, respectively:

$$s = x + y, \quad t_0 = s - t_1 3, \quad t_1 = \frac{s}{2}$$

where t_1 is nearest integer of $s/3$.

The device is a multigate MOSSET (metal on insulator single-electron transistor) [73]; see Fig. 11. The three ternary inputs of the adder are encoded in the three gates of the device; the two numbers to be added are encoded in the top and side gate, and the carry-in in the back gate. An alternating bias voltage applied between the source and drain gates results in an average current that is positive, zero, or negative depending on the value of the gate voltages. Its mapping in ternary variables provides the outputs. Heat maps of the averaged current obtained upon application of an AC bias voltage measured as a function of the top and side gates

for a given value of the back gate exhibit strips of positive, zero, and negative current that can be mapped on the truth table of the ternary sum-out and carry-out functions; see Fig. 11 for the current map for a carry-in value $= 0$. The heat maps for the carry-in values of -1 and $+1$ are obtained by varying the back gate; for more details, see [35]. Being fully CMOS compatible, this device is scalable, cascadable, and inherently CMOS compatible.

4 Finite-State Machines

Molecular systems respond to a perturbation according to the state they are in. As such, they are inherently suitable to implement finite-state machines [47] at the hardware level. A schematic representation of a finite-state machine is shown in Fig. 1 above. Finite-state machines can execute linear and nonlinear logic operations. A well-known and simple model for a nonlinear implementation is that of a set-reset machine [47], of which several implementations have been proposed on various molecular and nanosystems using optical [74–76], electrical [52, 77, 78], biochemical [79, 80], or electrochemical [81–83] addressing. Finite-state machines can also be used to implement a full addition. We have proposed optical [45, 84] and electrical [85] implementations. In these schemes, the full addition is performed as two half additions. In the implementations that we proposed, a half addition requires the addressing of three quantum states optically [84] and of two quantum states electrically [85]. As discussed above, a full addition has three inputs, the two digits to be added, x and y, and the carry in from the previous addition. It produces two outputs, a sum out and a carry out. For the first half addition, the carry-in bit is stored in the state of the device, and the input digit x is encoded in the pulse of light [45, 84] or of voltage [85] that triggers the dynamics that processes the logic operation. The first half addition adds the carry-in bit to one of the digits to be added and gives as outputs an intermediate sum, $S_{\text{int}} = C_{\text{in}} \oplus x$, and an intermediate carry, $C_1 = C_{\text{in}} \cdot x$, where "$\cdot$" means an AND operation and $\oplus$ means an XOR (addition modulo 2) operation. The symbol "$+$" is used for an OR operation. The intermediate sum is stored in the state of the device. The second half addition proceeds as the first one; the second digit to be added, y, is encoded in a pulse of photon or of voltage and combined with the intermediate sum to give the sum out, $S_{\text{out}} = S_{\text{int}} \oplus y = C_{\text{in}} \oplus x \oplus y$, that is stored in the state of the device and a second carry, $C_2 = S_{\text{int}} \cdot y$. The second carry must be combined in an OR operation with the first one to give the carry out, $C_{\text{out}} = C_1 + C_2 = x \cdot y + x \cdot C_{\text{in}} + y \cdot C_{\text{in}}$. Since the two carries cannot be 1 simultaneously [84], detecting the signal corresponding to C_1 or C_2 during the two half additions gives the carry out. The finite-state machine implementation of a full adder is nonlinear and requires a one-state memory.

We first illustrate this design by the implementation of a full adder on a molecule of dopant atoms in a Si transistor. The physical system we consider is a single electron bound to a shallow-donor pair (e.g., P_2^+) in silicon. In the experimental setup, a time-dependent source-drain bias applied in a direction parallel to the
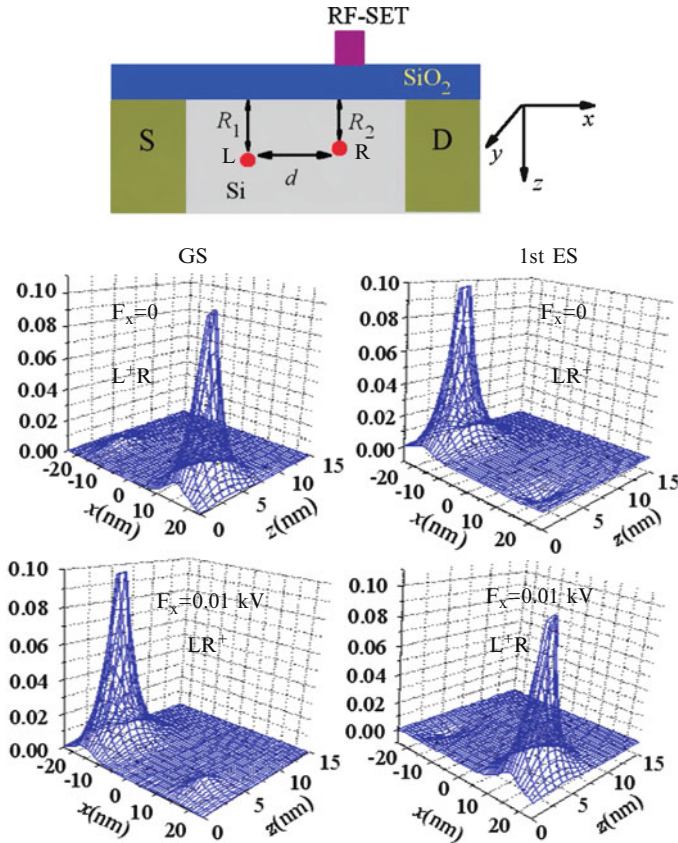
Fig. 12 *Top*: Schematic of the device. Two donor atoms are placed at the depths R_1 (L, left dopant) and R_2 (R, right dopant) along the z direction from the $Si - SiO_2$ interface and separated by a distance $d = |x_1 - x_2|$ in the x direction. The source and drain electrodes are used to apply an electric field along the x direction. The RF-SET is used to detect the charge on the right-dopant atom. *Bottom*: The localization of the one-electron wave function computed for the ground state (GS, left) and the first excited state (1st ES, right) at zero field and at $F_x = 0.01 \, \text{kV}$; for more details, see [85]

$Si - SiO_2$ (001) interface allows to control the localization of the charge on one or the other dopant atom; see top of Fig. 12. The two donors are not placed at equal distance from the interface, $R_1 \neq R_2$. Since the ionization potential of the dopant atom is controlled by its distance to the interface, this gives us the ability to build a "heteronuclear" dopant molecule and to control the degree of covalent vs. ionic bonding, using dopant atoms of the same chemical nature, here phosphorous. This flexibility is important for the design of logic schemes.

In the single-valley approximation, the time-dependent Hamiltonian for 2 dopants written in Cartesian coordinates reads

$$H(t) = -\left[\frac{\hbar}{2m_\perp} \left(\frac{\partial^2}{\partial x^2} + \frac{\partial^2}{\partial y^2} \right) + \frac{\hbar}{2m_\parallel} \frac{\partial^2}{\partial z^2} \right] - \sum_{i=1}^{2} \frac{e^2}{\varepsilon_{\text{Si}} \sqrt{(x - x_i)^2 + y^2 + (z - z_i)^2}}$$

$$+ \sum_{i=1}^{2} \frac{Qe^2}{\varepsilon_{\text{Si}} \sqrt{(x - x_i)^2 + y^2 + (z - z_i)^2}} - \frac{Qe^2}{4\varepsilon_{\text{Si}} Z} + e\mathbf{F}(t) \cdot r \tag{1}$$

where the first term is the kinetic energy of the electron, the second is the time-dependent external electric-field potential, the third is the Coulomb potential of the two centers, and the fourth and the last are the image-charge potential of the donors and of the electron. $m_\perp = 0.191\, m_e$ and $m_\parallel = 0.916\, m_e$ (m_e is the mass of a free electron) are the transverse and longitudinal effective masses, respectively. In the logic device that we discuss below, there are $N = 2$ dopants. $Q = (\varepsilon_{\text{SiO}_2} - \varepsilon_{\text{Si}})/(\varepsilon_{\text{SiO}_2} + \varepsilon_{\text{Si}})$ where $\varepsilon_{\text{Si}} = 11.4$ and $\varepsilon_{\text{SiO}_2} = 3.8$ [86, 87]. The ground state and lowest excited-state wave functions at zero and finite fields are solved for numerically on a grid by the Lanczos method [88].

By positioning the two dopants at a slightly different distance from the interface and far from each other so that they are weakly coupled, it is possible to almost completely localize the electron on the left or on the right in the ground state of the two-donor molecule, without applying any external field. In the configuration shown in Fig. 12, the right dopant has a lower energy than the left dopant, and since the two dopants are very weakly coupled, in the ground state of the dopant molecule, the electron is localized on the right-dopant atom (positive x coordinate). We denote the ground state of the one-electron two-dopant molecule as L^+R. In the first excited state denoted LR^+, the electron is localized on the left.

The electron charge distribution can be shifted by applying a static electric field. If a strong field is applied along the x direction, $F_x = 0.01\,\text{kV/cm}$, the ground state is of the form LR^+ with the electron localized on the left dopant, and in the excited state, L^+R, the electron is localized on the right. The corresponding charge distributions are shown in the bottom panels of Fig. 12.

The full addition is implemented as a nonlinear finite-state machine, using a pulse voltage with an asymmetric time profile:

$$F_x(t) = \begin{cases} F_{\text{max}} \exp\left(-(t - t_{\text{on}})^2/2t_w^2\right) & t \leq t_{\text{on}} \\ F_{\text{max}} & t_{\text{on}} < t \leq t_{\text{off}} \\ F_{\text{max}} \exp(-(t - t_{\text{off}})^2/2t_w'^2) & t > t_{\text{off}} \end{cases} \tag{2}$$

where $t_w = 10\,\text{ns}$ is the adiabatic switching constant and $t_w' = 100\,\text{ps}$ the diabatic switching-off constant. These switching times ensure that the switching-on process ($t < t_{\text{on}}$) of the electric field is long so that it is an adiabatic process where the quantum state of the system is maintained as can be seen in Fig. 13. Say that the system is initially in the ground state at zero field, cf. Fig. 13a. Then the electron is localized around the right donor. By adiabatically switching on the electric field, we move the electron from the right donor to the left, or from state L^+R to LR^+. In such a process the system stays in the ground state. The quantum state is preserved
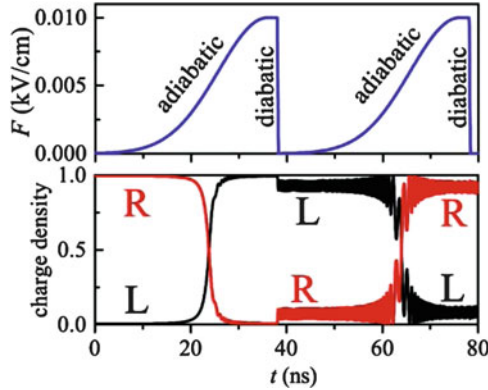
Fig. 13 Computed charge densities on the left and on the right dopants as a sequence of two pulses is applied to the two-donor pair. *Top*: The sequence of applied pulses. The total duration of one pulse is 40 ns. The shape of the pulse is given by Eq. (2). $t_{on} = 36$ ns, $t_{off} = 38$ ns, $t_w = 10$ ns, and $t'_w = 100$ ps. $F_{max} = 0.01$ kV/cm. *Bottom*: The initial condition is the ground state when $F_x = 0$. After the first pulse, the charge has switched on the left dopant. Upon application of the second pulse of voltage, the charge is back to the right dopant

even though the electron has switched sides. Next, at t_{off}, we suddenly switch off the field very fast. The system has little time to adjust to this change and continues to stay essentially in the same state of the electron, namely, LR^+. Since this state is not an exact eigenstate of the Hamiltonian at the final stage (when $F_x = 0$), the charge density oscillates with a small amplitude around a mean value that is not exactly 1 or 0.

The net effect after one cycle, duration 40 ns in Fig. 13, is that the electron is moved from a zero-field state L^+R to a zero-field excited state LR^+, going through the intermediate state LR^+ at finite field. This intermediate state is actually the ground state of the system when the field is on. In the next cycle, the initial state at zero field is the excited state of the donor pair, localized on the left donor and upon applying the voltage pulse, the charge is moved back to the right donor.

The full adder operates as a finite-state machine. We use two internal states of the machine whose localization switches when the gate pulse voltage reaches its maximum value (see Fig. 13). At zero field, in the ground state, L^+R, the electron is localized on the right, and in the first excited state, LR^+, the electron is on the left. At finite high field, the ground state is LR^+ (electron on the left), and the first excited state is L^+R (electron localized on the right).

A full addition proceeds along the general lines given above. The "carry-in" bit is stored in an internal state of the machine at zero field. We take that the electron on the right, which is the state L^+R, corresponds to the logic value 0, while the electron on the left, which is LR^+, corresponds to the logic value 1. For the machine to be cyclable, it is necessary that at the end of the addition, the "carry-out" digit is stored as an internal state of the machine, ready to be used as the "carry-in" bit for the next addition.

Table 4 Operation of the second half adder

Intermediate state = intermediate sum	Voltage pulse = y	Final state = sum out	Charge on R at F_{max} = output of AND (C_2)
L^+R (0)	0	L^+R (0)	0
L^+R (0)	1	LR^+ (1)	0
LR^+ (1)	0	LR^+ (1)	0
LR^+ (1)	1	L^+R (0)	1

The second half adder realizes that addition of the intermediate sum and the second of the input digits. The state of the machine is always defined at zero field. The charge on the right dopant is measured at the maximum field strength

The first digit to be added is encoded in applying or not a voltage pulse. If the digit to be added has logical value 0, no pulse is applied, while if the digit has the value 1, a pulse is applied.

The localization of the electron is changed from left to right or vice versa when the pulse field is applied, which performs an XOR (or addition modulo 2) operation between the input and the state of the machine. The intermediate carry output is encoded into the localization of the electron on the right dopant at high field, before it is diabatically switched off. If the electron is localized on the right dopant at high field, the intermediate carry has logical value 1 and if not, it has logical value 0. The measure of the charge of the right dopant at high field corresponds to the AND operation between the input digit and the state of the machine and gives the intermediate carry. These operations are summarized in Table 3.

At the end of the first half addition, the intermediate sum is stored as the state of the machine, and the intermediate carry, C_1, has been measured at the high-field end. In the second half addition, Table 4, the second input digit is added to the intermediate sum, leading to the sum out and the second carry C_2. The sum out is the state of the machine at zero field, after the second pulse is over. The C_2 output is given by the value, 0 or 1, of the charge on the right dopant at high field. Since the two carries, C_1 and C_2, cannot be 1 simultaneously, to detect a charge on the right dopant at high field during either one of the two cycles means that the carry out is 1.

The full adder logic scheme discussed above can be experimentally realized by integrating the two-donor system with a single-electron transistor (RF-SET) and a pulse gate. The entire gate pulse sequence for a full adder requires three pulses, which rise adiabatically and fall suddenly. The first pulse sets the system in its initial state, depending on the carry in. The next two pulses correspond to the logic inputs and are kept at F_{max} for a time long enough ($\sim\mu s$) for the RF-SET to measure whether the charge is on the right dopant. After applying these pulses, the final state of the system, which is the sum, is read out by the RF-SET. The total length of a pulse sequence is much shorter than the computed decoherence lifetime of the system [89, 90], which was experimentally verified in [90].

The optical implementation relies on the same basic design [45, 84]. It requires the coherent addressing of a three-level system with two laser pulses. The energetics of the three levels must obey a Λ shape (see Fig. 14a). Level 1 is the ground state,
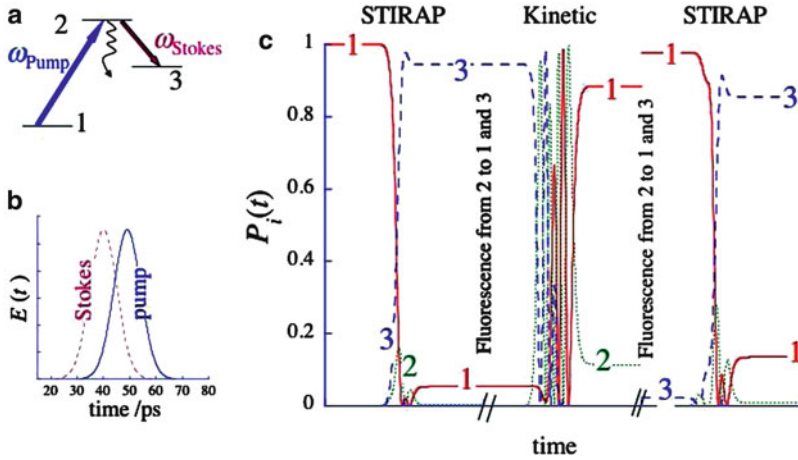
Fig. 14 Principles of the design of the STIRAP adder implemented by a finite-state machine. (**a**) The Λ level scheme. State 1 is the ground state; state 2 is a metastable state that can fluoresce and be transiently populated via the kinetic route. State 3 is a metastable state with a long lifetime. States 1 and 3 serve to encode the logic values of the memory state of the finite-state machine. (**b**) The *SP* pulse that serves as the inputs. (**c**) A quantum simulation of the dynamics of a full addition cycle. The two inputs are 1, so two *SP* pulses are applied. The C_{in} value is 0, so initially the system is in state 1. The sum out is zero, so the final state is state 1. The C_{out} is 1, which is measured by monitoring the fluorescence from state 2 during the second *SP* pulse. The longer time state flipping on the right illustrates the possibility to reset the machine; for more details, see [84]

level 2 is an intermediate state that can fluoresce, and level 3 is a metastable state, stable for a time longer than that required for the implementation of the two cycles necessary for the full addition. For the excitation, we use two overlapping strong laser pulses, one that is quasi resonant with the transition between state 1 and state 2 (the pump pulse) and one that is quasi resonant with the transition between state 2 and state 3 (the Stokes pulse). The input is encoded in the two overlapping pulses that we define as an *SP* pulse (see Fig. 14b), Stoke first and then pump. The essential point of the design is that using such a pulse, there are two distinct ways for going between states 1 and 3, depending on which state is the initial state. We adjust the parameters of the *SP* pulse, strength, overlap between the *S* and the *P* pulses, detuning from resonance, in such a way that (a) if the initial state is the GS, state 1, the population will be transferred to state 3 following a STIRAP (stimulated Raman adiabatic passage) mechanism [91–93], with 100% efficient without any transient population into state 2. This route is called the counterintuitive route because the input pulse, *SP*, first dresses the 2–3 transition and then is quasi resonant with the 1–2 transition. When the parameters of the *SP* pulse are correctly adjusted, one can show that the system follows adiabatically an eigenstate of the time-dependent Hamiltonian that has no amplitude on state 2. Because, in the scheme, only state 2 can fluorescence, this route is also called the dark route. (b) If on the other hand, the initial state is state 3, the same *SP* pulse will take the system to state 1 via the kinetic (or intuitive) route. In that case, the *S* pulse is quasi resonant with the transition 2–3,

and there will be a transient population in state 2. That population will be then taken to state 1 by the *P* pulse. For this route, the parameters of the *SP* pulse must be such that it is a "bright" state of the time-dependent Hamiltonian of the system that is adiabatically followed. The parameters of the *SP* pulse are therefore adjusted to be optimal for the two routes [45, 84, 94]; a quantum simulation is shown in Fig. 14c.

The logic encoding of the variables is very similar to the one used above in the electrical implementation. Tables 3 and 4 are valid for describing the operation of the finite-state machine, providing the states L^+R and LR^+ are replaced by states 1 and 3 and that the encoding of the intermediate carries into the charge on the right dopant is replaced by measuring fluorescence from state 2. State 1 and state 3 serve to encode the memory state of the finite-state machine. The carry-in bit is encoded in the initial state of the system, in state 1 if its value is 0 and in state 3 if it value is 1. One of the numbers to be added, let us say x, is encoded in the *SP* pulse, $x = 0$ if no pulse is applied, and $x = 1$ if a pulse is applied. The next state of the machine stores the intermediate sum of the first half addition (Table 3) and the intermediate carry C_1 is detected by fluorescence from state 2. Depending on the value of the carry in, the flipping of the state of the memory by the *SP* pulse will go via the STIRAP dark route (no fluorescence from state 2, $C_1 = 0$) or via the kinetic bright route (fluorescence from state 2, $C_1 = 1$). In the second half addition, the second input, y, is combined with the intermediate sum that is stored in the memory state to give the sum out and the second carry. As discussed above for the two-dopant adder, since the two intermediate carries cannot be 1 simultaneously, to measure the C_{out}, it is enough to monitor fluorescence from state 2 during the two cycles. After the two cycles that perform the full addition, one needs to read the sum out and to encode the carry out into the state of the machines. This is possible but requires extra *SP* pulses. As shown in Fig. 14c, it is also possible to reset the machine when the reading of the states is not secure enough. This can be due to the fact that the state flipping does not occur with a 100% efficiency and to decoherence processes and external noise. This principle of operation has been demonstrated by coherent STIRAP addressing of a doped solid [45].

The finite-state machines discussed above possess a single state in its memory. To close this section, we discuss briefly an example of optical addressing by a short pulse that simultaneously addresses several states of a molecular system [50]. The experiment consists in a fs IR pump-probe experiment on the vibrational states of metal carbonyl complexes in solution, $W(CO)_6$ or $Mn(CO)_5Br$. The fast relaxation induced by the collision with the solvent molecules allows us to describe the vibrational dynamics by a kinetic scheme, $d\mathbf{P}(t)/dt = \mathbf{KP}(t)$. The relaxation is probed by frequency-resolved measurements of the time-delayed probe pulse (see Fig. 15), and the two-dimensional spectrum is fitted by the kinetic scheme.

The several vibrational states that can be probed and are involved in the relaxation kinetic scheme can be thought of the memory states of a finite-state machine, Fig. 16, the processing of the logic being realized by the kinetic matrix [49, 50]. The machine is massively parallel because at every time step, its output is a new population vector where each component is a transform of the input. Note that in this case, we implement a linear finite-state machine [48].
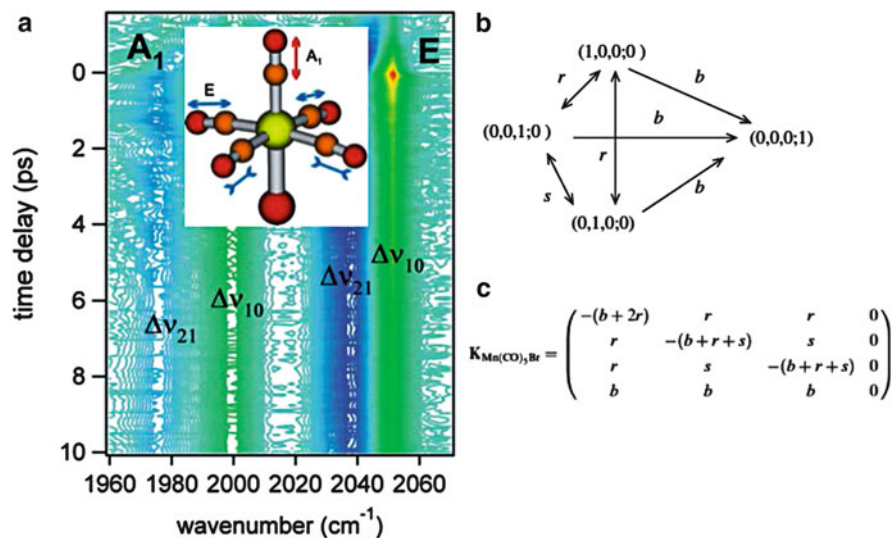
Fig. 15 (**a**) 2D transient absorption spectrum (ΔOD) of the $Mn(CO)_5Br$ complex in CCl_4 at 298 K, plotted as a function of time delay and frequency. The weak pump fs laser pulse excites the complex at $2,025\,cm^{-1}$. The transient absorption signals for the fundamental bleaching transitions ($\Delta\nu_{10}$) at 2,052 and $2,001\,cm^{-1}$ and the first excited-state transitions ($\Delta\nu_{21}$) at 2,039 and $1,980\,cm^{-1}$ for the E and A_1 states, respectively, are indicated. (**b**) The solvent-induced relaxation scheme of the $\nu = 1$ manifold of $Mn(CO)_5Br$. The states are labeled as the number of vibrational quanta in (A1,Ex,Ey; bath). (**c**) The corresponding kinetic matrix. Adapted from [50]
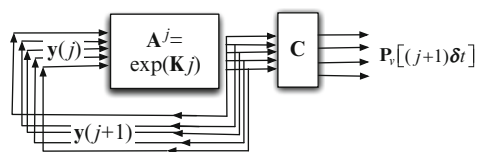
Fig. 16 A schematic of the operation of the finite-state machine based on the $Mn(CO)_5Br$ complex. $\mathbf{y}(j)$ refers to the internal states of the machine at time $j\delta t$. The output is the measurement of the probability vector $\mathbf{P}$ at time $j\delta t$. It is the result of the operation of two matrices. The matrix $\mathbf{A}^j = \exp(\mathbf{K}j)$ operates on the internal states at time $j\delta t$, and the matrix $\mathbf{C}$ transforms the state vector $\mathbf{y}(j + 1)$ into the output vector, $\mathbf{P}$

5 Perspectives

Confined nanosystems are systems of choice for the implementation of complex logic operations at the hardware level. We showed that the same principles govern the implementation of composite logic on various systems, single-atom transistors electrically addressed [32, 33, 35], nanoparticles addressed by electric force microscopy [67] and DNAzyme complexes chemically addressed in solution [21, 59, 60], transition metal complexes addressed by fs laser pulses [50], and coherently

addressed doped solids [45]. Cascade of logic operations can be implemented in an efficient way for both types of systems, as well as finite-state machines [45, 59, 85]. Furthermore, the implementation of finite-state machines addressed by laser pulses opens the way to the realization of quasi-classical parallelism [49,50]. One essential advantage of these structures is that their many internal states make them suitable for multivalued logic [34, 35, 67, 68]. These systems are of interest for different kinds of technological applications. Single-atom transistors are CMOS compatible and could be integrated in CMOS architectures as task-dedicated units. For this, one needs to be able to take advantage of the technique of deterministic doping [31] to design more complex structures in Si and use dopant atoms with electronic spacings compatible with operation at room temperature. DNAzyme systems are promising systems for intelligent sensing and nanomedicine [57].

In our future work we expect to combine the different multiprocessing ideas that we discussed above. This will adapt the architecture of finite-state machines that allows the use of multivalued variables in a natural way. We envisage such machines with multimemories or, equivalently, multistate. And we shall use parallelism so that multiprocesses are executed in parallel.

References

1. Steinitz, D., Remacle, F., Levine, R.D.: Spectroscopy, control and molecular processing. Chem. Phys. Chem. **3**, 43–51 (2002)
2. Remacle, F., Levine, R.D.: Inter- and intra- molecular level logic devices. In: Waser, R. (ed.) Information Technology IV, vol. 4. Nanotechnology, pp. 213–248. Wiley, Weinheim (2008)
3. De Silva, A.P., Gunaratne, H.Q.N., McCoy, C.P.: A molecular photoionic AND gate based on flourescent signaling. Nature **364**(6432), 42–44 (1993)
4. de Silva, A.P., Gunaratne, H.Q.N., McCoy, C.P.: Molecular photoionic and logic gates with bright fluorescence and "off-on" digital action. J. Am. Chem. Soc. **119**(33), 7891–7892 (1997)
5. de Silva, A.P., Uchiyama, S.: Molecular logic and computing. Nature Nano. **2**(7), 399–410 (2007)
6. Szacilowski, K.: Digital information processing in molecular systems. Chem. Rev. **108**(9), 3481–3548 (2008)
7. Andreasson, J., Pischel, U.: Smart molecules at work-mimicking advanced logic operations. Chem. Soc. Rev. **39**(1), 174–188 (2010)
8. de Ruiter, G., van der Boom, M.E.: Surface-confined assemblies and polymers for molecular logic. Accounts Chem. Res. **44**(8), 563–573 (2011)
9. Joachim, C., Renaud, N., Hliwa, M.: The different designs of molecule logic gates. Adv. Mater. **24**(2), 312–317 (2012)
10. Gust, D., Andreasson, J., Pischel, U., Moore, T.A., Moore, A.L.: Data and signal processing using photochromic molecules. Chem. Comm. **48**(14), 1947–1957 (2012)

11. Benenson, Y., Adar, R., Paz-Elizur, T., Livneh, Z., Shapiro, E.: DNA molecule provides a computing machine with both data and fuel. Proc. Natl. Acad. Sci. USA **100**(5), 2191–2196 (2003)
12. Benenson, Y., Paz-Elizur, T., Adar, R., Keinan, E., Livneh, Z., Shapiro, E.: Programmable and autonomous computing machine made of biomolecules. Nature **414**(6862), 430–434 (2001)
13. Shapiro, E., Benenson, Y.: Bringing DNA computers to life. Sci. Am. **294**(5), 44–51 (2006)
14. Xie, Z., Liu, S.J., Bleris, L., Benenson, Y.: Logic integration of mRNA signals by an RNAi-based molecular computer. Nucleic Acids Res. **38**(8), 2692–2701 (2010)
15. Lederman, H., Macdonald, J., Stefanovic, D., Stojanovic, M.N.: Deoxyribozyme-based three-input logic gates and construction of a molecular full adder. Biochem. **45**(4), 1194–1199 (2006)
16. Pei, R., Matamoros, E., Liu, M., Stefanovic, D., Stojanovic, M.N.: Training a molecular automaton to play a game. Nature Nanotechnology **5**(11), 773–777 (2010)
17. Stojanovic, M.N., Stefanovic, D.: A deoxyribozyme-based molecular automaton. Nature Biotech. **21**(9), 1069–1074 (2003)
18. Qian, L., Winfree, E.: Scaling up digital circuit computation with DNA strand displacement cascades. Science **332**(6034), 1196–1201 (2011)
19. Qian, L., Winfree, E., Bruck, J.: Neural network computation with DNA strand displacement cascades. Nature **475**(7356), 368–372 (2011)
20. Seelig, G., Soloveichik, D., Zhang, D.Y., Winfree, E.: Enzyme-free nucleic acid logic circuits. Science **314**(5805), 1585–1588 (2006)
21. Elbaz, J., Lioubashevski, O., Wang, F., Remacle, F., Levine, R.D., Willner, I.: DNA computing circuits using libraries of DNAzyme subunits (vol 5, pg 417, 2010). Nature Nanotechnology **6**(3), 190–190 (2011)
22. Gupta, T., van der Boom, M.E.: Redox-active monolayers as a versatile platform for integrating Boolean logic gates. Angew. Chem. Int. Ed. **47**(29), 5322–5326 (2008)
23. Duchemin, I., Joachim, C.: A quantum digital half adder inside a single molecule. Chem. Phys. Lett. **406**(1–3), 167–172 (2005)
24. Joachim, C., Martrou, D., Rezeq, M., Troadec, C., Jie, D., Chandrasekhar, N., Gauthier, S.: Multiple atomic scale solid surface interconnects for atom circuits and molecule logic gates. J. Phys. Cond. Mat. **22**(8) (2010)
25. Renaud, N., Ito, M., Shangguan, W., Saeys, M., Hliwa, M., Joachim, C.: A NOR-AND quantum running gate molecule. Chem. Phys. Lett. **472**(1–3), 74–79 (2009)
26. Stadler, R., Ami, S., Joachim, C., Forshaw, M.: Integrating logic functions inside a single molecule. Nanotechnology **15**(4), S115-S121 (2004)
27. Prins, F., Shaikh, A.J., van Esch, J.H., Eelkema, R., van der Zant, H.S.J.: Platinum-nanogaps for single-molecule electronics: room-temperature stability. Phys. Chem. Chem. Phys. **13**(32), 14297–14301 (2011)
28. Manheller, M., Trellenkamp, S., Waser, R., Karthaeuser, S.: Reliable fabrication of 3 nm gaps between nanoelectrodes by electron-beam lithography. Nanotechnology **23**(12) (2012)
29. Lansbergen, G.P., Rahman, R., Wellard, C.J., Woo, I., Caro, J., Collaert, N., Biesemans, S., Klimeck, G., Hollenberg, L.C.L., Rogge, S.: Gate-induced quantum confinement transition of a single dopant atom in a silicon FinFET. Nature Phys. **4**, 656–661 (2008)
30. Sellier, H., Lansbergen, G.P., Caro, J., Rogge, S., Collaert, N., Ferain, I., Jurczak, M., Biesemans, S.: Transport spectroscopy of a single dopant in a gated silicon nanowire. Phys. Rev. Lett. **97**, 206805 (2006)
31. Fuechsle, M., Miwa, J.A., Mahapatra, S., Ryu, H., Lee, S., Warschkow, O., Hollenberg, L.C.L., Klimeck, G., Simmons, M.Y.: A single-atom transistor. Nat Nano **7**(4), 242–246 (2012)
32. Klein, M., Lansbergen, G.P., Mol, J.A., Rogge, S., Levine, R.D., Remacle, F.: Reconfigurable logic devices on a single dopant atom-operation up to a full adder by using electrical spectroscopy. Chemphyschem **10**(1), 162–173 (2009)
33. Mol, J.A., Verduijn, J., Levine, R.D., Remacle, F., Rogge, S.: Integrated logic circuits using single-atom transistors. Proc. Natl. Acad. Sci. USA **108**(34), 13969–13972 (2011)

34. Klein, M., Mol, J.A., Verduijn, J., Lansbergen, G.P., Rogge, S., Levine, R.D., Remacle, F.: Ternary logic implemented on a single dopant atom FET in Si. Appl. Phys. Lett. **96**, 043107 (2010)

35. Mol, J.A., van der Heijden, J., Verduijn, J., Klein, M., Remacle, F., Rogge, S.: Balanced ternary addition using a gated silicon nanowire. Appl. Phys. Lett. **99**(26) (2011)

36. Kompa, K.L., Levine, R.D.: A Molecular Logic Gate. Proc. Natl. Acad. Sci. USA **98**, 410–414 (2001)

37. Kuznetz, O., Salman, H., Eichen, Y., Remacle, F., Levine, R.D., Speiser, S.: All optical Full-adder Based on Intramolecular Electronic Energy transfer in the Rhodamine-Azulene Bichromophoric system. J. Phys. Chem. C **112**, 15880–15885 (2008)

38. Remacle, F., Speiser, S., Levine, R.D.: Intermolecular and intramolecular logic gates. J. Phys. Chem. B **105**, 5589–5591 (2001)

39. Kling, M.F., Vrakking, M.J.J.: Attosecond electron dynamics. Ann. Rev. Phys. Chem. **59**(1), 463–492 (2008)

40. Krausz, F., Ivanov, M.: Attosecond physics. Rev. Modern Phys. **81**(1), 163–234 (2009)

41. Woerner, H.J., Bertrand, J.B., Fabre, B., Higuet, J., Ruf, H., Dubrouil, A., Patchkovskii, S., Spanner, M., Mairesse, Y., Blanchet, V., Mevel, E., Constant, E., Corkum, P.B., Villeneuve, D.M.: Conical intersection dynamics in NO(2) probed by homodyne high-harmonic spectroscopy. Science **334**(6053), 208–212 (2011)

42. Remacle, F., Levine, R.D.: An electronic time scale for chemistry. Proc. Natl. Acad. Sci. USA **103**(May 2), 6793–6798 (2006)

43. Beil, F., Buschbeck, M., Heinze, G., Halfmann, T.: Light storage in a doped solid enhanced by feedback-controlled pulse shaping. Phys. Rev. A **81**(5) (2010)

44. Heinze, G., Rudolf, A., Beil, F., Halfmann, T.: Storage of images in atomic coherences in a rare-earth-ion-doped solid. Phys. Rev. A **81**(1) (2010)

45. Beil, F., Halfmann, T., Remacle, F., Levine, R.D.: Logic operations in a doped solid driven by stimulated Raman adiabatic passage. Phys. Rev. A **83**(3) (2011)

46. Hurst, S.L.: Multiple-valued logic - its status and its future. IEEE Trans. Comp. **C-33**, 1160–1179 (1984)

47. Kohavi, Z.: Switching and Finite Automata Theory. Tata McGraw-Hill, New Delhi (1999)

48. Gill, A.: Linear Sequential Circuits. McGraw Hill, New York (1966)

49. Remacle, F., Levine, R.D.: Towards parallel computing: representation of a linear finite state digital logic machine by a molecular relaxation process. Eur. Phys. J. D **42**, 49–59 (2007)

50. Torres, E.A., Kompa, K.L., Remacle, F., Levine, R.D.: Ultrafast vibrational spectroscopy and relaxation in polyatomic molecules: Potential for molecular parallel computing. Chem. Phys. **347**(1–3), 531–545 (2008)

51. Kaye, P., Laflamme, R., Mosca, M.: An Introduction to Quantum Computing. Oxford University Press, New York (2007)

52. Klein, M., Levine, R.D., Remacle, F.: Principles of design of a set-reset finite state logic nanomachine. J. Appl. Phys. **104**, 044509–044511 (2008)

53. Margulies, D., Melman, G., Shanzer, A.: A molecular full-adder and full-subtractor, an additional step toward a moleculator. J. Am. Chem. Soc. **128**(14), 4865–4871 (2006)

54. Remacle, F., Weinkauf, R., Levine, R.D.: Molecule-based photonically-switched half and full adder. J. Phys. Chem. A **110**(1), 177–184 (2006)

55. Mano, M.M., Kime, C.R.: Logic and Computer Design Fundamentals. Prentice Hall, Upper Saddle River, NJ (2000)

56. ELin, J.F., Hwang, Y.T., Sheu, M.H.A., Ho, C.C.: A novel high-speed and energy efficient 10-transistor full adder design. IEEE Trans. Circ. Syst. **54**(5), 1050–1059 (2007)

57. Shlyahovsky, B., Li, Y., Lioubashevski, O., Elbaz, J., Willner, I.: Logic gates and antisense DNA devices operating on a translator nucleic acid scaffold. ACS Nano **3**(7), 1831–1843 (2009)

58. Soloveichik, D., Seeliga, G., Winfree, E.: DNA as a universal substrate for chemical kinetics. Proc. Natl. Acad. Sci. USA, **107**, 5393–5398 (2010)

59. Wang, Z.-G., Elbaz, J., Remacle, F., Levine, R.D., Willner, I.: All-DNA finite-state automata with finite memory. Proc. Natl. Acad. Sci. USA **107**(51), 21996–22001 (2010)
60. Elbaz, J., Wang, F., Remacle, F., Willner, I.: pH-Programmable DNA logic arrays powered by modular DNAzyme libraries. Nano Lett.(published on web), DOI: 10.1021/nl300051g (2012)
61. Breaker, R.R., Joyce, G.F.: A DNA enzyme with Mg2+ dependent RNA phosphoesterase activity. Chem. Biol. **2**(10), 655–660 (1995)
62. Bajec, I.L., Zimic, N., Mraz, M.: The ternary quantum-dot cell and ternary logic. Nanotechnology **17**(8), 1937–1942 (2006)
63. Chattopadhyay, T.: All-optical symmetric ternary logic gate. Optic Laser Tech. **42**(6), 1014–1021 (2010)
64. Jin, X., Li, C., Liu, J., Jiang, X., Zeng, X.: Ternary logic dynamic CMOS comparators. In, vol. 317–319. pp. 1177–1182 (2011)
65. Lin, S., Kim, Y.B., Lombardi, F.: CNTFET-based design of ternary logic gates and arithmetic circuits. IEEE Trans. Nanotechnology **10**(2), 217–225 (2011)
66. Uemura, T., Yamamoto, M.: Three-valued magnetic tunnel junction for nonvolatile ternary content addressable memory application. J. Appl. Phys. **104**(12) (2008)
67. Medalsy, I., Klein, M., Heyman, A., Shoseyov, O., Remacle, F., Levine, R.D., Porath, D.: Logic implementations using a single nanoparticle-protein hybrid. Nature Nanotechnology **5**(6), 451–457 (2010)
68. Klein, M., Rogge, S., Remacle, F., Levine, R.D.: Transcending binary logic by gating three coupled quantum dots. Nano. Lett. **7**, 2795–2799 (2007)
69. Halpern, I., Yoeli, M.: Ternary arithmetic unit. Proc. IEE **115**(10), 1385–1388 (1968)
70. Yoeli, M., Rosenfeld, G.: Logic design of ternary switching circuits. IEEE Trans. Elect. Comp. **EC-14**, 19–29 (1965)
71. Remacle, F., Levine, R.D.: Configuration interaction between covalent and ionic states in the quantal and semiclassical limits with application to coherent and hopping charge migration. J. Phys. Chem. A **104**(11), 2341–2350 (2000)
72. Remacle, F., Levine, R.D., Schlag, E.W., Weinkauf, R.: Electronic control of site selective reactivity: a model combining charge migration and dissociation. J. Phys. Chem. A **103**, 10149–10158 (1999)
73. Pierre, M., Wacquez, R., Roche, B., Jehl, X., Sanquer, M., Vinet, M., Prati, E., Belli, M., Fanciulli, M.: Compact silicon double and triple dots realized with only two gates. Appl. Phys. Lett. **95**(24), 242107–242103 (2009)
74. Remacle, F., Levine, R.D.: Towards molecular logic machines. J. Chem. Phys. **114**(23), 10239–10246 (2001)
75. Chattopadhyay, T., Reis, C., Andre, P., Teixeira, A.: Theoretical analysis of all-optical clocked D flip-flop using a single SOA assisted symmetric MZI. Optic Comm. **285**(9), 2266–2275 (2012)
76. Remon, P., Balter, M., Li, S.M., Andreasson, J., Pischel, U.: An all-photonic molecule-based d flip-flop. J. Am. Chem. Soc. **133**(51), 20742–20745 (2011)
77. Sun, J., Wallin, D., He, Y., Maximov, I., Xu, H.Q.: A sequential logic device realized by integration of in-plane gate transistors in InGaAs/InP. Appl. Phys. Lett. **92**(1), (2008)
78. Remacle, F., Heath, J.R., Levine, R.D.: Electrical addressing of confined quantum systems for quasiclassical computation and finite state logic machines. Proc. Natl. Acad. Sci. USA **102**, 5653–5658 (2005)
79. Elbaz, J., Moshe, M., Willner, I.: Coherent activation of DNA tweezers: A "SET-RESET" logic system. Angew. Chem. Int. Ed. **48**(21), 3834–3837 (2009)
80. Elbaz, J., Wang, Z.-G., Orbach, R., Willner, I.: pH-stimulated concurrent mechanical activation of two DNA "Tweezers". A "SET-RESET" logic gate system. Nano Lett. **9**(12), 4510–4514 (2009)
81. Baron, R., Onopriyenko, A., Katz, E., Lioubashevski, O., Willner, I., Sheng, W., Tian, H.: An electrochemical/photochemical information processing system using a monolayer-functionalized electrode. Chem. Comm. (20), 2147–2149 (2006)

82. Periyasamy, G., Collin, J.-P., Sauvage, J.P., Levine, R.D., Remacle, F.: Electrochemically driven sequential machine: an implementation on copper rotaxanes. Chem. Eur. J. **15**(6), 1310–1313 (2009)
83. De Ruiter, G., Tartakovsky, E., Oded, N., Van Der Boom, M.E.: Sequential logic operations with surface-confined polypyridyl complexes displaying molecular random access memory features. Angew. Chem.– Int. Ed. **49**(1), 169–172 (2010)
84. Remacle, F., Levine, R.D.: All optical digital logic: full addition or subtraction on a three-state system. Phys. Rev. A **73**, 033820–033827 (2006)
85. Yan, Y., Mol, J.A., Verduijn, J., Rogge, S., Levine, R.D., Remacle, F.: Electrically addressing a molecule-like donor pair in silicon: an atomic scale cyclable full adder logic. J. Phys. Chem. C **114**(48), 20380–20386 (2010)
86. MacMillen, D.B., Landman, U.: Variational solutions of simple quantum systems subject to variable boundary conditions. II. Shallow donor impurities near semiconductor interfaces: Si, Ge. Phys. Rev. B **29**(8), 4524 (1984)
87. Calderon, M.J., Koiller, B., Hu, X., Das Sarma, S.: Quantum control of donor electrons at the Si-SiO[sub 2] interface. Phys. Rev. Lett. **96**(9), 096802–096804 (2006)
88. Cullum, J.K., Willoughby, R.A.: Lanczos Algorithm for Large Symmetric Eigenvalues Computations. Birkhauser, Boston (1985)
89. Andresen, S.E.S., Brenner, R., Wellard, C.J., Yang, C., Hopf, T., Escott, C.C., Clark, R.G., Dzurak, A.S., Jamieson, D.N., Hollenberg, L.C.L.: Charge state control and relaxation in an atomically doped silicon device. NanoLett. **7**(7), 2000–2003 (2007)
90. Barrett, S.D., Milburn, G.J.: Measuring the decoherence rate in a semiconductor charge qubit. Phys. Rev. B **68**(15), 155307 (2003)
91. Bergmann, K., Theuer, H., Shore, B.W.: Coherent population transfer among quantum states of atoms and molecules. Rev. Mod. Phys. **70**(3), 1003–1025 (1998)
92. Halfmann, T., Bergmann, K.: Coherent population transfer and dark resonance in SO2. J. Chem. Phys. **104**(18), 7068–7072 (1996)
93. Vitanov, N.V., Fleischhauer, M., Shore, B.W., Bergmann, K.: Coherent manipulation of atoms and molecules by sequential pulses. Adv. At. Mol. Opt. Phys. **46**, 55–190 (2001)
94. Vitanov, N.V., Halfmann, T., Shore, B.W., Bergmann, K.: Laser-induced population transfer by adiabatic passage technique. Ann. Rev. Phys. Chem. **52**, 763–809 (2001)

Binary Full-Adder in a Single Quantum System

Parallelization Using the Quantum Hamiltonian Computing Approach

N. Renaud and C. Joachim

Abstract In this short book chapter we show how to implement a complex Boolean function in a simple quantum system using the quantum Hamiltonian computing approach (QHC) [Ref: J. Phys. A: Math. Theor. 44 (2011) 155302 (15pp)]. Following the QHC approach, the logical inputs are encoded in local modifications of the system's Hamiltonian, and the outputs are read in the oscillation frequency of the population of well-defined target states. Few simple examples are presented first introducing a graphical aid that facilitates the design of QHC circuits. Using this graphical analogue to our symbolic analysis, we demonstrate how to easily implement multiple-inputs multiple-outputs logic gates taking benefit from the superposition principle. A binary full-adder is presented using this generalization of the QHC approach. We also show that using their nonlocal effect, each logical input needs to appear only once in the system and that different logical outputs are computed simultaneously.

1 Introduction

Taking benefit of the quantum superposition principle, it has already been demonstrated how to compute one Boolean function for all the possible values of the logical inputs in a single time step using quantum bits [1, 2]. Using this quantum parallelization scheme, one can set up quantum algorithms able to extract the prime factors of a given integer [3] or search a data base [4] much faster than any other

N. Renaud (✉)
Non-Equilibrium Energy Research Center, Northwestern University, 2145 Sheridan Road, 60201, Evanston, Ill

C. Joachim
CEMES-CNRS 29 rue Jeanne Marvig, BP 94347, 31055 Toulouse Cedex 4

classical implementations. However it's much harder to use this parallel schemes to improve simple arithmetic circuits like half- or full-adder [2, 5, 25] where one would like to perform several Boolean operations in a single time step.

In their simplest forms, Boolean logic gates compute a single logical output from two logical inputs, and several logic gates need to be cascaded with each other to form an arithmetic circuit able to add multi-digit numbers [6]. This cascading approach requires several clock time to complete a given complex logical operation with information transfer from one step to the next. This sequential procedure leads to the well-known carry rippling problem encountered during the computation of a sum [7]. Digital electronic circuits also suffer from another issue: most of the times, each logical input must be duplicated at several points of the circuit. These duplications generate a cluttering problem on the circuit and increase its energy consumption. Therefore, great efforts have been made to limit these duplications, but more than sixty years have been necessary to save one transistor in the implementation of a simple 2-input XOR logic gate [8, 9].

The so-called quantum Hamiltonian computing (QHC) is a recent idea in the field of quantum computing and proposes to use the logical inputs to deform the trajectory of a quantum system [10–16]. It is therefore quite different from the traditional quantum computing scheme where operations are performed by an assembly of qubits. In the QHC approach, the logical inputs, labeled $\boldsymbol{\alpha} = \{\alpha_1, \ldots, \alpha_M\}$, are encoded in well-identified parameters of the system's Hamiltonian, $\mathcal{H}(\boldsymbol{\alpha})$. Starting from a fixed nonstationary initial state, $|\Phi_a\rangle$, the system evolves following the solution of the Schrödinger equation: $|\Psi(t)\rangle = \exp(-i\mathcal{H}(\boldsymbol{\alpha})t/\hbar)|\Phi_a\rangle$. Any modifications of the logical inputs change the Hamiltonian and ultimately deform the quantum trajectory of the system. Designing correctly this Hamiltonian one is able to decide where the system's trajectory goes for a given value of the logical inputs or at which frequency it oscillates in a given direction of its phase's space. The logical outputs are probed at target states, labeled $|\Phi_{b_n}\rangle$, via the value of the oscillation frequency, noted Ω_n, of their populations : $\mathcal{P}(t) = |\langle \Phi_{b_n}|\Psi(t)\rangle|^2$. If Ω_n is a low frequency, the corresponding logical output is 0 and the logical output equals 1 for a high oscillation frequency. The exact meaning of "high" and "low" depends on the nature of the system whose typical oscillation frequencies can range from the gigahertz to the petahertz [16]. Here we will consider frequencies above the terahertz for a 1 logical output and frequencies below the gigahertz for the logical level 0. This corresponds to the standard time scale for through-bond superexchange electron transfer mechanisms [17]. This peculiar output encoding is motivated by the relationship between this oscillation frequency and the electronic transmission coefficient through the system when embedded in a tunneling junction [18]. Our QHC approach has already led to experimental implementations of a simple NOR logic gate whose logical output status was probed using the tunneling current intensity passing through a single molecule [19, 20] and new molecules have been recently proposed [21].

In this chapter we present our symbolic analysis of the QHC approach that has recently been used to design a programmable quantum system that can be tuned to perform different Boolean functions [16]. Although efficient, this analytical method

is cumbersome, and we present here a simple graphical analogue. We then extend our analysis to larger systems where the initial and the target states are defined as coherent superposition of several noninteracting states. This extended version of the QHC approach allows us to implement complex Boolean logic functions in simple quantum systems. As an example, a full-adder is presented.

2   A Symbolic Analysis for Simple QHC Systems

The symbolic analysis of the QHC circuit presented in [16] is based on a complex analysis of the resonant transfer between the initial and target state. A more comprehensive graphical analysis of the analytical development presented in [16] is represented in Fig. 1. The system is composed of the initial state: $|\Phi_a\rangle$, the target state: $|\Phi_b\rangle$, and three quantum states forming the core of the device and where the logical input α_1 and α_2 are encoded. The initial and the target states interact with the central system via weak couplings, ε. The results obtained in [16] for the simplest logic gates are reported in Fig. 1. The oscillation frequency from $|\Phi_a\rangle$ to $|\Phi_b\rangle$ varies with the logical inputs, and the NOR, AND, and XOR logic gates are easily and efficiently implemented. These three logic gates are obtained for different values of the energy E. To determine these values of E, one can use the symbolic analysis developed in [16] or a graphical aid like the one represented in Fig. 1. This figure shows the spectral dynamic of the central system, that is, the displacement of its eigenvalues and deformation of its eigenvectors, induced by a modification of the logical inputs. When $\alpha_1 = \alpha_2 = 0$, only one eigenstate, with an energy e_0, interacts with the initial and the final state. If one input is set to 1, a bonding and antibonding eigenstates are created, and when the two inputs are set to 1, three eigenstates are available to go from the initial to the target state. These three situations are labeled $\mathscr{S}_0(\boldsymbol{\alpha})$, $\mathscr{S}_1(\boldsymbol{\alpha})$, and $\mathscr{S}_2(\boldsymbol{\alpha})$ in reference of the symmetric Boolean operators $\mathscr{S}_i(\boldsymbol{\alpha})$ they correspond to [16]. As a reminder, the symmetric Boolean operator $\mathscr{S}_n(\boldsymbol{\alpha})$ equals 1 if and only if n of logical inputs are set to 1. For example, the case $\alpha_1 = \alpha_2 = 0$ corresponds to $\mathscr{S}_0(\boldsymbol{\alpha}) = 1$ and so on. All these eigenstates have different energies and can be used as resonant pathways between the initial and target sate. If one of this eigenstate is in resonance with $|\Phi_a\rangle$ and $|\Phi_b\rangle$, the population of the target state oscillates rapidly and the logical output is consequently 1. On the other hand, if none of the eigenstates are in resonance with the initial and the target states, the oscillations on $|\Phi_b\rangle$ are very slow and a 0 logic output is obtained. Tuning the energy E, specific pathways, corresponding to given values of the logical input, can be chosen as well. Hence, setting E equal to the antibonding state created when only one input is set to 1 leads to the implementation of a XOR gate. Indeed, for this value of E, slow off-resonant oscillations are obtained between the initial and target state the system when the two logical output are set to 0. When one logical input is set to 1, the antibonding state of the central system is in resonance with the initial and the target state and fast resonant oscillations are obtained at the target state. Finally, when both inputs are set
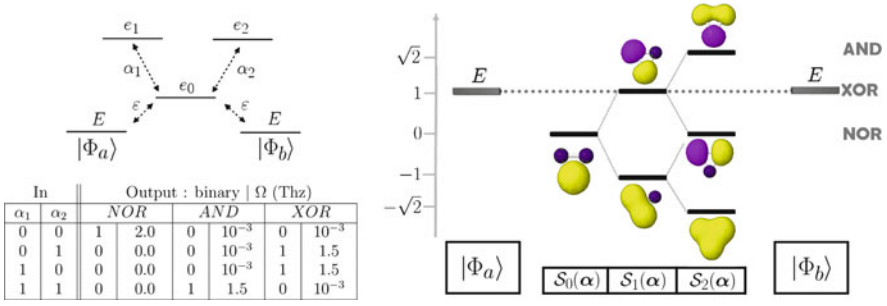
Fig. 1 Comprehensive picture of the mechanism underlying the programmable device designed in [16]. Depending on the value of E, different eigenstates of the central can provide a resonant channel that creates fast coherent oscillations between the initial and the target states leading ultimately to different logic functions

to 1, none of the three eigenstates are in resonance with the initial and the target state and the fast resonant oscillation are replaced by slow off-resonant ones. An XOR logic gate is therefore obtained since the populations of the target state oscillates rapidly only when one and only one logical input is set to 1. By the same token, setting $E = \pm\sqrt{2}$ leads to an AND gate and tunning E is resonance with e_0 leads to a NOR gate. A complexification of the system is then necessary to implement other Boolean function, but the general mechanism remains the same [16]. In simple terms, the QHC approach proposes to control the spectrum of a quantum system via the logical inputs and to read this spectrum at precise energies to measure the value of the logical output. The QHC approach takes then benefit from the large difference between the resonant and off-resonant transfer rate to obtain a large ON/OFF ratio for the different logical outputs status.

The mathematical formulation of the graphical aid presented above relies on the expression of the oscillation frequency, labeled Ω, from $|\Phi_a\rangle$ to $|\Phi_b\rangle$ through the central Hamiltonian $\mathscr{H}_0(\boldsymbol{\alpha})$ where the logical inputs, $\boldsymbol{\alpha}$, are encoded. This oscillation frequency can be expressed using the Löwdin effective Hamiltonian and can be written as [16]:

$$\Omega(\boldsymbol{\alpha}) = \mathscr{P}\left(\mathscr{F}^{-1}(E, \boldsymbol{\alpha})\right) \mp i\pi\delta\left(\mathscr{F}(E, \boldsymbol{\alpha})\right) \tag{1}$$

where $\mathscr{P}$ is the Cauchy principal part, δ the Dirac distribution, and $\mathscr{F}$ a function characteristic of the system that localize the eigenvalues of $\mathscr{H}_0(\boldsymbol{\alpha})$ (see appendix for details). In (1), the principal parts characterize the slow oscillations obtained out of resonance and that encode for a 0 logical output. At the contrary, the Dirac distribution represents the fast resonant oscillations obtained when one eigenstate of $\mathscr{H}_0$ is in resonance with $|\Phi_a\rangle$ and $|\Phi_b\rangle$ and that encodes for a 1 logical output. Consequently, only the Dirac distribution is kept to define the logical response of the system. This distribution was then decomposed over the set of values that the logical inputs can take [16]. In the case where all the logical inputs are equivalent, this expression reads:

$$\mathfrak{B}(E,\boldsymbol{\alpha}) = \sum_{i=0}^{N} \mathscr{S}_i(\boldsymbol{\alpha}) \cdot \delta\big(\mathscr{F}(E,\boldsymbol{\alpha}_i)\big) \tag{2}$$

where $\mathscr{S}_i(\boldsymbol{\alpha})$ is the i-th symmetric Boolean operator. $\boldsymbol{\alpha}_i$ refers to any combination of the logical inputs in which i of the logical inputs is set to 1 and the other is set to 0. In that frame $\{\alpha_1 = 1, \alpha_2 = 0\}$ is equivalent to $\{\alpha_1 = 0, \alpha_2 = 1\}$ and is noted $\boldsymbol{\alpha}_1$. The function $\mathscr{F}$ depends on the parameters of $\mathscr{H}_0(\boldsymbol{\alpha})$ and is the corner stone of our approach. Locating the zeros of this function allows to determine analytically the value of the Hamiltonian's parameters that lead to a given Boolean function. When applied to the system shown in Fig. 1, (2) reads :

$$\mathfrak{B}(E,\alpha_1,\alpha_2) = \mathscr{S}_0(\alpha_1,\alpha_2) \cdot \delta\big(E - e\big) \tag{3}$$

$$+ \mathscr{S}_1(\alpha_1,\alpha_2) \cdot \delta\big(\frac{1}{E}[E^2 - 1]\big)$$

$$+ \mathscr{S}_2(\alpha_1,\alpha_2) \cdot \delta\big(\frac{1}{E}[E^2 - 2]\big)$$

In this equation, specific Boolean operators can be selected by tunning E to cancel the arguments of the corresponding Dirac distributions. For example, the value: $E = \pm 1$ are the roots of the function in argument of the Boolean distribution associated with the operator $\mathscr{S}_1(\alpha_1,\alpha_2)$. Setting E to this value selects this operator, and a XOR function is implemented. Similarly, setting $E = 0$ selects the Boolean operator $\mathscr{S}_0(\alpha_1,\alpha_2)$ and gives a NOR gate, and with $E = \pm \sqrt{2}$, an AND gate is obtained by selecting the operator $\mathscr{S}_2(\alpha_1,\alpha_2)$. These results are of course identical to the ones obtained with the graphical aid represented in Fig. 1, and both methods are employed in the following to implement much more complex Boolean functions.

3 Extending the System

To implement larger Boolean functions, one could think of finding a system that presents a common eigenvalue for different configurations of the logical inputs. If a system as an eigenvalue equals to e_x for $\alpha_1 \neq \alpha_2$ and for $\alpha_1 = \alpha_2 = 1$, then setting the energy of the $|\Phi_a\rangle$ and $|\Phi_b\rangle$ to $E = e_x$ gives fast oscillations frequencies in this two cases and would lead to the implementation of a OR gate. This approach leads to an interesting problem of topologically equivalent isospectral operators but is far from being convenient to implement logical devices. To simplify this design, a much simpler solution consists in reading the spectrum of the central system at different energies. To do so, the initial and the target state must be a superposition of several noninteracting states of different energies. Let us hence write the initial state as:

$$|\Phi_a\rangle = \frac{1}{\sqrt{L}} \sum_{\lambda=1}^{L} |\phi_a^{(\lambda)}\rangle \tag{4}$$

where the states $|\phi_a^{(1)}\rangle, \ldots, |\phi_a^{(L)}\rangle$ have the energy $\{E_1, \ldots, E_L\}$ and do not interact with each other. To implement a logic function with N logical outputs, N target states are required. Let us write each of the n-th state as:

$$|\Phi_{b_n}\rangle = \frac{1}{\sqrt{L_n}} \sum_{\lambda=1}^{k_n} |\phi_{b_n}^{(\lambda)}\rangle \tag{5}$$

Each of the $|\Phi_{b_n}\rangle$ can be a superposition of any number of states, but to each state, $|\phi_{b_n}^{(\lambda)}\rangle$ must correspond a state $|\phi_a^{(\lambda)}\rangle$ both having the same energy to allow fast resonant transfer between $|\Phi_a\rangle$ and $|\Phi_{b_n}\rangle$. If an eigenstate of the central system is in resonance with $|\phi_a^{(\lambda)}\rangle$ and $|\phi_{b_n}^{(\lambda)}\rangle$, fast resonant oscillations are obtained on the target state defining a 1 logical value for the n-th output. Using multiple states to define the initial and target states, different pathways with different energies can be used to obtain resonant oscillations from $|\Phi_a\rangle$ to a given $|\Phi_{b_n}\rangle$. This avoids the delicate problem of finding isospectral operators and makes the design of our systems considerably easier.

The symbolic expression of the response of such system can be obtained by following the same approach than in [16]. This demonstration, given in appendix, leads to:

$$\mathfrak{B}_n(\boldsymbol{\alpha}) = \sum_{i=0}^{M} \mathscr{S}_i(\boldsymbol{\alpha}) \cdot \left[\sum_{\lambda=1}^{k_n} \delta\big(\mathscr{F}(E_n^{(\lambda)}, \boldsymbol{\alpha}_i)\big) \right] \tag{6}$$

where $E_n^{(\lambda)}$ is the energy of $|\phi_a^{(\lambda)}\rangle$ and $|\phi_{b_n}^{(\lambda)}\rangle$. As previously, $\mathscr{S}_i(\boldsymbol{\alpha})$ is the i-th, the symmetric Boolean operators, $\mathscr{F}$ a function that localizes the eigenvalues of $\mathscr{H}_0(\boldsymbol{\alpha})$, and $\boldsymbol{\alpha}_i$ a configuration of the logical inputs where i and only i logical inputs are set to 1 (see appendix for detail). Compared to (2), an additional sum is found in (6). This new sum reflects the possibility to read the spectrum at different energies and is the key to implement complex logic functions in simple systems taking benefit from the superposition principle.

To illustrate this approach, let us consider the case of a 2-input NAND gate with $\boldsymbol{\alpha} = \{\alpha_1, \alpha_2\}$ and where the target state $|\Phi_b\rangle$ is a coherent superposition of two states of energy E_1 and E_2. The response of the system on $|\Phi_b\rangle$ reads:

$$\begin{aligned}
\mathfrak{B}(\boldsymbol{\alpha}) &= \mathscr{S}_0(\alpha_1, \alpha_2) \cdot \big[\delta\big(\mathscr{F}(E_1, 00)\big) + \delta\big(\mathscr{F}(E_2, 00)\big)\big] \\
&+ \mathscr{S}_1(\alpha_1, \alpha_2) \cdot \big[\delta\big(\mathscr{F}(E_1, 01)\big) + \delta\big(\mathscr{F}(E_2, 01)\big)\big] \\
&+ \mathscr{S}_2(\alpha_1, \alpha_2) \cdot \big[\delta\big(\mathscr{F}(E_1, 11)\big) + \delta\big(\mathscr{F}(E_2, 11)\big)\big]
\end{aligned} \tag{7}$$

To implement a OR gate in this system, one can impose the condition $\mathscr{F}(E_1, \boldsymbol{\alpha}_1 = 01) = 0$ and $\mathscr{F}(E_2, \boldsymbol{\alpha}_2 = 11) = 0$. As pointed earlier, using (2) (obtained in the case where $|\Phi_b\rangle$ was not a superposition of two states) requires to find an Hamiltonian for which the function $\mathscr{F}$ cancels out for the same value of E in the cases $\alpha_1 \neq \alpha_2$ and $\alpha_1 = \alpha_2 = 1$ [16]. Using the superposition principle releases this constraints and allows us to use one value of E for $\alpha_1 \neq \alpha_2$ and another value of E for $\alpha_1 = \alpha_2 = 1$.
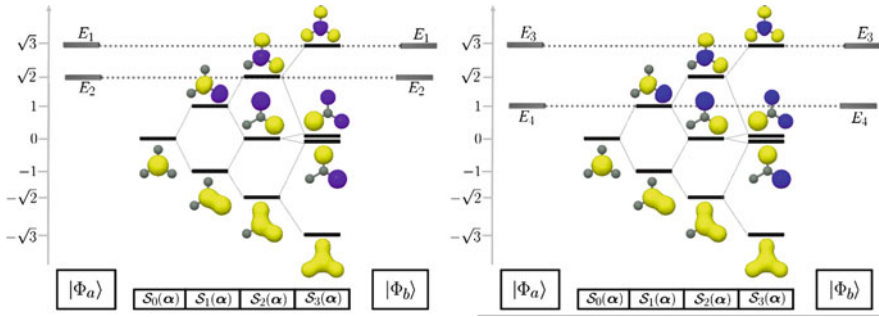
Fig. 2 Graphical representation of a full-adder implemented following the QHC approach. The energy of the states composing the initial and the target state are easily determined using the dynamics of the eigenvalues of the central system

4   A Full-Adder in a QHC Approach

To give an example of a multiple-input multiple-output logic function, let us focus on the simple case of the full-adder that performs the addition of three binary digits $\alpha = \{\alpha_1, \alpha_2, \alpha_3\}$. The expressions of the two logical outputs of a full-adder are:

$$\text{CARRY}(\alpha) = \mathscr{S}_2(\alpha) + \mathscr{S}_3(\alpha) \qquad \text{SUM}(\alpha) = \mathscr{S}_1(\alpha) + \mathscr{S}_3(\alpha) \qquad (8)$$

To construct the quantum system performing this operation in the QHC approach, two target states, $|\Phi_{b_1}\rangle$ and $|\Phi_{b_2}\rangle$, are required. We suppose that the logical output of CARRY(α) and SUM(α) are, respectively, probed on $|\Phi_{b_1}\rangle$ and $|\Phi_{b_2}\rangle$. To implement this 3-input Boolean function, we propose to use the central system whose Hamiltonian is:

$$\mathscr{H}_0(\alpha) = \begin{matrix} & \begin{matrix} |\xi_1\rangle & |\xi_2\rangle & |\xi_3\rangle & |\xi_4\rangle \end{matrix} \\ & \begin{pmatrix} e & \alpha_1 & \alpha_2 & \alpha_3 \\ \alpha_1 & e & 0 & 0 \\ \alpha_2 & 0 & e & 0 \\ \alpha_3 & 0 & 0 & e \end{pmatrix} \end{matrix} \qquad (9)$$

since it is the simpler system where the three logical inputs are equivalent. Each of the three logical input links a central state to a peripheral one and has the same effect on the eigenvalues and eigenvectors of $\mathscr{H}_0(\alpha)$. A brief diagonalization of this matrix leads to the analytical value of its eigenvalues which are $E_\pm = e \pm \sqrt{\sum_n \alpha_n^2}$ and $E_0 = e$ with this last eigenvalues being degenerated three times. To implement a full-adder using this system, one can use a graphical representation similar to the one used in the previous section and represented in Fig. 2.

Using this graphical tool, it is easy to find at which energy to read the spectrum to implement the two functions of (8). Hence to implement the CARRY, the energies E_1 and E_2 can be set to $E_1 = \sqrt{2}$ and $E_2 = \sqrt{3}$. Following the same strategy, the SUM is performed setting $E_3 = 1$ and $E_4 = \sqrt{3}$. Hence, the initial state is a superposition of 4 noninteracting states and each target state the superposition of two states:

$$|\Phi_a\rangle = \frac{1}{2}\left(|\phi_a^{(1)}\rangle + |\phi_a^{(2)}\rangle + |\phi_a^{(3)}\rangle + |\phi_a^{(4)}\rangle\right) \tag{10}$$

$$|\Phi_{b_1}\rangle = \frac{1}{\sqrt{2}}\left(|\phi_b^{(1)}\rangle + |\phi_b^{(2)}\rangle\right) \quad |\Phi_{b_2}\rangle = \frac{1}{\sqrt{2}}\left(|\phi_b^{(3)}\rangle + |\phi_b^{(4)}\rangle\right) \tag{11}$$

To read the spectrum, these states has to be connected to the central state of $\mathscr{H}_0(\boldsymbol{\alpha})$ through weak coupling strength $\varepsilon = 10^{-3}$ eV leading to the system represented in Fig. 3a. The same results could be obtained using the formal version of the symbolic analysis described by (6). Applying this equation to the system studied above, the symbolic expression of $\mathfrak{B}_1(\boldsymbol{\alpha})$ reads:

$$\begin{aligned}
\mathfrak{B}_1(\boldsymbol{\alpha}) = {} & \mathscr{S}_0(\boldsymbol{\alpha})\left[\delta\left((E_1 - e)\right) + \delta\left((E_2 - e)\right)\right] \\
& + \mathscr{S}_1(\boldsymbol{\alpha})\left[\delta\left((E_1 - e)^2 - 1\right)) + \delta\left((E_2 - e)^2 - 1\right))\right] \\
& + \mathscr{S}_2(\boldsymbol{\alpha})\left[\delta\left((E_1 - e)^2 - 2\right)) + \delta\left((E_2 - e)^2 - 2\right))\right] \\
& + \mathscr{S}_3(\boldsymbol{\alpha})\left[\delta\left((E_1 - e)^2 - 3\right)) + \delta\left((E_2 - e)^2 - 3\right))\right]
\end{aligned} \tag{12}$$

Tuning the values of the reading energies allows to select given symmetric Boolean operators. For $\mathfrak{B}_1(\boldsymbol{\alpha})$ to match CARRY$(\boldsymbol{\alpha})$, the arguments of the Dirac distributions associated with $\mathscr{S}_2(\boldsymbol{\alpha})$ and $\mathscr{S}_3(\boldsymbol{\alpha})$ must be null. This leads to $E_1 - e = \pm\sqrt{2}$ and $E_2 - e = \pm\sqrt{3}$. Similarly, the symbolic expression of $\mathfrak{B}_2(\boldsymbol{\alpha})$ reads:

$$\begin{aligned}
\mathfrak{B}_2(\boldsymbol{\alpha}) = {} & \mathscr{S}_0(\boldsymbol{\alpha})\left[\delta\left((E_3 - e)\right) + \delta\left((E_4 - e)\right)\right] \\
& + \mathscr{S}_1(\boldsymbol{\alpha})\left[\delta\left((E_3 - e)^2 - 1\right)) + \delta\left((E_4 - e)^2 - 1\right))\right] \\
& + \mathscr{S}_2(\boldsymbol{\alpha})\left[\delta\left((E_3 - e)^2 - 2\right)) + \delta\left((E_4 - e)^2 - 2\right))\right] \\
& + \mathscr{S}_3(\boldsymbol{\alpha})\left[\delta\left((E_3 - e)^2 - 3\right)) + \delta\left((E_4 - e)^2 - 3\right))\right]
\end{aligned} \tag{13}$$

It is once again easy to show that for $\mathfrak{B}_2(\boldsymbol{\alpha})$ to match SUM$(\boldsymbol{\alpha})$, the arguments of the Dirac distributions associated with $\mathscr{S}_1(\boldsymbol{\alpha})$ and $\mathscr{S}_3(\boldsymbol{\alpha})$ must be zero. This directly leads to $E_3 - e = \pm 1$ and $E_4 - e = \pm\sqrt{3}$.

To confirm this QHC implementation of a full-adder, the oscillation frequencies of the target states populations have been numerically computed for all the possible values of the logical inputs and are reported in Fig. 3b. These calculations show clearly that an accurate implementation of the full-adder have been reached. When either CARRY$(\boldsymbol{\alpha})$ or SUM$(\boldsymbol{\alpha})$ equals 1, the oscillation frequency of the corresponding target state population is about $1/5$ Thz, whereas it falls down to approximately $1/6$ Ghz when those functions equal to 0.
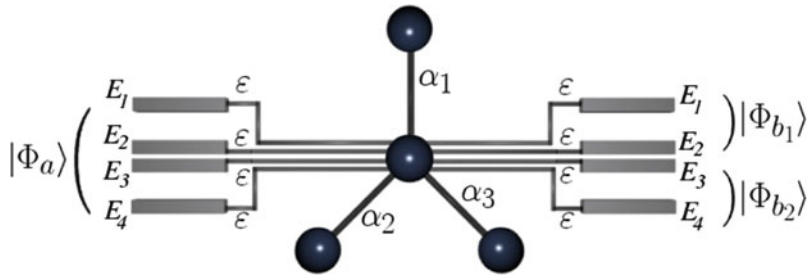
Inputs (eV)			Output : binary | Ω (Thz)			
α_1	α_2	α_3	CARRY		SUM	
0	0	0	0	0.001	0	0.001
0	0	1	0	0.001	1	0.166
0	1	0	0	0.001	1	0.166
0	1	1	1	0.182	0	0.001
1	0	0	0	0.001	1	0.166
1	0	1	1	0.195	0	0.001
1	1	0	1	0.195	0	0.001
1	1	1	1	0.201	1	0.192

Fig. 3 *Top*—representation of the Hamiltonian performing the full addition of α_1, α_2, and α_3. *Bottom*—numerical calculations of the oscillation frequencies on the target states $|\Phi_{b_1}\rangle$ and $|\Phi_{b_2}\rangle$. These values respect the desired truth table

With the initial and the target state being defined as superposition of state, only a part of the initial state cross the system each time a resonant transfer pathway is provided by the central system. The maximum population on a given target state decreases with the number of noninteracting states used to define the initial superposition and to create this target state. It can be easily shown that with the definition (4) and (5), the maximum value of the population is $\mathscr{A}_{\max} = (L \cdot L_n)^{-1}$. For example, in the case of the full-adder designed above, this maximum amplitude reaches $1/8$. In a more general way, this decrease of the output signal amplitude with the complexity of the logic device can be estimated via the number of logical outputs, N and the average number of symmetric Boolean operators, noted $\langle N_{\mathscr{S}(\boldsymbol{\alpha})} \rangle$, involved in the expression of the logical function. In this situation, each logical output must be, in average, the superposition of $\langle N_{\mathscr{S}(\boldsymbol{\alpha})} \rangle$ states and the initial state must be a superposition of $N \times \langle N_{\mathscr{S}(\boldsymbol{\alpha})} \rangle$ states. The maximum population follows then: $\mathscr{A}_{\max} = \left[N \times \langle N_{\mathscr{S}(\boldsymbol{\alpha})} \rangle^2 \right]^{-1}$. The maximum amplitude decrease linearly with the number of logical outputs but is drastically reduced when the complexity of each output increases. It is hence more advantageous to realize a lot of simple logic functions than a handful of complex ones.

Despite this decrease of the output amplitude, the implementation presented above presents significant improvements compared to its classical counterpart. First, the two logical outputs, CARRY($\boldsymbol{\alpha}$) and SUM($\boldsymbol{\alpha}$), are computed simultaneously without any delay and without carry rippling. Usually, SUM($\boldsymbol{\alpha}$) is computed first, and its output status is injected in a second stage to compute CARRY($\boldsymbol{\alpha}$). This sequential procedure is replaced by a parallelization of the two operations in the QHC approach. Besides, the QHC implementation of the full-adder does not require the duplication of the logical inputs at different points of the Hamiltonian whereas each one of them are distributed at many locations of a full-adder electrical circuit [9, 23, 24].

The same procedure has been used to implement larger logic functions such as a 2-bit adder in a 31×31 matrix Hamiltonian or a 3-bit adder in a 107×107 matrix Hamiltonian. The severe decrease of the maximum population reaching the target states of these large systems is the strongest limitation of our approach. Nevertheless, following the QHC approach, the addition of two words of n-bits can be performed in a single step and using each logical input only once in the circuit. This approach is consequently a suitable solution for highly parallel computational schemes taking benefit from the quantum properties of the system.

5   Conclusion

The symbolic analysis of a QHC circuit has been generalized accounting for the possible superposition of the initial state and the presence of several superposed target states. The nonlocal effect of the α_i on the $\mathcal{H}_0(\boldsymbol{\alpha})$ eigenvectors makes available any modification of the logical inputs all over the quantum system. Using this quantum conversion of the $\boldsymbol{\alpha}$ classical inputs, the QHC approach overcomes the classical electronic architecture on several points. First, each α_i is used only once in the Hamiltonian whereas they are duplicated at many points of an electrical circuit. We have, for example, designed a full-adder with only three commuting elements, whereas a minimum of eight is required in the most recent transistor-based electronic circuit. We have also demonstrated that a QHC circuit is able to compute different logic functions in parallel. For example, we have designed a QHC circuit adding two words of two bits in a single computational step where dozen of steps are required in an electronic circuits. This QHC architecture will have now to be converted in a realistic molecular chemical structure as it was the case for the simple NOR logic gate [19, 20].

A.1   Simple Symbolic Analysis of the QHC Approach

A brief overview of the recently developed symbolic analysis of simple quantum systems is presented in this appendix. The development of the general symbolic analysis developed in Sect. 2 is based on this previous work, and the interested reader should refer to the reference [16] for further details. The general form of the Hamiltonian implementing a 1-output logic gate reads:

$$\mathscr{H}(\boldsymbol{\alpha}) = \begin{array}{c} |\phi_a\rangle \; |\phi_b\rangle \\ \left(\begin{array}{cc|c} E & 0 & \\ 0 & E & \mathscr{V}^\dagger \\ \hline & \mathscr{V} & \mathscr{H}_0(\boldsymbol{\alpha}) \end{array} \right) \end{array} \tag{A.1}$$

where $|\phi_a\rangle$ is the initial state of the evolution and $|\phi_b\rangle$ the target state where the logical output status is monitored. If the population of $|\phi_b\rangle$ oscillates with a high frequency, the logical output is 1 and is 0 if this oscillation frequency is low. The Lowdin partitioning of the system is used to access the value of this oscillation frequency, noted Ω in the following. Introducing the projector P on the $\{|\phi_a\rangle, |\phi_b\rangle\}$ subspace and the projector Q on the rest of the system, the effective Lowdin partitioning reads [22]:

$$\mathscr{H}_{\text{eff}}(E, \boldsymbol{\alpha}) = P\mathscr{H}(\boldsymbol{\alpha})P + \lim_{\eta \to 0} P\mathscr{V}Q \frac{1}{E \pm \mathrm{i}\eta - \mathscr{H}_0(\boldsymbol{\alpha})} Q\mathscr{V}P \tag{A.2}$$

The evolution generated by this 2×2 Hamiltonian smooth the complex evolution going through the $\mathscr{H}_0(\boldsymbol{\alpha})$ subspace by a Rabi-like evolution whose oscillation frequency is precisely Ω. An expression of Ω is given by the difference of the two eigenvalues of $\mathscr{H}_{\text{eff}}(E, \boldsymbol{\alpha})$. This expression can be written in term of a Cauchy principal part and a Dirac distribution as:

$$\Omega(\boldsymbol{\alpha}) = \mathscr{P}\left(\mathscr{F}^{-1}(E, \boldsymbol{\alpha})\right) \mp \mathrm{i}\pi\delta\left(\mathscr{F}(E, \boldsymbol{\alpha})\right) \tag{A.3}$$

where the function $\mathscr{F}(E, \boldsymbol{\alpha})$ comes from the diagonalization of $\mathscr{H}_{\text{eff}}(E, \boldsymbol{\alpha})$ and reads:

$$\mathscr{F}(E, \boldsymbol{\alpha}) = \mathscr{A} \times \det\left(E - \mathscr{H}_0(\boldsymbol{\alpha})\right) \tag{A.4}$$

with $\mathscr{A} = \left[\sqrt{(h_{aa} - h_{bb})^2 + 4h_{ab}^2}\right]^{-1}$ and $h_{ij} = \langle\phi_i|V\,adj[E - \mathscr{H}_0(\boldsymbol{\alpha})]V|\phi_j\rangle$. The principal part refers to the slow oscillation frequency obtained when $\mathscr{F}(E, \boldsymbol{\alpha}) \neq 0$. At the contrary, when $\mathscr{F}(E, \boldsymbol{\alpha}) = 0$, the Dirac distribution dominates (1), and this leads to a high oscillation frequency. We are particularly interested by locating the points where $\mathscr{F}(E, \boldsymbol{\alpha}) = 0$ since they correspond to the rare values of the phase space where a 1 logical output is obtained. Consequently, we approximate the expression of Ω only considering the Dirac distributions. Our symbolic analysis relies therefore on the expression:

$$\mathfrak{B}(E, \boldsymbol{\alpha}) = \delta\left(\mathscr{F}(E, \boldsymbol{\alpha})\right) \tag{A.5}$$

This last expression is however not a symbolic analysis since it does no involve Boolean operators. A decomposition of $\mathfrak{B}(E, \boldsymbol{\alpha})$ over the possible values of the logical inputs can be obtained using the properties of the Fourier transform of Dirac distributions. Using this decomposition, (A.5) is reexpressed as a sum of Dirac distribution weighted by Boolean operators. In its most general form, these operators are symmetric Boolean operators, $\mathscr{S}_i(\boldsymbol{\alpha})$, that equals 1 if i logical inputs equal one. This expression reads:

$$\mathfrak{B}(E, \boldsymbol{\alpha}) = \sum_{i=0}^{N} \mathscr{S}_i(\boldsymbol{\alpha}) \cdot \delta\big(\mathscr{F}(E, \boldsymbol{\alpha}_{2^i - 1})\big) \tag{A.6}$$

Each Dirac distribution is associated with one of the Boolean operator. Therefore, one or several $\mathscr{S}_i(\boldsymbol{\alpha})$ operators can be selected by canceling out the argument of their respective distribution.

A.2 Pseudo-Boolean Symbolic Expression in the General Case

The demonstration of (6) can be obtained from the same Lowdin partitioning used in the A.1. However, a simpler and more insightful demonstration is possible studying the properties of the population of the target states. To demonstrate (6), the complete expression of $\mathscr{P}_n(t)$, when the $|\Phi_a\rangle$ and $|\Phi_{b_n}\rangle$ are given by (4) and (5), reads:

$$\mathscr{P}_{ab_n}(t) = \frac{1}{LL_{b_n}} \left| \sum_{\lambda_a=1}^{L} \sum_{\lambda=1}^{L_{b_n}} \langle \phi_b^{(s_n^\lambda)} | e^{-i\mathscr{H}(\boldsymbol{\alpha})t} | \phi_a^{(\lambda_a)} \rangle \right|^2 \tag{A.7}$$

A very fast oscillation is only obtained between two states $|\phi_b^{(s_n^\lambda)}\rangle$ and $|\phi_a^{(\lambda_a)}\rangle$ with the same energy. Therefore, to have a resonant oscillation, we must have $s_n^\lambda = \lambda_a$. Neglecting the low-frequency components of (A.7) which does not respect this last condition leads to:

$$\mathscr{P}_{ab_n}(t) \simeq \frac{1}{LL_{b_n}} \left| \sum_{\lambda=1}^{L_{b_n}} \langle \phi_b^{(s_n^\lambda)} | e^{-i\mathscr{H}(\boldsymbol{\alpha})t} | \phi_a^{(s_n^\lambda)} \rangle \right|^2 \tag{A.8}$$

Considering only the cases where only one eigenenergy of $\mathscr{H}_0(\boldsymbol{\alpha})$ is possibly equal to one $E_l = \langle \phi_a^{(l)} | \mathscr{H} | \phi_a^{(l)} \rangle = \langle \phi_b^{(l)} | \mathscr{H} | \phi_b^{(l)} \rangle$ energy leads to:

$$\mathscr{P}_{ab_n}(t) \simeq \frac{1}{LL_{b_n}} \sum_{\lambda=1}^{L_{b_n}} \left| \langle \phi_b^{(s_n^\lambda)} | e^{-i\mathscr{H}(\boldsymbol{\alpha})t} | \phi_a^{(s_n^\lambda)} \rangle \right|^2 \tag{A.9}$$

since the crossed terms $\langle\phi_b^{(k)}|e^{-i\mathcal{H}(\alpha)t}|\phi_a^{(k)}\rangle\langle\phi_b^{(l)}|e^{-i\mathcal{H}(\alpha)t}|\phi_a^{(l)}\rangle$ are null unless $k = l$. We clearly see here that if only one term of this sum is resonant, then the maximum amplitude for small times of (A.9) is $(LL_{b_n})^{-1}$. Now, if κ $\mathcal{H}_0(\alpha)$ eigenenergies are equal to κ different E_λ, then very high-frequency components appear in $\mathscr{P}_{ab_n}(t)$ and the maximum amplitude this function reaches for small times is $\kappa^2/(LL_{b_n})$. For example, if one $\mathcal{H}_0(\alpha)$ eigenenergy is equal to E_i and another one to E_j, then a $1/\hbar|E_i - E_j|$ frequency appears in the $\mathscr{P}_{ab_n}(t)$ spectrum and the small time amplitude of this function increases to $4/(LL_{b_n})$. Such a situation is however not explored in the following.

Since (A.9) is the superposition of elementary terms, the secular oscillation rate, Ω_n, is also the superposition of the secular oscillation rates of each $\left|\langle\phi_b^{(s_n^\lambda)}|e^{-i\mathcal{H}(\alpha)t}|\phi_a^{(s_n^\lambda)}\rangle\right|^2$ function given by:

$$\Omega_n(\alpha) = \sum_{\lambda=1}^{L_{b_n}} \mathscr{P}\left(\mathscr{F}^{-1}(E_{s_n^\lambda}, \alpha)\right) \mp i\pi\delta\left(\mathscr{F}(E_{s_n^\lambda}, \alpha)\right) \tag{A.10}$$

Neglecting the principal part in (A.10) to define the pseudo-Boolean symbolic expression of $\Omega_n(\alpha)$ leads to:

$$\mathfrak{B}(\alpha) = \sum_{\lambda=1}^{L_{b_n}} \delta\left(\mathscr{F}(E_{s_n^\lambda}, \alpha)\right) \tag{A.11}$$

Using the decomposition of each term of this sum over the symmetric Boolean operators introduced in the previous section leads finally to :

$$\mathfrak{B}(\alpha) = \sum_{i=1}^{M} \mathscr{S}_i(\alpha) \cdot \left[\sum_{\lambda=1}^{L_{b_n}} \delta\left(\mathscr{F}(E_{s_n^\lambda}, \alpha_{2^i-1})\right)\right] \tag{A.12}$$

$$\mathscr{F}(E_{s_n}, \alpha) = \frac{\det(E_{s_n} - \mathcal{H}_0(\alpha))}{\sqrt{(h_{aa} - h_{bb})^2 + 4h_{ab}^2}} \tag{A.13}$$

with $h_{ij} = \langle\phi_i^{(s_n)}|V \text{ adj}[E_{s_n} - \mathcal{H}_0(\alpha)]V|\phi_j^{(s_n)}\rangle$. This completes the demonstration of our generalization of the QHC approach to large systems.

References

1. Deutsch, D.: Quantum theory, the Church-Turing principle and the universal quantum computer. Proc. Roy. Soc. A **400**, 97–117 (1985)
2. Nielsen, A.M., Chuang, I.L.: Quantum Computation and Quantum Information. Cambridge University Press, Cambridge (2000)

 3. Shor, P.W.: Polynomial-time algorithms for prime factorisation. SIAM J. Sci. Stat. Comput. **26**, 1484 (1997)
 4. Grover, L.: Quantum mechanics helps in searching for a needle in a haystack. Phys. Rev. Lett. **79**, 325 (1997)
 5. Henessy, J.L., Patterson, D.A.: Computer Architecture, A Quantitative Approach. Elsevier, Amsterdam (1990)
 6. Gates, E.D.: Introduction to Electronics, 4th edn. Delmar Thomson (Cengage) Learning. Cengage (2000)
 7. Chang, T.-Y., Hsiao, M.-J.: Carry-select adder using single ripple-carry adder. Electron. Lett. **34**, 2101 (1998)
 8. Shannon C.E.: A symbolic analysis of relay and switching circuits. Master's thesis, MIT, Cambridge (1936)
 9. Chowdhurry, S.R., Banerjee, A., Roy, A., Saha, H.: A high speed 8 transistor full adder design using 3 transistor XOR gates. Int. J. Elec. **2**, 217 (2008)
10. Fiurasek, J., Cerf, N.J., Duchemin, I., Joachim, C.: Intramolecular Hamiltonian logic gates. Physica E **24**, 161 (2004)
11. Duchemin, I., Fiurasek, J., Cerf, N.J., Joachim, C.: Hamiltonian logic gates: computing inside a molecule. Int. J. Nano. **4**, 107 (2005)
12. Duchemin, I., Joachim, C.: A quantum digital half adder inside a single molecule. Chem. Phys. Lett. **406**, 167 (2005)
13. Duchemin, I., Renaud, N., Joachim, C.: An intramolecular digital 1/2-adder with tunneling current drive and read-outs. Chem. Phys. Lett. **452**, 269–274 (2008)
14. Renaud, N., Joachim, C.: Design and stability of NOR and NAND logic gates constructed with three quantum states. Phys. Rev. A **78**, 062316 (2008)
15. Renaud, N., Ito, M., Shangguan, M., Saeys, M., Hliwa, M. Joachim, C.: A NOR-AND quantum running gate molecule. Chem. Phys. Lett. **472**, 74–79 (2009)
16. Renaud, N., Joachim, C.: Classical Boolean Logic gates with quantum systems. J. Phys. A: Math. Theor. **44**, 155302 (2011)
17. Joachim, C., Ratner, M.A.: Molecular electronics: Some view on transport junction and beyond. PNAS **102**, 8801 (2001)
18. Renaud, N., Ratner, M.A., Joachim, C.: A time-dependent approach to electronic transmission in model molecular junctions. J. Phys. Chem. B **11518**, 5582 (2011)
19. Soe, W.-H., Manzano, C., Renaud, N., de Mendoza, P., de Sarkar, A., Ample, F., Hliwa, M., Echavarren, A.M., Chandrasekhar, N., Joachim, C.: Manipulating molecular quantum states with classical metal atom inputs: demonstration of a single molecule NOR logic gate. ACS Nano **5**, 1436 (2011)
20. Soe, W.-H., Manzano, C., Renaud, N., de Mendoza, P., de Sarkar, A., Ample, F., Hliwa, M., Echavarren, A.M., Chandrasekhar, N., Joachim, C.: Demonstration of a NOR logic gate using a single molecule and two surface gold atoms to encode the logical input. Phys. Rev. B **83**, 155443 (2011)
21. Renaud, N., Hliwa, M., Joachim, C.: Quantum desing rules for single molecule logic gates. Phys. Chem. Chem. Phys. **13**, 14404 (2011)
22. Cohen-Tannoudji, C., Dupont-Roc, J., Grynberg, G.: Atom-Photon Interactions. Wiley, New York (1992)
23. Wei, H., Gristede, G., Sanda, P., Wang, S.Y., Heidel, D.F.: Implementation of a self-resetting CMOS 64-bit parallel adder with enhanced testability. IEEE J. Solid-State Circ. **34**, 1108 (1999)
24. Kabanets, V., Cai, J.: Circuit minimization problem. In: Proceedings of the Thirty-Second Annual ACM Symposium on Theory of Computing, STOC'00, 73–79. ACM press (2000)
25. Barbosa, G.A.: Quantum half-adder. Phys. Rev. A **73**, 052321 (2006)

Part V
Molecular Qubits

A Controlled Quantum SWAP Logic Gate in a 4-center Metal Complex

Mohamed Hliwa, Jacques Bonvoisin, and Christian Joachim

Abstract A monomolecular four center low spin paramagnetic organometallic complex is proposed and theoretically studied to work as a controlled quantum swap molecule logic gate. The magnetic super-exchange interaction between the 2 intramolecular qubits depends on the oxydation state of a third intermediate center itself controlled by an intervalence electron transfer process. A model system is build up using entangled spin qubits in the framework of an Heisenberg-Dirac-Van Vleck like spin Hamiltonian demonstrating the effective swapping operation of this complex.

1 Introduction

Interconnected in an electrical circuit, single molecules can enter in the construction of a calculating unit [1]. A single molecule can also be the calculating unit by itself either in a semi-classical [2, 3] or in a quantum like architecture approach [4]. For a quantum like architecture, the input data can be encoded either in the initial quantum state [5] or in the Hamiltonian [6] of the electronic states of the molecule. For the former, the qubits are positioned along the molecular board. The quantum inputs are

M. Hliwa
Faculty of Sciences Ben M'Sik, University Hassan II-Mohammedia-Casablanca, BP 7955-Sidi Othman, Casablanca, Maroc. Nanoscience Groupe and MANA Satellite, CEMES/CNRS, 29 rue Jeanne Marvig, 31055, Toulouse, France
e-mail: hliwa@cemes.fr

J. Bonvoisin · C. Joachim
Nanoscience Groupe and MANA Satellite, CEMES/CNRS, 29 rue Jeanne Marvig, 31055, Toulouse, France
e-mail: bonvoisin@cemes.fr; joachim@cemes.fr

encoded in specific non stationnary states of the molecule electronic structure. For performing a quantum computation, Rabi like oscillations result which will fade out due to decoherence and relaxation processes [7]. In the time interval between the initial qubit preparation and the progressive involvement of a decoherence process, it is therefore important to control when to start and when to stop the quantum computation.

Let us consider the simple example of an interacting 2 qubits system described by the hamiltonian $H = H_0 + \lambda I$ defined on the $\{|i\ j\rangle\}_{i,j=0,1}$ canonical basis set where I describes the qubit interactions. When λ is no zero, a swapping operation U_S on the 2 qubits is defined by $U_S |i\ j\rangle = |j\ i\rangle$[8]. Over the t_n time series, $U_S = exp\left(-i\frac{H}{\hbar}t\right)$ for $t = t_n$. When λ is set to zero the $\{|i\ j\rangle\}$ basis set is the H eigenbasis set and there is no swapping. Therefore to control a swapping operation, the solution presented in this letter is to switch ON and OFF the interactions between the qubits using an external stimulus. Mixed valence organo-metallic complex molecules are very well adapted for such a control swapping. First, an organometallic complexe can be prepared in low spin oxydation states. Under a static magnetic field, this defines a set of qubits each localized on one metallic center [9]. Second, through bond magnetic superexchange interactions along the organic board of the organo-metallic molecule mediate the quantum information between the qubits with a moderate interaction decay between them as a function of the board length [10]. Third, intramolecular electron transfer processes are known to control the magnetic super exchange interaction [14], a nice way to control the swapping.

In this letter, a generic 4-metal center organometallic mixed valence complex is proposed able to perform a swapping operation controlled by light. After the initial preparation of the intramolecular qubits system, the swap can be initiated at will and stop before the decoherence by a reverse intramolecular electron transfer process. In the subsection 2.1, the chemical structure, the swapping process and its control on this 4-center organometallic complex are presented. In the subsection 2.2, the Hilbert space to model this 3-center/3-electron system is presented and in subsection 2.3 the corresponding valence bond like magnetic Hamiltonian. In section 3, this Hamiltonian is used to demonstrate how the swapping is performed when the qubit magnetic interactions is ON.

2 The Swaping Molecule Gate Structure and Design

2.1 The Controlled Swapping Mechanism

The structure of a controlled swap molecule is presented in figure 1. In this 4 metal center organometallic complex, the $\mathbf{M_1}$ and $\mathbf{M_2}$ sites are carrying the two qubits which are paramagnetic Low Spin (LS) within a doublet ground state. M_1^{n+} and M_2^{n+} are stabilized in their respective oxidation state by their own coordination
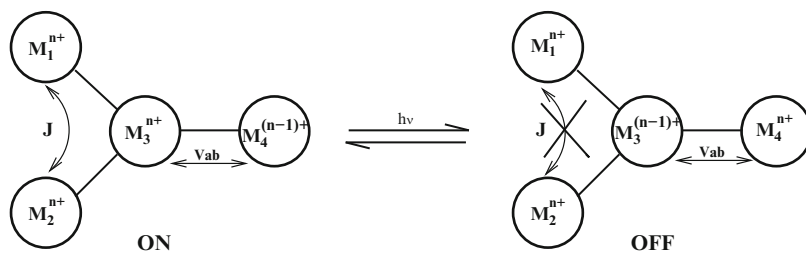
Fig. 1 The model structure of a 4-center controlled swap organometallic complex. The magnetic interaction between the metal centers M_1 and M_2 can be switched ON or OFF depending on the oxidation state of M_3 which changes respectively from n to $(n-1)$ under electron transfer between M_3 and M_4 induced by a specific light radiation. "OFF" is the initial ground state configuration and "ON" the swapping state of the molecule. V_{ab} is the electronic through bond interaction between M_3 and M_4 in their respective oxidation states. J is the spin super-exchange interactions between M_1 and M_2 centers through M_3

sphere. They are in magnetic interaction via conjugated organic bridges, through a third central metal ion M_3^{m+}. This through bond super-exchange magnetic interaction can be switched ON and OFF depending on the M_3 oxidation state. This state can be changed from $m = n$ (doublet electronic ground state) to $m = n - 1$ (singlet electronic ground state) by exciting the Inter-Valence Transition (IVT) (or Metal-Metal Charge Transfer (MMCT)) band of the lateral $M_3 - M_4$ mixed valence part of this 4 center complex. M_3 is the control swapping site of the gate.

When constituted of four identical metallic centers **M**, the special feature of this molecular structure is that the coordination spheres around each metal ion can be different by chosen different substituents on the surrounding ligands opening a possible optical selective excitation of each center to prepare a given qubits state superposition. A realistic chemical structure of this swap molecule is presented in figure 2 where **M** is a ruthenium. As required, this molecule is a non symmetric tetranuclear complex where all the peripheral ruthenium entities are different from each other due to their different coordination spheres ($R_1 \neq R_2 \neq R_4$). Several necessary chemical steps towards this target molecules have been made [11–13]

2.2 The Model Electronic Basis Set

Each external metal ion M_1^{n+} and M_2^{n+} of the complex hold an unpaired electron ($s = \frac{1}{2}, m_s = \pm \frac{1}{2}$) spin state. Under a static external magnetic field, each defines a well localised qubit which can be prepared in a quantum superposition $\alpha \left| \frac{1}{2} \right\rangle + \beta \left| -\frac{1}{2} \right\rangle$. When M_3 is in its $(n-1)+$ oxidation state, the magnetic interaction between M_1^{n+} and M_2^{n+} is negligible and the two qubits are not in interaction and each qubit center can be prepared separatly. When the M_3 is switched on in its $n+$ oxidation state, M_1^{n+} and M_2^{n+} are magnetically coupled through the organic ligands via M_3^{n+} and the swapping begin [14].
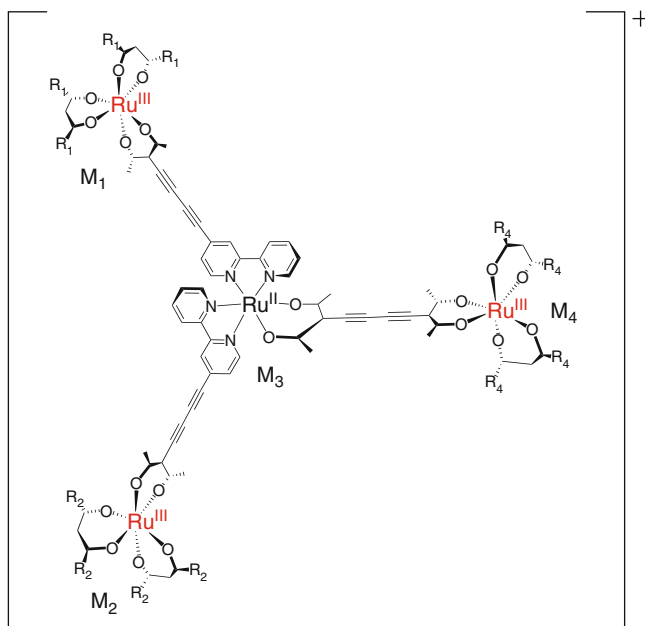
Fig. 2 A possible chemical structure of the proposed swap molecule whose controlled swapping process is presented in this letter

Thus, to model this swapping operation, we have to consider the spin interaction between two unpaired electrons each one localized on one metal of two bonded centers, namely $M_1^{n+} - M_3^{n+}$ and $M_2^{n+} - M_3^{n+}$. The spin interaction between the electrons on sites $\mathbf{M_1}$ and $\mathbf{M_2}$ is described by an effective magnetic coupling by considering only two 1-qubits, one on each of the two target centers. The initial state is prepared within two paired electrons on the site $\mathbf{M_4}$ and a single electron on each one of the sites $\mathbf{M_1}$, $\mathbf{M_2}$ and $\mathbf{M_3}$. Therefore, to construct the basis set describing the swapping process, only 3 active centers have to be considered that is the 3 paramagnetic sites $\mathbf{M_1}$, $\mathbf{M_2}$ (the qubits sites) and $\mathbf{M_3}$ (the control site).

Electron indicernability imposes the use of a Slater determinant canonical basis set:

$$\{|101\rangle, |011\rangle, |100\rangle, |010\rangle, |001\rangle, |110\rangle\} \tag{1}$$

to model the swaping operation on this 3-electron/3-active sites electronic system.

The swap mechanism using the $\mathbf{M_1}$-$\mathbf{M_2}$ spin super-exchange mechanism is represented in figure 3 for each possible canonical preparation state. The intermediate states described by the determinants $|110\rangle$ and $|001\rangle$ correspond to states in which the spin of the qubit sites have the same m_s value. The preparation state can be one of the states represented by one of the determinants at the left or at the right in figure 3 and the final state is its antagonist. To model the swapping, the model Hilbert space generated by those 6 determinants can be partitioned into two subspaces :
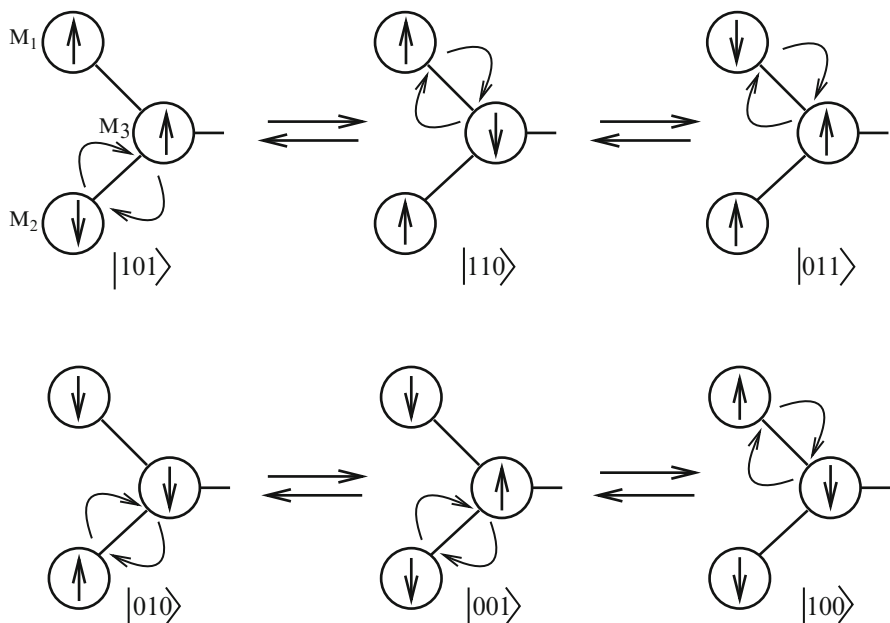
Fig. 3 schematic representation of the swapping mechanism

(i) A model subspace which contains the configurations where the qubit sites M_1 and M_2 have spins with the opposite signs and for which the control site M_3 have either α or β spin.

$$\{|010\rangle, |100\rangle, |011\rangle, |101\rangle\} \quad (2)$$

(ii) an intermediate subspace which contains the configurations for which the qubit sites have spins oriented in the same direction and where the control site have either α or β spin.

$$\{|110\rangle, |001\rangle\} \quad (3)$$

Whatever the electron spin state on the M_3 site and to prepare an initial doublet state ($S = \frac{1}{2}$) of type $|010\rangle$ or $|011\rangle$, there is a probability $|C_0|^2$ to form $|010\rangle$; ($m_s = -\frac{1}{2}$) and a probability $|C_1|^2$ to form $|011\rangle$; ($m_s = \frac{1}{2}$). Because of the degeneracy of those 2 states and by symmetry $|C_0|^2$ and $|C_1|^2$ can be taken equal to $\frac{1}{2}$.

Those six configurations (micro-states) are two by two maximally quantum entangled so that instead of (2) and (3), two other subspaces of our model Hilbert space can be defined : a swaping subspace generated by (4) and the control subspace generated by (5):

$$\begin{cases} \frac{1}{\sqrt{2}} \left[|101\rangle \pm |100\rangle \right] = \left| \Phi^{g,u}_{M_1 \bar{M}_2} \right\rangle \\ \frac{1}{\sqrt{2}} \left[|011\rangle \pm |010\rangle \right] = \left| \Phi^{g,u}_{\bar{M}_1 M_2} \right\rangle \end{cases} \tag{4}$$

$$\frac{1}{\sqrt{2}} \left[|110\rangle \pm |001\rangle \right] = \left| \Phi^{g,u}_{M_1 M_2, \bar{M}_1 \bar{M}_2} \right\rangle \tag{5}$$

They are expressed as symmetric and antisymmetric linear combinations of the entangled components of the above defined model and intermediate spaces. Note that those new symmetric and anti-symmetric states are orthonormal and consequently not coupled together by symmetry. This allows to describe the qubits super-exchange interactions by a 2-bloc diagonal hamiltonian built separately on the symmetric g and on the anti-symmetric u parts.

2.3 The Controlled Swap Hamiltonian in the Interaction Picture

In absence of an external magnetic field and when the spin-orbit interactions are neglected, the interaction between two or more paramagnetic centers can be described through spin operators which acts only on local effective spin eigenfunctions and therefore represented on the basis set of its localized spin eigenstates. In a such case, the so-called Heisenberg-Dirac-Van Vleck spin-hamiltonian H_{HDVV} [15–17] is the most commonly used. Many formulations of the H_{HDVV} can be founded in literature [18–20], it is a pair interaction operator and usually it takes the form :

$$\hat{H}_{HDVV} = \sum_{i>j} -J(\vec{r_{ij}}) \hat{\vec{S_i}} . \hat{\vec{S_j}} \tag{6}$$

where J is the spin exchange coupling constant, generally depending on the distance r_{ij} between two electrons localized on centers i and j. Let us consider the two qubit magnetic sites M_1 and M_2 so distant from each other that they do not interact through space directly. Each one is through ligand interacting with the third magnetic site M_3 (control site). In such case, we can write

$$\begin{cases} J = J_{13} = J_{23} \\ J_{12} = 0 \end{cases} \tag{7}$$

between the spin exchange constants and $\hat{H}_{HDVV}$ can be simply rewriten:

$$\hat{H}_{HDVV} = -J(\hat{S}_1 \hat{S}_3 + \hat{S}_2 \hat{S}_3) \tag{8}$$

Then, if one uses the 6 Slater determinants in (2) and (3) plus the two determinants $|000\rangle$ and $|111\rangle$ corresponding to the degenerated and non-interacting quadruplet states, a (8×8) HDVV hamiltonian matrix can be constructed to describe our magnetic system. This matrix is bloc-diagonal and contains two diagonal elements which correspond to the pure quadruplet states and two (3×3) bloc matrices

involving configurations (micro-states) which are doublets formed by two electrons holding the same spin and the third one with a spin of the opposite orientation. Inside the (3×3) bloc built on the partial basis set $\{|001\rangle, |010\rangle, |100\rangle\}$, the configurations $|010\rangle$ *and* $|100\rangle$ are not directly coupled but are mutually interacting via the configuration $|001\rangle$. In the second (3×3) bloc, the interaction between the configurations $|011\rangle$ *and* $|101\rangle$ is also passing through the configuration $|110\rangle$. This is resulting from two successive permutations between spin of opposite signs, firstly for a single occupied magnetic sites M_1 and M_3 (or M_2 and M_3) and secondly a spin permutation (or a spin exchange) between electrons on sites M_3 and M_2 (or M_3 and M_1). The first spin exchange operation gives rise to an intermediate micro-state in which the spin momentum at sites M_1 and M_2 have the same m_s value and the *control* site M_3 has an m_s value with the opposite sign of its initial value. The second operation restores the m_s value on the magnetic site M_3 and performs the complete interchange between the sign-opposite m_s values on the *target* sites M_1 and M_2. the relative energy of the intermediate micro-states is equal to $+\frac{J}{2}$ and the magnetic coupling exchange energy is equal to $-\frac{J}{2}$. Diagonalization of this *HDVV* matrix will provide 8 eigenstates corresponding to 8 non-entangled quantum states which are 2 by 2 degenerated and consequently the configurational mixed states define four doubly degenerated energy levels.

On this magnetic Hamiltonian, the effect of an external static magnetic field $\overrightarrow{B_z}$ can be modeled by the hamiltonian:(9)

$$\begin{aligned}
\hat{H}_B &= \mu_B \overrightarrow{\hat{B}}_z . \overrightarrow{\hat{S}} = \mu_B \hat{B}_z \hat{S}_z \\
&= \Lambda_z \hat{S}_z = \Lambda_z (\hat{S}_{1_z} + \hat{S}_{2_z} + \hat{S}_{3_z})
\end{aligned} \tag{9}$$

where μ_B, $\hat{B}_z$ and $\hat{S}_{i_z}$ are respectively the Bohr magneton, the quantification $z-axis$ projection of the magnetic field vector and of the spin momentum localized at a given magnetic site M_i. By introducing (9) in (8), one obtains a new H_{HDVV} Hamiltonian matrix in which the doubly degeneracy in each (3×3)-bloc diagonal sub-matrix are removed as it is shown in the matrix given in (10). The effect of $\overrightarrow{B_z}$ is to shift the energies of the matrix diagonal elements and consequently to remove the degeneracies between each pair of the H_{HDVV} eigenstates. The final $H_{HDVV} + H_B$ (8×8)-Hamiltonian matrix is given by:

$$\begin{array}{c}
\begin{array}{cccccccc}
|000\rangle & |001\rangle & |010\rangle & |100\rangle & |011\rangle & |101\rangle & |110\rangle & |111\rangle
\end{array} \\
\begin{array}{c}
|000\rangle \\ |001\rangle \\ |010\rangle \\ |100\rangle \\ |011\rangle \\ |101\rangle \\ |110\rangle \\ |111\rangle
\end{array}
\left[
\begin{array}{cccccccc}
-\frac{J-3\Lambda_z}{2} & 0 & 0 & 0 & 0 & 0 & 0 & 0 \\
0 & +\frac{J+\Lambda_z}{2} & -\frac{J}{2} & -\frac{J}{2} & 0 & 0 & 0 & 0 \\
0 & -\frac{J}{2} & \frac{\Lambda_z}{2} & 0 & 0 & 0 & 0 & 0 \\
0 & -\frac{J}{2} & 0 & \frac{\Lambda_z}{2} & 0 & 0 & 0 & 0 \\
0 & 0 & 0 & 0 & -\frac{\Lambda_z}{2} & 0 & -\frac{J}{2} & 0 \\
0 & 0 & 0 & 0 & 0 & -\frac{\Lambda_z}{2} & -\frac{J}{2} & 0 \\
0 & 0 & 0 & 0 & -\frac{J}{2} & -\frac{J}{2} & +\frac{J-\Lambda_z}{2} & 0 \\
0 & 0 & 0 & 0 & 0 & 0 & 0 & -\frac{J+3\Lambda_z}{2}
\end{array}
\right]
\end{array} \tag{10}$$

In the framework of the Heisenberg interaction representation, this is the valence bond like Hamiltonian matrix used in the next section to get the swapping Hamiltonian matrix on the canonical basis set of the 3-qubit supporting the swap logic function between the two qubits at the magnetic sites $\mathbf{M_1}$ and $\mathbf{M_2}$ controlled by the qubit at the site $\mathbf{M_3}$. The spin super-exchange mechanism between the site $\mathbf{M_1}$ and $\mathbf{M_2}$ is performed in two steps. A super-exchange occurs firstly between one of the target sites $\mathbf{M_1}$ (or $\mathbf{M_2}$) and the control site $\mathbf{M_3}$. The second step consists in a spin permutation between the site $\mathbf{M_3}$ and the other qubit site $\mathbf{M_2}$ (or $\mathbf{M_1}$). For its initial and final states, a two step transformation has a configuration where the two spins localised on each qubit site have an opposite sign m_s value ($+\frac{1}{2}$ or $-\frac{1}{2}$), but has an intermediate state configuration within spins on the target sites having the same m_s value.

3 The Time Dependent Swapping Operation

Since the swap system is only defined on the doublet states, one need, for example, to use the symmetric determinant combinations g. In this case, the final model Hilbert space is generated by the three determinants $\left| \Phi^g_{M_1 \bar{M}_2} \right\rangle$, $\left| \Phi^g_{\bar{M}_1 M_2} \right\rangle$ and $\left| \Phi^g_{M_1 M_2, \bar{M}_1 \bar{M}_2} \right\rangle$ given in (4) and (5). Describing the swaping process and given in J unit, the corresponding (3×3)-block Hamiltonian matrix coming from (11) can be written on this basis set:

$$
\begin{array}{c}
\begin{array}{ccc}
\left| \Phi^g_{M_1 \bar{M}_2} \right\rangle & \left| \Phi^g_{\bar{M}_1 M_2} \right\rangle & \left| \Phi^g_{M_1 M_2, \bar{M}_1 \bar{M}_2} \right\rangle
\end{array} \\
\begin{array}{c}
\left| \Phi^g_{M_1 \bar{M}_2} \right\rangle \\
\left| \Phi^g_{\bar{M}_1 M_2} \right\rangle \\
\left| \Phi^g_{M_1 M_2, \bar{M}_1 \bar{M}_2} \right\rangle
\end{array}
\left(
\begin{array}{ccc}
\frac{1}{2} & 0 & -\frac{1}{6\sqrt{2}} \\
0 & \frac{1}{2} & -\frac{1}{6\sqrt{2}} \\
-\frac{1}{6\sqrt{2}} & -\frac{1}{6\sqrt{2}} & \frac{5}{16}
\end{array}
\right)
\end{array}
\tag{11}
$$

Notice that (11) is free from the static magnetic field contribution. The total $\hat{S}_z$ operator action on each state of the final swap space gives zero as eigenvalue. On each site, the role played by the magnetic field is only to lift up the degeneracy between the α and β electron spins so that the swapping process can be initiated on well determined qubits inside the molecule with no direct influence on the process itself.

To determine the swap oscillation frequency and the time-dependent probability to find the system in a given quantum state, we have solved the time-dependent Schrödinger equation using (11). In this representation, the Rabi oscillation frequency between, for instance, an initial state $|\phi_i\rangle = \left| \Phi^g_{M_1 \bar{M}_2} \right\rangle$ and a final state $|\phi_f\rangle = \left| \Phi^g_{\bar{M}_1 M_2} \right\rangle$ is given by their effective magnetic coupling via the intermediate
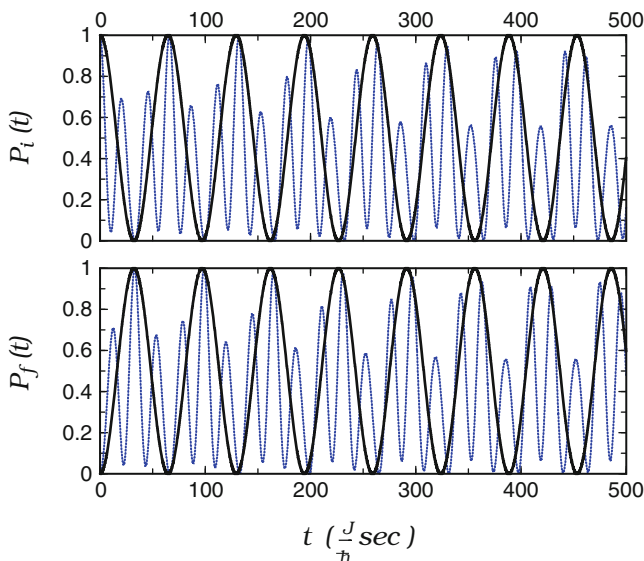
Fig. 4 The controlled swap time-dependent probability. $\mathscr{P}_f(t)$ and $\mathscr{P}_i(t)$. These Rabi oscillations curves are obtained by using H (solid lines) or H_{eff} (dashed lines)

state $|\phi_m\rangle = \left|\Phi^g_{M_1 M_2, \bar{M}_1 \bar{M}_2}\right\rangle$. The calculation of this effective coupling is performed by partitionning the total active space Hamiltonian H given in (11) as $H = PHP + QHQ + PHQ + QHP$, where $P = |\phi_i\rangle\langle\phi_i| + |\phi_f\rangle\langle\phi_f|$ and $Q = |\phi_m\rangle\langle\phi_m|$ are the projectors respectively defined on the qubits and the control subspaces. Then, starting from a given initial state, the time-dependent probability to find the system in a final state is given by $\mathscr{P}_f(t) = \left|\left\langle\phi_f\middle|\psi(t)\right\rangle\right|^2$, where $|\psi(t)\rangle = \sum_n C_n(t)|\psi_n\rangle$ and $|\psi_n\rangle$ are the (11) eigenvectors. The time-dependent quantum evolution of this 3-state swap system results from the superposition of 3 sinusoidals whose frequencies can be calculated by the 2-by-2 difference of the eigenvalues and their respective weight by using the time dependent population Fourier transform. The fundamental frequency of the corresponding Fourier spectrum can also be extracted using the effective Hamiltonian $H^{eff} = PU^{-1}HUP$ expressed on the basis set associated to the qubits P-space where U is a non unitary transformation which bloc-diagonalize the total swap Hamiltonian H [21]. Using this transformation, the calculated effective magnetic coupling $H^{eff}_{if} = \dfrac{\left|E^{eff}_f - E^{eff}_i\right|}{2}$ between the 2 qubits through the central control site is equal to 0.0497 (in J unit). The corresponding calculated time-dependent $(i \rightarrow f)$ oscillation probabilities are reported in figure 4. The first maximum of $\mathscr{P}_f(t)$ giving the fundamental swap oscillation frequency is reached at the time $t = \dfrac{\pi\hbar}{2H^{eff}_{if}}$ that is $31.562\frac{\hbar}{J}$ sec. As an example, for a standard $J = 100\, cm^{-1}$ [22], the swapping oscillation frequency is $597\, GHz$.

As compared to a non-controlled swapping system where the 2 qubits are directly through space interacting to operate a swap, our intermediate control site is not perturbing a lot the swapping operation. The time dependent evolution is a little deformed by the presence of the controlling intermediate site. But the 2 additional frequency components in the swapping time dependent quantum process have a small enough contribution to preserve a nice Rabi like oscillation of the swapping in time as presented in figure 4.

In conclusion, we have proposed a molecule and a model to implement a quantum controlled swap molecule logic gate. The swapping process involves 3 paramagnetic adjacents centers, the preparation of the active sites is firstly initiated by switching ON an appropriate light radiation to transfer an electron from the controlling site to the passive 4th center. The active qubits formation is initiated by applying an static magnetic field. This external static magnetic field is necessary to define the qubits on the molecule but its magnitude do not influences the swapping time. From an experimental point of view, several techniques are under development to detect [5, 23], adress [24], flip [25], visualize [26] or probe [27] single spins on a molecule with an enough spatial resolution to input the quantum information on our swap molecule logic gate. It remains to adapt the design of the presented molecule for the swapping operation to work on a surface.

References

1. Stadler, R., Ami, S., M. Forshaw, M., Joachim, C.: Integrating logic functions inside a single molecule. Nanotechnology **15**, S115 (2004).
2. Carter, F.L.: Molecular Electronic Devices II. ed. Dekker, New York (1987) : The molecular device computer : Point of departure for large scale cellular automata. Physica **D10**, 175 (1984).
3. Jlidat, N., Hliwa, M., Joachim, C.: A semi-classical XOR logic gate in a single molecule. Chem. Phys. Lett. **451**, 270 (2008).
4. Duchemin, I., Renaud, N., Joachim, C.: An intermolecular 1/2-adder with tunneling current drive and read-outs. Chem. Phys. Lett. **452**, 269 (2008).
5. Feng, M., Twamley, J.: Single spin detection by qubit swap to molecular nanomagnet. Europhys. Lett. **69**, 699 (2005).
6. Duchemin, I., Joachim, C.: A quantum digital half adder inside a single molecule. Chem. Phys. Lett. **406**, 167 (2005).
7. Bertaina, S., Gambarelli, S., Mitra, T, Tsukerblat, B., Müller, A., Barbara, B.: Quantum oscillations in a molecular magnet. Nature **453**, 203 (208).
8. Liu, J., Zhang, G.-F., Chen, Z.-Y.: Influence of magnetic field on swap operation in Heisenberg XXZ model. Physica **B 404**, 1116 (2009).
9. Fabre, M., Jaud, J., Hliwa, M., Launay, J.-P., Bonvoisin, J.: On the role of the bridging dicyanamidobenzene ligand in a new binuclear ruthenium complexe. Inorg. Chem. **45**, 9332 (2006).
10. Fabre, M., Bonvoisin, J.: Electronic and magnetic communication in mixed-valent and homovalent ruthenium complexes containing phenylcyanamide type bridging ligands. J. Am. Chem. Soc. **129**, 1434 (2007).

11. Munery, S., Ratel-Ramond, N., Benjalal, Y., Vernisse, L., Guillermet, O., Bouju, X., Coratger, R., Bonvoisin, J.: Synthesis and characterization of a series of ruthenium tris(β-diketonato) complexes by an UHV-STM investigation and numerical calculations. Eur. J. Inorg. Chem. 2698 (2011).
12. Viala, C., Bonvoisin, J.: Synthesis and characterization of β-diketonato ruthenium(II) complexes with two 4-bromo or protected 4-ethynyl-2,2'-bipyridine ligands. Inorg. chim. Acta **363**, 1409 (2010).
13. Munery, S., Jaud, J., Bonvoisin, J.: Synthesis and characterization of bis(bipyridine) ruthenium(II) complexes with bromo and protected ethynyl β-diketonato ligands. Inorg. Chem. Commun. **11**, 975 (2008).
14. Journeaux, Y., Sletten, J., Kahn, O.: Tunable interaction in (μ-oxamido) copper(II) binuclear complexes. Inorg. Chem. **25**, 439 (1986).
15. Heisenberg, W.: Zur theorie des ferromagnetismus. Z. Phys. **49**, 619 (1928).
16. Dirac, P.A.M.: Quantum mechanics of many-electron systems. Proc. R. Soc. London **A123**, 714 (1929).
17. Van Vleck, J.H.: The theory of electric and magnetic susceptibility. Oxford University Press, Oxford (1932).
18. Calzado, C.J., Cabrero, J., Malrieu, J.-P., Caballol, R.: Analysis of magnetic coupling in binuclear complexes. I and II- derivation of valence effective Hamiltonian from ab-inition CI and DFT calculations. J. Chem. Phys. **116**, 2728 (2002), J. Chem. Phys. **116**, 3985 (2002).
19. Doublet, M.-L., Lepetit, M.-B.: Correlation and dimerization effects on the physical behaviour of $NR_4[Ni(dmit)_2]_2$ charge transfer salts : density matrix renormalization group study of the quarter-filling t-J model. J. Chem. Phys. **110**, 1767 (1999).
20. Capelle, K., Libero, V.-L.: Spin density functional theory : Some open problems and application to inhomogeneous Heisenberg model. Int. J. Quant. Chem. **105**, 679 (2005).
21. Durand, Malrieu, J.-P.: Effective Hamiltonian and pseudo-operators as tools for rigorous modelling. Adv. Chem. Phys. **67**, 321 (1987).
22. M.A.S. Aquino, M.A.S., Lee, F., Gabe, L.E.J., Bensimon, C., Greedan, J.E., Crutchley, R.J.: Superexchange metal-metal coupling in dinuclear pentaamine rethenium complexes incorporating a 1,4-dicyanamidobenzene dianion bridging ligand. J. Am. Chem. Soc. **114**, 5130 (1992).
23. Rugar, D., Budakian, R., Mamin, R.J.: Single spin detection by magnetic resonance force microscopy. Nature **430**, 329 (2004).
24. Messina, P., Mannini, M., Caneschi, A., Gatteschi, D., Sorace, L., Sigalotti, P., Sandrin, C., Prato, S., Pittana, P., Manassen, Y.: Spin noise fluctuation from paramagnetic molecular adsorbate on surfaces. J. Appl. Phys. **101**, 053916 (2007).
25. Heinrich, A.J., Gupta, J.A., Lutz, C.P., Eigler, D.M.: Single atom-flip spectroscopy. Science **306**, 466 (2004).
26. Iacovita, C., Rastei, M.V., Heinrich, B.W., Brumme, T., Kortus, J., Limot, L., Bucher, J.-P.: Visualizing the spin of individual cobalt-phthalocyanine molecule. Phys. Rev. Lett. **101**, 116622 (2008).
27. Meier, F., Zhou, L., Wiebe, J., Wiesendanger, R.: Revealing magnetic interactions from single-atom magnetization curves. Science **320**, 82 (2008).

Artificial Molecular Nanomagnets as Spin-Based Quantum Logic Gates

Fernando Luis, Olivier Roubeau, and Guillem Aromí

Abstract Quantum coherence and entanglement give resources to enhance the capabilities of computers well beyond those achievable by present-day or even future classical devices. Quantum information processing can be carried out via a combination of two elementary logic operations: unitary rotations of individual qubits and quantum-gate operations that involve at least two coupled qubits. An outstanding challenge for science and technology is to find suitable realizations of these basic elements. In recent years, magnetic molecular clusters have become candidates to implement the quantum computer hardware. Here, we summarize some of the strategies that have been followed to design and synthesize molecular spin qubits and quantum gates. In particular, we show that molecular clusters containing two Tb^{3+} ions meet all ingredients required to implement a CNOT quantum logic gate. The definition of control and target qubits is based on the strong magnetic anisotropy and the magnetic inequivalence of the two ions, which can be achieved by chemically engineering dissimilar coordination spheres. The magnetic asymmetry also provides a method to realize a SWAP gate in the same cluster. The synthesis of related molecular structures enables a vast choice of quantum-gate designs. Chemically engineered molecular quantum gates can therefore open promising avenues for the realization of scalable quantum computing architectures.

F. Luis (✉) · O. Roubeau
Instituto de Ciencia de Materiales de Aragón (ICMA), CSIC-Universidad de Zaragoza, Pedro Cerbuna 12, 50009 Zaragoza, Spain
e-mail: fluis@unizar.es; roubeau@unizar.es

G. Aromí
Departament de Química Inorgànica, Universitat de Barcelona, Diagonal 645, 08028, Barcelona, Spain
e-mail: guillem.aromi@qi.ub.es

1 Introduction: Quantum Computation and Its Material Realization

Quantum computation (QC) is based on the idea that the laws of quantum physics can be used to implement logic operations [1]. Like ordinary (or classical) computers, quantum computers process information units, or qubits. The main difference between these two paradigms resides in the fact that each qubit can be in states "0" or "1" but also in any arbitrary quantum superposition of these two, i.e. any quantum state of the form $|\varphi\rangle = \alpha|0\rangle + \beta|1\rangle$. The computational gain associated with the use of such coherent superpositions, or "quantum parallelism", becomes obvious if one aims to simulate a quantum physical system: the size of the computer register required to simulate an ensemble of N quantum particles grows exponentially with N in classical, Boolean logics, while only linearly in a quantum machine [2]. In the last 20 years, some quantum algorithms have been developed that outperform classical ones in other complex computational tasks. These include the Deutsch–Josza algorithm for finding if a function f is either constant or balanced [3], the Shor algorithm for prime numbers factorization [4] and the Grover algorithm for searching in large databases [5]. The latter two are of especial significance for their applications in cryptography and data management, respectively.

Taking these expectations closer to reality largely depends on the development of (a) suitable physical realizations of quantum bits and gates and (b) efficient methods to initialize, read out and coherently control and interconnect these elementary units [6]. In spite of the progress achieved in the last two decades, it is by no means clear which (if any) of the different quantum computation schemes will prove successful. Outstanding challenges, common to existing proposals, are the robust physical implementation of the basic elements and finding methods to scale up quantum computation architectures to a level where they become of practical use in technological applications [7].

The material realization of a Boolean bit is a classical physical system with two well-defined states. In contrast, the counterpart in QC is a quantum two-level system (see Fig. 1) that can be placed in any arbitrary superposition $|\varphi\rangle = \alpha|0\rangle + \beta|1\rangle$ via the application of external stimuli. A crucial additional requirement is that quantum coherence (i.e. the relative phase between the different components of the quantum superposition) is not lost as the qubit changes from one state to another. This condition implies that the decoherence time T_2, associated with the interaction of the qubit with its environment, must be sufficiently long as compared with the period $1/\Omega_R$ of Rabi oscillations between different qubit states (Fig. 1).

A number of potential candidates have been proposed and investigated as the physical systems to constitute the hardware of QC [7]. The proposals span a wide spectrum of materials and include ion traps [8], photons [9], nuclear spins [10], superconducting circuits [11] or spin-based systems, such as electrons in quantum dots [12] or atomic impurities in semiconductors [13]. The qubit candidates based on electronic spins are, of course, not limited to spins confined in semiconductors. An isolated spin $s = 1/2$, e.g. from a radical or open-shell metal-containing

$$\Omega_R = 2g\mu_B \left| \langle 1 | \vec{b}_{rf} \vec{S} | 0 \rangle \right| / h$$
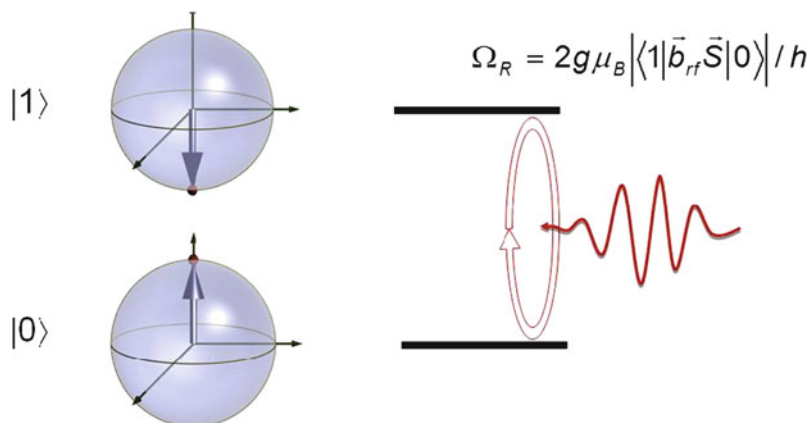
Fig. 1 Schematic representation of a spin qubit. Coherent oscillations between the two states of the basis $|0\rangle$ and $|1\rangle$, or between any pair of quantum superpositions of these states, can be achieved via the application of an external radiofrequency pulse at a Rabi frequency Ω_R

molecule, constitutes also a natural two-level system and can therefore provide an appropriate qubit realization [14]. In this chapter, we consider yet another family of materials, artificial molecular nanomagnets designed and synthesized by chemical methods [15], and describe how to implement with them some basic logic gates for quantum computation [16, 17].

2 Universal Quantum Logic Gates

A general result of quantum and classical computation science is that any complex logic operation can be carried out via the application of a few elementary operations, known as universal quantum gates. For reversible classical computation, in which logic operations can proceed at constant entropy, the universal gates are the NOT, the controlled NOT (CNOT), and the controlled controlled NOT (or Toffoli) gates, acting on one, two or three bits, respectively [18]. These gates are schematically described in Fig. 2. Classical reversible computation is a subset of quantum computation. Therefore, the choice of universal gates is larger in the latter case. It has been shown that single-qubit rotations and quantum CNOT gates form a set of universal gates for quantum computation, i.e. any multiple-qubit logic gate can be decomposed into CNOT and single-qubit gates [19, 20].

The operation of these gates exemplifies also some notable differences between classical and quantum machines. For instance, the classical NOT gate simply switches the state of a bit, say from '0' to '1' and vice versa. Acting on a $|\varphi_i\rangle = |0\rangle$ state, a qubit rotation produces instead an arbitrary superposition $\alpha|0\rangle + \beta|1\rangle$ of the initial $|0\rangle$ and the "switched" $|1\rangle$ states.
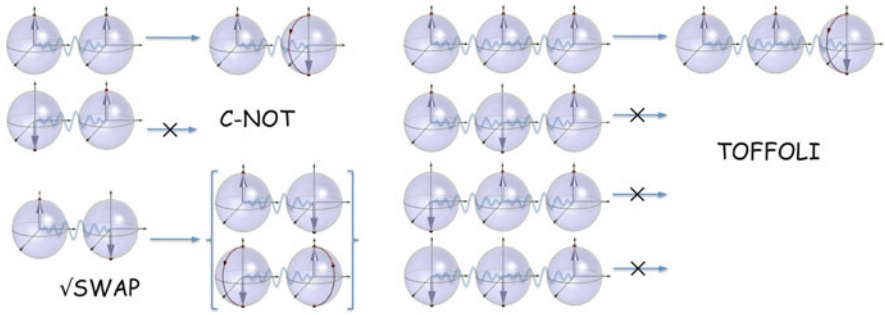
Fig. 2 Operations of logic gates acting on two and three qubits. The NOT (i.e. the reversal of an individual bit), CNOT and TOFFOLI gates form a complete set for reversible classical computation. In quantum computation, single-qubit rotations (Fig. 1) and CNOT quantum gates are universal

Let us now consider the CNOT gate. A classical CNOT switches a target bit if and only if a control is in state '1' (an alternative definition with the control being '0' is, of course, equivalent). A property of this classical gate is that it can be used to perform the COPY of the control bit 'a' (a being either '0' or '1'). For this, one only needs to set the input state of the target to '0'. The output is then $(a, 0) \underset{\text{CNOT}}{\rightarrow} (a,a)$; thus, the target adopts the state of the control. By contrast, this COPY operation cannot be performed for a quantum bit. To see this, we just need to consider an initial state of the CNOT gate in which the control lies in a quantum superposition. The operation of the gate then gives

$$(\alpha|0\rangle_C + \beta|1\rangle_C) \otimes |0\rangle_T \underset{\text{CNOT}}{\rightarrow} (\alpha|0\rangle_C \otimes |0\rangle_T + \beta|1\rangle_C \otimes |1\rangle_T) \tag{1}$$

where C and T refer to control and target states. The output in Eq. (1) is said to be an "entangled state" of the two qubits, i.e. a state that cannot be written as a product of states for each qubit [19]. The occurrence of such entangled states is another characteristic trait of quantum computation (e.g. via the application of quantum CNOT gates). As said above, this also implies that an arbitrary quantum bit cannot be copied [1].

Although the CNOT gate is the archetype of two-qubit universal gates, there are further possibilities. Another example of a two-qubit universal quantum gate is the $\sqrt{\text{SWAP}}$ (Fig. 2) [12, 20]. It turns a two-qubit state $|a, b\rangle$ (with a and b being '0' or '1', and different) into a superposition $[(|a, b\rangle + i|b, a\rangle)/(1 + i)]$. It can be seen that a $\sqrt{\text{SWAP}}$ gate also generates entanglement between the two qubits.

The definition of each two-qubit gate determines the properties that its physical realization must have. A CNOT gate, for instance, consists of two well-defined qubits, which need to be mutually coupled and be separately addressable via the application of some external stimulus.

Let us briefly summarize, in what follows, different implementations of universal quantum gates that have been achieved within the last 20 years. The first proposal to implement a CNOT quantum gate with an explicit physical system was based

on ions confined in a trap and cooled by laser beams [21]. In this proposal, two internal states of each ion define the qubit states. Each qubit can be addressed via the application of laser pulses focused on each ion. The coupling of two or more qubits is controlled via excitations of the centre of mass motions of these ions. The first experimental demonstration of a CNOT quantum gate was based on this scheme [22]. Another approach that met with early success is quantum computation with nuclear magnetic resonance techniques [10]. In 1998, Chuang and co-workers realized experimentally the Deutsch quantum algorithm [23]. They used the ^{1}H and ^{13}C nuclear spins in a solution of chloroform ($CHCl_3$) molecules as the input and output qubits of the algorithm, respectively. The qubit states are defined by the projections of these nuclear spins along the external magnetic field. The nuclear gyromagnetic ratios of ^{1}H and ^{13}C are very different, which leads also to different Zeeman splittings for the two nuclei under a homogeneous magnetic field. This property enables the rotation of either one or the other qubit via the application of electromagnetic pulses of the appropriate frequency. One step of the computation consisted of the implementation of a CNOT quantum gate on the two qubits.

Nuclear spins and cold ions have in common the fact that they are very well isolated from their environment, which results in relatively long coherence times. This fact represents an advantage over computation schemes that use solid-state devices or materials as qubits, for which decoherence is one of the main limiting factors. In return, these implementations might be easier to scale up into complex architectures. Different superconducting devices have been identified as potential qubits [24]. Their coherence timescales have been improved over the last ten years to values that are close to those required for the application of fault-tolerant quantum computation with error correction codes [25]. It is also relatively simple to engineer superconducting circuits able to couple two such qubits. These properties led in 2007 to the demonstration of CNOT gate operations on two coupled flux qubits [26]. In the following, we describe yet another alternative solid-state technology for the development of universal spin-based quantum gates that uses artificial, chemically engineered, molecular nanomagnets.

3   Chemical Design of Magnetic Complexes for Quantum Information Processing

Chemistry offers a very attractive route for realizing qubits with electronic spins. Its unlimited versatility allows the engineering of molecules containing *open-shell* moieties, disposed in optimal conditions for their use as qubits. In addition, chemical methods can also be applied to design and synthesize qubit ensembles within robust molecules, which can provide suitable candidates for diverse quantum logic gates (see below). A very attractive feature is that macroscopic numbers of identical molecules can be synthesized in a single chemical reaction.

These molecular materials added to the list of quantum hardware candidates about a decade ago when it was proposed that qubit states might be encoded

using the different molecular spin orientations and their quantum superpositions [27–30]. A differentiating factor with respect to other technologies is that single molecules can be more than single qubits: several theoretical proposals exist to use their magnetic energy structure to encode multiple-qubit states or even to perform quantum algorithms and simulations. Also, some molecular structures embody several weakly coupled, or entangled, qubits. In this and the following sections, we review some of the work done to design and realize single qubits and two (or multiple)-qubit gates in magnetic molecular complexes.

All that is needed to define a molecular qubit is a pair of spin states, which can be coherently taken from one to another via the application of electromagnetic radiation pulses, and a sufficiently long spin decoherence time. Organic radicals with a net spin $s = 1/2$ represent a simple approximation to this idea. An illustration of the great potential of molecular design is the preparation of a molecule containing two separated unpaired electrons (in form of nitronyl nitroxide radicals) exhibiting a magnetic interaction that can be switched by light irradiation [31]. The photoactive unit acting as switch is a benzothiophene-based diarylethene moiety. This molecule could constitute a prototype of a $\sqrt{\text{SWAP}}$ quantum gate (see Fig. 2). The quantum operations may be implemented by turning on and off, in a controlled manner and for a precise amount of time, a Heisenberg exchange coupling between the spins of two unpaired electrons.

Paramagnetic metal ions obviously provide a vast choice of tuneable electron-spin carriers, offering several possible spin values and many advantages over organic-based radicals. Magnetic energy levels, electronic-spin dynamics and even hyperfine couplings depend on the metal, which can be selected from the 3d, 4d, 5d, 4f and 5f groups. Coordination chemistry provides the means of organizing such potential qubits into scalable architectures or as mutually interacting ensembles. For example, strings of weakly coupled qubits have been synthesized by disposing paramagnetic metal ions as hexacoordinated centres along the axes of triple-stranded coordination helicates [32]. The strands of the helical assemblies consist of extended ligands such as oligoimidazoles. The principal axes of the gyromagnetic g tensor change from a metal ion in the chain to the next, as a result of the helical twist of the molecule. This provides a means for discriminating the different qubits that form the array, thus making them addressable individually by electron paramagnetic resonance (EPR).

Coordination clusters may also become realizations of single qubits. Of particular interest is a family of clusters with a magnetic core consisting of a [Cr$_7$Ni] ring (Fig. 3) [30]. Metals in these clusters are typically held together by means of a combination of bidentate carboxylate ligands and ligands that bridge two metals through one atom (typically fluoride or alkoxide groups). The antiferromagnetic interactions between these metal ions lead to a ground-state $S = 1/2$ for the ring. The first excited level, with $S = 3/2$, lies $\Delta E / k_B = 13$ K above the ground-state level [33]. At sufficiently low temperatures, the two spin orientations $m_S = \pm 1/2$ represent then a proper definition of qubit states $|0\rangle$ and $|1\rangle$, whose energies can be split via the application of a magnetic field.
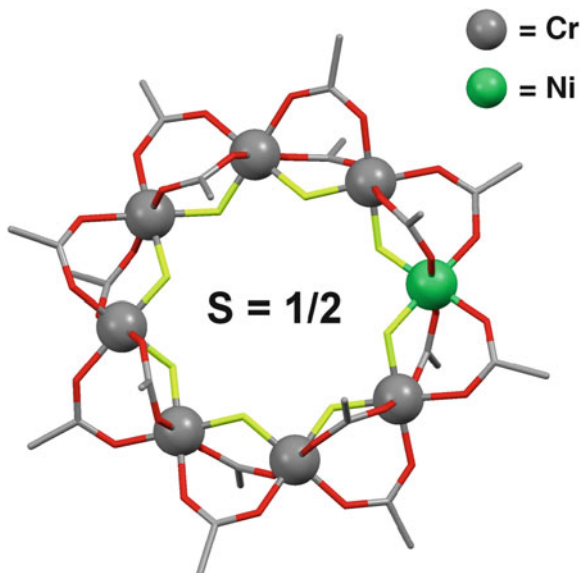
Coherent rotations of these spin qubits can be induced, as shown by A. Ardavan and co-workers [34,35], by resonant rf pulses using standard pulsed EPR techniques. These experiments give a maximum decoherence time $T_2 = 15\,\mu s$ and show that decoherence is dominated by dipole–dipole and hyperfine interactions. Quantum coherence has been optimized by chemical means: dissolving the molecules in toluene, reducing the number of magnetic nuclei via isotopic purification (e.g. replacing H with D) and choosing the appropriate ligand molecules to avoid fluctuations of the local magnetic fields associated with molecular motions [35].

Chemical design has allowed also the organization of various types of these heterometallic "wheels" into supramolecular dimeric ensembles [36] and some control on the intermolecular magnetic interactions [37]. Magnetic susceptibility experiments show the existence of entangled spin states in some of these supramolecular aggregates [38]. Magnetic coupling and entanglement has also been achieved in supramolecular structures of high-spin (i.e. $S > 1/2$) single-molecule magnets (SMMs). One of the first examples of this kind is a dimer of two [Mn$_4$] clusters with well-isolated $S = 9/2$ spin ground states and strong uniaxial magnetic anisotropy, connected via solid-state intermolecular interactions. The magnetic states of the dimer are quantum superpositions of the wave functions for each constituent [39].

In order to build quantum logic gates with molecular magnetic clusters, and especially if one aims to integrate these molecules into solid-state devices as a way of developing scalable computational architectures, it would be more convenient to have all qubits encapsulated inside a single and robust molecule, designed appropriately to carry out the desired operations. This represents, though, a significant challenge from the point of view of synthetic chemistry. Since their discovery, the literature has featured hundreds of SMMs, mainly involving 3d metals [40],
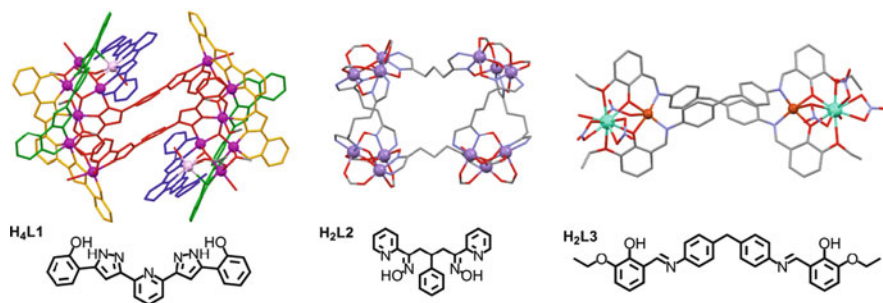
Fig. 4 Representation of various molecular aggregates of molecular nanomagnets, together with the ligands mainly responsible for their assembly. *Left*: $[Mn_{14}O_2(OH)_4(OMe)_4(OAc)_2(L1)_2 (HL1)_4(H2L1)_2(MeOH)_2(H_2O)_6](AcO)_2$, with hydrogen atoms not shown; *middle*: core of $[Mn_{12}O_4(O_2CMe)_{12}(L2)_6)](ClO_4)_4$; *right*: $[(CuTb)_2L3(NO_3)_6(H_2O)_2]$, with hydrogen atoms not shown
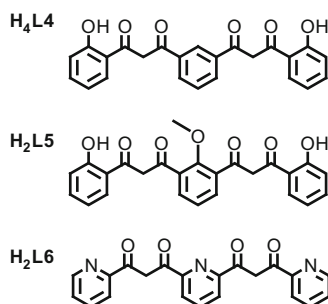

Fig. 5 Various bis-β-diketone ligands used for the synthesis of molecular cluster pairs

lanthanide ions [41] or both. However, the vast majority of these molecules have been prepared by *serendipitous self-assembly* and not through a rational design. This makes it extremely unlikely to obtain molecules containing two or more well-defined and weakly interacting metal aggregates, with predesigned magnetic properties.

On few occasions, this goal has been achieved by the use of extended multidentate ligands that facilitate both the aggregation of metals as strongly coupled clusters and the assembly of two or more such entities within stable, covalent molecules. The examples in Fig. 4 consist of (*a*) a molecular pair of [Mn$_7$] clusters, each showing SMM properties, linked by *bis*-hydroxyphenylpyrazolyl ligands (H$_4$L1) that also cement the metals within each cluster [42], (*b*) four [Mn$_3$] SMMs contained in one molecule [43], and (*c*) two well-separated SMM [TbCu] units linked into one molecule by double dinucleating Schiff-base moieties (H$_2$L3) [44].

The above very promising precedents have stimulated synthetic programs for the preparation of molecules containing metal cluster qubits, each of them with total or *effective* $S = 1/2$ ground states. One such initiative uses a family of extended bis-β-diketone ligands [45] (H$_4$L4, H$_2$L5 and H$_2$L6 in Fig. 5) to favour the assembly
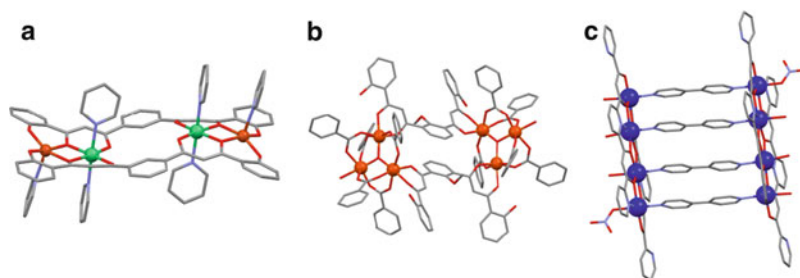
Fig. 6 Representation of three types of molecular cluster pairs made with bis-β-diketone ligands: (**a**) $[Cu_2Ni_2(L4)_2(py)_6]$, (**b**) $[Fe_6O_2(BzO)_{10}(H_2L5)_2(H_2O)_2]$ and (**c**) $[Co_8(OH)_2(NO_3)_2$ $(H_2O)_4(L6)_4(bpy)_4]^{4+}$

of molecular pairs of clusters. These may be of three classes, depending on the structural role played by the H_nLx ligand: (*a*) the bis-β-diketone ensures the aggregation of metals as clusters, also keeping the latter within one molecule, as in $[Cu_2Ni_2(L4)_2(py)_6]$ (Fig. 6a), which features two weakly interacting $S = 1/2$ moieties [46]; (*b*) H_nLx only links metal aggregates that have been formed by other auxiliary ligands (see the example $[Fe_6O_2(BzO)_{10}(H_2L5)_2(H_2O)_2]$ in Fig. 6b) [47]; and (*c*) the extended ligand is responsible for gathering metals as clusters that are then linked into molecular pairs by auxiliary ligands (Fig. 6c) [48]. All these molecular cluster pairs, as well as most of those present in the literature, do not allow distinguishing between both qubits, i.e. they are symmetric [49, 50]. As we discuss below, this is a problem if one aims to realize a universal CNOT gate. Solving this question represents a new and challenging synthetic goal.

Single lanthanide ions are also attractive spin qubit candidates. The interaction of the ion with the crystal field splits the $2J + 1$ levels associated with different projections of the total angular momentum. Often, this leads to a ground-state doublet, which can be seen as an *effective* $S = 1/2$. Some attractive features of lanthanide qubits are (a) that long spin coherence times have been demonstrated in lanthanide ions diluted in inorganic crystals [52] and (b) that they interact with external stimuli such as light and electric fields, thus providing alternative read-out and initialization schemes not readily available with other magnetic ions.

Mononuclear complexes, in which a lanthanide ion is encapsulated by organic ligand molecules, have been synthesized in the last decade [53–55]. These molecules aim to combine the best of the molecular and lanthanide-based proposals. Compared with molecules with a polynuclear magnetic core, these mononuclear qubits have the advantage of being easier to understand and offer a greater freedom for designing and modifying their electronic and magnetic properties, e.g. via changes in the coordination shell. In addition, magnetically diluted crystals of the same molecular structures can be prepared, in order to reduce decoherence induced by dipolar interactions [56]. The use of lanthanide qubits opens also very exciting perspectives for using chemistry to realize quantum gates, which will be examined in the following section.
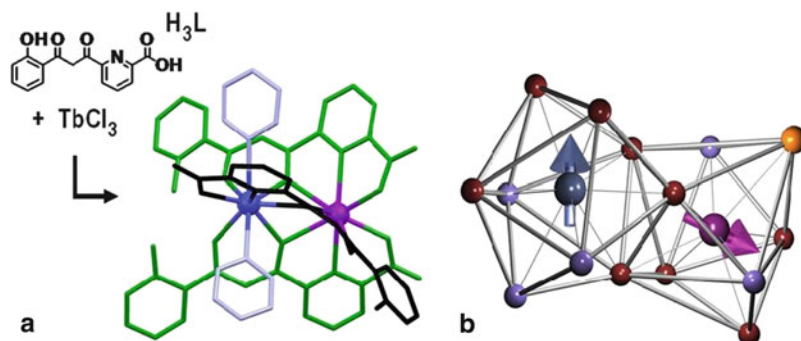
Fig. 7 (**a**) Representation of ligand H$_3$L7 and one of its dinuclear Ln^{3+} complexes; [Tb$_2$Cl(HL7)$_2$ (H$_2$L7)(py)$_2$]. Hydrogen atoms are not shown. (**b**) Schematic representation of the magnetic core of this complex, showing the different coordination spheres of the two Tb^{3+} spin qubits, represented here with two different colours (*dark blue and purple*) for clarity. The *arrows* represent the magnetic moments of the Tb^{3+} ions, each pointing along its local anisotropy axis

4 Molecular Prototypes for CNOT and SWAP Spin Quantum Logic Gates

4.1 Synthesis of Asymmetric [Tb]$_2$ Molecular Dimers

Following the same approach outlined in the previous section, molecules with two coupled lanthanide ions can be seen as potential candidates to implement two-qubit quantum gates. For CNOT molecular prototypes (see Fig. 2), the ingredients are (a) a weak magnetic coupling between the two spin qubits and (b) that both qubits are magnetically inequivalent (e.g. that they have different effective gyromagnetic factors). From the point of view of chemistry, a possible strategy is to synthesize molecules containing two anisotropic and weakly coupled lanthanide ions, coordinated to different environments. The literature is full with many dinuclear complexes of lanthanides. However, the cases where both metals are not equivalent are very scarce [57–59], as nature favours the formation of symmetric structures.

Recently [60], a very dissymmetric β-diketone ligand was prepared and used with lanthanide metals to prepare dinuclear complexes with general formula [Ln$_2$X(HL7)$_2$(H$_2$L7)(py)(S)] (S = py or H$_2$O; X = Cl$^-$ or NO$_3^-$). In all these complexes, the local coordination spheres of both metals are different. As we discuss in detail in what follows, such magnetic molecular systems are very promising candidates to perform as universal CNOT quantum gates.

The ligand 2-carboxy-6-(3-oxo-3-(2-hydroxyphenyl)propionylpyridine (H$_3$L7; Fig. 7) exhibits several donor atoms disposed linearly, with different coordination "pockets", and the potential to act as bridging ligand. It is thus a promising candidate to introduce the desired asymmetry. Indeed, the reaction of H$_3$L7 with salts of trivalent lanthanides (LnX$_3$; X = NO$_3^-$, Cl$^-$) conducted in pyridine produces
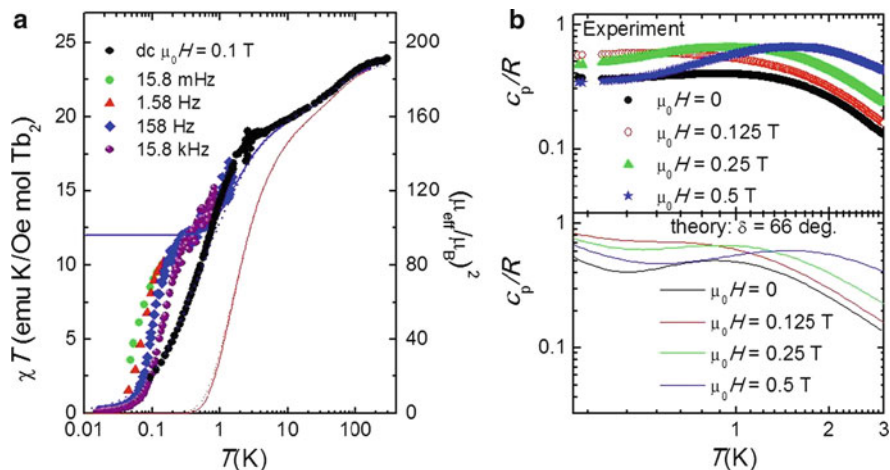
Fig. 8 *Left*: χT product of polycrystalline [Tb$_2$], where χ is the in-phase ac susceptibility or the dc susceptibility measured with $\mu_0 H = 0.1$ T and T the absolute temperature. The effective magnetic moment μ_{eff} of the cluster determined from these data is given on the right hand axis. The lines are least-square fits of the ac (*solid lines*) and dc (*dotted lines*) susceptibilities based on Eq. (2) for collinear ($\delta = 0$, *red thin lines*) and noncollinear ($\delta = 66°$, *blue thick lines*) anisotropy axes. *Right, top*: magnetic heat capacity of a powdered sample of [Tb$_2$]; *right, bottom*: theoretical predictions for noncollinear anisotropy axes

dinuclear complexes made of two Ln^{3+} ions chelated and bridged by three partially deprotonated H$_3$L7 moieties. In addition, two solvent molecules (pyridine or H$_2$O) and one X$^-$ anion also coordinate to the metals in a terminal fashion (Fig. 7).

The result is a series of dinuclear complexes with the desired structural properties. This reaction system is very promising since many other lanthanide ions can also be explored. In addition, the distinct properties of each coordination site could be exploited for the formation of heterometallic versions of these dinuclear complexes, which would enable a vast choice of quantum-gate designs. Of the three compounds published (Eu, Gd and Tb) [60], the terbium complex [Tb$_2$Cl(HL7)$_2$(H$_2$L7)(py)$_2$] is the only one that exhibits a highly anisotropic magnetic ground state. Hence, it can be studied for its suitability to act as a CNOT gate.

4.2 Physical Properties: Magnetic Asymmetry

We next describe the results of experiments that provide information on the magnetic moment and the magnetic energy level structure of the [Tb$_2$] complex shown in Fig. 7. Based on this information, we show that this molecule meets all conditions to act as a CNOT quantum logic gate.

The ac magnetic susceptibility χ, provides direct insight on the magnetic anisotropy of the Tb^{3+} ions and their mutual coupling. For the lowest frequency

(0.0158 Hz) and above 100 mK, the in-phase component χ' gives the equilibrium paramagnetic response. In this regime, the cluster effective magnetic moment can be determined by a direct application of Curie's law: $\mu_{\text{eff}} \simeq (3k_B \chi' T / N_A)^{1/2}$ as shown in Fig. 8a. At room temperature, this method gives $\mu_{\text{eff}} = 13.7(1)\mu_B$, which agrees well with the effective moment of two uncoupled Tb^{3+} free ions, i.e. $\mu_{\text{eff}} = g_J \mu_B [2J(J+1)]^{1/2} = 13.74\,\mu_B$, where $g_J = 3/2$ and $J = 6$ are the gyromagnetic ratio and the total angular momentum given by Hund's rules. The drop observed below approximately 100 K can be assigned to the thermal depopulation of magnetic energy levels split by the crystal field. The value $\mu_{\text{eff}} = 12.5(1)\mu_B$ measured between 3 and 10 K is close to $\mu_{\text{eff}} = g_J \mu_B 2^{1/2} J = 12.72\mu_B$, characteristic of two uncoupled Tb^{3+} ions whose angular momenta J_1 and J_2 point either up or down along their local anisotropy axes.

The magnetic anisotropy was determined by fitting $\chi' T$ between 3 and 300 K. The fitting expressions were derived [16,61] from the simplest Hamiltonian for two independent angular momenta with uniaxial anisotropy

$$\mathcal{H}_0 = -D(J_{z,1}^2 + J_{z,2}^2) - g_J \mu_B \vec{H}(\vec{J}_1 + \vec{J}_2) \tag{2}$$

The fit gives $D/k_B = 17$ K. The ground-state doublet of each ion is associated with the maximum projections $m_J = \pm J$ of the angular momentum along the local anisotropy axis ($\mathbf{z}_1$ for ion 1 and $\mathbf{z}_2$ for ion 2, which do not need to be parallel to each other, as it is discussed below). Excited levels are separated by more than 180 K from the ground-state doublet (see Fig. 9, left). These states provide then, for each ion, a proper definition of the qubit basis $|0\rangle \equiv |\Uparrow\rangle = |J = 6, m_J = 6\rangle$ and $|1\rangle \equiv |\Downarrow\rangle = |J = 6, m_J = -6\rangle$.

Below 3 K, we observe a second drop in $\chi' T$ (Fig. 8a) that we attribute to an antiferromagnetic coupling of the two spin qubits inside each molecular complex. The Hamiltonian of the two lanthanide electronic moments includes an additional exchange term

$$\mathcal{H}_{\text{el}} = \mathcal{H}_0 - 2J_{\text{ex}} \vec{J}_1 \vec{J}_2 \tag{3}$$

This interpretation is corroborated by the magnetic heat capacity $c_{m;P}$, shown in Fig. 8b (see also [16]). At zero field, $c_{m;P}$ shows a Schottky-type broad anomaly centred at $T_{\text{max}} \simeq 0.9$ K. The Schottky arises from the existence of an energy splitting $\varepsilon = 4J_{\text{ex}} J^2$ between antiferromagnetic ($|\Uparrow\rangle_1 \otimes |\Downarrow\rangle_2$ and $|\Downarrow\rangle_1 \otimes |\Uparrow\rangle_2$) and ferromagnetic ($|\Uparrow\rangle_1 \otimes |\Uparrow\rangle_2$ and $|\Downarrow\rangle_1 \otimes |\Downarrow\rangle_2$) states (see the scheme in the centre of Fig. 9). Using the condition $k_B T_{\text{max}} = 0.42\,\varepsilon$, we determine $\varepsilon/k_B \simeq 2.14$ K and, from this, $J_{\text{ex}}/k_B = -0.016(1)$ K.

Considering the value of ε, the fact that χ' monotonically increases with decreasing T down to 100 mK [16] would be puzzling unless the magnetic moments of the two Tb^{3+} ions do not exactly compensate each other. As the coordination sphere determines the magnetic anisotropy, the easy axes $\mathbf{z}_1$ and $\mathbf{z}_2$ of the two ions need not be parallel to each other but can instead make a tilting angle δ, as Fig. 7b shows. Because of this misalignment and the very strong anisotropy, even the states ($|\Uparrow\rangle_1 \otimes |\Downarrow\rangle_2$ and $|\Downarrow\rangle_1 \otimes |\Uparrow\rangle_2$) preserve a net magnetic moment. More importantly,
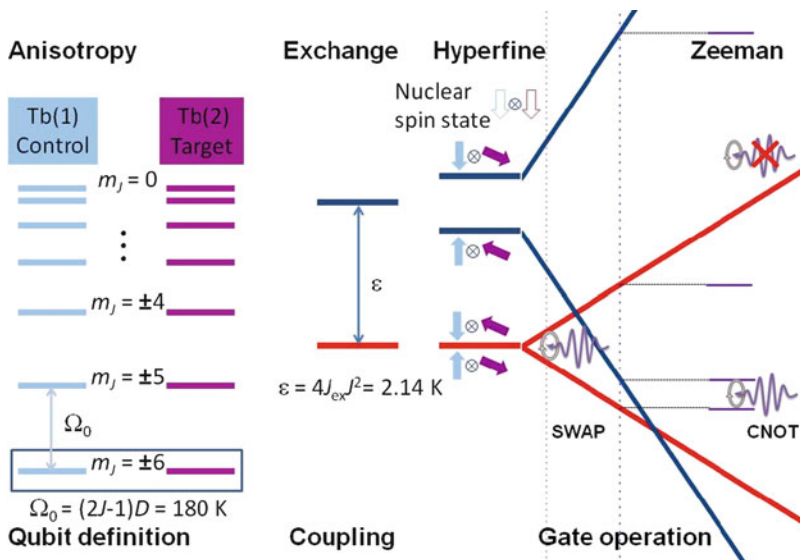
Fig. 9 Energy level structure of a [Tb$_2$] molecular complex. The magnetic anisotropy gives rise to a ground level doublet for each Tb qubit, well separated energetically from all excited states. The intramolecular exchange interaction splits energetically levels associated with antiferromagnetic and ferromagnetic alignments of the control and target qubits. Each level is further split by the hyperfine interaction with the $I = 3/2$ nuclear spins of Tb and by the Zeeman interaction with the external magnetic field. For clarity, in this energy diagram, we only show levels for $m_I(1) = m_I(2) = -3/2$. The operation of the molecule as a SWAP or a CNOT gate under the action of rf electromagnetic pulses is schematically shown

the two ions will couple differently to an external magnetic field, i.e. their effective gyromagnetic ratios g_1 and g_2 will be different. For instance, if H is applied along one of the anisotropy axes, say of qubit '1', $g_1 = g_J$ whereas $g_2 = g_J \cos \delta$, i.e. it makes the two spins inequivalent.

Susceptibility and heat capacity measurements confirm that $g_1 \neq g_2$. Indeed, below $10\,\mathrm{K}$ $\chi' T$ (and thus also μ_{eff}) is much larger than predicted for collinear anisotropy axes ($\delta = 0$). In contrast, an excellent agreement is obtained for $\delta = 66°$, as shown in Fig. 8a. We have also measured the dc susceptibility for $\mu_0 H = 0.1\,\mathrm{T}$, obtaining further experimental evidence for noncollinear axes with the same values of J_{ex} and δ estimated above. Heat capacity data measured under $H \neq 0$ are shown in Fig. 8b. This quantity reflects the magnetic field dependence of the energy levels, which, in its turn, should strongly depend on δ. As with the magnetic data, the results are in qualitative and quantitative agreement with calculations made for $\delta = 66°$.

4.3 Quantum-Gate Performance

The essential physics of the [Tb$_2$] system is captured by the Hamiltonian (3), which accounts for the effects of the local uniaxial anisotropies of both Tb^{3+} ions, the

exchange coupling between their spins, and the Zeeman interaction with the external magnetic field. In the reduced subspace defined by the relevant qubit states, with $m_J = \pm 6$, the Hamiltonian simplifies to [16]

$$\mathcal{H}_{\text{red}} = -2J_{\text{ex}}J_{z,1}J_{z,2} - g_1\mu_{\text{B}}HJ_{z,1} - g_2\mu_{\text{B}}HJ_{z,2}$$
$$+A_J(J_{z,1}I_{z,1} + J_{z,2}I_{z,2}) \tag{4}$$

where the last term accounts for the hyperfine interaction with the $I = 3/2$ nuclear spins of Tb and $A_J/k_{\text{B}} = 2.5 \; 10^{-2}$ K is the hyperfine constant.

Equation (4) enables us to discuss the performance of [Tb$_2$] as a two-qubit quantum gate. The ensuing energy level spectrum is shown in Fig. 9 for $\delta = 66°$. For clarity, only levels with nuclear spin projections $m_{I;1} = m_{I;2} = -3/2$ are shown. The magnetic asymmetry enables to univocally single out any of the desired transitions because all possible transitions between any pair of magnetic states have a different energy. For instance, at $\mu_0 H = 0.07$ T, only transitions between states $|\Uparrow\rangle_1 \otimes |\Downarrow\rangle_2$ and $|\Downarrow\rangle_1 \otimes |\Uparrow\rangle_2$ (SWAP) would be resonant with the energy of $\nu = 9.8$ GHz photons (X-band EPR). Notice that these two states are split by the magnetic field because $g_1 \neq g_2$. The fact that SWAP gate operations can be induced by electromagnetic radiation avoids the need of coherently turning on and off interactions between the two qubits that is characteristic of some other previous proposals [20]. At $\mu_0 H = 0.28$ T, the resonant transition would be that from $|\Uparrow\rangle_1 \otimes |\Uparrow\rangle_2$ to $|\Uparrow\rangle_1 \otimes |\Downarrow\rangle_2$, which corresponds to the operation of a CNOT gate that switches the target qubit (spin 2) if and only if the control qubit (spin 1) is in state '0'. Therefore, SWAP and CNOT operations can be selected by tuning H.

The state initialization can be also easily carried out by cooling: at both fields and at $T = 0.1$ K, the ground-state population amounts to 99.3%. The short spin-lattice relaxation times ($T_1 \simeq 4 \times 10^{-4}$ s at 0.1 K) determined from the frequency-dependent ac susceptibility data of Fig. 8a ensure that the thermal populations will be readily attained.

The realization of gate operations requires also that these transitions are allowed, e.g. by the presence of weak transverse anisotropy terms. Continuous-wave EPR measurements performed on a [Tb$_2$] powdered sample show that both CNOT and SWAP transitions are indeed allowed [17].

5   Summary and Outlook

The search for material candidates to realize the basic component of a future quantum computer is one of the most fascinating challenges faced by today's science and technology. In this chapter, we have reviewed some of the recent attempts made to build such elements using artificial molecular nanomagnets, designed and synthesized via chemical methods. One of the characteristic traits of these materials, as compared with other proposals, is that molecular clusters can be much more than

simple qubits. There are theoretical proposals to use the multilevel magnetic energy structure of magnetic molecules to implement simple quantum algorithms [27] or to perform quantum simulations [62]. Therefore, magnetic molecules can be designed to act as minimum-size quantum processors. Here, we have shown experimentally that molecular clusters containing two lanthanide ions meet all ingredients required to implement a universal CNOT quantum logic gate [16, 17]. The definition of control and target qubits is based on the magnetic inequivalence of the two ions, which has been achieved by chemically engineering dissimilar coordination spheres. The magnetic asymmetry also provides a method to realize a SWAP gate in the same cluster. An additional attractive feature is that quantum-gate operations are achieved in a single step, via the application of a single rf pulse.

Although we have only considered complex [Tb$_2$], for which the magnetic asymmetry can be easily determined on account of its large angular momentum, the same molecular structure can be realized with other lanthanide ions [60]. This flexibility enables a vast choice of quantum-gate designs. These molecular clusters are also stable in solution, which opens the possibility of depositing them onto devices able to manipulate its quantum spin state [63, 64]. Chemically engineered molecular quantum gates can therefore open promising avenues for the realization of hybrid quantum computing architectures.

References

1. Nielsen, M.A., Chuang, I.L.: Quantum Computation and Quantum Information. Cambridge University Press, Cambridge (2000)
2. Feynman, R.P.: Simulating physics with computers. Int. J. Theor. Phys. **21**, 467–488 (1982)
3. Deutsch, D.: Quantum-theory, the Church-Turing principle and the universal quantum computer. Proc. R. Soc. Lond. A **400**, 97–117 (1985)
4. Shor, P.W.: Polynomial time algorithms for prime factorization and discrete algorithms on a quantum computer. SIAM J. Comput. **26**, 1484 (1997)
5. Grover, L.K.: Quantum mechanics helps in searching for a needle in a haystack. Phys. Rev. Lett. **79**, 325 (1997)
6. DiVincenzo, D.P.: The physical implementation of quantum computation. Fortschr. Phys. **48**, 771–783 (2000)
7. Ladd, T.D., Jelezko, F., Laflamme, R., Nakamura, Y., Monroe, C., O'Brien, J.L.: Quantum computers. Nature **464**, 45–53 (2010)
8. Cirac, J.I., Zoller, P.: Quantum computation with Cold Trapped Ions. Phys. Rev. Lett. **74**, 4091–4094 (1995)
9. Knill, E., Laflamme, R., Milburn, G.J.: A scheme for efficient quantum computation with linear optics. Nature **409**, 46–52 (2001)
10. Gershenfeld, N.A., Chuan, I.L.: Bulk spin-resonance quantum computation. Science **275**, 350 (1997)

11. Clarke, J., Wilhelm, F.K.: Superconducting quantum bits. Nature **453**, 1031–1042 (2008)
12. Loss, D., DiVincenzo, D.P.: Quantum computation with quantum dots. Phys. Rev. A **57**, 120–126 (1998)
13. Hanson, R., Awschalom, D.D.: Coherent manipulation of single spins in semiconductors. Nature **453**, 1043–1049 (2008)
14. Sato, K., Nakazawa, S., Rahimi, R., Ise, T., Nishida, S., Yoshino, T., Mori, N., Toyota, K., Shiomi, D., Yakiyama, Y., Morita, Y., Kitagawa, M., Nakasuji, K., Nakahara, M., Hara, H., Carl, P., Hofer, P., Takui, T.: Molecular electron-spin quantum computers and quantum information processing: pulse-based electron magnetic resonance spin technology applied to matter spin-qubits. J. Mater. Chem. **19**, 3739–3754 (2009)
15. Gatteschi, D., Sessoli, R., Villain, J.: Molecular Nanomagnets. Oxford University Press, Oxford (2006)
16. Luis, F.; Repollés, A., Martínez-Pérez, M.J., Aguilà, D., Roubeau, O., Zueco, D., Alonso, P.J., Evangelisti, M., Camón, A., Sesé, J., Barrios, L.A., Aromí, G.: Molecular prototypes for spin-based CNOT and SWAP quantum gates. Phys. Rev. Lett. **107**(117203), 1–5 (2011)
17. Aromí, G., Aguilà, D., Gamez, P., Luis, F., Roubeau, O.: Design of magnetic coordination complexes for quantum computing. Chem. Soc. Rev. **41**, 537–546 (2012)
18. Toffoli, T.: Bicontinuous extensions of invertible combinatorial functions. Math. Syst. Theor. **14**, 13–23 (1981)
19. Bell, J.: Speakable and unspeakable in quantum mechanics. Cambridge University Press, Cambridge (1987)
20. Lehmann, J., Gaita-Ariño, A., Coronado, E., Loss, D.: Spin qubits with electrically gated polyoxometalate molecules. Nat. Nanotech. **2**, 312 (2007)
21. Cirac, J.I., Zoller, P.: Quantum computation with cold trapped ions. Phys. Rev. Lett. **74**, 4091 (1995)
22. Monroe, C., Meekhof, D.M., King, B.E., Itano, W.M., Wineland, D.J.: Demonstration of a fundamental quantum logic gate. Phys. Rev. Lett. **75**, 4714 (1995)
23. Chuang, I.L., Vandersypen, L.M.K., Zhou, X. Leung, D.W., Lloyd, S.: Experimental realization of a quantum algorithm. Nature **393**, 143 (1998)
24. Clarke, J., Wilhelm, F.K.: Superconducting quantum bits. Nature **453**, 1031–1042 (2008)
25. Paik, H., Schuster, D.I., Bishop, L.S., Kirchmair, G., Catelani, G., Sears, A.P., Johnson, B.R., Reagor, M.J., Frunzio, L., Glazman, L.I., Girvin, S.M., Devoret, M.H., Schoelkopf, R.J.: Observation of high coherence in Josephson junction qubits measured in a three-dimensional circuit QED architecture. Phys. Rev. Lett. **107,** 240501 (2011)
26. Plantenberg, J.H., De Groot, P.C., Harmans, C.J.P.M., Mooij, J.E.: Demonstration of controlled-NOT quantum gates on a pair of superconducting quantum bits. Nature **447**, 836–839 (2007)
27. Leuenberger, M., Loss, D.: Quantum computing in molecular magnets. Nature **410**, 789 (2001)
28. Tejada, J., Chudnovsky, E.M., del Barco, E., Hernández, J.M., Spiller, T.P.: Magnetic qubits as hardware for quantum computers. Nanotechnology **12**, 181 (2001)
29. Meier, F., Levy, J., Loss, D.: Quantum computing with spin cluster qubits. Phys. Rev. Lett. **90**, 047901 (2003)
30. Troiani, F., Ghirri, A., Affronte, M., Carretta, S., Santini, P., Amoretti, G., Piligkos, S., Timco, G., Winpenny, R.E.P.: Molecular engineering of antiferromagnetic rings for quantum computation. Phys. Rev. Lett. **94**, 207208 (2005)
31. Matsuda, K., Irie, M.: Photochromism of diarylethenes with two nitronyl nitroxides: Photo-switching of an intramolecular magnetic interaction. Chem. Eur. J. **7**, 3466–3473 (2001)
32. Morita, Y., Yakiyama, Y., Nakazawa, S., Murata, T., Ise, T., Hashizume, D., Shiomi, D., Sato, K., Kitagawa, M., Nakasuji, K., Takui, T.: Triple-stranded metallo-helicates addressable as Lloyd's electron spin qubits. J. Am. Chem. Soc. **132**, 6944–6946 (2010)
33. Caciuffo, R., Guidi, T., Amoretti, G., Carretta, S., Liviotti, E., Santini, P., Mondelli, C., Timco, G., Muryn, C.A., Winpenny, R.E.P.: Spin dynamics of heterometallic Cr_7M wheels (M = Mn, Zn, Ni) probed by inelastic neutron scattering. Phys. Rev. B **71**(174407), 1–8 (2005)

34. Ardavan, A., Rival, O., Morton, J.J.L., Blundell, S.J., Tyryshkin, A.M., Timco, G.A., Winpenny, R.E.P.: Will spin-relaxation times in molecular magnets permit quantum information processing? Phys. Rev. Lett. **98**(057201), 1–4 (2007)

35. Wedge, C.J., Timco, G.A., Spielberg, E.T., George, R.E., Tuna, F., Rigby, S., McInnes, E.J.L., Winpenny, R.E.P., Blundell, S.J., Ardavan, A.: Chemical engineering of molecular qubits. Phys. Rev. Lett. **108**, 107204 (2012)

36. Timco, G.A., Carretta, S., Troiani, F., Tuna, F., Pritchard, R., Muryn, C.A., McInnes, E.J.L., Ghirri, A., Candini, A., Santini, P., Amoretti, G., Affronte, M., Winpenny, R.E.P.: Engineering the coupling between molecular spin qubits by coordination chemistry. Nat. Nanotech. **4**, 173 (2009)

37. Bellini, V., Lorusso, G., Candini, A., Wernsdorfer, W., Faust, T.B., Timco, G.A., Winpenny, R.E.P., Affronte, M.: Propagation of spin information at the supramolecular scale through Heteroaromatic linkers. Phys. Rev. Lett. **106**(227205), 1–4 (2011)

38. Candini, A., Lorusso, G., Troiani, F., Ghirri, A., Carretta, S., Santini, P., Amoretti, G., Muryn, C., Tuna, F., Timco, G., McInnes, E.J.L., Winpenny, R.E.P., Wernsdorfer, W., Affronte, M.: Entanglement in supramolecular spin systems of two weakly coupled antiferromagnetic rings (purple-CrNi$_7$). Phys. Rev. Lett. **104**(037203), 1–4 (2010)

39. Hill, S., Edwards, R.S., Aliaga-Alcalde, N., Christou, G.: Quantum coherence in an exchange-coupled dimer of single-molecule magnets. Science **302**, 1015–1018 (2003)

40. Aromí, G., Brechin, E.K.: Synthesis of 3d metallic single-molecule magnets. Struct. Bond **122**, 1–67 (2006)

41. Sessoli, R., Powell, A.K.: Strategies towards single molecule magnets based on lanthanide ions. Coord. Chem. Rev. **253**, 2328–2341 (2009)

42. Costa, J.S., Barrios, L.A., Craig, G.A., Teat, S.J., Luis, F., Roubeau, O., Evangelisti, M., Camón, A., Aromí, G.: A molecular [Mn$_{14}$] coordination cluster featuring two slowly relaxing nanomagnets. Chem. Commun. **48**, 1413–1415 (2012)

43. Nguyen, T.N., Wernsdorfer, W., Abboud, K.A., Christou, G.: A supramolecular ggregate of four exchange-biased single-molecule magnets. J. Am. Chem. Soc. **133**, 20688–20691 (2011)

44. Novitchi, G., Costes, J.P., Tuchagues, J.P., Vendier, L., Wernsdorfer, W.: A single molecule magnet (SMM) with a helicate structure. New J. Chem. **32**, 197–200 (2008)

45. Aromí, G., Gamez, P., Reedijk, J.: Poly beta-diketones: Prime ligands to generate supramolecular metalloclusters. Coord. Chem. Rev. **252**, 964–989 (2008)

46. Barrios, L.A., Aguilà, D., Roubeau, O., Gamez, P., Ribas-Ariño, J., Teat, S.J., Aromí, G.: Designed topology and site-selective metal composition in tetranuclear [MM′●●●M′M] linear complexes. Chem. Eur. J. **15**, 11235–11243 (2009)

47. Sañudo, E.C., Cauchy, T., Ruiz, E., Laye, R.H., Roubeau, O., Teat, S.J., Aromí, G.: Molecules composed of two weakly magnetically coupled [Mn(III)$_4$] clusters. Inorg. Chem. **46**, 9045–9047 (2007)

48. Sañudo, E.C., Salinas-Uber, J., Pons-Balagué, A., Roubeau, O., Aromí, G.: Molecular [(Fe$_3$)Fe$_3$)] and [(Fe$_4$)Fe$_4$)] Coordination Cluster Pairs as Single or Composite Arrays. Inorg. Chem. **51**, 8441–8446 (2012)

49. Aguilà, D., Barrios, L.A., Roubeau, O., Teat, S.J., Aromí, G.: Molecular assembly of two [Co(II)$_4$] linear arrays. Chem. Commun. **47**, 707–709 (2011)

50. Inglis, R., Katsenis, A.D., Collins, A., White, F., Milios, C.J., Papaefstathiou, G.S., Brechin, E.K.: Assembling molecular triangles into discrete and infinite architectures. Cryst. Eng. Comm. **12**, 2064–2072 (2010)

51. Eppley, H.J., deVries, N., Wang, S., Aubin, S.M., Tsai, H.L., Folting, K., Hendrickson, D.N., Christou G.: [Mn$_3$O(O$_2$CPh)$_6$(py)$_2$]$_2$(4, 4′ - bpy) and [Mn$_9$O$_7$(O$_2$CC$_6$H$_4$ - p - OMe)$_{13}$ (4, 4′ - bpy)]$_2$: new multinuclear manganese complexes. Inorg. Chim. Acta **263**, 323–340 (1997)

52. Bertaina, S., Gambarelli, S., Tkachuk, A., Kurkin, I.N., Malkin, B., Stepanov, A., Barbara, B.: Rare-earth solid-state qubits. Nat. Nanotech. **2**, 39–42 (2007)

53. Ishikawa, N., Sugita, M., Wernsdorfer, W.: Quantum tunneling of magnetization in lanthanide single-molecule magnets: Bis(phthalocyaninato)terbium and bis(phthalocyaninato)dysprosium anions. Ang. Chem. Int. Ed. **44**, 2931 (2005)

54. AlDamen, M.A., Clemente-Juan, J.M., Coronado, E., Martí-Gastaldo, C., Gaita-Ariño, A.: Mononuclear lanthanide single-molecule magnets based on polyoxometalates. J. Am. Chem. Soc. **130**, 8874 (2008)

55. AlDamen, M.A., Cardona-Serra, S., Clemente-Juan, J.M., Coronado, E., Martí-Gastaldo, C., Luis, F., Montero, O.: Mononuclear lanthanide single molecule magnets based on the polyoxometalates $[Ln(W_5O_{18})_2]^{9-}$ and $[Ln(\beta_2 - SiW_{11}O_{39})_2]^{13-}$ ($Ln^{III} = $ Tb, Dy, Ho, Er, Tm, and Yb). Inorg. Chem. **48**, 3467 (2009)

56. Luis, F., Martínez-Pérez, M.J., Montero, O., Coronado, E., Cardona-Serra, S., Martí-Gastaldo, C., Clemente-Juan, J.M., Sesé, J., Drung, D., Schurig, T.: Spin-lattice relaxation via quantum tunneling in an Er^{3+}-polyoxometalate molecular magnet. Phys. Rev. B **82**, 060403 (2010)

57. Setyawati, I.A., Liu, S., Rettig, S.J., Orvig, C.: Homotrinuclear lanthanide(III) arrays: Assembly of and conversion from mononuclear and dinuclear units. Inorg. Chem. **39**, 496–507 (2000)

58. Piggot, P.M.T., Hall, L.A., White, A.J.P., Williams, D.J.: Attempted syntheses of lanthanide(III) complexes of the anisole- and anilinosquarate ligands. Inorg. Chem. **42**, 8344–8352 (2003)

59. Evans, W.J., Greci, M.A., Ziller, J.W.: Chem. Commun. 2367–2368 (1998)

60. Aguilà, D., Barrios, L.A., Luis, F., Repollés, A., Roubeau, O., Teat, S.J., Aromí, G.: Synthesis and properties of a family of unsymmetric dinuclear complexes of Ln^{III}(Ln = Eu, Gd, Tb). Inorg. Chem. **49**, 6784–6786 (2010)

61. García-Palacios, J.L., Gong, J.B., Luis, F.: Equilibrium susceptibilities of superparamagnets: longitudinal and transverse, quantum and classical. J. Phys. Condens. Matter **21**, 456006 (2009)

62. Santini, P., Carretta, S., Troiani, F., Amoretti, G.: Molecular nanomagnets as quantum simulators. Phys. Rev. Lett. **107**, 230502 (2011)

63. Urdampilleta, M., Klyatskaya, S., Cleuziou, J.P., Ruben, M., Wernsdorfer, W.: Supramolecular spin valves. Nat. Mater. **10**, 502 (2011)

64. Imamoglu, A.: Cavity QED based on collective magnetic dipole coupling: spin ensembles as hybrid two-level systems. Phys. Rev. Lett. **102**, 083602 (2009)

Toward a Molecular Ion Qubit

**J. Mur-Petit, J. Pérez-Ríos, J. Campos-Martínez, M.I. Hernández,
S. Willitsch, and J.J. García-Ripoll**

Abstract We discuss the application of a novel spectroscopy protocol to study the Zeeman structure of single molecular ions. From molecular structure calculations for $^{14}N_2^+$ and $^{16}O_2^+$ we deduce their Zeeman spectra and discuss their potential to be used as a resource to encode quantum information.

1 Introduction

Information is central to our society, but for it to become a major commodity, a century of theoretical and technological developments was needed. Central to our understanding, processing and communication of information is the notion of bit, the smallest quantum of information, that can usually take on the values zero or one. As Shannon showed [22], bits also adapt beautifully to the type of logic, machines, and electrical circuits that conform our technology. In other words, all classical technology, from the earliest machines to the latest transistor-based circuits, accommodates perfectly to the paradigm of Boolean logic and our classical understanding of information as a collection of symbols.

The developments in the last decade have seriously challenged the *statu quo* in information processing. To start with, we are rapidly approaching the limits of what is currently achievable by silicon-integrated technologies. As we reduce the size of circuits and strive for faster and less energy-consuming information processing, or as we increase the storage density of information, we get closer to the nanoscale, a physical domain governed by the rules of quantum mechanics. At these scales,

J. Mur-Petit (✉) · J. Pérez-Ríos · J. Campos-Martínez · M.I. Hernández · J.J. García-Ripoll
Instituto de Física Fundamental, IFF-CSIC, Madrid, Spain
e-mail: jordi.mur@csic.es

S. Willitsch
Department of Chemistry, University of Basel, Basel, Switzerland

the states of electrons, atoms, and molecules are ill defined, and, while the theory is deterministic, the outcomes of measurements are not. More precisely, we no longer have 0s and 1s, but *quantum bits* or *qubits*, which are superpositions of these possibilities with different (complex) amplitudes. Surprisingly, this apparent complexity turns out to be an advantage. A novel information theory can be built using the concepts and tools from quantum mechanics [17], centered on the notions of qubit and quantum operations. This new theory accommodates new types of algorithms for standard procedures, such as factorization, database search, or unbreakable cryptography, with a performance that sometimes exceeds exponentially that of their classical counterparts. The double promise of a technology at the nanoscale which is more efficient both energetically and computationally has spun an extraordinary development of quantum technologies at all levels: from superconducting circuits, quantum dots, and nanomechanical resonators down to atoms and molecules.

In general terms, a qubit can be made of any two-level quantum system. Among the many possible ways or possible platforms for quantum information, trapped ions have many advantages. The ions can be trapped by electric fields and/or cooled down and manipulated with laser sources. So far the practical materialization has been mainly carried out using *atomic* ions. In this regard there are typically three types of qubits using the energy levels of an ion:

(a) *Zeeman qubits.* Here the energy splitting between the qubit levels is linearly dependent on the magnetic field B. They usually have lifetimes on the order of milliseconds or larger. One obvious drawback of the Zeeman qubit is that since the energy difference between the two-qubit states depends linearly on the magnetic field, any relevant magnetic field fluctuations in the environment of the ion will cause dephasing, which in practice limits their applicability, unless a suitable pair of states can be found where this effect is not present, at least to first order.

(b) *Hyperfine qubits.* In isotopes with nonzero nuclear spin, we can have hyperfine splittings. At low magnetic field, there is also a linear dependence that can remove the degeneracy of different Zeeman levels. A clear advantage of the hyperfine qubit choice is that pairs of levels can be found such that their energy separation does not depend, to first order, on the magnetic field (we present below a molecular example, where this is the case too). Hyperfine qubits are extremely long-lived (with lifetimes on the order of thousands to even millions of years!) and phase/frequency stable, which has led to their application for defining time and frequency standards.

(c) *Optical qubits.* In atomic ions with a low-lying D level, such as $^{40}Ca^+$, there exists the possibility of using the $S \rightarrow D$ optical transition. This typically gives a lifetime of the order of seconds, not large but long enough to perform logic gate operations (on the order of microseconds). There is therefore a rather wide range of possible applications and laboratory implications. In the case of molecules, this is a less popular choice, and we will not consider it here.

2 Quantum Technology with Molecular Ions

With all these possibilities at hand with an *atomic ion*, it is immediate to enquire about the use of *molecular ions* instead. A molecule presents the advantage of much closer energy levels (rotation and vibration vs. only electronic in atoms) that gives, in principle, longer lifetimes for excited states since the Einstein's coefficients are proportional to the third power of the radiation frequency. As in most situations, these features have advantages and inconveniences. The most obvious advantage is the large number of energy levels and frequency scales available in molecules that envisages many possible future applications, for example, as novel types of qubits or as interfaces between other quantum systems which operate on different frequency scales. Moreover, the intricate couplings between the different angular momenta in molecular systems often lead to a breakdown of the linear dependence of the level energies with applied magnetic fields at smaller values than for atomic ions, which open up new opportunities for the design of qubits with minimal decoherence. These in turn could serve, for instance, as long-lived quantum memories as a part of a hybrid quantum system. In this context, maybe the biggest advantage of molecules lies in their enormous chemical diversity: it is practically always possible to find (or indeed "engineer") a molecule with the desired properties for the relevant application.

On the other hand, the large density of quantum states in molecules complicates their preparation in *single* states as well as their coherent manipulation, which are fundamental requirements for quantum information processing, novel approaches to precision spectroscopy [1, 19, 20], and quantum-controlled chemistry [18, 26, 27]. Moreover, the large density of states implies the presence of a variety of decay and dephasing mechanisms which render the implementation of high-fidelity quantum operations in molecules very challenging.

However, over the past years, there has been impressive progress in the localization of single molecular ions in traps by sympathetic cooling of their translational motion with laser-cooled atomic ions [14]. Very recently, also the initialization of sympathetically cooled molecular ions in well-defined quantum states has been accomplished, either by optical pumping in molecules like MgH^+ [23] and HD^+ [1, 21] or by the state-selective generation of the ions prior to sympathetic cooling in N_2^+ [24, 25] (see Fig. 1). These developments now pave the way for the first realization of coherent experiments with single, localized molecular ions in traps.

With atomic ions, a number of very accurate preparation, manipulation, and measurement techniques have been developed [7], among which we remark the detection by electron shelving. Unfortunately, no such scheme is generally available for molecular ions due to the general absence of cycling transitions. This has led to using alternative detection methods, such as laser-induced charge transfer [24, 25] or state-selective photodissociation [1, 21, 23], which, however, entail the destruction of the molecular ion and are hence inapplicable if repeated measurements are desired, as in quantum metrology [20] or quantum information [7].
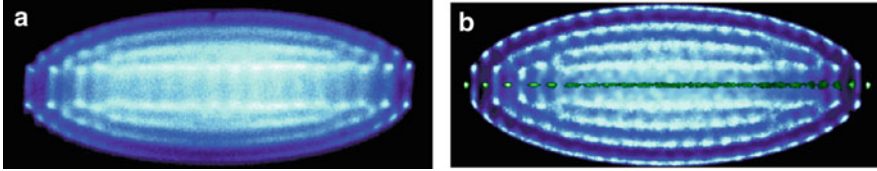
Fig. 1 (**a**) False-color fluorescence image of 24 quantum state selected, sympathetically cooled N_2^+ ions embedded into an ensemble of localized, laser-cooled Ca^+ ions in an ion trap. Because the molecular ions are not laser-cooled and therefore do not fluoresce, their location is only visible as a nonfluorescing region in the center of the image. (**b**) Simulation of the experimental image. The distribution of the molecular ions has been made visible in green. Adapted from [26]

In a recent work [15], we have proposed a fast, accurate, and *nondestructive* spectroscopy protocol suitable to address the different internal degrees of freedom—rotational, vibrational, hyperfine—of molecular ions. Here, we briefly review the main ideas underlying that work and focus on addressing hyperfine states of a molecular ion and go forward to analyze the prospects of two particular molecular ions, $^{14}N_2^+$ and $^{16}O_2^+$, for quantum information processing tasks.

3 Phase-Sensitive Quantum Logic Spectroscopy

One can define spectroscopy as the study of the effect of a periodic force or driving on a physical system of interest. Typically, one observes the back action of the system on the driving field, for example, by measuring absorption spectra, or how the intensity or phase of the driving field is changed by the interaction with the system. In [20], the idea of quantum logic spectroscopy (QLS) was introduced, which advocates a careful study of the changes on the driven system itself (in that case, an Al^+ ion), by using quantum gates to enhance the precision of the measurements performed. The protocol utilized in [20] had stringent requirements on the temperature of the ions studied, and the overall speed of the process was limited by using the collective motional modes of the system as a quantum bus. By appealing to ideas from coherent control, it is possible to remove these limitations [5, 6]. We have resorted on these ideas to design a novel protocol that extends QLS to molecular ions. In the following, we present a brief summary of the main concepts involved, and then we apply them to analyze two molecular ions in the light of their potential use as qubits.

As it was shown in [5, 6, 11], it is possible to increase the versatility and robustness of the original QLS protocol by using geometric gates based on state-dependent forces. Geometric gates are quantum gates whose performance does not depend on the motional state of system and are thus particularly appealing to address sympathetically cooled ions, such as molecular ions trapped in Ca^+ or Be^+ Coulomb crystals. The physical principle at the root of these quantum operations
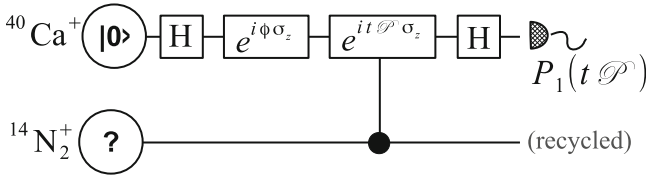
Fig. 2 *State detection protocol.* The control ion is subject to a series of single-qubit gates together with a two-qubit gate in which the observable property $\mathscr{P}$ of the spectroscopy ion induces a state-dependent phase on the two-ion quantum state. Measurement of the control ion then allows access to information on $\mathscr{P}$

is that a chain of ions shaken by an external driving will have its quantum state modified by the acquisition of a phase depending on the driving forces. Now, for the particular case of the system being two trapped ions, if the forces applied on them are such that their effect depends on the internal state of the ion (as can be realized, e.g., by applying a laser of a given polarization that can only affect one internal state of the ion), then the phase accumulated by the two-ion system will also depend on their internal states. As a consequence, if one is able to measure this accumulated phase (e.g., via an interferometric process), one will gain information on the state of the trapped ions.

Let us consider a system composed of two trapped ions, a control or logic ion (that in our case will be an atomic ion such as ^{40}Ca$^+$ or ^{9}Be$^+$) and a spectroscopy ion (such as a molecular ion). The first ion is actively laser-cooled, while the spectroscopy ion is sympathetically cooled by the control ion thanks to the Coulomb interaction. Let us assume that the control ion can be described as a qubit and that we apply some force on it which depends on its internal state, $f_C(t)\sigma_C^z$, where σ_C^z is the Pauli z-matrix for the internal state space of the control ion. On the other hand, the spectroscopy ion can have in principle any number of internal levels, and applying a force to it will depend on some internal property, $\mathscr{P}$, such as a magnetic moment of a dipole moment, $f_S(t)\mathscr{P}$. As explained in [15], under the influence of these forces, the quantum state of the two-ion system will acquire a total phase due to both forces $f_{C,S}$ given by

$$\Phi_{\mathscr{P}} = \sigma_C^z \mathscr{P} \phi_{CS}, \tag{1}$$

where ϕ_{CS} is a function of the collective modes of the two-ion complex, ω_{com} and ω_{str}, and of the forces applied on the ions. Let us emphasize at this point that the forces on the control and spectroscopy ions are independent and do not need to have a common origin or even be based on the same effect. In particular, below we consider applying an AC Stark shift to the atomic ion and a magnetic field gradient (Zeeman shift) on the molecular ion.

The phase 1 does not depend on the motional state of the ions at the start of the operation, which makes the gate temperature-independent and robust. This allows us to design the following spectroscopy protocol (cf. Fig. 2) to accurately measure the phase $\Phi_{\mathscr{P}}$ and, hence, obtain a measurement of the physical observable $\mathscr{P}$.

1. Prepare the control ion in the initial state $|0\rangle$.
2. Apply a Hadamard gate on this ion, $H = \exp(-i\sigma_C^y \pi/2)$; in practice, this amounts to starting a Ramsey sequence.
3. Optionally, apply a reference phase on the control ion, $\exp(i\phi\sigma_C^z)$.
4. Apply the state-dependent forces $f_{C,S}(t)$ on the control and spectroscopy ions, ensuring that the initial motional state of the ions is restored (see Sect. 4).
5. Close the Ramsey sequence by applying again a Hadamard gate, H.
6. Measure whether the control ion is in the excited state $|1\rangle$.

After Steps 1–5, the control ion and the spectroscopy ions will be entangled, and the excited state population of the control ion will oscillate as

$$P_1 = \sin^2(t\,\mathscr{P}\phi_{CS} + \xi). \tag{2}$$

The measurement Step 6 projects the entangled state, and, after reinitializing the control ion to $|0\rangle$, a repeated application of the protocol allows to determine the value of $\mathscr{P}$ with high precision [8].

## 4 QLS Protocol for Molecular Zeeman States

In this section we present a particular application of the protocol described in Sec. 3 when one is interested in discriminating the Zeeman levels within a rovibrational level of the molecular ion of interest. The different magnetic field dependence of the Zeeman shifts for different levels results in general in different magnetic moments for each state. Hence, we envision to use the magnetic moment as our observable of interest, $\mathscr{P} = \mu$, and to use magnetic field gradients to couple to it [9, 13]: $f_S(t) = \mu \partial B(t)/\partial x$. Without loss of generality, we take the forces to be characterized by a driving frequency ν and have a Gaussian envelope of duration T:

$$f_{C,S}(t) = f_{C,S}^0 \, e^{-(2t/T)^2} \cos(\nu t). \tag{3}$$

With this time dependence, and for a sufficiently long pulse, $T \geq 5\pi/\tilde{\omega}$ ($\tilde{\omega} = \min\{|\nu - \omega_{com}|, |\nu - \omega_{str}|\}$), one can ensure that *all* motional degrees of freedom of the system are restored to their initial state, and the two ions accumulate a quantum phase given by (1) with (cf. [15])

$$\phi_{CS} = \frac{1}{4}\sqrt{\frac{\pi}{2}} \frac{f_C^0 f_S^0 a^2 T}{\omega} \left[\frac{\omega^2}{\omega_{com}^2(\tilde{m}) - \nu^2} - \frac{\omega^2}{\omega_{str}^2(\tilde{m}) - \nu^2} \right], \tag{4}$$

where ω is the frequency of the control ion trap, $\tilde{m} = m_S/m_C$ is the mass ratio of the two ions, and $a^2 = \hbar/[(m_C + m_S)\omega]$. We note that the driving frequency ν is a free parameter. This can be useful for the case of ions with small magnetic moments, where one can set ν close to one of the collective mode frequencies of the system to enhance the effect (at the expense of a longer gate time, see [15] for details).
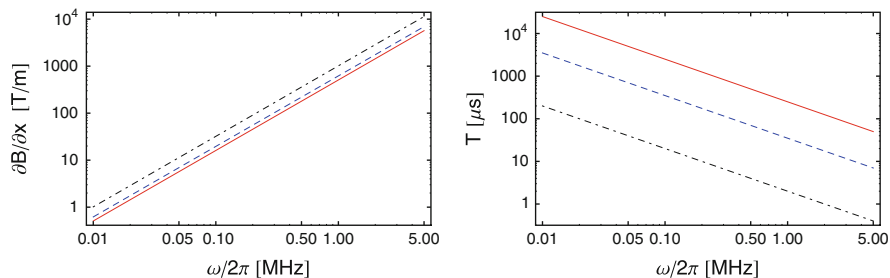
Fig. 3 *Experimental requirements.* Gradient (*left*) and gate time (*right*) required to perform the spectroscopy protocol with $^{40}Ca^+$ and $^{14}N_2^+$ ions, utilizing a magnetic field gradient $\partial B/\partial x = \exp[-(2t/T)^2]B' \cos(\nu t)$ in a harmonic trap of frequency ω, driven at frequencies $\nu/\omega = 0, 1.1$ and 1.01 (*dash-dotted, blue dashed, red solid*)

Using this protocol, it would be possible to study the Zeeman structure of, for example, $^{14}N_2^+$ molecular ions trapped with $^{40}Ca^+$ as in [24,25]. We have performed structure calculations to estimate the magnetic moments of the corresponding states and found them to be on the order of the Bohr magneton, see the left panels in Fig. 4. With this, it is straightforward to calculate the required field gradients to realize the spectroscopy protocol, assuming a laser is driving AC Stark forces on the $^{40}Ca^+$ ion. It turns out that for typical trap frequencies $\omega/2\pi = 10^2 - 10^3$ Hz, field gradients on the order of 10 T/m applied during a few hundred microseconds will suffice, see Fig. 3. Moreover, even lower gradients and shorter times can be used in case of smaller trap frequencies, making this approach very attractive.

5 Toward a Molecular Ion Qubit: Comparison of $^{14}N_2^+$ and $^{16}O_2^+$

As an example of the different features that molecules may exhibit in this context, we have considered the effect of an external magnetic field in the lowest energy levels of $^{14}N_2^+$ and $^{16}O_2^+$. We write a general Hamiltonian as

$$H = H_0 + H_Z, \tag{5}$$

where H_0 is the field-free molecular Hamiltonian and H_Z represents the interaction with the magnetic field. The ground electronic state of $^{14}N_2^+$ is $^2\Sigma_g^+$ and, in this way, H_0 involves rotational, spin rotation, and, in addition, hyperfine interactions (the nuclear spin of ^{14}N is one). The $^{16}O_2^+$ cation, on the other hand, has a $^2\Pi_g$ ground state and the zero-field Hamiltonian includes rotational, spin-orbit, spin rotation, and Λ-doubling terms[4]. There is no hyperfine structure involved since the ^{16}O nuclei have zero spin. Another consequence of the oxygen nuclear spin statistics
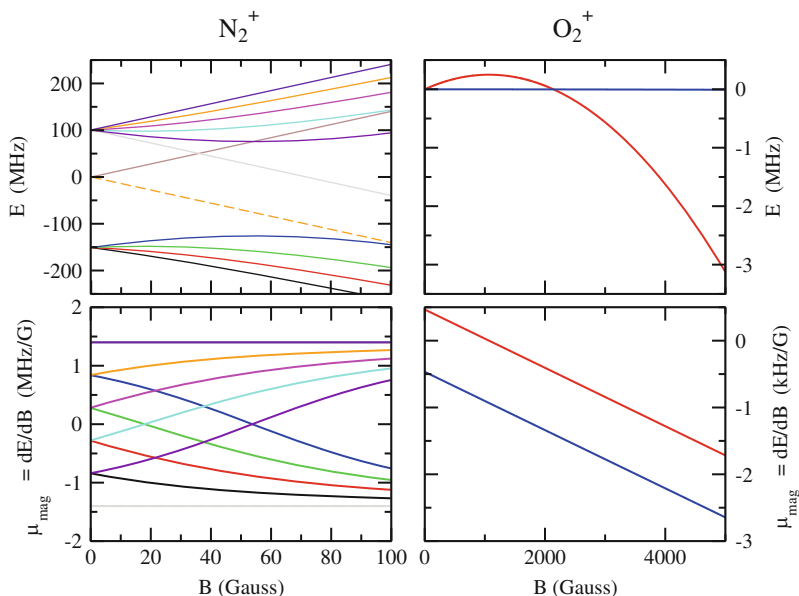
Fig. 4 *Zeeman diagrams. Upper panels*: Zeeman energy shifts of the ground rovibronic states of $^{14}N_2^+$ (*left*) and $^{16}O_2^+$ (*right*). *Lower panels*: $^{14}N_2^+$ (*left*) and $^{16}O_2^+$ (*right*) magnetic moments, $\mu = (\partial E / \partial B)$, for the levels above

is that one of the two Λ-doublet components is always missing for each value of the total angular momentum J [4]. All this will make the $^{16}O_2^+$ spectrum much less congested than that of $^{14}N_2^+$. Differences also arise regarding the coupling with the applied magnetic field. First, the leading term of the Zeeman Hamiltonian for a $^2\Sigma$ molecule such as $^{14}N_2^+$ reads

$$H_Z(N_2^+) = \mu_B B g_S S_Z, \tag{6}$$

where g_S is the electron spin gyromagnetic factor (taken as $g_S = 2.002$), B is the magnetic field, μ_B is the Bohr magneton, and S_Z is the component of the electronic spin along the direction of the external field. This interaction differs in $^{16}O_2^+$ since the orbital motion of the unpaired electron also couples to the field, so, in this case,

$$H_Z(O_2^+) = \mu_B B \left(g_L L_Z + g_S S_Z \right), \tag{7}$$

where g_L is the electron orbital g-factor (taken as $g_L = 1$) and L_Z is the projection of the electronic orbital angular momentum onto the external field.

The Zeeman splittings and corresponding magnetic moments, $\mu = \partial E / \partial B$, of the rovibrational ground states of $^{14}N_2^+$ ($^2\Sigma_g^+$) and $^{16}O_2^+$ ($^2\Pi_g$) as functions of B are shown in Fig. 4. For nitrogen, the hyperfine structure at zero field gives three distinct

sublevels corresponding to total angular momenta $F = 3/2$, $1/2$ and $5/2$ in order of ascending energy (for total nuclear spin $I = 2$, 0 and 2, respectively). Details of the calculations and the molecular constants used can be found in [15]. For $^{16}O_2^+$, there is only one level at zero field corresponding to a total angular momentum, $F = J = 1/2$. The calculations at various values of B were performed by diagonalizing the Hamiltonian matrix using a Hund's case (a) representation [2, 3] and taking the molecular constants for the ground vibrational state from the work of Coxon and Haley [4] (a more complete account will be given elsewhere [16]). We note that, for both ionic species, the levels plotted in Fig. 4 are well separated from the next upper rotational levels of both ionic species studied (energy splitting of about $\hbar \times 10^5$ MHz $\sim k_B \times 4.8$ K) .

It is quite noticeable the very different behavior of both ions in the presence of a magnetic field. The $^{14}N_2^+$ levels have a much stronger dependence with B leading, in most cases, to rather high values of the state-dependent magnetic moments: for the highest fields, they tend to μ_B in absolute value, and for lower fields ($B < 80$ G), almost all states are distinguishable by the values of their magnetic moments, this feature serving for efficient nondestructive measurements as proposed in [15]. For oxygen, on the contrary, the magnetic sublevels depend extremely weakly on B: notice the very different scales in the axes of the graphs with respect to nitrogen. This is due to the fact that for this level, the Zeeman effect is governed by $g_L - g_S/2 \approx 0.001$ (see [12] for a discussion). Hence, the $^{16}O_2^+$ magnetic moments are about 1,000 smaller than the $^{14}N_2^+$ ones. As a consequence, the two lowest Zeeman levels in the ground rovibrational state of $^{16}O_2^+$ will feature very small coupling to ambient magnetic field fluctuations. In other words, they may constitute a convenient two-level (qubit) system for storage of quantum information.

We finally note that the couplings with higher molecular states (off-diagonal matrix elements) play an important role in the dependence of the energy levels with the field, since they are the cause for the departure of a linear dependence with B[10]. Indeed, it can be seen that the magnetic moments are not exactly constant with B and that the one corresponding to the upper level ($M = -1/2$, in red in the Fig. 4) changes sign at about 1,000 Gauss.

6 Conclusions and Outlook

In conclusion, we have presented a nondestructive molecular spectroscopy protocol and discussed in detail its application to study the Zeeman spectrum of molecular ions. From an analysis of the calculated spectra of $^{14}N_2^+$ and $^{16}O_2^+$, we deduce that the lowest Zeeman levels of the latter constitute an promising candidate to realize a quantum memory.

In the future, we will study the application of this protocol to other molecular ions of interest and analyze in further detail the susceptibility of each one to ambient fields, so as to determine the best candidates for several quantum information tasks.

References

1. Bressel, U, Borodin, A., Shen, J., Hansen, M., Ernsting, I., Schiller, S.: Addressing and manipulation of individual hyperfine states in cold trapped molecular ions and application to HD^+ frequency metrology. E-print arXiv:1203.2153 (2012)

2. Brown, J.M., Carrington, A.: Rotational Spectroscopy of Diatomic Molecules. Cambridge University Press, Cambridge (2003)

3. Brown, J.M., Kaise, M., Kerr, C.M.L., Milton, D.J.: A determination of fundamental Zeeman parameters for the OH radical. Mol. Phys. **36**, 553 (1978)

4. Coxon, J.A., Haley, M.P.: Rotational analysis of the $A^2\Pi_u \rightarrow X^2\Pi_g$ second negative band system of $^{16}O_2^+$. J. Mol. Spectrosc. **108**, 119 (1984)

5. García-Ripoll, J.J., Zoller, P., Cirac, J.I.: Speed optimized two-qubit gates with laser coherent control techniques for ion trap quantum computing. Phys. Rev. Lett. **91**, 157901 (2003)

6. García-Ripoll, J.J., Zoller, P., Cirac, J.I.: Coherent control of trapped ions using off-resonant lasers. Phys. Rev. A **71**, 062309 (2005)

7. Haeffner, H., Roos, C.F., Blatt, R.: Quantum computing with trapped ions. Phys. Rep. **469**, 155 (2008)

8. Hume, D.B., Rosenband, T., Wineland, D.J.: High-fidelity adaptive qubit detection through repetitive quantum nondemolition measurements. Phys. Rev. Lett. **99**, 120502 (2007)

9. Johanning, M., Braun, A., Timoney, N., Elman, V., Neuhauser, W., and Wunderlich, Chr.: Individual addressing of trapped ions and coupling of motional and spin states using rf radiation. Phys. Rev. Lett. **102**, 073004 (2009)

10. Krems, R.V., Egorov, D., Helton, J.S., Maussang, K., Nguyen, S.V., Doyle, J.M.: Zeeman effect in CaF($^2\Pi_{3/2}$) J. Chem. Phys. **121**, 11639 (2004)

11. Leibfried, D., DeMarco, B., Meyer, V., Lucas, D., Barrett, M., Britton, J., Itano, W. M., Jelenković, B., Langer, C., Rosenband, T., Wineland, D.J.: Experimental demonstration of a robust, high-fidelity geometric two ion-qubit phase gate. Nature **422**, 412 (2003)

12. Leo Meerts, W., Veseth, L., Leibfried, D., Blatt, R., Monroe, C., and Wineland, D.: The zeeman spectrum of the NO molecule. J. Molec. Spectros. **82**, 202 (1980)

13. Mintert, F., Wunderlich, C.: Ion-trap quantum logic using long-wavelength radiation. Phys. Rev. Lett. **87**, 257904 (2001)

14. Molhave, K., Drewsen, M.: Formation of translationally cold MgH^+ and MgD^+ molecules in an ion trap. Phys. Rev. A **62**, 011401 (2000)

15. Mur-Petit, J., García-Ripoll, J.J., Pérez-Ríos, J., Campos-Martínez, J., Hernández, M.I., Willitsch, S.: Temperature-independent quantum logic for molecular spectroscopy. Phys. Rev. A **85**, 022308 (2012)

16. Mur-Petit, J., García-Ripoll, J.J., Pérez-Ríos, J., Campos-Martínez, J., Hernández, M.I., Willitsch, S.: Prospects for simple diatomic ions as Zeeman qubits. To be submitted

17. Nielsen, M., Chuang, I.: Quantum Information and Computation. Cambridge University Press, Cambridge (2011)

18. Ospelkaus, S., Ni, K.K., Wang, D., de Miranda, M.H.G., Neyenhuis, B., Quéméner, G., Julienne, P.S., Bohn, J.L., Jin, D.S., Ye, J.: Quantum-state controlled chemical reactions of ultracold potassium-rubidium molecules. Science **327**, 853 (2010)

19. Schiller, S., Korobov, V.: Tests of time independence of the electron and nuclear masses with ultracold molecules. Phys. Rev. A **71**, 032505 (2005)
20. Schmidt, P.O., Rosenband, T., Langer, C., Itano, W.M., Bergquist, J.C., Wineland, D.J.: Spectroscopy using quantum logic. Science **309**, 749 (2005)
21. Schneider, T., Roth, B., Duncker, H., Ernsting, I., Schiller, S.: All-optical preparation of molecular ions in the rovibrational ground state. Nat. Phys. **6**, 275 (2010)
22. Shannon, C.M..: A symbolic analysis of relay and switching circuits Trans. Am. Inst. Elec. Eng. **52**, 713–723 (1938)
23. Staanum, P.F., Hojbjerre, K., Hansen, A.K., Drewsen, M.: Rotational laser cooling of vibrationally and translationally cold molecular ions. Nat. Phys. **6**, 271 (2010)
24. Tong, X., Wild, D., Willitsch, S.: Collisional and radiative effects in the state-selective preparation of translationally cold molecular ions in ion traps. Phys. Rev. A **83**, 023415 (2011)
25. Tong, X., Winney, A.H., Willitsch, S.: Sympathetic cooling of molecular ions in selected rotational and vibrational states produced by threshold photoionization. Phys. Rev. Lett. **105**, 143001 (2010)
26. Willitsch, S.: Coulomb-crystallized molecular ions in traps: methods, applications, prospects. Int. Rev. Phys. Chem. **31**, 175–199 (2012)
27. Willitsch, S., Bell, M.T., Gingell, A.D., Softley, T.P.: Chemical applications of laser- and sympathetically-cooled ions in ion traps. Phys. Chem. Chem. Phys. **10**, 7200 (2008)

Implementing Quantum Gates and Algorithms in Ultracold Polar Molecules

S. Vranckx, A. Jaouadi, P. Pellegrini, L. Bomble, N. Vaeck, and M. Desouter-Lecomte

Abstract We numerically investigate the implementation of small quantum algorithms, an arithmetic adder and the Grover search algorithm, in registers of ultracold polar molecules trapped in a lattice by concatenating intramolecular and intermolecular gates. The molecular states are modulated by the exposition to static electric and magnetic fields different for each molecule. The examples are carried out in a two-molecule case. Qubits are encoded either in rovibrational or in hyperfine states, and intermolecular gates involve states of neighboring molecules. Here we use π pulses (i.e., laser pulses such that the integral of the product of the transition dipole moment and their envelope is equal to π, thus ensuring a total population inversion between two states) and pulses designed by optimal control theory adapted to a multi-target problem to drive unitary transformations between the qubit states.

S. Vranckx
Laboratoire de Chimie Physique, Université de Paris-Sud and CNRS,
UMR 8000, Orsay F-91405, France

Service de Chimie Quantique et Photophysique, Université Libre de Bruxelles,
CP160/09, avenue F.D. Roosevelt 50, 1050 Brussels, Belgium

A. Jaouadi · P. Pellegrini · L. Bomble · M. Desouter-Lecomte (✉)
Laboratoire de Chimie Physique, Université de Paris-Sud and CNRS,
UMR 8000, Orsay F-91405, France
e-mail: Michele.desouter-lecomte@u-psud.fr

N. Vaeck
Service de Chimie Quantique et Photophysique, Université Libre de Bruxelles,
CP160/09, avenue F.D. Roosevelt 50, 1050 Brussels, Belgium
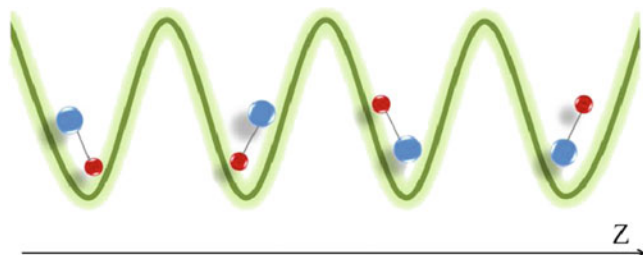
Fig. 1 Schematic of a network of polar molecules trapped in a one-dimensional optical lattice. Electric and magnetic fields are applied in the Z direction connecting the mass centers. Both fields have a gradient along the Z-axis so that each molecule is individually addressable

1 Introduction

Information processing based on quantum mechanics is a promising way to speed up operations [1, 2]. The superiority should come from the possibility of exploiting superposed and entangled states. The qubit states are mapped onto states of a physical system, and in the optical strategy, the unitary transformations among the computational basis states are driven by laser pulses. However, it is expected that at least a hundred of qubits approximately will be necessary to overcome the power of classical computers [3]. Scalability is thus a central problem for any possible support: atoms, trapped ions, quantum dots, or molecules. In the last decade, a lot of works have analyzed the possibilities offered by the rovibrational states of diatomic and polyatomic molecules [4–21]. Nevertheless, increasing the number of qubits encoded in a single molecule is challenging since the number of individually addressable eigenstates cannot grow exponentially. Recently, the field of ultracold polar molecules has suggested a new platform: the original proposal of DeMille [22] consists in arrays of ultracold polar molecules trapped in a one-dimensional optical lattice, as schematized in Fig. 1, and oriented by an external field with a gradient so that each molecule is subjected to a different Stark effect. Trapped polar diatomic molecules [23] are very interesting candidates to encode qubit states [21, 24–27] due to their long rovibrational lifetimes in the ground electronic state, their long coherence times, and their ability to be manipulated by optical and microwave pulses with unprecedented accuracy [28]. Their most important property comes from the long-range dipole–dipole interaction, which enables coupling between neighboring molecules and the creation of entangled states [29]. Moreover, their inner rotational and hyperfine level structure can be modified and specifically designed by external electrical or magnetic field [30].

2 Model

The dipolar molecules are assumed to be trapped in a one-dimensional optical lattice as shown in Fig. 1, whose frequency does not interfere with any internal excitation. We do not use the translational motion of the mass centers to realize the gates. As the molecules are ultracold, this translational motion corresponds to the ground state of the trapped well (a Gaussian function in the harmonic approximation). The mass centers are assumed to be fixed at their average position in each well.

Each diatomic molecule noted i is thus described by its internal Hamiltonian in its ground electronic state which includes interaction with static electric or magnetic fields:

$$H_{\text{in}}^i = H_{\text{vib}}^i + H_{\text{rot}}^i + H_{\text{hf}}^i + H_{\text{S}}^i + H_{\text{Z}}^i \tag{1}$$

where H_{vib}^i is the vibrational Hamiltonian in the ground electronic state and $H_{\text{rot}}^i = B_v N^2$ is the rotational Hamiltonian in each vibrational state $|v\rangle$ (with N being the rotational angular momentum operator). The hyperfine structure is described by

$$H_{\text{hf}}^i = \sum_{k=1}^{2} V_k Q_k + \sum_{k=1}^{2} c_k \vec{N} \cdot \vec{I}_k + c_4 \vec{I}_1 \cdot \vec{I}_2 \tag{2}$$

where the first contribution comes from the electric quadrupole Q_k coupling, the second one is the spin–rotation coupling with the nuclear spin I_k of the nucleus k characterized by coupling constants c_1 and c_2, and the third term is the nuclear spin–spin interaction. For the considered alkali metal dimers, we have neglected the nuclear tensor spin–spin interaction usually associated with constant c_3, which is here an order of magnitude smaller than spin–spin coupling constant c_4. The values of the constants are taken from references [29, 31]. The electric and magnetic fields are applied in the Z direction. The electric field presents a gradient in this direction so that the pendular rotational states due to the Stark interaction are different for each molecule:

$$H_{\text{S}}^i = -\mu_z^i E_i \cos\theta_i - \frac{1}{2}\alpha_{//} E_i \cos^2\theta_i - \frac{1}{2}\alpha_\perp E_i \sin^2\theta_i \tag{3}$$

where E_i is the electric field experienced by molecule i, μ_z^i is the component of the dipolar moment of the ith molecule along the internuclear Z-axis, and θ_i defines the angle between the z and Z-axis. $\alpha_{//}$ and $\alpha_\perp$ are the parallel and perpendicular polarizabilities, respectively [32]. The Zeeman Hamiltonian for a magnetic field B reads

$$H_{\text{Z}}^i = -g_r^i \mu_N \vec{N} \cdot \vec{B} - \sum_{k=1}^{2} g_k \mu_N \vec{I}_k \cdot \vec{B} \tag{4}$$

with μ_N the nuclear magneton, g_r^i the rotational g factor, and g_k the nuclear g factor of each nucleus k in molecule i.

We consider a two-molecule case. The time-independent Hamiltonian is

$$H_0 = \sum_{i=1}^{2} H_{\text{in}}^{i} + V_{\text{dd}} \tag{5}$$

where H_{in}^{i} is the internal Hamiltonian for each molecule $i = 1, 2$ and V_{dd} is the dipole–dipole interaction which depends on the intermolecular distance R:

$$V_{\text{dd}} = \frac{1}{4\pi\varepsilon_0} \frac{\vec{\mu}_1 . \vec{\mu}_2 - 3\left(\vec{\mu}_1 . \vec{e}_Z\right)\left(\vec{\mu}_2 . \vec{e}_Z\right)}{R^3} \tag{6}$$

where $\vec{e}_Z$ is the unit vector characterizing the magnetic and electric field orientation, with which we suppose that the two internuclear axes of the molecules are aligned.

3 Qubit Assignment

In quantum computing, a qubit is a two-level system whose basis states are associated to the logical states $|0\rangle$ and $|1\rangle$, respectively. A qubit can exist in any superposed state $\alpha |0\rangle + \beta |1\rangle$ contrarily to a classical bit, which can only be in one basis state. A register of n qubits requires the selection of $2n$ states of the molecular system.

For the case of two interacting molecules in their ground electronic state, we define a product basis set formed by tensor product of the basis sets of each molecule $|v, N, m_N, m_1, m_2\rangle_1 \otimes |v, N, m_N, m_1, m_2\rangle_2$, where v and N respectively denote the vibrational and rotational quantum numbers and where m_N, m_1, m_2 are the projections in the direction of the field of the rotational and nuclear spin angular momenta. We assign the 2^n logical states of our n-qubit register to eigenstates of H_0 including the dipole–dipole interaction and the coupling with the static fields. The eigenvectors have a dominant weight on a particular product basis state and are denoted by this component noted with the tilde sign. For instance, $|\varphi\rangle = |\tilde{0}, \tilde{0}, \tilde{0}, \tilde{m}_1, \tilde{m}_2\rangle_1 \otimes |\tilde{0}, \tilde{1}, \tilde{0}, \tilde{m}_1, \tilde{m}_2\rangle_2$ means that this particular eigenvector is adiabatically connected to the basis state corresponding to a single rotational excitation in molecule 2. When the state mixing is well calibrated, a lot of eigenstates have a clearly dominant component which allows us to keep the representation of encoding different qubits in different molecules.

When the assignment of the qubit states is chosen, the realization of a gate by optical addressing involves finding a laser pulse which acts on every state of the computational basis set and steers them to the final state corresponding to a truth table of a logical gate. For instance, a controlled-NOT gate (CNOT) is a two-qubit gate which corresponds to the classical exclusive OR (XOR) gate. It requires four molecular states, mapped with the four basis states $|00\rangle$, $|01\rangle$, $|10\rangle$, and $|11\rangle$, respectively. The gate operates on each basis state so that CNOT $|x, y\rangle = |x, x \oplus y\rangle$ where $x, y = 0, 1$ and where $\oplus$ is the addition modulo 2. In this example, the gate corresponds to the following unitary transformation among the states:

$$U_{\text{CNOT}} = \begin{pmatrix} 1 & 0 & 0 & 0 \\ 0 & 1 & 0 & 0 \\ 0 & 0 & 0 & 1 \\ 0 & 0 & 1 & 0 \end{pmatrix}$$

The single pulse able to steer the transformation for any input, be it a basis state or any superposition of the four basis states, is usually called the gate's "universal" pulse.

The desired algorithms are broken down into a sequence of elementary gates, each corresponding to a specific population transfer between the states of our basis. In our approach, these population transfers are implemented theoretically through optimized laser fields which we determine by different quantum control strategies.

4 Control Strategies

The coupling with a control field is described in the dipolar approximation, and the field $W(t)$ is polarized linearly in the Z direction in the laboratory frame:

$$W(t) = -\sum_{i=1}^{2} \varepsilon(t)\mu_{i,z}\cos\theta_i \tag{7}$$

Where $\mu_{i,z}$ and θ_i are defined in Eq. (3). We illustrate two completely different control strategies in the following sections. In the first example, a selected population inversion between a given couple of states j, k is driven by π pulses $\varepsilon(t) = A(t)\sin^2(\pi t/\tau)\cos(\omega_{jk}t)$ with a resonant carrier frequency and an envelope $A(t)$ chosen so that the integral of the Rabi frequency $\Omega(t) = A(t)\mu_{jk}/\hbar$ is an integer multiple of π [7]. The main problem in this context is to avoid unwanted transitions which are off resonant and which therefore could lead to a transition with a probability smaller than one but still too high to be acceptable for a logic gate. The duration of the pulse τ is then adapted to avoid unwanted transitions. By the Rosen–Zener expression [33] giving the probability of an off-resonant transition for a hyperbolic secant pulse, we have determined that the duration of a sine square pulse must satisfy $\tau > 10/\delta$ where δ is the detuning in frequency.

In the second example, the pulse is designed by optimal control theory. The field is obtained on a time grid by iteratively optimizing a functional measuring the performance index under the constraints that the time-dependent Schrödinger equation is verified at any time and that the laser fluence remains acceptable. The objective is here to realize the $2^n \times 2^n$ unitary transformation associated with the n-qubit gate so that any input, be it a computational basis state or a superposed state, is driven toward the corresponding output. We adopt the procedure of the multi-target optimal control theory with a phase constraint to ensure that the gate is correct for superposed states [4].
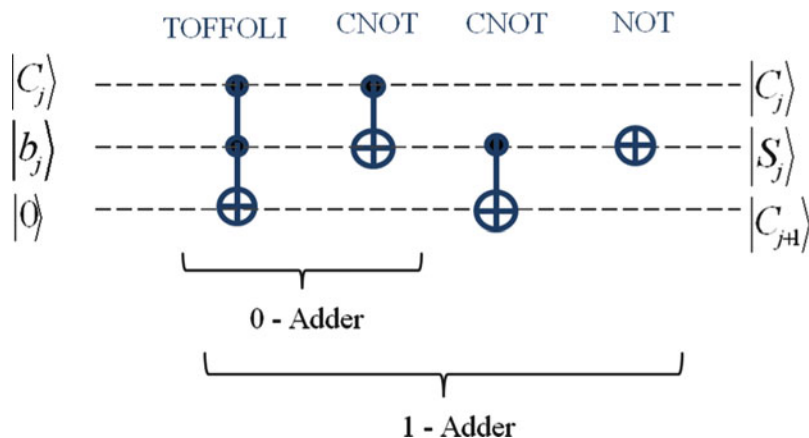
Fig. 2 Scheme of the quantum gates for the 0- and 1-adder. The three lines represent qubit 1, qubit 2, and qubit 3, respectively. The carry-in C_j and the added binary number b_j are encoded in rotational and vibrational states of the first molecule. The carry-out C_{j+1} is encoded in the rotation of the second molecule, which is ready for cycling. The *black circles* represent control qubits, while the *crossed circles* represent target qubits, i.e., qubits whose value will be flipped if the corresponding control qubit(s) is equal to 1. For example, the Toffoli gate will flip the value of the third qubit if and only if the first two qubits are equal to 1

5   Adder with Two NaCs Molecules

An adder is an arithmetic operation which only involves population inversion between selected states. It operates rank by rank to add 0 or 1 to a binary digit b_j at a rank j with a carry-in C_j and provides at each cycle a sum S_j and a carry-out C_{j+1} for the following cycle. It is appealing to use internal states of a trapped molecule to operate an addition cycle within this molecule while transmitting the carry C_{j+1} to the neighboring one to continue the process. A full quantum adder for a single cycle of addition requires four qubits. Simulations using qubits encoded in vibrational states of a single polyatomic molecule have been carried out recently [9,16,17]. In the context of trapped molecules, we simulate the first step of a network by focusing on the transmission of the carry [16]. We begin with a simpler gate, the 0- or 1-adder which needs three qubits only. The first qubit encodes C_j, the second one the digit b_j, and the third C_{j+1}. The first two qubits C_j and b_j are encoded in the first molecule and C_{j+1} in the neighboring one. Whether we add 0 or 1 is determined by the pulse itself: one pulse drives the 0-adder while another one drives the 1-adder. The logical circuit is given in Fig. 2. The CNOT and TOFFOLI gates inverse the state of the target qubit only if the control qubit or the two control qubits are in state 1. One sees in Fig. 2 that some gates are intramolecular when control and target qubits are encoded in a single molecule, while some gates are intermolecular when the qubits are distributed between the two sites.

For arithmetic operations, the system is always in a computational basis state. No superposed states are used, so one can first optimize the population inversion by
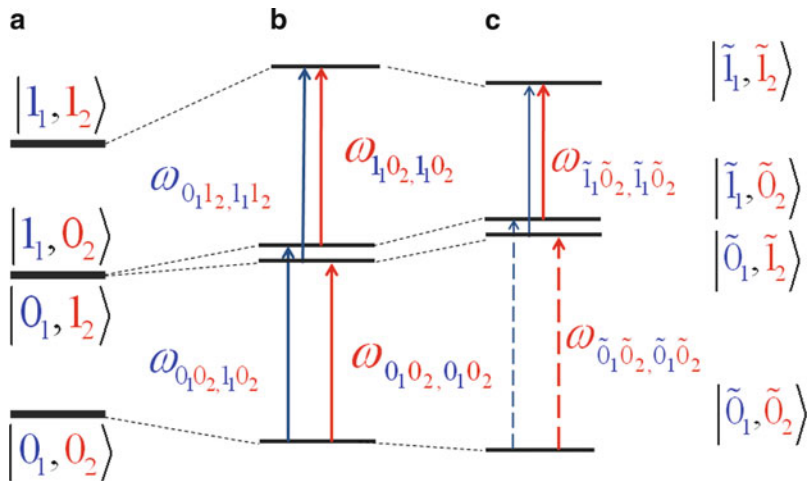
Fig. 3 Lowest rotational states of two neighboring molecules for three situations: (**a**) without Stark field or dipole–dipole interaction, (**b**) with a Stark field with $E_1 > E_2$, and (**c**) with a Stark field and dipole–dipole coupling. The *dashed arrow* represents the transition which must be selectively driven to realize a CNOT gate, i.e., to inverse the state of the second molecule if and only if when the first one is in state 1 only

neglecting the control of the phase. This can be done by using π pulses calibrated to induce particular transitions selectively. A phase control could be imposed by using optimal control theory as done in the next section. We start by illustrating the case of an intermolecular CNOT gate encoded in two molecules. In this simulation we do not take the hyperfine structure into account. The qubits are encoded in the eigenstates correlated with rotational states of the ground vibrational state $|\tilde{v}, \tilde{N}, \tilde{m}_N\rangle_1 \otimes |\tilde{v}, \tilde{N}, \tilde{m}_N\rangle_2$ with $\tilde{v} = 0$ and $\tilde{m}_N = 0$. They are noted $|\tilde{N}_1, \tilde{N}_2\rangle$ with $N_1 = 0$ or 1 and $N_2 = 0$ or 1. Figure 3 shows how the zero-order states (part a) evolve with the Stark field with $E(Z_1) > E(Z_2)$ (part b) and finally by the dipole–dipole interaction (part c). A conditional rotational transfer in molecule 2, i.e., a transfer which only takes place if molecule 1 is in state $\tilde{N}_1 = 1$, can be driven by a π pulse calibrated to induce the resonance transition $\omega_{\tilde{1}_1\tilde{0}_2,\tilde{1}_1\tilde{0}_2}$ selectively. By assuming an intermolecular distance of 300 nm and two electric fields of $2\,\text{kVcm}^{-1}$ and $1.5\,\text{kVcm}^{-1}$, respectively, the active transition and the unwanted one differ by $4.001\ 10^{-9}\,\text{cm}^{-1}$ so that the duration of the pulse falls in the microsecond time scale. We use $\tau = 13.2\ \bar{}$ s for a maximum amplitude $A_{\max} = 7.5\ \text{Vm}^{-1}$.

Three qubits are necessary to simulate the 0- or 1-adder: $Q_1 = C_j$, $Q_2 = b_j$, and $Q_3 = 0$, as shown in Fig. 2 The logical states are encoded in states $|\tilde{v}_1, \tilde{N}_1, \tilde{v}_2, \tilde{N}_2\rangle$ connected with the highest weight on the product state corresponding to vibrational and rotational excitation in the first molecule and only rotational excitation in the second molecule. This allows a representation with the carry-in C_j encoded in the rotation of the first molecule and the first digit b_j in the vibration, while the carry-out C_{j+1} is in the rotation of the second molecule. The assignment is $010 \rightarrow |\tilde{0}_1\tilde{0}_1\tilde{0}_2\tilde{0}_2\rangle$,
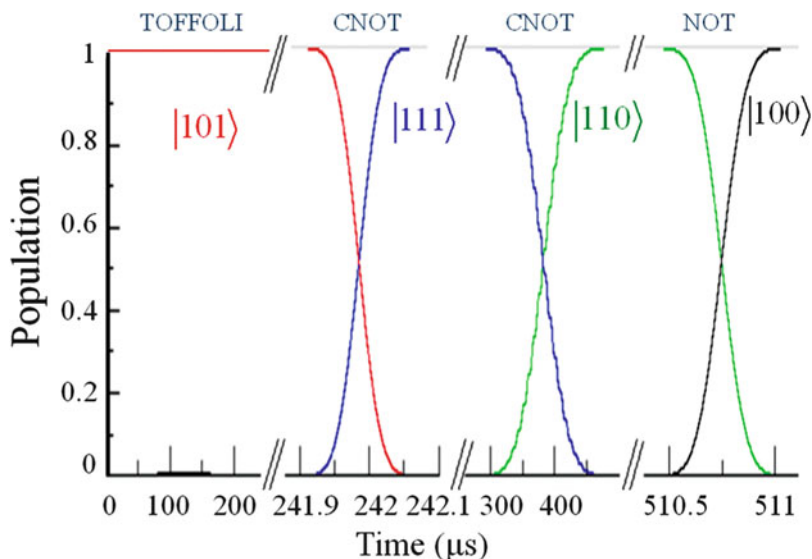
Fig. 4 Example of evolution of the states $|101\rangle$ ($C_j = 1$ and $b_j = 0$), $|111\rangle$, and $|110\rangle$ during the four gates of the 1-adder to yield the output $|100\rangle$ ($C_j = 1$, $S_j = 0$, $C_{j+1} = 1$)

$011 \rightarrow |\tilde{0}_1\tilde{0}_1\tilde{0}_2\tilde{1}_2\rangle$, $110 \rightarrow |\tilde{0}_1\tilde{1}_1\tilde{0}_2\tilde{0}_2\rangle$, $111 \rightarrow |\tilde{0}_1\tilde{1}_1\tilde{0}_2\tilde{1}_2\rangle$, $000 \rightarrow |\tilde{2}_1\tilde{2}_1\tilde{0}_2\tilde{0}_2\rangle$, $001 \rightarrow |\tilde{2}_1\tilde{2}_1\tilde{0}_2\tilde{1}_2\rangle$, $100 \rightarrow |\tilde{2}_1\tilde{3}_1\tilde{0}_2\tilde{0}_2\rangle$, and $101 \rightarrow |\tilde{2}_1\tilde{3}_1\tilde{0}_2\tilde{1}_2\rangle$.

As seen in Fig. 2 the first Toffoli gate is an intermolecular gate. It requires the population inversion $|\tilde{0}_1, \tilde{1}_1, \tilde{0}_2, \tilde{0}_2\rangle \leftrightarrow |\tilde{0}_1, \tilde{1}_1, \tilde{0}_2, \tilde{1}_2\rangle$, while the transition $|\tilde{2}_1, \tilde{2}_1, \tilde{0}_2, \tilde{0}_2\rangle \leftrightarrow |\tilde{2}_1, \tilde{2}_1, \tilde{0}_2, \tilde{1}_2\rangle$ must be avoided. In the subspace of the 2^3 states, one can identify two active transitions for a CNOT gate and four transitions for a NOT gate since the 2-qubit CNOT gate must be steered for any state of the third qubit and similarly a 1-qubit gate is to be realized for the four states of the two other qubits. The length of the π pulses is calibrated to drive all the active transitions with a single-carrier frequency and to avoid all the unwanted transitions. For example, Fig. 4 shows the action of the 1-adder network on a computational basis state $|101\rangle$ corresponding to the inputs $C_j = 1$ and $b_j = 0$ to provide the logical state $|100\rangle$ associated to $C_j = 1$, $S_j = 0$, and $C_{j+1} = 0$. The intermolecular gates mainly involve rotational excitations in the microwave domain and are in the microsecond time scale, while the intramolecular gates involve vibrational excitation and can be carried out in the infrared spectrum in the nanosecond range.

# 6 Grover's Algorithm with Two ^{41}K^{87}Rb Molecules

This quantum algorithm is more demanding than the previous example because it involves superposed states and therefore requires a control of the phase. A simulation of another quantum algorithm with two NaCs molecules was also

performed [16]. The aim of the Grover search algorithm [34] is to find a specific item $|a\rangle$ in an unsorted database containing $N = 2^n$ elements. The most efficient classical algorithm would be to examine each item one by one and would require at least $0.5N$ queries on average, while the quantum search will retrieve the item with only $O(\sqrt{N})$ queries thanks to quantum parallelization. Each element of the database is associated with a basis state of an n-qubit register. The first step of the algorithm prepares the register in a superposed state $|\psi_0\rangle = N^{-1/2} \sum_{i=1}^{N} |i\rangle$ of all the basis states with an equal weight. This can be done by a Hadamard gate (*HAD*) on each qubit, i.e., $HAD\,|0\rangle = 2^{-1/2}(|0\rangle + |1\rangle)$ and $HAD\,|1\rangle = 2^{-1/2}(|0\rangle - |1\rangle)$. The idea is then to iterate the application of two gates to transform the well-balanced $|\psi_0\rangle$ state into a superposition with an increasing weight for state $|a\rangle$. After k iterations, $|\psi_0\rangle$ becomes

$$|\psi_k\rangle = \sin\left[(k + 1/2)\,\theta\right]|a\rangle + \cos\left[(k + 1/2)\,\theta\right]|\psi - a\rangle \qquad (8)$$

where $\sin(\theta/2) = N^{-1/2}$. The first of the two gates adds a phase π to the selected $|a\rangle$ state. It is sometimes called the *oracle gate* because it marks the target item. It is therefore a unitary transformation **O** represented by a diagonal matrix with $O_{jj} = 1$ for $j \neq a$ and $O_{aa} = -1$. The second gate **I** is called the *inversion about average*, i.e., an operation which transforms the amplitudes so that they are as much above or below their average as they were below or above before the operation [34]. The corresponding matrix is $I_{ij,j\neq i} = 2/N$ and $I_{ii} = -1 + 2/N$. If m_k is the average of the amplitudes at the kth iteration, each amplitude after the phase gate becomes $c_j^{(k)} \rightarrow m_k - \left(c_j^{(k)} - m_k\right)$. We illustrate below the simplest case with two qubits which are encoded in two neighboring molecules. In a 2-qubit case, $\theta = \pi/3$ so that a single iteration is necessary to obtain the chosen item $|\psi_1\rangle = |a\rangle$, for instance, $|a\rangle = |10\rangle$. The desired item out of four is found by a single query, i.e., a single application of the two gates after the Hadamard preparation step. The three steps, Hadamard, phase, and inversion about average, are illustrated in Fig. 5. The simulation is carried out with two $^{41}K^{87}Rb$ molecules with $I_1 = I_2 = 3/2$ [18]. The distance between the two molecules is assumed to be 100 nm and is chosen to increase the dipole–dipole interaction and reduce the pulse duration. The magnetic field on each molecule is equal to 500 Gauss and 400 Gauss, respectively. The electric field has also a gradient in the Z direction so that the field affecting each molecule is equal to $1\,\mathrm{kVm^{-1}}$ and $0.8\,\mathrm{kVm^{-1}}$, respectively. The four basis states of the two qubits are eigenstates of the full Hamiltonian correlating to the product states $|v, N, m_N, m_1, m_2\rangle_1 \otimes |v, N, m_N, m_1, m_2\rangle_2$ with $N_1 = 0, 1$, $N_2 = 0, 1$ and $v = 0$, $m_N = 0$, and $m_1 = m_2 = 3/2$ with a weight higher than 99%. The states involve zero or a single rotational excitation in the first or second molecule. They are coupled via excited states, and we selected a group of intermediary levels according to the most significant transition dipole moments to obtain a reduced dynamical basis set out of a very large number of eigenstates including all the states up to $N = 2$. Figure 5 shows the evolution of the population of state $|a\rangle = |10\rangle$. During the Hadamard gate applied on the fiducial state $|00\rangle$, the probability of state
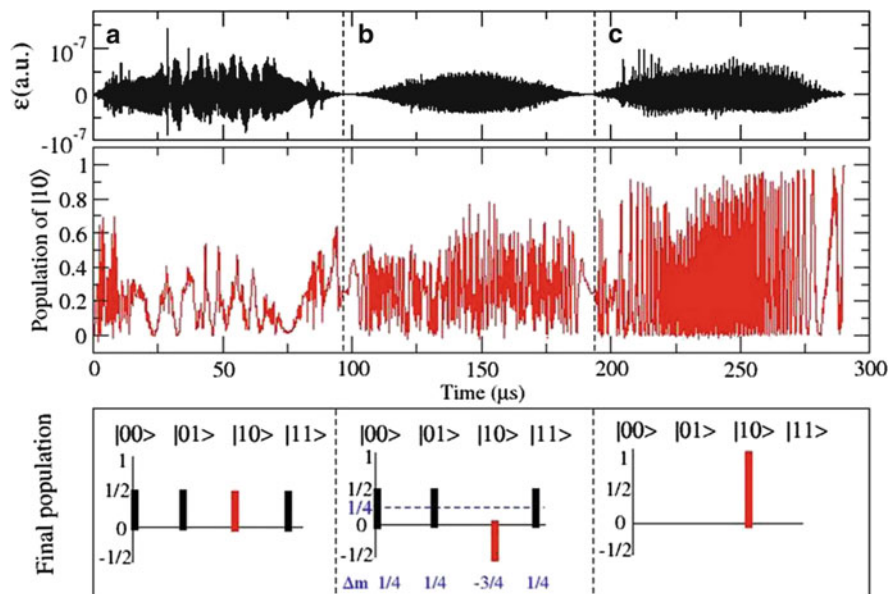
Fig. 5 Illustration of the action of the three gates (Hadamard, oracle, and inversion about average) of the 2-qubit Grover algorithm in a case for which the searched item is associated to the state $|10\rangle$: evolution of the population of the state $|10\rangle$ during the optimal pulses for each quantum gate implemented in the $^{41}K^{87}Rb$ molecule. After the oracle, the average (*dashed line*) is $m = 1/4$. The inversion about average yields $c_j \rightarrow m - \Delta m_j$

$|a\rangle = |10\rangle$ reaches 0.25. Then sequence of the oracle pulse and the inversion around the average leads to a probability of 1 for the $|a\rangle = |10\rangle$ state.

7 Concluding Remarks

Using different control strategies, π pulses, or optimal control pulses, we have numerically investigated the implementation of both intra- and intermolecular gates on qubit states encoded in the rotational or hyperfine states of ultracold polar diatomic molecules trapped in an optical lattice and coupled by the dipole–dipole interaction. The energy level structure is modulated by external electric or magnetic fields so that each molecule is addressable. The rich structure of the hyperfine levels, the long lifetimes, the possibility of entanglement by the dipolar coupling, and the availability of pulse shaping in the microwave regime make the hyperfine states potential candidates for qubit encoding and open interesting perspectives toward scalability.

References

1. Nielsen, M.A., Chuang, I.L.: Quantum Computation and Quantum Information. Cambridge University Press, Cambridge (2000)
2. Ladd, T.D., Jelezko, F., Laflamme, R., Nakamura, Y., Monroe, C., O'Brien, J.L.: Quantum computers. Nature **464**, 45–53(2010)
3. Aspuru–Guzik, A.: Dutoi, A.D., Love, P.J., Head-Gordon, M. Simulated quantum computation of molecular energies. Science **309**, 1704–1707 (2005)
4. Tesch, C.M., de Vivie–Riedle, R.: Vibrational molecular computing basis set independence and theoretical realization of the Deutsch–Jozsa algorithm. J. Chem. Phys. **121**, 12158–12168 (2004)
5. Troppmann, U., de Vivie–Riedle, R.: Mechanisms of local and global molecular quantum gates and their implementation prospects. J. Chem. Phys. **122**, 154105–1–9 (2005)
6. Korff, B.M.R., Troppmann, U., Kompa, K.L., de Vivie–Riedle, R.: Manganese pentacarbonyl bromide as candidate for a molecular qubit system operated in the infrared regime. J. Chem. Phys. **123**, 244509–1–9 (2005)
7. Cheng, T., Brown, A.: Quantum computing based on vibrational eigenstates: pulse area theorem analysis. J. Chem. Phys. **124**, 034111–1–8 (2006)
8. Ndong, M., Lauvergnat, D., Chapuisat, X., Desouter-Lecomte, M.: Optimal control simulation of the Deutsch-Jozsa algorithm in a two-dimensional well coupled to an environment. J. Chem. Phys. **126**, 244505–244511 (2007)
9. Bomble, L., Lauvergnat, D., Remacle, F., Desouter-Lecomte, M.: Vibrational computing: simulation of a full adder by optimal control. J. Chem. Phys. **128**, 064110–1–11 (2007)
10. Tsubouchi, M., Momose, T.: Rovibrational wave packet manipulation using shaped mid-infrared femtosecond pulses toward quantum computation: optimization of pulse shape by genetic algorithms. Phys. Rev. A **77**, 052366–1–14 (2008)
11. Bomble, L., Lauvergnat, D., Remacle, F., Desouter-Lecomte, M.: Controlled full adder or subtractor by vibrational computing. Phys. Rev. A **80**, 022332–1–8 (2009)
12. Schröder, M., Brown, A.: Realization of a CNOT quantum gate operation in six–dimensional ammonia using the OCT–MCTDH approach. J. Chem. Phys. **131**, 034101–1–10 (2009)
13. Mishima, K., Yamashita, K.: Free–time and fixed end-point optimal control theory in quantum mechanics: application to entanglement generation. J. Chem. Phys. **130**, 034108–1–11 (2009)
14. Sugny, D., Bomble, L., Ribeyre, T., Dulieu, O., Desouter-Lecomte, M.: Rovibrational CNOT gates using optimized stimulated Raman adiabatic passage techniques and optimal control theory. Phys. Rev. A **80**, 042325–1–11 (2009)
15. Ohtsuki, Y.: Simulating quantum search algorithm using vibronic states of I_2 manipulated by optimally designed gate pulses. New J. Phys. **12**, 045002–1–18 (2010)
16. Bomble, L., Pellegrini, P., Ghesquière, P., Desouter-Lecomte, M.: Toward scalable information processing with ultra–cold polar molecules in an electric field. A numerical investigation. Phys. Rev. A **82**, 062323–1–12 (2010)
17. Bomble, L., Lauvergnat, D., Remacle, F., Desouter-Lecomte, M.: Controlled full adder-subtractor by vibrational computing. Phys. Chem. Chem. Phys. **12**, 15628–15635 (2010)
18. Pellegrini, P., Vranckx, S., Desouter-Lecomte, M.: Implementing quantum algorithms in hyperfine levels of ultracold polar molecules by optimal control theory. Phys. Chem. Chem. Phys. **13**, 18864–18871 (2011)
19. Pellegrini, P., Desouter-Lecomte, M.: Quantum gates driven by microwaves pulses in hyperfine levels of ultracold heteronuclear dimers. Eur. Phys. J. D **64**, 163–170 (2011)

20. Zaari, R.R., Brown, A.: Effect of diatomic molecular properties on binary laser pulse optimizations of quantum gate operations. J. Chem. Phys. **135**, 044317–1–7 (2011)
21. Wei, Q., Kais, S., Friedrich, B., Herschbach, D.: Entanglement of polar symmetric top molecules as candidate qubits. J. Chem. Phys. **135**, 154102–1–10 (2011)
22. DeMille, D.: Quantum computation with trapped polar molecules. Phys. Rev. Lett. **88**, 067901–1–4 (2002)
23. Danzl, J.G., Mark, M.J., Haller, E., Gustavsson, M., Hart, R., Aldegunde, J., Hutson, J.M., Nägerl, H.C.: An ultra cold high-density sample of rovibronic ground state molecules in an optical lattice. Nat. Phys. **6**, 265–270 (2010)
24. Yelin, S.F., Kirby, K., Côté, R.: Schemes for robust quantum computation with polar molecules. Phys. Rev. A **74**, 050301–1–4 (2006)
25. Kuznetsova, E., Côté, R., Kirby, K., Yelin, S.F.: Analysis of experimental feasibility of polar–molecule–base phase gates. Phys. Rev. A **78**, 012313–1–11 (2008)
26. Brickman Soderberg, K.A., Gemelke, N., Chin, C.: Ultracold molecules: vehicles to scalable quantum information processing. New J. Phys. **11**, 055022–14 (2009)
27. Carr, L.D., DeMille, D., Krems, R.V., Ye, J.: Cold and ultracold molecules: science, technology and applications. New J. Phys. **11**, 055049–1–87 (2009)
28. Aldegunde, J., Ran, H., Hutson, J.M.: Manipulating ultracold polar molecules with microwave radiation: The influence of hyperfine structure. Phys. Rev. A **80**, 043410–1–5 (2009)
29. Charron, E., Milman, P., Keller, A., Atabek, O.: Quantum phase gate and controlled entanglement with polar molecules. Phys. Rev. A **78**, 012313–1–9 (2007)
30. Ospelkaus, S., Ni, K.K., Quéméner, G., Neyenhuis, B., Wang, D., de Miranda, M.H.G., Bohn, J.L., Ye, J., Jin, D.S.: Controlling the hyperfine state of rovibronic ground-state polar molecules. Phys. Rev. Lett. **104**, 030402–1–4 (2010)
31. Aldegunde, J., Rivingston, B.A., Zuchowski, P.S., Hutson, J.M.: Hyperfine energy levels of alkali-metal dimers: Ground–state polar molecules in electric and magnetic fields. Phys. Rev. A **78**, 033434–1–033434–8 (2008)
32. Deiglmayr, J., Aymar, M., Wester, R., Weidenmüller, M., Dulieu, O.: Calculations of the static dipole polarizabilities of alkali dimers: Prospects for alignment of ultracold molecules. J. Chem. Phys. **129**, 064309–1–13 (2008)
33. Rosen, N., Zener, C.: Double Stern-Gerlach experiment and related collision phenomena. Phys. Rev. **40**, 502–507 (1932)
34. Grover, K.L.: Quantum mechanics helps in searching a needle in haystack. Phys. Rev. Lett. **79**, 325–328 (1997)